# MODELING AND VIBRATION CONTROL WITH A NANOPOSITIONING MAGNETIC-LEVITATION SYSTEM

A Dissertation

by

YOUNG HA KIM

Submitted to the Office of Graduate Studies of
Texas A&M University
in partial fulfillment of the requirements for the degree of

DOCTOR OF PHILOSOPHY

December 2011

Major Subject: Mechanical Engineering

# MODELING AND VIBRATION CONTROL WITH A NANOPOSITIONING MAGNETIC-LEVITATION SYSTEM

A Dissertation

by

YOUNG HA KIM

Submitted to the Office of Graduate Studies of
Texas A&M University
in partial fulfillment of the requirements for the degree of

DOCTOR OF PHILOSOPHY

Approved by:

| | |
|---|---|
| Chair of Committee, | Won-jong Kim |
| Committee Members, | Alan Palazzolo |
| | Yong-Joe Kim |
| | John E. Hurtado |
| Head of Department, | Jerald A. Caton |

December 2011

Major Subject: Mechanical Engineering

# ABSTRACT

Modeling and Vibration Control with a Nanopositioning Magnetic-Levitation System.

(December 2011)

Young Ha Kim,

B. Eng., Inha University, Incheon, Korea

M. S., Pennsylvania State University

Chair of Advisory Committee: Dr. Won-jong Kim

This dissertation demonstrates that a magnetic-levitation (maglev) stage has the capabilities to control movements and reject vibration simultaneously. The mathematical model and vibration control scheme with a 6-degree-of-freedom (6-DOF) maglev stage for nanoscale positioning are developed for disturbance rejection. The derived full nonlinear dynamic equation of motions (EOMs) of the maglev stage include translational and rotational motions with differential kinematics. The derived EOMs and the magnetic forces are linearized to design a multivariable controller, a Linear Quadratic Gaussian with Loop Transfer Recovery (LQG/LTR), for vibration disturbance rejection in a multi-input multi-output (MIMO) system. For a more accurate model, the dynamics of an optical table with a pneumatic passive isolation system is also considered. The model of the maglev stage with the optical table is validated by experiments. Dual-loop controllers are designed to minimize the influence of the vibration disturbance between the moving platen and the optical table in the *x*-, *y*-, and *z*-axes motions. The inner-loop compensator

regulates the velocity to reject vibration disturbance and the outer-loop compensator tracks positioning commands. When the vibration disturbances of 10 to 100 Hz are applied, the vibration-reduction ratios are about 30 to 65 percent in horizontal motion and 20 to 45 percent in vertical motion. In addition, the vibration disturbances of 45.45 Hz are attenuated by about 4 to 40 percent in angular motions. The vibration control schemes are effective in not only translational but rotational motions. In step responses, the vibration control schemes reduce the wandering range in the travel from the origin to another location. Positioning and tracking accuracies with the vibration controller are better than those without the vibration controller. In summary, these dual-loop control schemes with velocity feedback control improved the nanopositioning and vibration/disturbance rejection capabilities of a maglev system.

# DEDICATION

*To my parents Kye Won Kim and Gab Seon Jung,*

*my son Yale Kim,*

*and*

*my wife Min Jung Cha*

## ACKNOWLEDGMENTS

This dissertation cannot be completed without the encouragement, support, help and guidance of many. First of all, I would like to thank my parents, Kye Won Kim and Gab Seon Jung, for all the trust, support, and devoted love that they have given me. I truly owe them every success of my life.

I would like to thank my committee chair, Dr. Won-jong Kim, for his consistent encouragement, motivation and patience until I completed this dissertation. I appreciate his giving me a chance to formulate my research problem and to pursue it my own way. My interaction with him over the past six years was a great learning experience in all aspects of research.

I wish to thank Dr. Alan Palazzolo, Dr. Yong-Joe Kim, and Dr. John E. Hurtado for serving as my committee members and sharing their wisdom, expertise, and precious comments with me. I sincerely appreciate the time, advice and support they provided me during my doctoral study.

I am grateful to Dr. Kim's former students Shobhit Verma who worked on the design and fabrication, precision assembly of the Y-shaped stage, Jie Gu who developed software for the user interface, and Vu Nguyen who helped to debug my programs. In addition, I also thank Yi-chu Chang, Jiawei Dong, Naveen Kumar Bibinagar, Rohit Chintala, and Jose Christian Silva-Rivas in the Precision Mechatronics and Nanotechnology Lab for the friendly environment they made.

A special note of thanks goes to my wife Min Jung for her unbounded love, encouragement, understanding, and prayer. I also owe appreciation to Pastors Hong Il Lim and Young Sik An, and all members of Vision Mission Church for encouraging and praying for me. Above all, I express my deepest gratitude to God, Jesus Christ, and the Holy Spirit for creating, loving, calling, training, and blessing me. “By the grace of God I am what I am” (1 Corinthians 15:10).

# TABLE OF CONTENTS

CHAPTER Page

CHAPTER Page

Page

# LIST OF TABLES

# LIST OF FIGURES

FIGURE Page

FIGURE Page

FIGURE Page

FIGURE Page

FIGURE Page

FIGURE Page

FIGURE Page

# CHAPTER I

# INTRODUCTION

## 1.1 Background and Motivation

The importance of nanopositioning systems increases as nanotechnology research requires more precise positioning control and manipulation of material and devices in nanoscale. After the invention of the scanning tunneling microscope (STM) by the IBM Zurich researchers, Binning and Rohrer in 1981 [1], and later, the atomic-force microscope (AFM) by Binning, Quate, and Gerber in 1986 [2], nanopositioning began to have practical importance in many areas such as microelectronics manufacturing, fiber optic component manufacturing technology, photonics, ultra-precision machining and processing, molecular biology, and integrated-circuit manufacturing.

Many instruments are sensitive to mechanical vibration and acoustic noise. These vibrations can arise from sources like traffic, wind, earthquakes, human action, heating, ventilation and air conditioning equipment (HVAC), and production machinery both outside and inside a building. The vibration disturbances are major obstacles in nanotechnology. Advanced instruments and high-precision machines including AFMs,

---

This dissertation follows the style of *IEEE Transactions on Mechatronics.*

laser interferometers, and semiconductor photolithograph equipment are vibration-sensitive and must be operated in a stable environment. Therefore, vibrations should be reduced in these types of machines.

## 1.2 High-Precision Positioning Technologies

High-precision positioning systems can be classified by the actuators utilized in nanopositioning systems. Following are three major categories: conventional motor-driven types, piezoelectric-driven types, and maglev types. This dissertation focuses on maglev systems.

### 1.2.1 Conventional Motor-Driven Stages

Conventional precision positioning platforms use crossed-axis stages driven by linear or rotary motor. These devices typically consist of a DC servomotor or stepper motor, a precision screw-and-nut set, and ball or roller bearings for guidance and suspension. Two representative examples of conventional motor-driven stages are shown in Fig. 1-1.

DC motors provide smooth, continuous motion as well as high speed and submicron accuracy when used with an encoder. However, a DC motor requires constant power or an external brake to maintain position. In set-and-hold applications, it is not a good candidate due to energy inefficiency. It generates a significant amount of undesired

heat and requires feedback mechanisms to control position and velocity. The bulky DC motors often dither or oscillate around the position because of hysteresis.

Unlike DC motors, a stepper motor has an inherent holding torque that can be used to maintain the position of devices in the power-off mode for a period time. Therefore, stepper motors provide inexpensive open-loop method to achieve relatively high accuracy. However, stepper motors do not provide smooth continuous motion and generate a significant amount of undesired heat. In addition, they are bulky and noisy.

(a) (b)

Fig. 1-1. Griffin Motion LLC's CXY-BS series stages are designed for factory automation and semiconductor processing equipment: (a) a brushless servo-motor-driven stage and (b) a stepper-motor-driven stage. The photographs can be obtained from the website at www.griffinmotion.com [3].

### 1.2.2 Piezoelectric-Driven Stages

These days, lead-zirconate-titanate (PZT) actuators are one of the most popular actuating mechanisms in ultra-high precision systems [4]. They use the piezoelectric effect, where certain crystalline materials change shape or dimension when electrostatic potential is applied.

However, difficulties of the control of piezoelectric actuators are limited in bandwidth and resolution by actuator dynamics that includes creep, hysteretic nonlinearities, and vibrations. Closed-loop control is required to eliminate hysteresis and creep. An example of the positioning stage with closed-loop control is shown in Fig. 1-2.

Fig. 1-2. Physik Instrumente (PI)'s P-915KHDS XY scanning stage is driven by four multilayer stack piezo actuators. The photograph can be obtained from the website at www.physikinstrumente.com [5].

All of the above problems can be overcome with the use of flexure-guided stages presented in Fig. 1-3. Flexure-guided stages restrict each axis of the stage to move in

only one direction. These stages effectively decouple the unwanted motions in the piezoactuator and produce pure linear translation [6, 7]. A flexure-guided stage driven by piezoelectric actuators exhibits subnanometer resolution. However, a very small motion range is another major disadvantage of the piezoelectric actuator. A flexure-guided stage has a few to tens of micrometers of travel range.

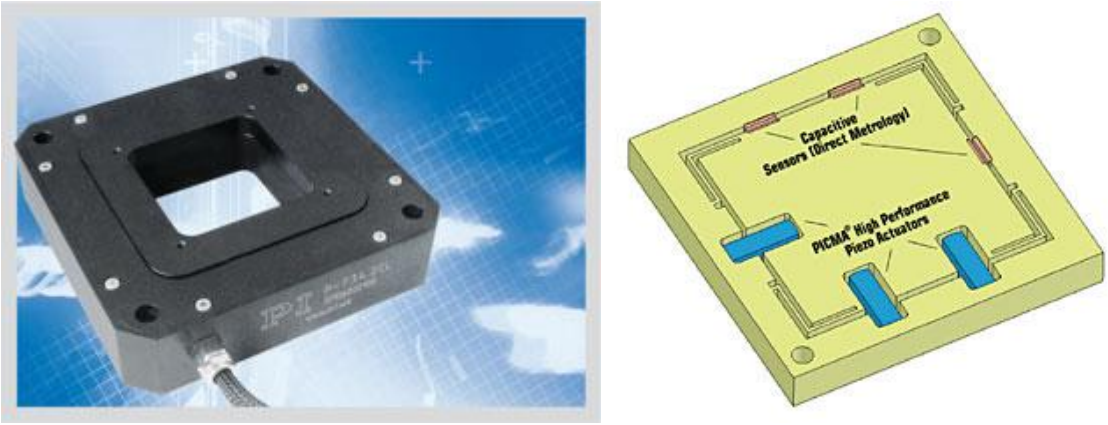


(a) (b)

Fig. 1-3. (a) PI's P-734 flexure nanopositioning stage with ultra-precise trajectory [8]. (b) Working principle of a flexure-guided XY piezo stage [9]. The photographs can be obtained from the website at www.physikinstrumente.com.

To overcome the small travel range, stacking multiple piezoactuators that amplify the displacement have been developed in many ways. Nevertheless, due to the stress generated in piezoelectric slice and the position error in the end of stack, the length of a piezoelectric stack is limited. According to Masi [4], changing the thickness of a 10-mm-thick piece of PZT by 100 nm would require a potential of 2,670 V.

A piezoelectric linear motor is an alternative solution of limitation of small range motion. Piezoelectric linear motors can be classified into two groups: resonant motors

(ultrasonic motors), and non-resonant motors (step motors). A piezoelectric step motor generally consists of several individual piezoelectric actuators and generates motion through succession of coordinated clamp/unclamp and expand/contract cycles. Theoretically, the travel range of a piezoelectric linear motor is unlimited. However, the limiting factors of a piezoelectric step motor are relatively small payload due to its friction-based working principle and slow movement at a speed of up to 10 mm/s [10]. An ultrasonic motor can produce velocity up to several hundred millimeters per second but has lower resolution.

The stages driven by conventional motors or piezoelectric actuators are generally cross-axis stages and do not have capability in rotational motion inherently. Hexapod parallel-kinematic positioning systems in Fig. 1-4 were developed to generate a full 6-DOF motion. They have a large travel range in translation and rotation. However, the best resolution of the hexapod is about 300 nm [11].

Fig. 1-4. PI's M-850 compact 6-axis-positioning system [12]. The photograph can be obtained from the website at www.physikinstrumente.com.

### 1.2.3 Maglev System and Its Advantages

An ideal precision-positioning system should have the large range of motion, six DOFs, and nanometer positioning resolution because objects in nanoscale are required to be scanned, pushed or pulled, cut, picked, positioned, moved, oriented, indented, bended, twisted, assembled, and so on.

Because crossed-axis stages driven by conventional motors or piezoelectric actuators cannot generate rotational motion, they require additional independent actuators for the small rotational motion. Those actuators make the system more complex and difficult to control in positioning. Besides, mechanical positioning systems suffer from friction especially when precision in the nanometer scale is required. Friction modeling has been studied by several research groups and various models have been proposed in the literature [13]. However, it is still difficult to find a proper friction model under nanoscale circumstance [14].

A maglev positioning system is an excellent candidate for the ideal precision positioning system that has six DOFs, nanoscale resolution without any friction, hysteresis, creep, and backlash. In addition, because maglev technology does not require any lubricants or generate wear particles, it is suitable for clean-room or vacuum environments.

Although maglev principles have been applied to the various areas such as maglev train, magnetic suspension, magnetic bearing, and so on, Slocum and Eisenhaure suggested the first precision positioning system using magnetic levitation called as the Angstrom Resolution Measurement Machine (ARMM) [15]. Trumper modified the

original ARMM and developed a magnetic bearing X-Y stage system [16]. Williams, et al. introduced a one-main-axis maglev stage that uses electromagnetic force to control three rotational and two translational motions of a platen and a permanent-magnetic linear motor to control translational motion in one main axis. They demonstrated that an existing linear magnetic bearing has the capability for precision X-Y positioning at the level required for photolithography [17]. Several research groups developed multi-axis precision positioning devices using maglev technology since it has been demonstrated successfully for nanopositioning applications. Kim introduced a planar magnetically levitated stage [18]. This is the first stage that is capable of providing all the motions required for photolithography with only one moving part. Four permanent-magnet linear motors provide both suspension and driving force and levitate the platen without contact.

Like other technologies, maglev systems also have drawbacks. They are open-loop unstable and highly nonlinear systems because of nonlinear dependencies in position in electromagnetic forces and EOMs in six DOFs. However, those difficulties can be overcome by enhanced modeling of the system and applying advanced feedback control.

## 1.3 Prior Arts of Vibration-Isolation Systems

Vibration-isolation systems can be categorized as active or passive. The categorization depends on whether or not external power is required for the isolators to

perform their functions. Vibration criteria provide the standardization of vibration conditions in the precision manufacturing or nanotechnology.

### 1.3.1 Vibration Criteria

Vibration disturbance has the specific frequency range depending on sources. The frequencies of human-induced vibrations [19] are usually lower than 10 Hz, and depend on the speed of movement. The vibration frequencies caused by fans and motors are in the ranges of 10 to 100 Hz [20]. The vibration sensitivity of certain equipment and instrument used in the cutting-edge manufacturing technology and the research at a nanoscale has been a matter of serious concern. Each equipment or instrument manufacturer has provided requirements or recommendations for vibration environments. Subsequently, generic vibration criteria are essentially required in the sense that they meet the needs of all equipments within specifications provided by manufacturers.

Standardizations of vibration conditions in the precision manufacturing or nanotechnology are proposed by several research groups. Ungar and Gordon [21, 22] developed the vibration-criterion (VC) curves which are originally known as the Bolt Beranek & Newman Inc. (BBN) criteria. These curves commonly used in the design of facilities that house vibration-sensitive instruments and tools in the early 1980's. They reviewed the curves in the context of the late 1990's tools and process and proposed changes [23]. A generic criterion in common usage for nanotechnology, currently denoted NIST-A was developed in the early 1990's for the Advanced Measurement

Laboratory at the U.S. National Institute of Standards and Technology (NIST) [24]. Criterion VC-E has a one-third octave band rms velocity amplitude of 125 micro-inches/s at frequencies between 1 and 100 Hz. Criterion NIST-A has a one-third octave band rms displacement amplitude of 1 micro-inch at frequencies between 1 and 20 Hz and a one third octave band rms velocity amplitude of 125 micro-inches/s at frequencies between 20 and 100 Hz. Rinvin [25] provided a systemic analysis of vibratory environments as well as principles and criteria of vibration isolation and the results were applied to determine requirements for vibration isolation of four high-precision pieces of apparatus for electronic production and numerous precision machine tools.

However, the newest generation of photolithography tools imposes an additional requirement for the dynamic resistance properties of the tool's support points. Amick, et al. [26] discussed the current scanner support criteria in terms of reacceptance spectra, and compared them with reacceptance measurements. Amick, et al. [27] presented an overview of vibration requirements of nanotechnology facilities, drawn from both the semiconductor world and that of precision metrology.

Fraumeni, et al. [28] proposed to extend the vibration and noise criteria (VC & NC) for the use in nanotechnology facilities considering the higher level of sensitivity of new equipment without manufacturer's vibration criteria. The new criteria were referred to as 'VC-NT and NC-NT' curves.

### 1.3.2 Passive Isolation

Passive isolators do not require any external power. A classical approach to vibration isolation used a passive system of springs and dampers. The spring resists the movement of the vibration because it exerts an opposing force proportional to its displacement. A damper consists of a piston moving through a viscous fluid, or a conductor moving in a magnetic field as shown in Fig. 1-5. The damper removes kinetic energy and dissipates it as heat. However, the spring has a natural resonant frequency that depends on its spring constant *k*. If the frequency of vibration approaches this natural frequency, the spring becomes an amplifier. The spring-damper system does not work well with vibrations below about 10 Hz.

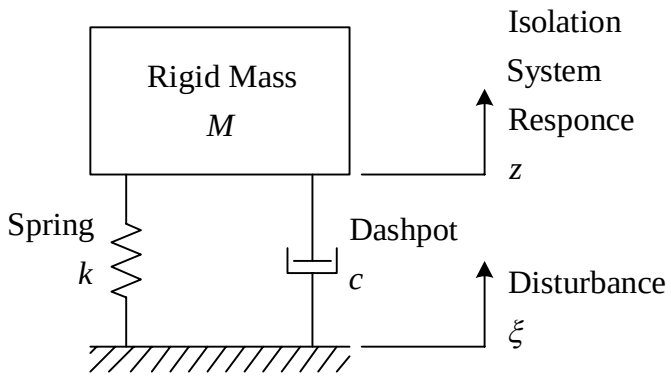


Fig. 1-5. Passive vibration isolation system of spring and damper.

Another traditional passive vibration isolation system is a passive pneumatic vibration isolator. It is popular for reducing vibration disturbance from the floor. Passive pneumatic vibration isolators are frequently used because of their simple structure and low cost, and they can easily support a range of loads by setting the appropriate air

pressure. Additionally, the pneumatic isolator rejects high-frequency vibration disturbance quite effectively owing to the high compressibility of compressed air. Some designs of the passive pneumatic vibration isolator use legs with air-filled chambers, an elastomeric diaphragm, and a piston. The chambers are pressurized so that the piston can support a range of loads. This configuration of the pneumatic vibration isolator is shown in Fig. 1-6.

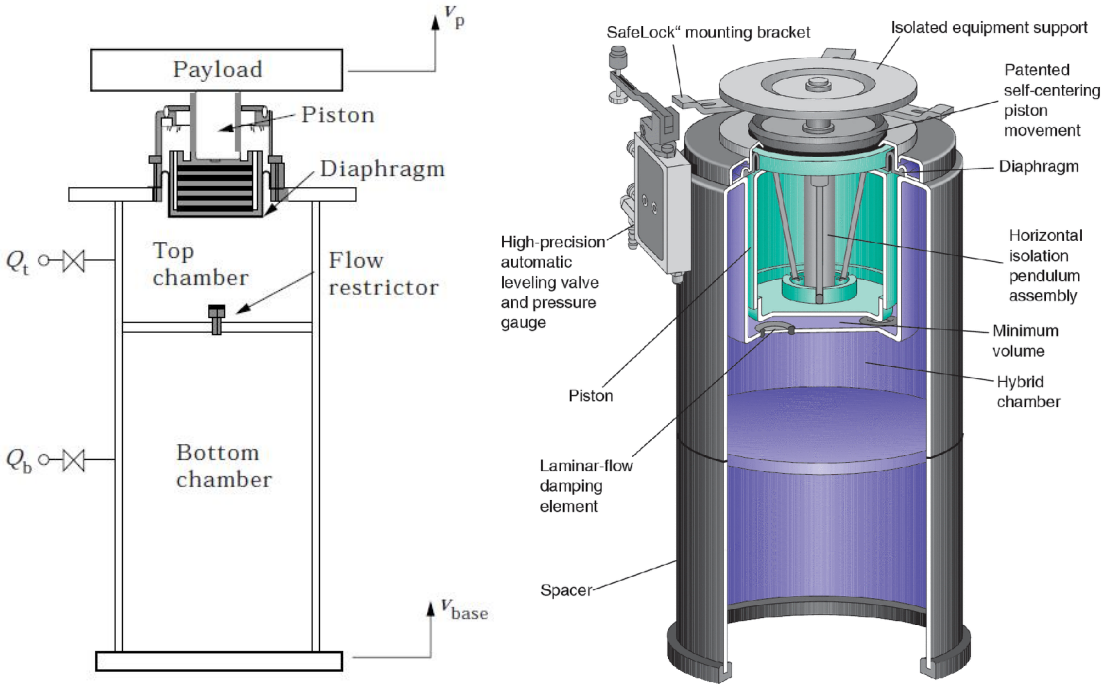


Fig. 1-6. (a) Diagram of pneumatic vibration isolator [29]. (b) Section view of pneumatic isolator I-2000 of Newport® [30].

However, for this isolator, vibration disturbance is amplified at the low resonant frequency, which is normally less than 3 Hz [29, 31]. This resonant cannot be removed by passive isolators [32].

### 1.3.3 Active Isolation

Active isolation system senses electrically and cancels vibration with actuators in real time. An actuator provides force or displacement to the system based on measurement of the response of the system using a feedback control system. The active isolation system has fundamental advantages over the passive isolation systems. Overall performance improvements are significant.

Hence, many researchers developed various active isolations to improve the isolation performance. Piezoelectric actuators to carry active vibration isolation were employed in Mizutani, et al. [33] and El-Sinawi and Kashani [34]. Shaw [35] used the magnetostrictive actuator to develop the active vibration isolation system with adaptive control. However, the stroke of the piezoelectric and magnetostrictive actuators is only several dozens of micrometers, thus restricting the performance of the low-frequency isolation.

The active control of a pneumatic vibration isolator has recently been developed to suppress the vibration disturbance shown in Fig. 1-7 [32]. It improved the performance in the low-frequency range and the resonant peak of passive isolator is reduced effectively. The pneumatic drive can provide larger actuating stroke and lower magnetic field than piezoelectric and magnetostrictive actuators can.

As demands of clean-room environments are increasing in the integrated-circuit production and research facilities in nanoscience, vapor of lubricant and dust due to mechanical friction and wear should be avoided. Hence, noncontact vibration isolation system is required in those facilities.

Fig. 1-7. TMC's electro-damp® II active pneumatic vibration damping system [36]. The photograph can be obtained from the website at www.techmfg.com.

The maglev system is the perfect noncontact vibration isolation that does not require lubricant [37]. The system consists of permanent magnets and electromagnets or coils. The maglev isolation system has a number of advantages that make it more suitable for a wide range of frequency of vibration problems.

## 1.4 Overview of the Y-Shaped Maglev Stage

An overview of the Y-shaped maglev nanopositioning system is given in this section. Mechanical design, fabrication, and assembly of the Y-shaped stage were done by Verma [38]. The Y-shaped stage shown in Fig. 1-8 has the horizontal travel range of 5×5 mm. Its payload capacity exceeds 2 kg. The nominal power consumption per unit actuator is 135 mW. The unique advantages of this stage are small number of parts and

no mechanical restriction [39]. Fig. 1-9 shows three magnet pieces with six coils. A pair of coils share magnetic field of a magnet piece. One of them is placed on the bottom of a magnet piece and the other is on the side, in parallel. The coils are stationary and the magnet is attached to the platen that is a single moving part. Fig. 1-10 presents how each actuator unit generates force in two directions on each magnet. Proper combinations of 6 actuator forces achieve forces and moments in all axes for 6-DOFs motion. The magnetic-field lines generated by the permanent magnet are shown in Fig. 1-11. The magnitude and directions of currents flowing through coils govern the forces exerted on the magnet following the Lorentz-force law. Due to the absence of any mechanical restriction among magnet pieces and coils, the moving platen has advantage to be replaced or to load and unload the objects.

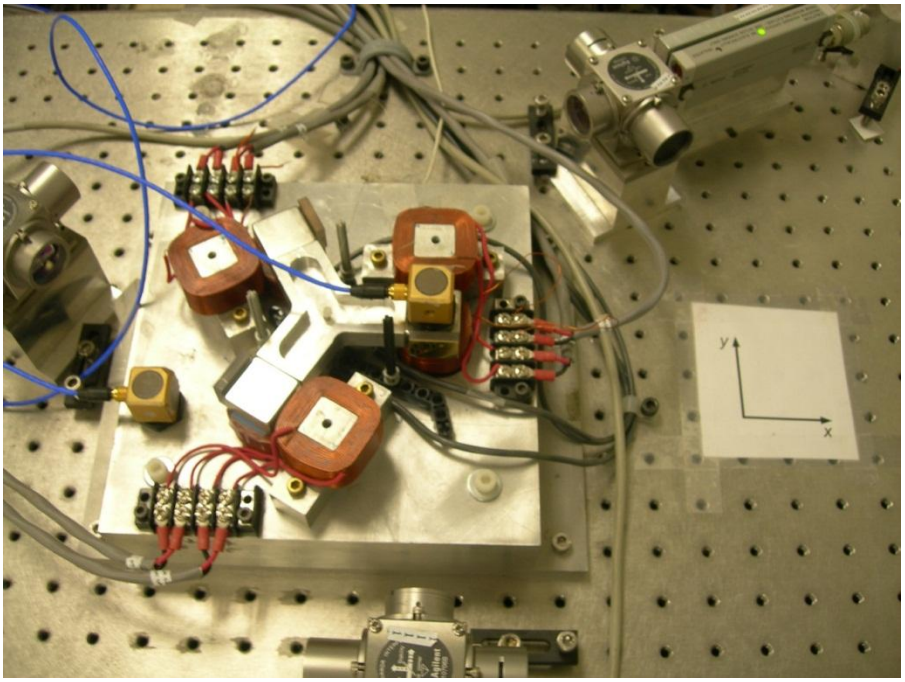


Fig. 1-8. The Y-shaped nanopositioning system [38].

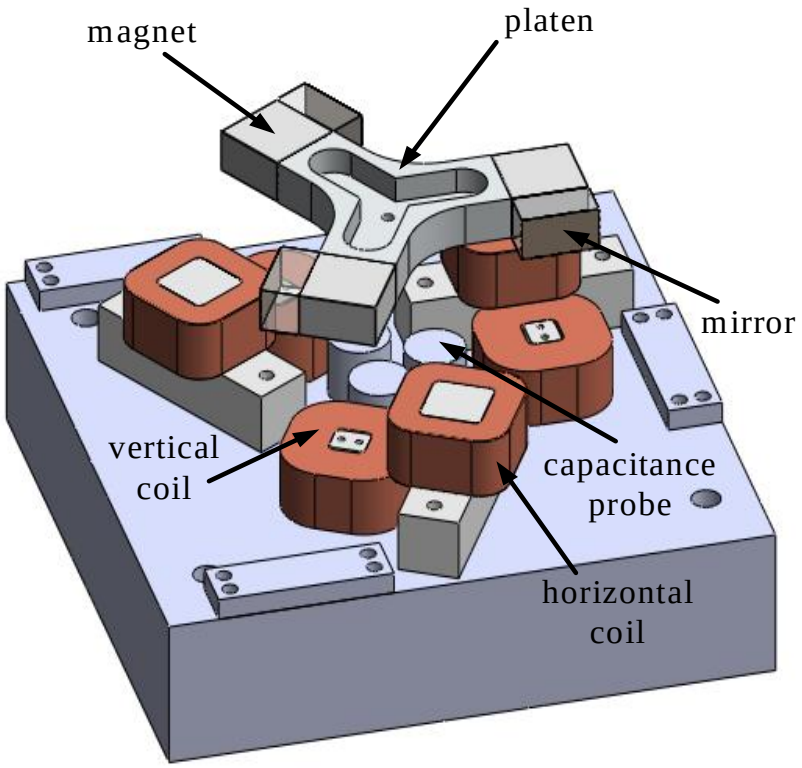


Fig. 1-9. Exploded view of Y-shaped maglev stage [38].

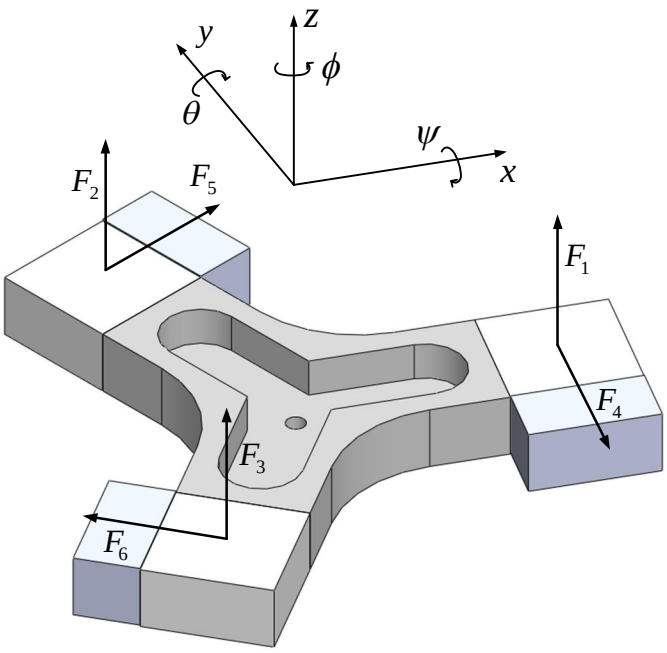


Fig. 1-10. Coordinate axes and directions of forces [38].

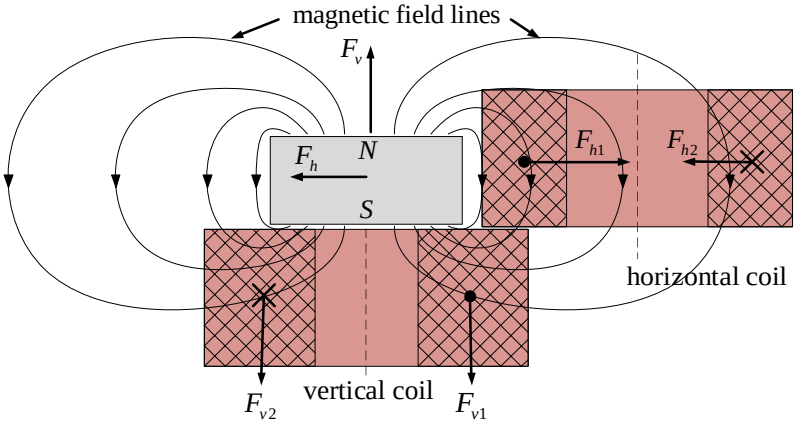


Fig. 1-11. Cross-sectional side view of the unit actuator [38].

In order to measure the horizontal motion, a laser-interferometer system from Agilent is used. The beam from He-Ne laser head (5517D) is split into three ways by beam splitters (10701A, 10706A) and a beam bender (10707A). Three split-beams are reflected by three mirrors attached on the platen. Each split reflected beam from mirror goes through a laser interferometer (10706B) and reach laser receivers (10780C). Each laser-axis board (10897B) connected to a receiver measures the relative position of the attached mirror on the platen. From three laser-axis boards (10897B), we can measure the *x*- and *y*- positions and a rotational angle about the *z*-axis. Three capacitance probes (ADE 2810) located on the bottom of the platen are used for sensing vertical position. Each probe with a signal conditioning board (ADE 3800) measures the distance from the bottom surface of the platen as shown in Fig. 1-9. The average distance of three measurements is the vertical position of the platen. Rotational angles about the *x*- and *y*-axes are converted from the distance differences among three probes.

A VME (Versa Module Eurocard) chassis is used as a communication backbone among hardware boards. A VME PC (VMIC 7751) is a bus controller in the VME system. A Pentek 4284 DSP board acts as the real-time controller. A 16-bit data acquisition board (Pentek 6102) and three laser-axis boards are inserted in the VME chassis. The DSP board has a TMS320C40 DSP by Texas Instruments. It takes care of all computing tasks for real-time control. It obtains the position and velocity data from the laser-axis boards and the data acquisition boards. The DSP board takes user commands, applies control laws, and calculates the control outputs. Digital-to-analog

converters (DACs) on Pentek 6102 generate the output signals from the control commands.

## 1.5 Dissertation Overview

This dissertation consists of nine chapters. Background and motivation of the research presented were explained in the first chapter. A review of the prior art and the trends in nanopositioning technology in industry was also provided. Vibration criteria and importance of vibration isolation were introduced. Passive and active vibration isolation methods were briefly addressed. Advantages of maglev positioning systems were discussed in both positioning and vibration isolation. The overview of the Y-shaped maglev stage, instrumentation, electromechanical design and sensing schemes were described for positioning and vibration control. The working principle of the maglev stage was also explained in Chapter I.

Chapter II shows the full nonlinear dynamic model of the Y-shaped maglev stage that includes translational and rotational equations of motion with differential kinematics. Modal force and displacement transformation are also described between the stationary and the inertial coordinate systems.

Chapter III discusses the LQG/LTR methodology and state space form of the Y-shaped stage system. The design procedure of the LQG/LTR compensator is briefly introduced. The way to shape the target feedback loop and how to make the loop transfer function match to the target feedback loop shaping are suggested. To design the

LQG/LTR compensator for the maglev stage, the state space form is derived from the full nonlinear dynamic model and an LQG/LTR controller is designed to rejec vibration disturbance. The performance of the vibration rejection is shown in simulation.

To derive a more accurate model of the maglev system, a dynamic model of the optical table is also considered in Chapter IV. The model of the maglev system with the optical table in vertical motion includes the pneumatic passive isolators. EOMs of the maglev system present the optical table and platen motions with damping and stiffness terms. A magnetic stiffness term is generated by linearization of the nonlinear magnetic force. The model is validated by comparing the responses between experiment and simulation.

Chapter V introduces a dual-loop control scheme with velocity feedback for vibration-regulation. Stability of the controller is analyzed and the stable region of the controller gains is calculated. The feasibility of the dual-loop controller with velocity feedback is presented by showing the performance of the vibration-reduction performance in simulations and experiments.

Chapter VI discusses about modeling of the maglev system with the optical table in horizontal motion. The procedure and methodology of modeling in the horizontal motion is similar to in vertical motion. However, the stiffness term disappears in horizontal EOMs.

Chapter VII presents a vibration control methodology with velocity feedback in the horizontal motion. The stability analysis to determine gains of velocity feedback controller is performed. The frequency response of the transfer function between the

disturbance input and the position output is explained to show the feasibility of the vibration-reduction with various controller gains. The experimental results verify the performance of the controller with various frequencies of the vibration disturbance. The performance discrepancy between the simulation and experiment is also discussed.

Chapter VIII discusses the vibration disturbances and step response analysis in six-axis motions. The performance of the vibration reduction of the dual-loop controllers is presented in not only translational but rotational motion. Trajectories with step responses in the *x-y* plane show the accuracy differences between with vibration control and without vibration control in position regulation and tracking.

Chapter IX concludes this dissertation summarizing the achievements and contributions in this work.

## 1.6 Dissertation Contributions

The main contribution of this dissertation is to enhance the dynamic model of a 6-DOF maglev stage and to develop the dual-loop control system for nanoscale positioning and vibration disturbance rejection with the maglev system. This dissertation presents the full nonlinear dynamic EOMs of the maglev stage including translational and rotational motions with differential kinematics for rotations. The derived nonlinear EOMs and the magnetic forces are linearized and the state-space representation of the maglev system is introduced to design robust control schemes rejecting disturbance in

the MIMO system. An LQG/LTR controller is designed to reject vibration disturbance in a MIMO system.

To derive a more accurate model of the maglev system, a dynamic model of the optical table with a pneumatic passive vibration isolator is also considered. The stiffness and damping parameters of the optical table are obtained from an impulse response. The magnetic stiffness has been added by the linearization of the EOMs of the optical table and the platen in vertical motion. The enhanced model is validated by comparing between the simulations and the experiments. To test the performance in the vibration control, an unbalanced vibrating motor is designed for generating vibration disturbances.

The dual-loop control system with velocity feedback makes it possible that the maglev system tracks positioning commands and rejects vibration disturbance simultaneously. The design procedures of the dual-loop control systems are introduced in vertical and horizontal motions. The inner-loop compensator regulating the velocity is developed for vibration rejection, and the outer-loop compensator is designed to position of the platen. The stabilizing regions of the gain values for vibration-rejecting compensators are analyzed. The capacitance probes as vertical motion sensors do not directly provide the velocity information. The velocity in vertical motion is obtained by differentiating the noisy position signals. A software low-pass filter is designed to prevent amplification of the high frequency noise of position signal by differentiation.

The influence of the vibration disturbance acts on the optical table is analyzed by presenting the frequency response of the transfer function from the disturbance to the position output. The inner-loop compensators for velocity-regulation in the *x*-, *y*-, and *z*-

axes attenuate the influence of the vibration disturbance up to 65% in horizontal motion and 45% in vertical motion within target frequency range in the experiments.

The vibration control schemes synthesized in three-axis motions perform well in six-axis vibration reduction. The capabilities of the dual-loop controllers for position tracking and vibration rejection are demonstrated in six axes.

# CHAPTER II

# DYNAMIC MODELING OF THE Y-SHAPED MAGLEV STAGE

## 2.1 Dynamics of the Platen in Translational Motion

The mass and moment of inertia of the platen were calculated by Solidworks$^{TM}$. The mass matrix of the platen is

$$M = \begin{bmatrix} m & 0 & 0 \\ 0 & m & 0 \\ 0 & 0 & m \end{bmatrix} = \begin{bmatrix} 0.2671 & 0 & 0 \\ 0 & 0.2671 & 0 \\ 0 & 0 & 0.2671 \end{bmatrix} \text{kg.} \qquad (2.1.1)$$

Since the platen is magentically leviated with no contact, the palten is modeled as a pure mass system and the translational EOMs of the platen are

$$M\ddot{\boldsymbol{x}}_n = \boldsymbol{f}_n - \boldsymbol{g}_n \qquad (2.1.2)$$

where $\ddot{\boldsymbol{x}}_n = (\ddot{x}, \ddot{y}, \ddot{z})^T$, $\boldsymbol{f}_n$, and $\boldsymbol{g}_n$ are a position vector, force vector, and a gravity force based on the stationary frame. The stationary and body-fixed coordinates are presented in Fig. 2-1. However, the forces, $\boldsymbol{F} = (F_1, F_2, F_3, F_4, F_5, F_6)^T$ shown in Fig. 1-10 generated by actuators were calculated in the body-fixed frame. The directions of force vectors are not aligned with the axes. Therefore, the transformation matrix between the body-fixed frame and stationary frame is required. A direction cosine matrix (DCM)

derived by the Euler angles is a good method to describe the orientation between of the body-fixed frame and the stationary frame.

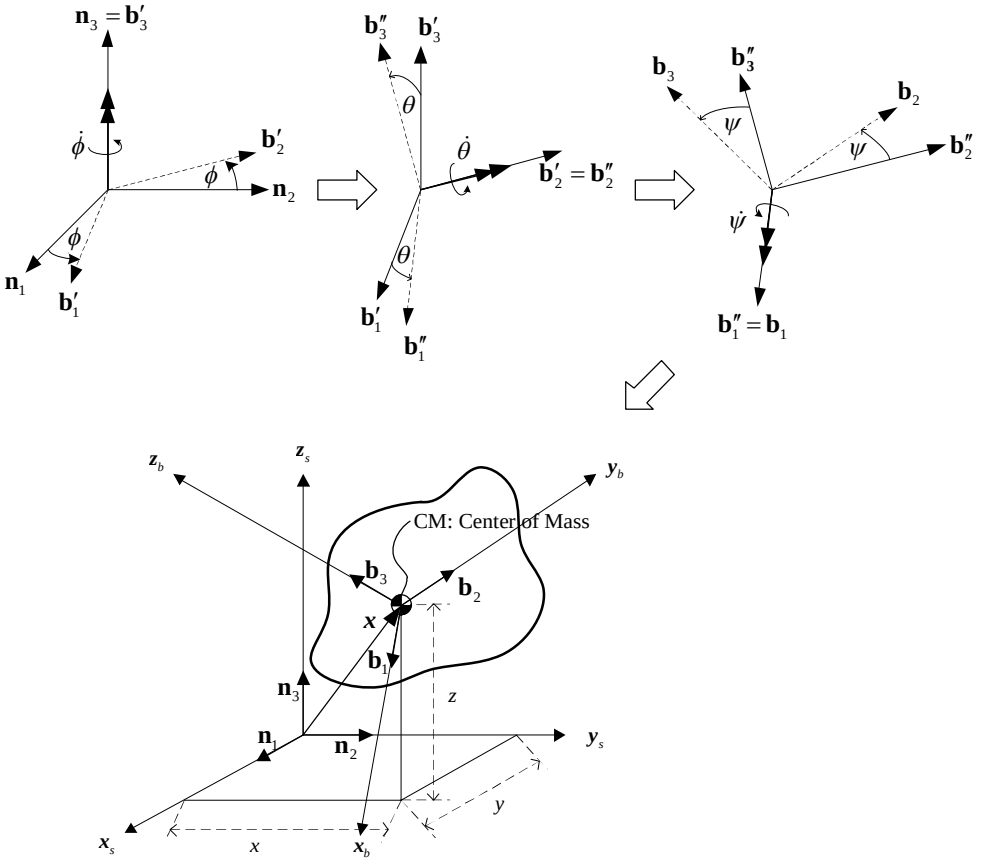


Fig. 2-1. The stationary and body-fixed coordinates system. $\boldsymbol{n}_1$, $\boldsymbol{n}_2$, and $\boldsymbol{n}_3$ are basis vectors in the stationary frame, $(x_s, y_s, z_s)$. $\boldsymbol{b}_1$, $\boldsymbol{b}_2$, and $\boldsymbol{b}_3$ are basis vectors in the body-fixed frame $(x_b, y_b, z_b)$. $\phi$, $\theta$, and $\psi$ are angles in the 3-2-1 Euler angle rotation sequence.

## 2.2 Euler Angles (3-2-1)

For rotation about the first axis ($\boldsymbol{n}_3$) shown in Fig. 2-2,

$$\boldsymbol{b}' = \begin{bmatrix} \cos\phi & \sin\phi & 0 \\ -\sin\phi & \cos\phi & 0 \\ 0 & 0 & 1 \end{bmatrix} \boldsymbol{n}. \tag{2.2.1}$$

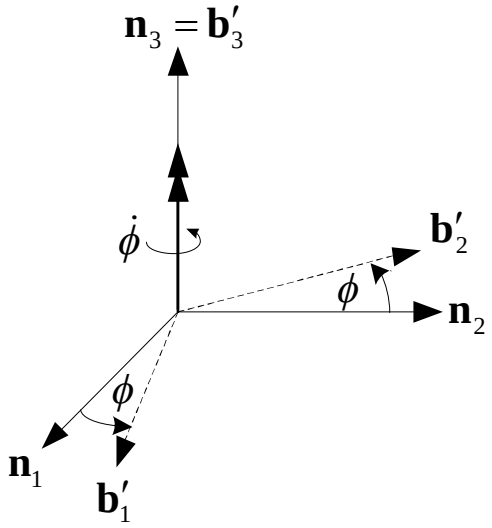


Fig. 2-2. The stationary and the first rotated coordinates system. $\boldsymbol{n}_1$, $\boldsymbol{n}_2$, and $\boldsymbol{n}_3$ are basis vectors in the stationary frame, $(x_s, y_s, z_s)$. $\boldsymbol{b}'_1$, $\boldsymbol{b}'_2$, and $\boldsymbol{b}'_3$ are basis vectors in the first rotated about the axis $\boldsymbol{n}_3$.

For next rotation about the second axis ($\boldsymbol{b}_2'$) shown in Fig. 2-3,

$$\boldsymbol{b}'' = \begin{bmatrix} \cos\theta & 0 & -\sin\theta \\ 0 & 1 & 0 \\ \sin\theta & 0 & \cos\theta \end{bmatrix} \boldsymbol{b}' \tag{2.2.2}$$

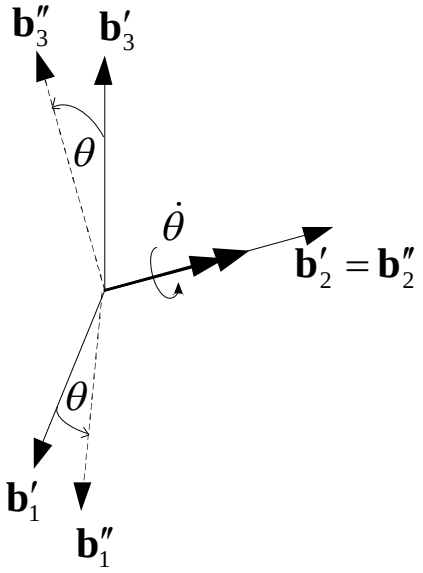


Fig. 2-3. The first rotated and the second rotated coordinates system. $\boldsymbol{b}_1'$, $\boldsymbol{b}_2'$, and $\boldsymbol{b}_3'$ are basis vectors in the first rotated frame, $(x', y', z')$. $\boldsymbol{b}_1''$, $\boldsymbol{b}_2''$, and $\boldsymbol{b}_3''$ are basis vectors in the second rotated about the axis $\boldsymbol{b}_2'$.

For the last rotation about the third axis ($\boldsymbol{b}_1''$) in shown in Fig. 2-4,

$$\boldsymbol{b} = \begin{bmatrix} 1 & 0 & 0 \\ 0 & \cos\psi & \sin\psi \\ 0 & -\sin\psi & \cos\psi \end{bmatrix} \boldsymbol{b}''. \tag{2.2.3}$$

To find the DCM, $C(\phi, \theta, \psi)$,

$$\begin{aligned} \boldsymbol{b} &= \left[C(\phi, \theta, \psi)\right]\boldsymbol{n} \\ &= \left[C(\psi)\right]\left[C(\theta)\right]\left[C(\theta)\right]\boldsymbol{n} \\ &= \begin{bmatrix} 1 & 0 & 0 \\ 0 & \cos\psi & \sin\psi \\ 0 & -\sin\psi & \cos\psi \end{bmatrix} \begin{bmatrix} \cos\theta & 0 & -\sin\theta \\ 0 & 1 & 0 \\ \sin\theta & 0 & \cos\theta \end{bmatrix} \begin{bmatrix} \cos\phi & \sin\phi & 0 \\ -\sin\phi & \cos\phi & 0 \\ 0 & 0 & 1 \end{bmatrix} \boldsymbol{n} \end{aligned} \tag{2.2.4}$$

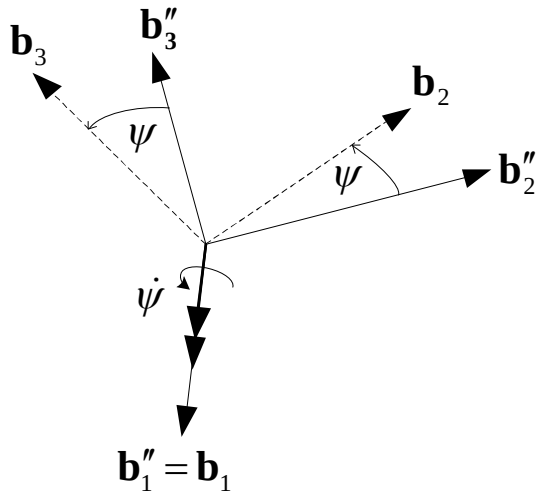


Fig. 2-4. The second rotated and the body-fixed coordinates system. $\boldsymbol{b}_1''$, $\boldsymbol{b}_2''$, and $\boldsymbol{b}_3''$ are basis vectors in the second rotated frame, $(x'', y'', z'')$. $\boldsymbol{b}_1$, $\boldsymbol{b}_2$, and $\boldsymbol{b}_3$ are basis vectors in the third rotated about the axis $\boldsymbol{b}_1''$.

$$\boldsymbol{b} = \begin{bmatrix} \cos\theta\cos\phi & \cos\theta\sin\phi & -\sin\theta \\ \sin\psi\sin\theta\cos\phi - \cos\psi\sin\phi & \sin\psi\sin\theta\sin\phi + \cos\psi\cos\phi & \sin\psi\cos\theta \\ \cos\psi\sin\theta\cos\phi + \sin\psi\sin\phi & \cos\psi\sin\theta\sin\phi - \sin\psi\cos\phi & \cos\psi\cos\theta \end{bmatrix} \boldsymbol{n} \quad (2.2.5)$$

$$\left[C(\phi,\theta,\psi)\right] = \begin{bmatrix} \cos\theta\cos\phi & \cos\theta\sin\phi & -\sin\theta \\ \sin\psi\sin\theta\cos\phi - \cos\psi\sin\phi & \sin\psi\sin\theta\sin\phi + \cos\psi\cos\phi & \sin\psi\cos\theta \\ \cos\psi\sin\theta\cos\phi + \sin\psi\sin\phi & \cos\psi\sin\theta\sin\phi - \sin\psi\cos\phi & \cos\psi\cos\theta \end{bmatrix}$$

(2.2.6)

$$\left[C(\phi,\theta,\psi)\right]^{-1} = \begin{bmatrix} \cos\theta\cos\phi & \sin\psi\sin\theta\cos\phi - \cos\psi\sin\phi & \cos\psi\sin\theta\cos\phi + \sin\psi\sin\phi \\ \cos\theta\sin\phi & \sin\psi\sin\theta\sin\phi + \cos\psi\cos\phi & \cos\psi\sin\theta\sin\phi - \sin\psi\cos\phi \\ -\sin\theta & s\,\text{in}\psi\cos\theta & \cos\psi\cos\theta \end{bmatrix}$$

(2.2.7)

Because the DCM is an orthogonal matrix,

$$\left[C(\phi,\theta,\psi)\right]^{-1} = \left[C(\phi,\theta,\psi)\right]^{T}. \quad (2.2.8)$$

The modal force transformation matrix $T_f$ and the DCM, $C(\phi,\theta,\psi)$, based on three Euler rotation angles $(\phi,\theta,\psi)$, are required to perform the coordinate transformation of a vector in the stationary frame into a vector in the body-fixed frame.

The dynamics of translational motion and modal forces transformation matrix becomes

$$M\ddot{\boldsymbol{x}}_n = C^{-1}\boldsymbol{f}_b - \boldsymbol{g}_n \tag{2.2.9}$$

$$M\ddot{\boldsymbol{x}}_n = C^{-1}T_f\boldsymbol{F} - \boldsymbol{g}_n \tag{2.2.10}$$

$$T_f = \begin{bmatrix} 0 & 0 & 0 & 0 & \cos 30^\circ & -\cos 30^\circ \\ 0 & 0 & 0 & -1 & \sin 30^\circ & \sin 30^\circ \\ 1 & 1 & 1 & 0 & 0 & 0 \end{bmatrix}. \tag{2.2.11}$$

where, $\boldsymbol{f}_b$ is a force vector based on the body-fixed frame, and $T_f$ is the modal force transformation matrix.

## 2.3 Dynamics of the Platen in Rotational Motion

The monent of inertia of the platen is

$$I = \begin{bmatrix} I_{xx} & -I_{xy} & -I_{xz} \\ -I_{yx} & I_{yy} & -I_{yz} \\ -I_{zx} & -I_{zy} & I_{zz} \end{bmatrix} = \begin{bmatrix} 340.37 & 0 & 0 \\ 0 & 340.37 & 0 \\ 0 & 0 & 653.61 \end{bmatrix} \times 10^{-6} \text{ kg-m}^2 . \tag{2.3.1}$$

The fundamental equation of motion of a rotating body in an inertia frame is

$$I\dot{\boldsymbol{\omega}} + \boldsymbol{\omega} \times I\boldsymbol{\omega} = \boldsymbol{\tau} \tag{2.3.2}$$

where $\boldsymbol{\omega}$ is an angular velocity vector and $[\tilde{\omega}]$ is a skew-symmetric matrix. A moment vector is defined as $\boldsymbol{\tau}$.

In addition, the differential kinematics for rotational motion is required to calculate rotational angles. The angular velocity of the body-fixed coordinate is

$$\begin{aligned}\boldsymbol{\omega}_{B/N} &= \dot{\phi}\boldsymbol{n}_3 + \dot{\theta}\boldsymbol{b}_2' + \dot{\psi}\boldsymbol{n}_1'' \\ &= \dot{\phi}\boldsymbol{b}_3' + \dot{\theta}\boldsymbol{b}_2'' + \dot{\psi}\boldsymbol{b}_1\end{aligned} \tag{2.3.3}$$

where

$$\begin{aligned}\boldsymbol{b}_3' &= -\sin\theta\boldsymbol{b}_1'' + \cos\theta\boldsymbol{b}_3'' \\ &= -\sin\theta\boldsymbol{b}_1 + \cos\theta\sin\psi\boldsymbol{b}_2 + \cos\theta\cos\psi\boldsymbol{b}_3\end{aligned} \tag{2.3.4}$$

$$\boldsymbol{b}_2'' = \cos\psi\boldsymbol{b}_2 - \sin\psi\boldsymbol{b}_3. \tag{2.3.5}$$

Therefore,

$$\begin{aligned}\boldsymbol{\omega}_{B/N} &= \dot{\phi}\left(-\sin\theta\boldsymbol{b}_1 + \cos\theta\sin\psi\boldsymbol{b}_2 + \cos\theta\cos\psi\boldsymbol{b}_3\right) + \dot{\theta}\left(\cos\psi\boldsymbol{b}_2 - \sin\psi\boldsymbol{b}_3\right) + \dot{\psi}\boldsymbol{b}_1 \\ &= \left(\dot{\psi} - \dot{\phi}\sin\theta\right)\boldsymbol{b}_1 + \left(\dot{\phi}\cos\theta\sin\psi + \dot{\theta}\cos\psi\right)\boldsymbol{b}_2 + \left(\dot{\phi}\cos\theta\cos\psi - \dot{\theta}\sin\psi\right)\boldsymbol{b}_3\end{aligned} \tag{2.3.6}$$

$$\begin{Bmatrix}\omega_1 \\ \omega_2 \\ \omega_3\end{Bmatrix} = \begin{bmatrix}1 & 0 & -\sin\theta \\ 0 & \cos\psi & \cos\theta\sin\psi \\ 0 & -\sin\psi & \cos\theta\cos\psi\end{bmatrix}\begin{Bmatrix}\dot{\psi} \\ \dot{\theta} \\ \dot{\phi}\end{Bmatrix}. \tag{2.3.7}$$

These differential equations are derived as

$$\begin{Bmatrix}\dot{\psi} \\ \dot{\theta} \\ \dot{\phi}\end{Bmatrix} = \begin{bmatrix}1 & \sin\psi\tan\theta & \cos\psi\tan\theta \\ 0 & \cos\psi & -\sin\psi \\ 0 & \dfrac{\sin\psi}{\cos\theta} & \dfrac{\cos\psi}{\cos\theta}\end{bmatrix}\begin{Bmatrix}\omega_1 \\ \omega_2 \\ \omega_3\end{Bmatrix}. \tag{2.3.8}$$

They have to be solved simultaneously with the equations of motion for rotation. A modal moment transformation matrix $T_\tau$,

$$T_\tau = \begin{bmatrix} 0 & l_3 & -l_3 & 0 & 0 & 0 \\ -l_1 & l_2 & l_2 & 0 & 0 & 0 \\ 0 & 0 & 0 & -l_1 & -l_1 & -l_1 \end{bmatrix} \tag{2.3.9}$$

is required between the moment vector $\boldsymbol{\tau}$ and the forces $\boldsymbol{F}$, and the moment vector becomes

$$\boldsymbol{\tau} = \begin{Bmatrix} \tau_1 \\ \tau_2 \\ \tau_3 \end{Bmatrix} = \begin{bmatrix} 0 & l_3 & -l_3 & 0 & 0 & 0 \\ -l_1 & l_2 & l_2 & 0 & 0 & 0 \\ 0 & 0 & 0 & -l_1 & -l_1 & -l_1 \end{bmatrix} \boldsymbol{F} . \tag{2.3.10}$$

Finally, the full nonlinear equation of rotational motion of the platen is

$$\dot{\boldsymbol{\omega}} = -I^{-1}\boldsymbol{\omega} \times I\boldsymbol{\omega} + I^{-1}T_\tau \boldsymbol{F} . \tag{2.3.11}$$

The readings of the capacitance probes and the laser interferometer can be written in matrix form of the displacements and angles in the body-fixed frame.

$$\begin{bmatrix} L_1 \\ L_2 \\ L_3 \\ C_1 \\ C_2 \\ C_3 \end{bmatrix} = \begin{bmatrix} 0 & -1 & 0 & 0 & 0 & -l_1 \\ \cos 30^\circ & \cos 60^\circ & 0 & 0 & 0 & -l_1 \\ -\cos 30^\circ & \cos 60^\circ & 0 & 0 & 0 & -l_1 \\ 0 & 0 & 1 & 0 & -d_1 & 0 \\ 0 & 0 & 1 & d_3 & d_2 & 0 \\ 0 & 0 & 1 & -d_3 & d_2 & 0 \end{bmatrix} \begin{bmatrix} x \\ y \\ z \\ \psi \\ \theta \\ \phi \end{bmatrix}, \tag{2.3.12}$$

where $C_1$, $C_2$, and $C_3$ are displacements of the capacitance probes. $L_1$, $L_2$, and $L_3$ are displacements of the plane mirrors.

The lengths of physical dimensions in Fig. 2-5 are as follows:

$l_1$: distance between the center of magnet 1 and the center of the platen = 0.050595 m;

$l_2$: distance between the center of magnets 2 or 3 and the center of the platen along the $x$-axis = 0.0253 m;

$l_3$: distance between the center of magnets 2 or 3 and the center of the platen along the $y$-axis = 0.04382 m;

$d_1$: distance between the center of capacitance probe $C_1$ and the origin of the stationary coordinated system along the $x$-axis = 0.01443 m;

$d_2$: distance between the center of capacitance probes $C_2$ or $C_3$ and the origin of the stationary coordinated system along the $x$-axis = 0.007215 m;

$d_3$: distance between the center of capacitance probes $C_2$ or $C_3$ and the origin of the stationary coordinated system along the $y$-axis = 0.012496 m.

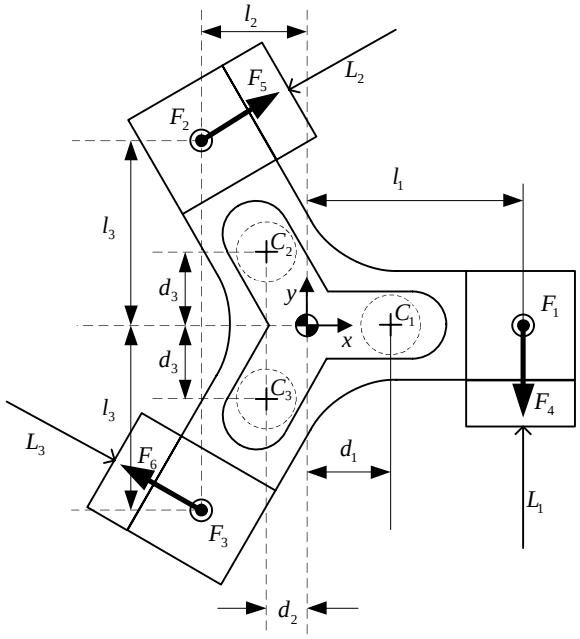


Fig. 2-5. Definitions of forces and distances of points of applications from the center of mass [38].

## 2.4 Linearization of Dynamics of the Platen in Translational Motion

From (2.2.8)–(2.2.9), the dynamics of the platen in translation motion can be presented as

$$M\ddot{\boldsymbol{x}}_n = C^T \boldsymbol{f}_b - \boldsymbol{g}_n, \tag{2.4.1}$$

where the subcript *n* or *b* indicates that the vector is based on the stationary or body-fixed frame.

For linearization, let us set the perturbation equations

$$\ddot{\boldsymbol{x}}_n = \ddot{\boldsymbol{x}}_{n_0} + \ddot{\tilde{\boldsymbol{x}}}_n \tag{2.4.2}$$

$$C^T = C_0{}^T + \tilde{C}^T \tag{2.4.3}$$

$$\boldsymbol{f}_b = \boldsymbol{f}_{b_0} + \tilde{\boldsymbol{f}}_b \tag{2.4.4}$$

$$\boldsymbol{g}_n = \boldsymbol{g}_{n_0} + \tilde{\boldsymbol{g}}_n \tag{2.4.5}$$

where $\tilde{\boldsymbol{g}}_n$ is zero because $\boldsymbol{g}_n$ is a constant vector and subscript 0 means the values in the opertation points.

From (2.4.2)–(2.4.5), (2.4.1) can be expressed as

$$M\left(\ddot{\tilde{\boldsymbol{x}}}_n + \ddot{\boldsymbol{x}}_{n_0}\right) = \left(\tilde{C}^T + C_0{}^T\right)\left(\tilde{\boldsymbol{f}}_b + \boldsymbol{f}_{b_0}\right) - \left(\boldsymbol{g}_{n_0} + \cancel{\tilde{\boldsymbol{g}}_n}\right). \tag{2.4.6}$$

For small-angle rotation, the DCM becomes

$$
\begin{aligned}
C^T &= \begin{pmatrix} 1 & -\phi & \theta \\ \phi & 1 & -\psi \\ -\theta & \psi & 1 \end{pmatrix} = \begin{pmatrix} 1 & 0 & 0 \\ 0 & 1 & 0 \\ 0 & 0 & 1 \end{pmatrix} + \begin{pmatrix} 0 & -(\phi_0 + \tilde{\phi}) & (\theta_0 + \tilde{\theta}) \\ (\phi_0 + \tilde{\phi}) & 0 & -(\psi_0 + \tilde{\psi}) \\ -(\theta_0 + \tilde{\theta}) & (\psi_0 + \tilde{\psi}) & 0 \end{pmatrix} \\
&= \begin{pmatrix} 1 & -\phi_0 & \theta_0 \\ \phi_0 & 1 & -\psi_0 \\ -\theta_0 & \psi_0 & 1 \end{pmatrix} + \begin{pmatrix} 0 & -\tilde{\phi} & \tilde{\theta} \\ \tilde{\phi} & 0 & -\tilde{\psi} \\ -\tilde{\theta} & \tilde{\psi} & 0 \end{pmatrix} \qquad (2.4.7) \\
&= C_0^{\,T} + \tilde{C}^T
\end{aligned}
$$

$$
\tilde{C}^T \cong \begin{pmatrix} 0 & -\tilde{\phi} & \tilde{\theta} \\ \tilde{\phi} & 0 & -\tilde{\psi} \\ -\tilde{\theta} & \tilde{\psi} & 0 \end{pmatrix}. \qquad (2.4.8)
$$

After removing some terms cancelled at the operation point and higher-order terms, (2.4.6) becomes

$$
M\ddot{\tilde{\boldsymbol{x}}}_n = \tilde{C}^T \boldsymbol{f}_{b_0} + C_0^{\,T} \tilde{\boldsymbol{f}}_b . \qquad (2.4.9)
$$

From $\ddot{\boldsymbol{x}}_{n_0} = C_0^{\,T} \boldsymbol{f}_{b_0} - \boldsymbol{g}_{n_0} = 0$, we find

$$
C_0^{\,T} \boldsymbol{f}_{b_0} = \begin{bmatrix} 0 \\ 0 \\ mg \end{bmatrix}. \qquad (2.4.10)
$$

The final linearized dynamic EOMs from (2.4.8)–(2.4.10) is

$$
M\ddot{\tilde{\boldsymbol{x}}}_n = C_0^{\,T} \tilde{\boldsymbol{f}}_b + \begin{bmatrix} mg\tilde{\theta} \\ -mg\tilde{\psi} \\ 0 \end{bmatrix}. \qquad (2.4.11)
$$

## 2.5 Linearization of Dynamics of the Platen in Rotational Motion

The full nonlinear equation of rotational motion of the platen, (2.3.11), is

$$\dot{\boldsymbol{\omega}} = -I^{-1}\boldsymbol{\omega} \times I\boldsymbol{\omega} + I^{-1}\boldsymbol{\tau} \tag{2.5.1}$$

(2.5.1) can be presented in another way,

$$\dot{\omega}_1 = \frac{I_{yy} - I_{zz}}{I_{xx}}\omega_2\omega_3 + \frac{1}{I_{xx}}\tau_1 \tag{2.5.2}$$

$$\dot{\omega}_2 = \frac{I_{zz} - I_{xx}}{I_{yy}}\omega_1\omega_3 + \frac{1}{I_{yy}}\tau_2 \tag{2.5.3}$$

$$\dot{\omega}_3 = \frac{I_{xx} - I_{yy}}{I_{zz}}\omega_2\omega_1 + \frac{1}{I_{zz}}\tau_3. \tag{2.5.4}$$

where, $I_{xx}$ and $I_{yy}$ are identical because of the symmetry of the platen.

To linearize (2.5.2)–(2.5.4), we recall the differential kinematics for rotational motion, (2.3.7),

$$\begin{Bmatrix} \omega_1 \\ \omega_2 \\ \omega_3 \end{Bmatrix} = \begin{bmatrix} 1 & 0 & -\sin\theta \\ 0 & \cos\psi & \cos\theta\sin\psi \\ 0 & -\sin\psi & \cos\theta\cos\psi \end{bmatrix} \begin{Bmatrix} \dot{\psi} \\ \dot{\theta} \\ \dot{\phi} \end{Bmatrix}. \tag{2.5.5}$$

The time derivative of (2.5.5) becomes

$$\begin{aligned} \begin{Bmatrix} \dot{\omega}_1 \\ \dot{\omega}_2 \\ \dot{\omega}_3 \end{Bmatrix} = & \begin{bmatrix} 0 & 0 & -\dot{\theta}\cos\theta \\ 0 & -\dot{\psi}\sin\psi & -\dot{\theta}\sin\theta\sin\psi + \dot{\psi}\cos\theta\cos\psi \\ 0 & -\dot{\psi}\cos\psi & -\dot{\theta}\sin\theta\cos\psi - \dot{\psi}\cos\theta\sin\psi \end{bmatrix} \begin{Bmatrix} \dot{\psi} \\ \dot{\theta} \\ \dot{\phi} \end{Bmatrix} \\ & + \begin{bmatrix} 1 & 0 & -\sin\theta \\ 0 & \cos\psi & \cos\theta\sin\psi \\ 0 & -\sin\psi & \cos\theta\cos\psi \end{bmatrix} \begin{Bmatrix} \ddot{\psi} \\ \ddot{\theta} \\ \ddot{\phi} \end{Bmatrix} \end{aligned} \tag{2.5.6}$$

To linearize the trigonometric function for small-angle perturbation, let us use the trigonometric identities,

$$\begin{aligned}\sin(\alpha) &= \sin(\alpha_0 + \tilde{\alpha}) \\ &= \sin\alpha_0 \cos\tilde{\alpha} + \cos\alpha_0 \sin\tilde{\alpha} \\ &\cong \sin\alpha_0 + \tilde{\alpha}\cos\alpha_0\end{aligned} \tag{2.5.7}$$

$$\begin{aligned}\cos(\alpha) &= \cos(\alpha_0 + \tilde{\alpha}) \\ &= \cos\alpha_0 \cos\tilde{\alpha} - \sin\alpha_0 \sin\tilde{\alpha} \\ &\cong \cos\alpha_0 - \tilde{\alpha}\sin\alpha_0,\end{aligned} \tag{2.5.8}$$

where $\alpha_0$ is the angle at an operation point and $\tilde{\alpha}$ is perturbation.

From (2.5.6)–(2.5.8) with assumption of small angle motion, the perturbation of terms in the left-hand side of (2.5.2)–(2.5.4) become

$$\begin{aligned}\dot{\omega}_1 &= -\dot{\phi}\dot{\theta}\cos\theta + \ddot{\psi} - \ddot{\phi}\sin\theta \\ &\cong \ddot{\tilde{\psi}} - \sin\theta_0\ddot{\tilde{\phi}}\end{aligned} \tag{2.5.9}$$

$$\begin{aligned}\dot{\omega}_2 &= -\dot{\psi}\dot{\theta}\sin\psi - \dot{\phi}\dot{\theta}\sin\theta\sin\psi + \dot{\phi}\dot{\psi}\cos\theta\cos\psi + \ddot{\theta}\cos\psi + \ddot{\phi}\cos\theta\sin\psi \\ &\cong \ddot{\tilde{\theta}}\cos\psi_0 + \ddot{\tilde{\phi}}\cos\theta_0\sin\psi_0\end{aligned} \tag{2.5.10}$$

$$\begin{aligned}\dot{\omega}_3 &= -\dot{\psi}\dot{\theta}\cos\psi - \dot{\phi}\dot{\theta}\sin\theta\cos\psi - \dot{\phi}\dot{\psi}\cos\theta\sin\psi - \ddot{\theta}\sin\psi + \ddot{\phi}\cos\theta\cos\psi \\ &\cong -\ddot{\tilde{\theta}}\sin\psi_0 + \ddot{\tilde{\phi}}\cos\theta_0\cos\psi_0\end{aligned} \tag{2.5.11}$$

To linearaze the terms in the right-hand side of (2.5.2)–(2.5.4) , we need an alternative form of (2.5.5),

$$\omega_1 = \dot{\psi} - \dot{\phi}\sin\theta \tag{2.5.12}$$

$$\omega_2 = \dot{\theta}\cos\psi + \dot{\phi}\cos\theta\sin\psi \tag{2.5.13}$$

$$\omega_3 = -\dot{\theta}\sin\psi + \dot{\phi}\cos\theta\cos\psi\ . \tag{2.5.14}$$

To linearize the terms in right-hand side of (2.5.2)–(2.5.4),

$$\omega_2\omega_3 = \left(\dot{\theta}\cos\psi + \dot{\phi}\cos\theta\sin\psi\right)\left(-\dot{\theta}\sin\psi + \dot{\phi}\cos\theta\cos\psi\right) \cong 0 \quad (2.5.15)$$

$$\omega_1\omega_3 = \left(\dot{\psi} - \dot{\phi}\sin\theta\right)\left(-\dot{\theta}\sin\psi + \dot{\phi}\cos\theta\cos\psi\right) \cong 0 \quad (2.5.16)$$

$$\omega_1\omega_2 = \left(\dot{\psi} - \dot{\phi}\sin\theta\right)\left(\dot{\theta}\cos\psi + \dot{\phi}\cos\theta\sin\psi\right) \cong 0. \quad (2.5.17)$$

From (2.5.9)–(2.5.11) and (2.5.15)–(2.5.17), the linearized (2.5.2)–(2.5.4) are

$$\ddot{\tilde{\psi}} - \sin\theta_0\ddot{\tilde{\phi}} = \frac{1}{I_{xx}}\tau_1 \quad (2.5.18)$$

$$\ddot{\tilde{\theta}}\cos\psi_0 + \ddot{\tilde{\phi}}\cos\theta_0\sin\psi_0 = \frac{1}{I_{yy}}\tau_2 \quad (2.5.19)$$

$$-\ddot{\tilde{\theta}}\sin\psi_0 + \ddot{\tilde{\phi}}\cos\theta_0\cos\psi_0 + \frac{1}{I_{zz}}\tau_3. \quad (2.5.20)$$

If we put (2.5.18)–(2.5.20) in matrix form,

$$\begin{bmatrix} 1 & 0 & -\sin\theta_0 \\ 0 & \cos\psi_0 & \cos\theta_0\sin\psi_0 \\ 0 & \sin\psi_0 & \cos\theta_0\cos\psi_0 \end{bmatrix} \begin{Bmatrix} \ddot{\tilde{\psi}} \\ \ddot{\tilde{\theta}} \\ \ddot{\tilde{\phi}} \end{Bmatrix} = \begin{bmatrix} \frac{1}{I_{xx}} & 0 & 0 \\ 0 & \frac{1}{I_{yy}} & 0 \\ 0 & 0 & \frac{1}{I_{zz}} \end{bmatrix} \begin{Bmatrix} \tau_1 \\ \tau_2 \\ \tau_3 \end{Bmatrix}. \quad (2.5.21)$$

An alternative matrix form is

$$\begin{Bmatrix} \ddot{\tilde{\psi}} \\ \ddot{\tilde{\theta}} \\ \ddot{\tilde{\phi}} \end{Bmatrix} = \begin{bmatrix} \frac{1}{I_{xx}} & \frac{\sin\psi_0\tan\theta_0}{I_{yy}} & \frac{\cos\psi_0\tan\theta_0}{I_{zz}} \\ 0 & \frac{\cos\psi_0}{I_{yy}} & \frac{-\sin\psi_0}{I_{zz}} \\ 0 & \frac{\sin\psi_0}{I_{yy}\cos\theta_0} & \frac{\cos\psi_0}{I_{zz}\cos\theta_0} \end{bmatrix} \begin{Bmatrix} \tau_1 \\ \tau_2 \\ \tau_3 \end{Bmatrix}. \quad (2.5.22)$$

If we define

$$B_0 = \begin{bmatrix} \dfrac{1}{I_{xx}} & \dfrac{\sin\psi_0 \tan\theta_0}{I_{yy}} & \dfrac{\cos\psi_0 \tan\theta_0}{I_{zz}} \\ 0 & \dfrac{\cos\psi_0}{I_{yy}} & \dfrac{-\sin\psi_0}{I_{zz}} \\ 0 & \dfrac{\sin\psi_0}{I_{yy}\cos\theta_0} & \dfrac{\cos\psi_0}{I_{zz}\cos\theta_0} \end{bmatrix}, \qquad (2.5.23)$$

the linearized full dynamic equations of the platen in rotational motion is

$$\ddot{\boldsymbol{\theta}} = B_0 \boldsymbol{\tau} \qquad (2.5.24)$$

where $\ddot{\boldsymbol{\theta}} = \left(\ddot{\psi}, \ddot{\theta}, \ddot{\phi}\right)$ is the angular accelerations of the perturbed rotational angles.

## 2.6 State-Space Representation of the Linearized Full Dynamics of the Platen

To present the linearized translational and rotational EOMs as state-space form, the state variables and the input variables have to be defined.

Let us set $\tilde{x}$, $\tilde{y}$, $\tilde{z}$, $\dot{\tilde{x}}$, $\dot{\tilde{y}}$, $\dot{\tilde{z}}$, $\tilde{\psi}$, $\tilde{\theta}$, $\tilde{\phi}$, $\dot{\tilde{\psi}}$, $\dot{\tilde{\theta}}$, and $\dot{\tilde{\phi}}$ as state variables and $F_1$, $F_2$, $F_3$, $F_4$, $F_5$, and $F_6$ as input variables. After then, the EOMs will be expand as state variables and input variables form. The translational EOMs, (2.4.11), become

$$\begin{bmatrix} m & 0 & 0 \\ 0 & m & 0 \\ 0 & 0 & m \end{bmatrix} \begin{Bmatrix} \ddot{\tilde{x}} \\ \ddot{\tilde{y}} \\ \ddot{\tilde{z}} \end{Bmatrix} = \begin{pmatrix} 1 & -\phi_0 & \theta_0 \\ \phi_0 & 1 & -\psi_0 \\ -\theta_0 & \psi_0 & 1 \end{pmatrix} \begin{bmatrix} 0 & 0 & 0 & 0 & \cos 30^\circ & -\cos 30^\circ \\ 0 & 0 & 0 & -1 & \sin 30^\circ & \sin 30^\circ \\ 1 & 1 & 1 & 0 & 0 & 0 \end{bmatrix} \begin{Bmatrix} F_1 \\ F_2 \\ F_3 \\ F_4 \\ F_5 \\ F_6 \end{Bmatrix} + \begin{Bmatrix} mg\tilde{\theta} \\ -mg\tilde{\psi} \\ 0 \end{Bmatrix} \qquad (2.6.1)$$

$$\begin{Bmatrix} \ddot{\tilde{x}} \\ \ddot{\tilde{y}} \\ \ddot{\tilde{z}} \end{Bmatrix} = \frac{1}{m}\begin{bmatrix} \theta_0 & \theta_0 & \theta_0 & \phi_0 & \cos 30^\circ - \phi_0 \sin 30^\circ & -\cos 30^\circ - \phi_0 \sin 30^\circ \\ -\psi_0 & -\psi_0 & -\psi_0 & -1 & \sin 30^\circ + \phi_0 \cos 30^\circ & \sin 30^\circ - \phi_0 \cos 30^\circ \\ 1 & 1 & 1 & -\psi_0 & \psi_0 \sin 30^\circ - \theta_0 \cos 30^\circ & \theta_0 \cos 30^\circ + \psi_0 \sin 30^\circ \end{bmatrix} \begin{Bmatrix} F_1 \\ F_2 \\ F_3 \\ F_4 \\ F_5 \\ F_6 \end{Bmatrix} + \begin{bmatrix} g\tilde{\theta} \\ -g\tilde{\psi} \\ 0 \end{bmatrix} \tag{2.6.2}$$

$$\ddot{\tilde{\boldsymbol{x}}} = B_f \boldsymbol{F} + \begin{Bmatrix} g\tilde{\theta} \\ -g\tilde{\psi} \\ 0 \end{Bmatrix}, \tag{2.6.3}$$

where $B_f = \frac{1}{m}\begin{bmatrix} \theta_0 & \theta_0 & \theta_0 & \phi_0 & \cos 30^\circ - \phi_0 \sin 30^\circ & -\cos 30^\circ - \phi_0 \sin 30^\circ \\ -\psi_0 & -\psi_0 & -\psi_0 & -1 & \sin 30^\circ + \phi_0 \cos 30^\circ & \sin 30^\circ - \phi_0 \cos 30^\circ \\ 1 & 1 & 1 & -\psi_0 & \psi_0 \sin 30^\circ - \theta_0 \cos 30^\circ & \theta_0 \cos 30^\circ + \psi_0 \sin 30^\circ \end{bmatrix}$.

(2.6.4)

The rotational EOMs, (2.5.24), becomes

$$\begin{Bmatrix} \ddot{\tilde{\psi}} \\ \ddot{\tilde{\theta}} \\ \ddot{\tilde{\phi}} \end{Bmatrix} = B_0 T_\tau \boldsymbol{F} = \begin{bmatrix} \frac{1}{I_{xx}} & \frac{\sin\psi_0 \tan\theta_0}{I_{yy}} & \frac{\cos\psi_0 \tan\theta_0}{I_{zz}} \\ 0 & \frac{\cos\psi_0}{I_{yy}} & \frac{-\sin\psi_0}{I_{zz}} \\ 0 & \frac{\sin\psi_0}{I_{yy}\cos\theta_0} & \frac{\cos\psi_0}{I_{zz}\cos\theta_0} \end{bmatrix} \begin{bmatrix} 0 & l_3 & -l_3 & 0 & 0 & 0 \\ -l_1 & l_2 & l_2 & 0 & 0 & 0 \\ 0 & 0 & 0 & -l_1 & -l_1 & -l_1 \end{bmatrix} \begin{Bmatrix} F_1 \\ F_2 \\ F_3 \\ F_4 \\ F_5 \\ F_6 \end{Bmatrix} \tag{2.6.5}$$

$$\ddot{\tilde{\boldsymbol{\theta}}} = B_m \boldsymbol{F}\ , \tag{2.6.6}$$

where

$$B_m = \begin{bmatrix} \frac{-l_1 \mathrm{s}\psi_0 \mathrm{t}\theta_0}{I_{yy}} & \frac{l_3}{I_{xx}} + \frac{l_2 \mathrm{s}\psi_0 \mathrm{t}\theta_0}{I_{yy}} & \frac{-l_1 \mathrm{c}\psi_0 \mathrm{t}\theta_0}{I_{zz}} & \frac{-l_1 \mathrm{c}\psi_0 \mathrm{t}\theta_0}{I_{zz}} & \frac{-l_1 \mathrm{c}\psi_0 \mathrm{t}\theta_0}{I_{zz}} & \frac{-l_1 \mathrm{c}\psi_0 \mathrm{t}\theta_0}{I_{zz}} \\ \frac{-l_1 \mathrm{c}\psi_0}{I_{yy}} & \frac{l_2 \mathrm{c}\psi_0}{I_{yy}} & \frac{l_2 \mathrm{c}\psi_0}{I_{yy}} & \frac{l_1 \mathrm{s}\psi_0}{I_{zz}} & \frac{l_1 \mathrm{s}\psi_0}{I_{zz}} & \frac{l_1 \mathrm{s}\psi_0}{I_{zz}} \\ \frac{-l_1 \mathrm{s}\psi_0}{I_{yy} \mathrm{c}\theta_0} & \frac{l_2 \mathrm{s}\psi_0}{I_{yy} \mathrm{c}\theta_0} & \frac{l_2 \mathrm{s}\psi_0}{I_{yy} \mathrm{c}\theta_0} & \frac{-l_1 \mathrm{c}\psi_0}{I_{zz} \mathrm{c}\theta_0} & \frac{-l_1 \mathrm{c}\psi_0}{I_{zz} \mathrm{c}\theta_0} & \frac{-l_1 \mathrm{c}\psi_0}{I_{zz} \mathrm{c}\theta_0} \end{bmatrix}. \tag{2.6.7}$$

From (2.6.3), (2.6.4), (2.6.6), and (2.6.7),

$$\frac{d}{dt}\begin{Bmatrix} \dot{\tilde{\boldsymbol{x}}} \\ \dot{\tilde{\boldsymbol{\theta}}} \end{Bmatrix} = \begin{bmatrix} B_f \\ B_m \end{bmatrix} \boldsymbol{F} + \begin{Bmatrix} g\tilde{\theta} \\ -g\tilde{\psi} \\ 0 \end{Bmatrix} \tag{2.6.8}$$

The state-space representation of the combined EOMs of the translational and rotational motion is

$$\frac{d}{dt}\begin{Bmatrix} \tilde{x} \\ \tilde{y} \\ \tilde{z} \\ \dot{\tilde{x}} \\ \dot{\tilde{y}} \\ \dot{\tilde{z}} \\ \tilde{\psi} \\ \tilde{\theta} \\ \tilde{\phi} \\ \dot{\tilde{\psi}} \\ \dot{\tilde{\theta}} \\ \dot{\tilde{\phi}} \end{Bmatrix} = \begin{bmatrix} 0 & 0 & 0 & 1 & 0 & 0 & 0 & 0 & 0 & 0 & 0 & 0 \\ 0 & 0 & 0 & 0 & 1 & 0 & 0 & 0 & 0 & 0 & 0 & 0 \\ 0 & 0 & 0 & 0 & 0 & 1 & 0 & 0 & 0 & 0 & 0 & 0 \\ 0 & 0 & 0 & 0 & 0 & 0 & 0 & g & 0 & 0 & 0 & 0 \\ 0 & 0 & 0 & 0 & 0 & 0 & -g & 0 & 0 & 0 & 0 & 0 \\ 0 & 0 & 0 & 0 & 0 & 0 & 0 & 0 & 0 & 0 & 0 & 0 \\ 0 & 0 & 0 & 0 & 0 & 0 & 0 & 0 & 0 & 1 & 0 & 0 \\ 0 & 0 & 0 & 0 & 0 & 0 & 0 & 0 & 0 & 0 & 1 & 0 \\ 0 & 0 & 0 & 0 & 0 & 0 & 0 & 0 & 0 & 0 & 0 & 1 \\ 0 & 0 & 0 & 0 & 0 & 0 & 0 & 0 & 0 & 0 & 0 & 0 \\ 0 & 0 & 0 & 0 & 0 & 0 & 0 & 0 & 0 & 0 & 0 & 0 \\ 0 & 0 & 0 & 0 & 0 & 0 & 0 & 0 & 0 & 0 & 0 & 0 \end{bmatrix} \begin{Bmatrix} \tilde{x} \\ \tilde{y} \\ \tilde{z} \\ \dot{\tilde{x}} \\ \dot{\tilde{y}} \\ \dot{\tilde{z}} \\ \tilde{\psi} \\ \tilde{\theta} \\ \tilde{\phi} \\ \dot{\tilde{\psi}} \\ \dot{\tilde{\theta}} \\ \dot{\tilde{\phi}} \end{Bmatrix} + \begin{bmatrix} 0_{3\times 6} \\ B_f \\ 0_{3\times 6} \\ B_m \end{bmatrix} \begin{Bmatrix} F_1 \\ F_2 \\ F_3 \\ F_4 \\ F_5 \\ F_6 \end{Bmatrix}. \tag{2.6.9}$$

Let the state matrix *A*, the input matrix *B*, and the output matrix *C* be

$$A=\begin{bmatrix} 0_{3\times3} & I_{3\times3} & 0_{3\times6} \\ 0_{3\times6} & \begin{matrix} 0 & g & 0 \\ -g & 0 & 0 \\ 0 & 0 & 0 \end{matrix} & 0_{3\times3} \\ 0_{3\times6} & 0_{3\times3} & I_{3\times3} \\ 0_{3\times6} & 0_{3\times3} & 0_{3\times3} \end{bmatrix}_{12\times12} \tag{2.6.10}$$

$$B=\begin{bmatrix} 0_{3\times6} \\ B_f \\ 0_{3\times6} \\ B_m \end{bmatrix}_{12\times6} \tag{2.6.11}$$

$$C=\begin{bmatrix} I_{3\times3} & 0_{3\times3} & 0_{3\times6} \\ 0_{3\times6} & I_{3\times3} & 0_{3\times3} \end{bmatrix}. \tag{2.6.12}$$

Finally, we obtain the state-space form of the full dynamic EOMs,

$$\begin{aligned} \dot{\tilde{\boldsymbol{x}}} &= A\tilde{\boldsymbol{x}} + B\boldsymbol{u} \\ \tilde{\boldsymbol{y}} &= C\tilde{\boldsymbol{x}} \end{aligned} \tag{2.6.13}$$

where $\hat{\boldsymbol{x}}=\left(\tilde{x},\tilde{y},\tilde{z},\dot{\tilde{x}},\dot{\tilde{y}},\dot{\tilde{z}},\tilde{\psi},\tilde{\theta},\tilde{\phi},\dot{\tilde{\psi}},\dot{\tilde{\theta}},\dot{\tilde{\phi}}\right)^T$, and $\boldsymbol{u}=\left(F_1,F_2,F_3,F_4,F_5,F_6\right)^T$.

# CHAPTER III

# ADVANCED-CONTROL SYSTEM DESIGN

## 3.1 Linear Quadratic Gaussian with Loop Transfer Recovery (LQG/LTR) Controller Design

The LQG/LTR technique belongs to the class of the model-based compensator (MBC) [40, 41]. The LQG/LTR design method seeks the MIMO compensator $K(s)$ so that stability robustness and performance specifications are satisfied as close as possible in a MIMO feedback loop shown in Fig. 3-1 [40].

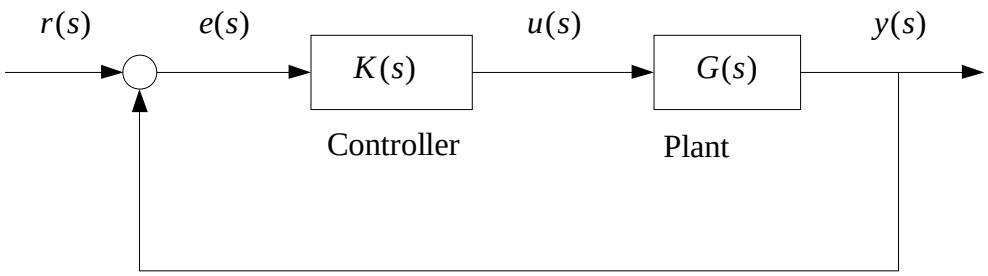


Fig. 3-1. The MIMO feedback loop.

Consider the linear system

$$\dot{\boldsymbol{x}}(t) = A\boldsymbol{x}(t) + B\boldsymbol{u}(t) + \boldsymbol{w}(t) \tag{3.1.1}$$

$$\boldsymbol{y}(t) = C\boldsymbol{x}(t) + \boldsymbol{v}(t), \tag{3.1.2}$$

where $\boldsymbol{w}(t)$ and $\boldsymbol{v}(t)$ are uncorrelated zero-mean white-Gaussian process and sensor noises with positive semidefinite covariance matrices $Q_f$ and $R_f$. The esimator design yields

$$\dot{\hat{\boldsymbol{x}}}(t) = A\hat{\boldsymbol{x}}(t) + B\boldsymbol{u}(t) + H(\boldsymbol{y}(t) - \boldsymbol{r}(t) - \hat{\boldsymbol{y}}(t)) \tag{3.1.3}$$

$$\hat{\boldsymbol{y}}(t) = C\hat{\boldsymbol{x}}(t) \tag{3.1.4}$$

$$G(s) = C\Phi(s)B \text{ with } \Phi(s) = (sI - A)^{-1} \tag{3.1.5}$$

where $\boldsymbol{x}(t)$ is the state vector, $\boldsymbol{r}(t)$ is the reference signal, $\boldsymbol{y}(t)$ is the output vector, $\hat{\boldsymbol{x}}(t)$ is the estimated state vector, $\boldsymbol{e}(t)$ is the error signal, $\hat{\boldsymbol{y}}(t)$ is the estimated output vector, $A$ is the state matrix, $B$ is the input matrix, $C$ is the output matrix, $G$ is the feedback gain matrix, $H$ is the Kalman-filter gain matrix, and $I$ is the identify matrix. The structure of an LQG/LTR compensator,

$$K(s) = G\left(sI - A + BG + HC\right)^{-1} H \tag{3.1.6}$$

is shown in Fig. 3-2. We assume that [$A$,$B$] is stabilizable, i.e. all unstable mode of (3.1.1) are controllable, and [$A$,$C$] is detectable, i.e. all unstable mode in (3.1.1) and (3.1.2) are observable. More detail tutorial for designing multivariable feedback control systems are presented in [40-46].

In the time domain, if we let $\hat{\boldsymbol{x}}(t) \in R^n$ denote the state vector of the compensator $K(s)$,

$$\dot{\hat{\boldsymbol{x}}}(t) = (A - BG - HC)\hat{\boldsymbol{x}}(t) - H\boldsymbol{e}(t) \tag{3.1.7}$$

$$\boldsymbol{u}(t) = -G\hat{\boldsymbol{x}}(t) \tag{3.1.8}$$

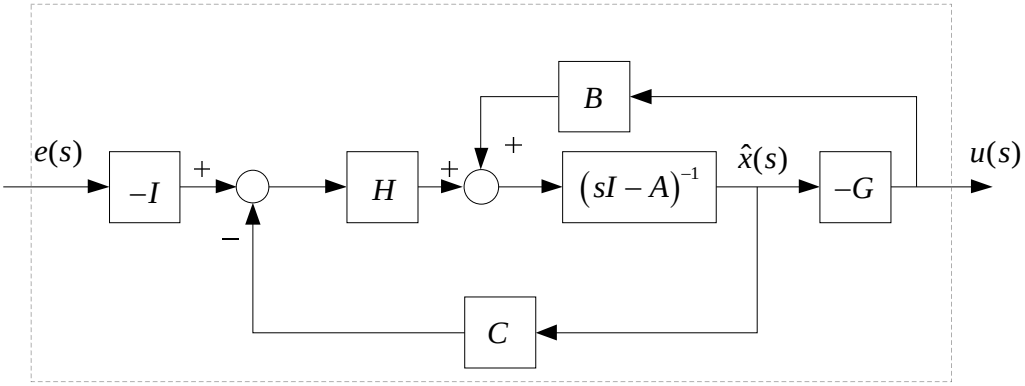


$K(s)$: Controller

Fig. 3-2. The structure of an LQG/LTR compensator.

Before designging a compensator, we set the target loop shape. The final goal of the LQG/LTR design is to make $G(s)K(s)$ as close as possible to the target feedback loop (TFL), $G_{KF}(s) = C\left(sI - A\right)^{-1} H$ . The first step to achieve this goal is to determine the filter gain matrix $H$ . The desired shape of the TFL is shown like in Fig. 3-3. The crossover frequency of the maximun singular value should be greater than the highest frequency of the disturbances and the crossover frequency of the minimun singular value has to be smaller than the lowest noise frequency of the measurements. The larger magnitude of the TFL in the low-frequency induces better disturbance rejection, and the smaller magnitude of the TFL in the high-frequency makes better sensor noise rejection.

The noise covariant matrices, $Q_f$ and $R_f$ , are treated as design knobs in the dynamic compensator design. Without loss of generality, let us choose $Q_f = LL^T$ and $R_f = \frac{1}{\mu} I$ . For target feedback loop shaping, it is suggested that $L = C^T \left(CA^{-1}C^T\right)^{-1}$ for

disturbance rejection in low-frequency, $L = C^T \left( CC^T \right)^{-1}$ for noise rejection in high-frequency, or $L = \left[ L_L ; L_H \right] = \left[ -\left( CA^{-1}B \right)^{-1} ; C^T \left( CC^T \right)^{-1} \right]$ for both rejections [40].

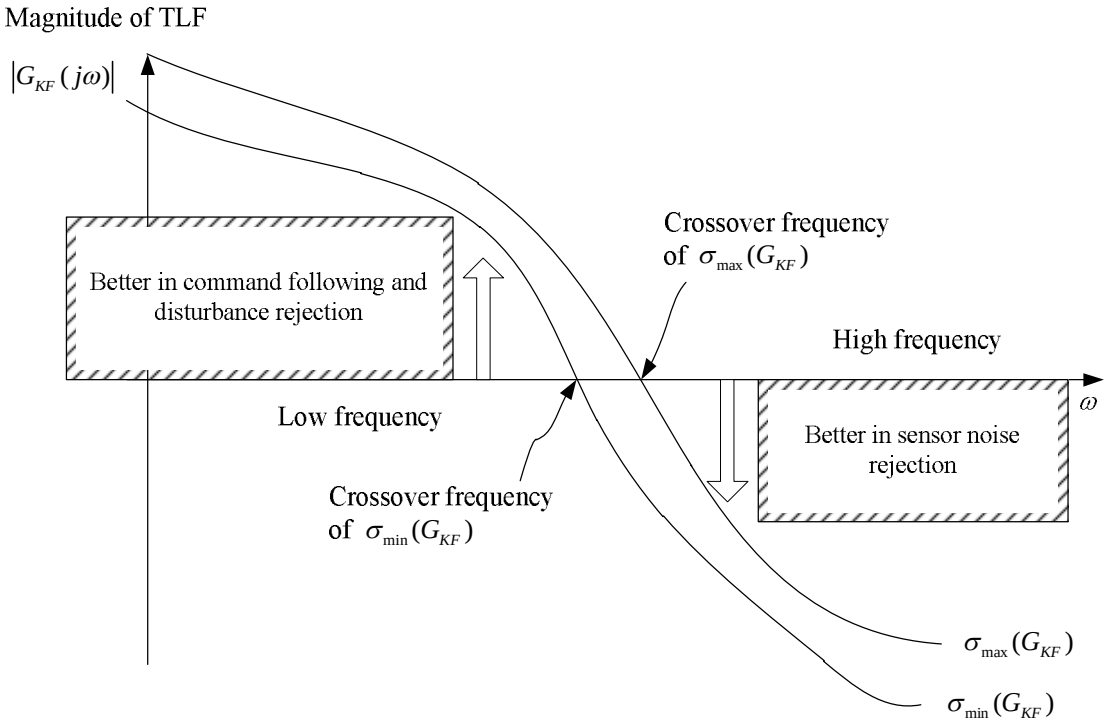


Fig. 3-3. Target feedback loop shaping.

However, if the state matrix *A* is singular, we have to find another way to choose $Q_f$. In many cases, $Q_f$ may be determined by trials and errors based on experience and intuition. If $Q_f$ and $R_f$ are decided, the Kalman-filter gain matrix *H* is calculated by solving the Kalman-filter Riccati equation,

$$0 = P_f A^T + A P_f - P_f C^T R_f^{-1} C P_f + Q_f \tag{3.1.9}$$

$$H = P_f C^T R_f^{-1}. \tag{3.1.10}$$

By tuning $Q_f$ and $R_f$, we can find a proper the Kalman-filter gain matrix to satisfy the TFL shape.

After shaping the TFL, the only undetermined design parameter in $K(s)$ is the control gain matrix $G$. This control gain matrix is computed by solving the cheap-control LQR problem [40]. It is to find the control gain matrix that makes the following performance index as small as possible

$$\min_u \left\{ J = \int_0^\infty \left( x^T Q_c x + u^T R_c u \right) dt \right\} \tag{3.1.11}$$

where $Q_c = C^T C$ is a positive semidefinite matrix, and $R_c = \frac{1}{\rho} I$ is a positive definite matrix. To calculate $G$ for the LQG/LTR compensator, we solve the following control Riccati equation,

$$0 = PA + A^T P - PBR_c^{-1} B^T P + Q_c \tag{3.1.12}$$

for $\rho \to 0$, then the computed control gain matrix $G$ becomes

$$G = R_c^{-1} B^T P = \rho B^T P. \tag{3.1.13}$$

The main result, the loop transfer recovery is as follows

$$\lim_{\rho \to 0} G(s)K(s) \to G_{KF}(s). \tag{3.1.14}$$

This result implies that the loop transfer function, $G(s)K(s)$ approximates the TFL $G_{KF}(s)$ as $\rho$ tends to zero.

## 3.2 State-Space Model and an LQG/LTR Compensator Design of the Y-Shaped Maglev Stage

The state variables of the platen in 6 DOFs can be chosen as its positions, velocities, rotational angles, and rotational velocities in 6 axes as

$$\left(x, y, z, \dot{x}, \dot{y}, \dot{z}, \psi, \theta, \phi, \dot{\psi}, \dot{\theta}, \dot{\phi}\right)^T . \tag{3.2.1}$$

The *x*, *y*, and *z* are the displacement components in m, and $\dot{x}$, $\dot{y}$, and $\dot{z}$ are the velocity components in m/s of the center of mass of the platen with respect to the origin of the stationary frame. The $\psi$, $\theta$, and $\phi$ are the Euler angles in rad, and $\dot{\psi}$, $\dot{\theta}$, and $\dot{\phi}$ are the angular velocities in rad/s about the are *x*, *y*, and *z* axes of the stationary frame.

The linearized full-state EOMs in state-space representation for perturbation in translation and rotational motions at an operation point are presented in (2.6.9)–(2.6.13). From the state-space form, we need to check the controllability and observability. Both the controllability matrix $\begin{bmatrix} B & AB & A^2B & \cdots & A^{n-1}B \end{bmatrix}$ and the observability matrix $\begin{bmatrix} C \\ CA \\ \vdots \\ CA^{n-1} \end{bmatrix}$ have full rank. Hence, the system is controllable and observable.

To find a proper Kalman-filter gain matrix *H*, $Q_f$ and $R_f$ should be determined. However, we cannot use the suggested way to determine $Q_f$ and $R_f$ in [40] because the state matrix *A* is not invertible. By trials and errors, $Q_f$ and $R_f$ are determined as

$$Q_f = diag(5\times10^4, 5\times10^4, 5\times10^4, 1\times10^{-2}, 1\times10^{-2}, 1\times10^{-2}, \cdots \\ 1\times10^3, 1\times10^3, 1\times10^3, 1\times10^{-2}, 1\times10^{-2}, 1\times10^{-2}) \tag{3.2.2}$$

$$R_f = \frac{1}{1.5\times10^3} I_{6\times6}. \tag{3.2.3}$$

From (3.2.2)–(3.2.3), the Kalman-filter Riccati equation (3.1.9) is solved and the Kalman-filter gain matrix $H$ is determined.

$$H = \begin{bmatrix} 8660 & -7.610\times10^{-13} & -2.636\times10^{-15} & -3.8956\times10^{-17} & 9.924\times10^{-4} & 6.016\times10^{-18} \\ -7.610\times10^{-13} & 8660 & 4.504\times10^{-14} & -9.924\times10^{-4} & 5.643\times10^{-15} & -9.296\times10^{-17} \\ -2.636\times10^{-15} & 4.504\times10^{-14} & 8660 & -9.405\times10^{-13} & 9.244\times10^{-13} & -3.630\times10^{-16} \\ 10.55 & 1.855\times10^{-12} & -1.345\times10^{-11} & 6.352\times10^{-13} & 9.810 & -2.581\times10^{-12} \\ -2.501\times10^{-12} & 10.547 & -8.217\times10^{-14} & -9.810 & 2.865\times10^{-12} & -4.087\times10^{-13} \\ 4.616\times10^{-13} & -1.780\times10^{-13} & 3.873 & -4.706\times10^{-12} & 9.228\times10^{-13} & -2.391\times10^{-12} \\ -3.896\times10^{-13} & -9.924\times10^{-4} & -9.405\times10^{-13} & 1225 & -2.063\times10^{-16} & 9.436\times10^{-17} \\ 9.924\times10^{-4} & 5.643\times10^{-15} & 9.244\times10^{-13} & -2.063\times10^{-16} & 1225 & 5.694\times10^{-15} \\ 6.016\times10^{-18} & -9.296\times10^{-17} & -3.630\times10^{-16} & 9.436\times10^{-17} & 5.694\times10^{-15} & 1225 \\ -9.464\times10^{-15} & 1.737\times10^{-7} & -6.653\times10^{-13} & 12.25 & -1.685\times10^{-12} & 7.357\times10^{-13} \\ -1.734\times10^{-7} & 6.839\times10^{-12} & 2.513\times10^{-13} & -2.369\times10^{-13} & 12.25 & 7.014\times10^{-12} \\ 3.017\times10^{-14} & 1.370e\text{-}13 & -8.636\times10^{-15} & -1.881\times10^{-13} & -9.777\times10^{-14} & 12.25 \end{bmatrix} \tag{3.2.4}$$

The target feedback loop $G_{KF}(s) = C\left(sI - A\right)^{-1} H$ has the crossover frequency at 1000 rad/s. It is designed to reduce the disturbances in the frequency less than 630 rad/s (100 Hz) of frequency in Fig. 3-4 because the range of mechanical vibration frequency is between 10 Hz and 100 Hz [20]. The shape of the singular values depends on $H$ derived by $Q_f$ and $R_f$.

The $Q_c$ and $R_c$ matrices should be determined prior to compute the control gain

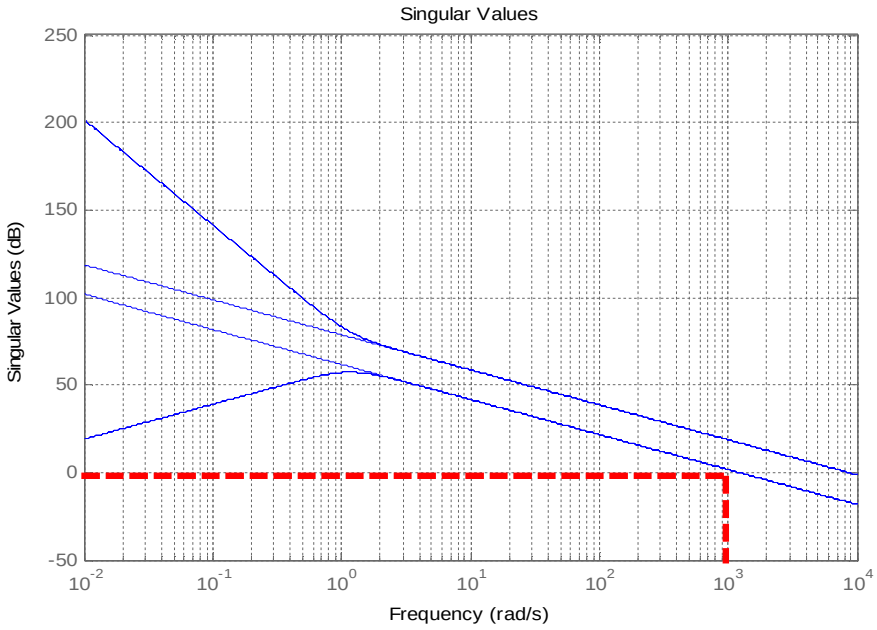


Fig. 3-4. Singular values of the designed target feedback loop. The dashed zone is the target frequency range to reject disturbance.

matrix $G$. Let us,

$$Q_c = C^T C = diag\left(1,1,1,0,0,0,1,1,1,0,0,0\right) \tag{3.2.5}$$

$$R_c = \rho I_{6\times 6} = 9\times 10^{-11} I_{6\times 6}. \tag{3.2.6}$$

From (3.2.7) and (3.2.8), we solve the control Riccati equation, (3,1,12) and determine the control gain matrix, $G$.

The loop transfer function, $G(s)K(s)$ is well approximated to the TFL in Fig. 3-5. The crossover frequency of the loop is about 600 rad/s. The loop shape approaches the target loop as $\rho$ tends to zero. Nevertheless, if $\rho$ is too small, the control gain becomes too large. It is possible to reach the limit of the control input capacity in a real system. Thus, $\rho$ must be chosen carefully.

$$G = \begin{bmatrix} 316228 & -2.514\times10^{-18} & -4.162\times10^{-40} & 1.975\times10^{-23} & 2.4363 & 0 \\ -9.724\times10^{-19} & 316228 & 1.937\times10^{-17} & -2.436 & 3.914\times10^{-11} & 0 \\ -4.326\times10^{-40} & 2.500\times10^{-17} & 316228 & 1.273\times10^{-10} & -1.566\times10^{-32} & 0 \\ 410.9 & -2.539\times10^{-21} & -3.967\times10^{-43} & 2.066\times10^{-26} & 3.282\times10^{-3} & 0 \\ -2.539\times10^{-21} & 410.9 & 2.388\times10^{-20} & -3.282\times10^{-3} & -9.354\times10^{-14} & 0 \\ -3.967\times10^{-43} & 2.3882\times10^{-20} & 410.9 & 1.141\times10^{-13} & -1.366\times10^{-35} & 0 \\ 1.145\times10^{-24} & -0.1837 & -3.133\times10^{-12} & 316228 & 4.299\times10^{-17} & 0 \\ 0.1837 & -4.953\times10^{-13} & -8.199\times10^{-35} & 3.890\times10^{-18} & 316228 & 0 \\ 0 & 0 & 0 & 0 & 0 & 316228 \\ 2.633\times10^{-29} & -4.184\times10^{-06} & 1.454\times10^{-16} & 14.67 & 1.007\times10^{-21} & 0 \\ 4.184\times10^{-6} & -1.192\times10^{-16} & -1.742\times10^{-38} & 1.007\times10^{-21} & 14.67 & 0 \\ 0 & 0 & 0 & 0 & 0 & 20.33 \end{bmatrix}^T$$

(3.2.7)

After completing the design procedure of the LQG/LTR compensator, the simulation in the full nonlinear dynamics model (2.2.9) and (2.3.11) is conducted to verify the feasibility in the vibration rejection. The simulated vibration rejection performances in *x*-, *y*-, and *z*-axes were compared in Figs. 3.6–3.8 with the lead-lag positioning compensator that was designed not for vibration rejection but for positioning [38].

The LQG/LTR compensator in the *x*- and *y*-axes attenuates about 10% more than the lead-lag compensator. In vertical motion, the vibration is reduced about 80% more by the LQG/LTR compensator than by a lead-lag compensator. The simulations provide the evidence of the feasibility of the LQG/LTR compensator for vibration.

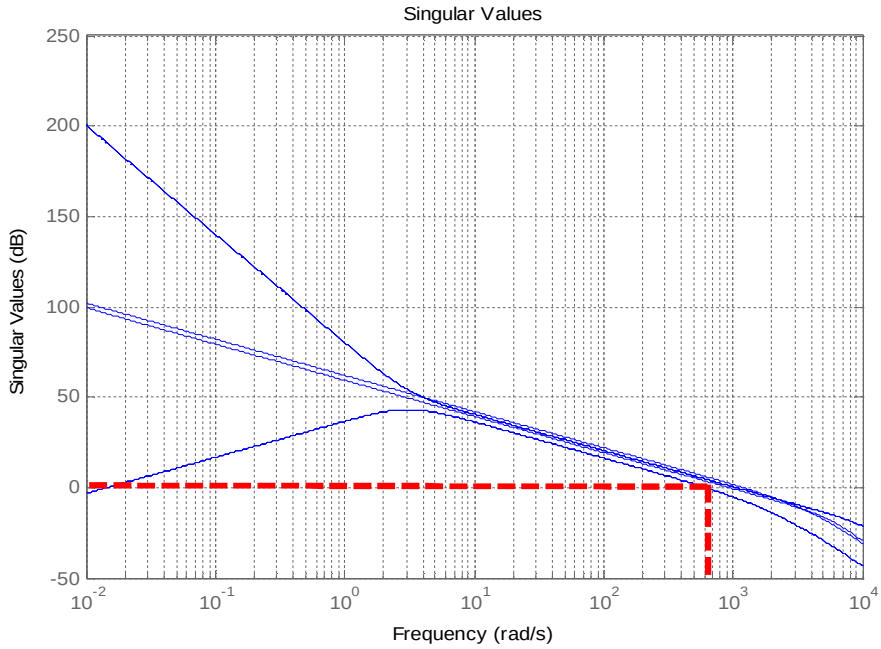


Fig. 3-5. Singular values of the loop transfer function. The dashed zone is the target frequency range to reject disturbance.

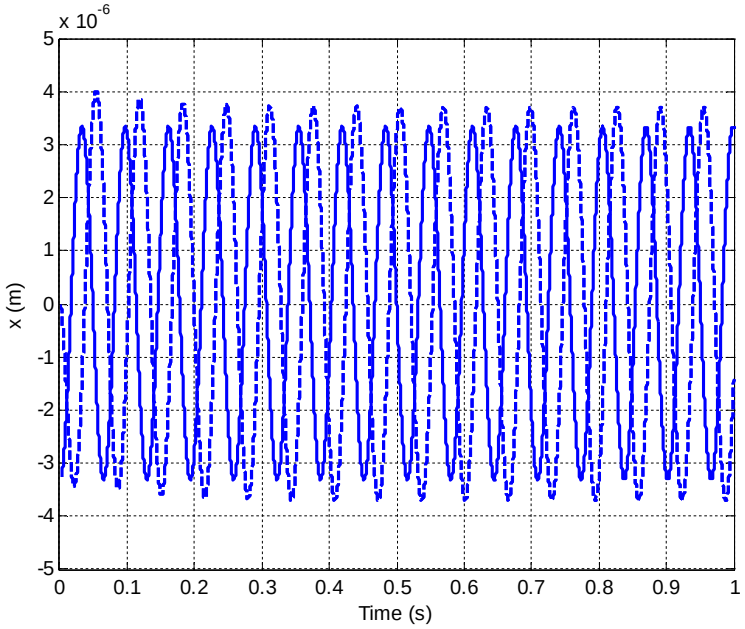


Fig. 3-6. Vibration rejection performances in the *x*-axis when vibration disturbance of 15.5 Hz is applied. The solid line indicates that by an LQG/LTR compensator, and the dashed line indicates that by a lead-lag compensator.

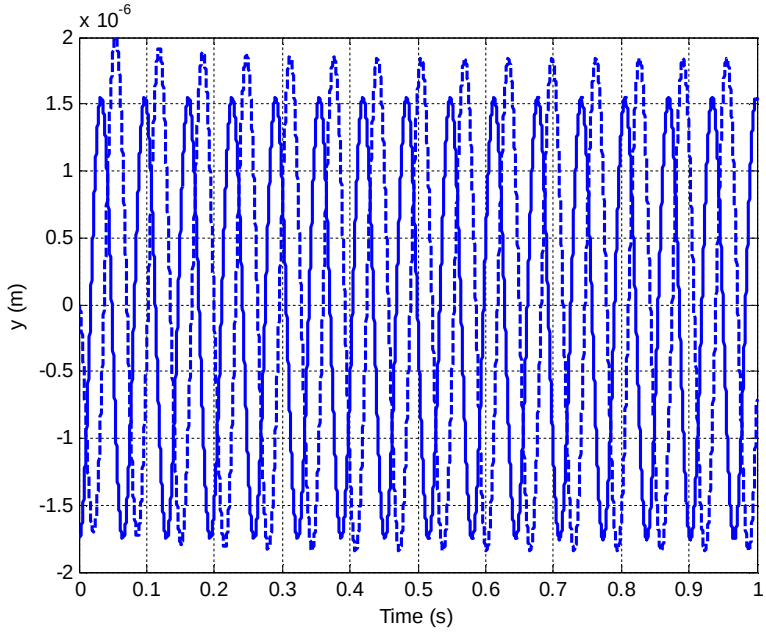


Fig. 3-7. Vibration rejection performances in the *y*-axis when vibration disturbance of 15.5 Hz is applied. The solid line indicates that by an LQG/LTR compensator, and the dashed line indicates that by a lead-lag compensator.

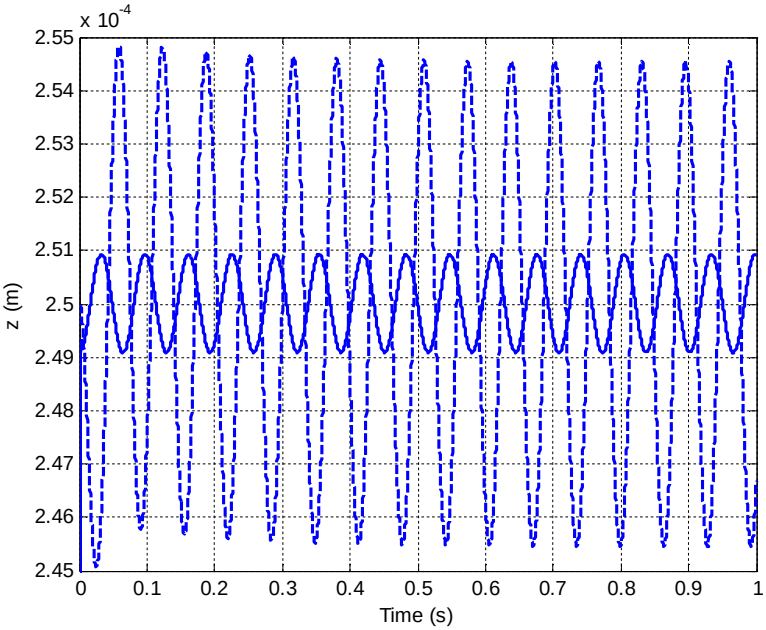


Fig. 3-8. Vibration rejection performances in the *z*-axis when vibration disturbance of 15.5 Hz is applied. The solid line indicates that by an LQG/LTR compensator, and the dashed line indicates that by a lead-lag compensator.

# CHAPTER IV

# MODELING OF THE MAGLEV SYSTEM WITH THE OPTICAL TABLE IN VERTICAL MOTION

## 4.1 Modeling of the Optical Table with Pneumatic Passive Vibration Isolators

Pneumatic isolation tables like the optical table used in this research are widely used in semiconductor manufacturing, precision machine tools and precision measurement apparatuses. A pneumatic isolation table is supported by several air springs consisting of air-filled chambers, an elastomeric diaphragm and a piston [29]. Models of pneumatic vibration isolators are based on nonlinear models of pneumatic cylinders by Shearer [47]. These models include the enthalpy equations for the pneumatic chambers, a flow equation for the restrictor connecting the chambers, and the equation of motion for the piston supporting the payload. Harris and Crede [48] proposed a linear model of the pneumatic vibration isolator. The linearity of this model is obtained by assuming small payload displacements. A simpler linear model provide linear damping at all payload displacement amplitudes was derived by DeBra and Bryan [49].

Although prior accurate models for pneumatic isolators were derived, they are too complicated to apply in this research. Since the amplitude of displacement by

vibration in nanotechnology application is very small, we simply represent the pneumatic isolation table as a mass-spring-damper system shown in Fig. 4-1.

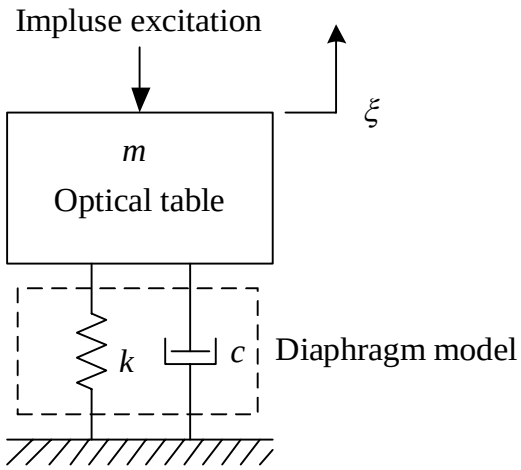


Fig. 4-1. Mechanical model for pneumatic vibration isolator with diaphragm.

To determine the stiffness and damping ratio, the impulse response of the optical table was measured with an accelerometer (PCB Piezotronics 356B18) in Fig. 4-2. The optical table is impacted by a rubber hamper of mass 595.8 g. The generated motion is assumed a decaying sinusoid $x = Ae^{-\zeta\omega_n t}$ where $\omega_n$ and $\zeta$ are the natural frequency and the damping ratio of the system.

$$\delta = \ln(\frac{x_1}{x_2}) = \zeta\omega_n(t_2 - t_1) = \zeta\omega_n T_d \tag{4.1.1}$$

$$\omega_d = \frac{2\pi}{T_d} = \omega_n\sqrt{1-\zeta^2} \tag{4.1.2}$$

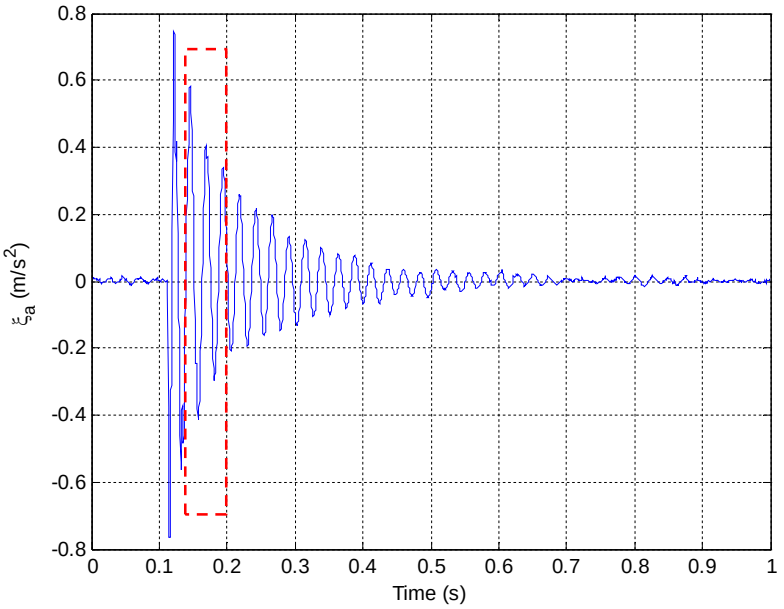


(a)

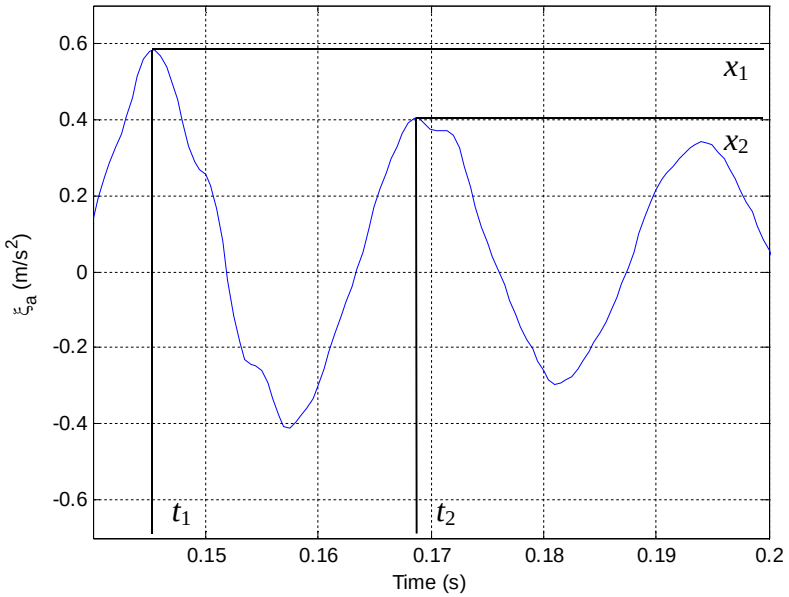


(b)

Fig. 4-2. Impulse response of the optical table in the *z*-axis: (a) original (b) zoomed in dashed zone.

where $t_1 = 0.1455$ s, $t_2 = 0.1685$ s, $x_1 = 0.5843$ m/s$^2$, and $x_2 = 0.4024$ m/s$^2$. From equations (4.1.1)–(4.1.2), we determine the natural frequency, $\omega_{nz} = \sqrt{\frac{k_{1z}}{m_1}} = 273.663$ rad/s, and the damping ratio $\zeta_z = \frac{c_{1z}}{2\sqrt{m_1 k_{1z}}} 0.0592554$ in the *z*-axis. Therefore, the stiffness is $k_{1z} = 3.11548 \times 10^7$ N/m, and the damping coefficient is $c_{1z} = 1.34917 \times 10^4$ N-s/m.

## 4.2 Unbalanced Vibrating Motor

A common source of such a sinusoidal force is unbalance in a rotating machine or rotor. Let us suppose that a rotating machine of mass $m_1$, can be modeled as being mounted on a spring of stiffness, $k_{1z}$, to a fixed support, and that there is viscous damping in the system, with a damping coefficient, $c_{1z}$.

Suppose that the unbalance can be represented by a mass $m_u$ at a distance $e$ from the center of rotation. $e$ is sometimes called the eccentricity. Let the angular speed of rotation of the rotor be Ω. The system is illustrated in Figs. 4-3–4-4.

The equation of motion is

$$m_1 \frac{d^2\xi}{dt^2} + m_u \frac{d^2}{dt^2}\left(e \sin \Omega t\right) = -k_1 \xi - c_1 \frac{d\xi}{dt}. \qquad (4.2.1)$$

This can be written as:

$$m_1 \ddot{\xi} + c_1 \dot{\xi} + k_1 \xi = F_d = m_u \Omega^2 e \sin \Omega t \qquad (4.2.2)$$

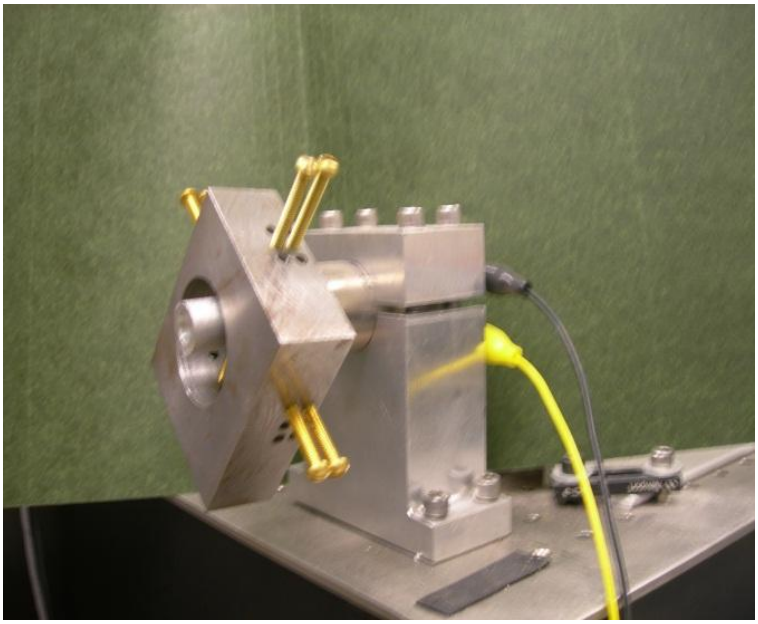

Fig. 4-3. Unbalanced mass vibration generator.

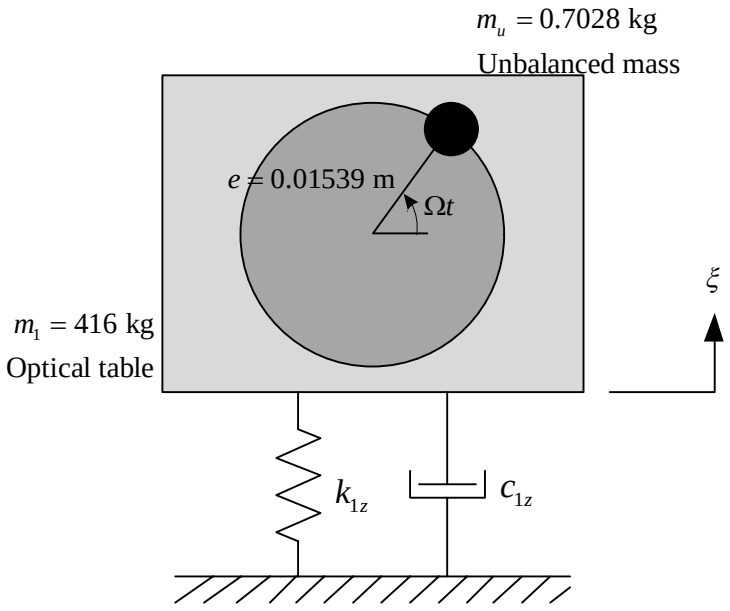


Fig. 4-4. Model of an unbalanced rotating machine.

## 4.3 Equations of Motion of the Maglev System with the Optical Table in Vertical Motion

Since we found the stiffness ($k_{1z}$) and damping coefficient ($c_{1z}$) of the optical table and derived the vibration disturbance ($F_{dz}$) generated by an unbalanced rotor in the previous two sections, we can provide all governing EOMs of the maglev system with the optical table. It is considered a two-mass problem as shown in Fig. 4-5.

The EOMs of the platen with mass ($m_2$) and the optical table with mass ($m_1$) become

$$m_2\ddot{z} = F_z\left(z,\xi,i\right) - m_2 g \tag{4.3.1}$$

$$m_1\ddot{\xi} = -c_{1z}\dot{\xi} - k_{1z}\xi - m_1 g - F_z\left(z,\xi,i\right) + F_{dz} \tag{4.3.2}$$

where the magnetic force $F_z(z,\xi,i)$ is a function of the distance between the magnet and coil, and the current through the coils.

The approximate quadratic polynomial fit is given by

$$F_z(z,\xi,i) = \left(\alpha_2\left(z-\xi\right)^2 + \alpha_1\left(z-\xi\right) + \alpha_0\right)i \tag{4.3.3}$$

where $\alpha_2 = 4.7418\times10^4$, $\alpha_1 = -8.7132\times10^2$, and $\alpha_0 = 6.7712$ [39].

## 4.4 Linearization of the Maglev System Model with the Optical Table

The only nonlinear term in the EOMs is position dependences in the magnetic force. To linearize the equations, let set the perturbation equations $z = z_0 + \tilde{z}$, $\xi = \xi_0 + \tilde{\xi}$,

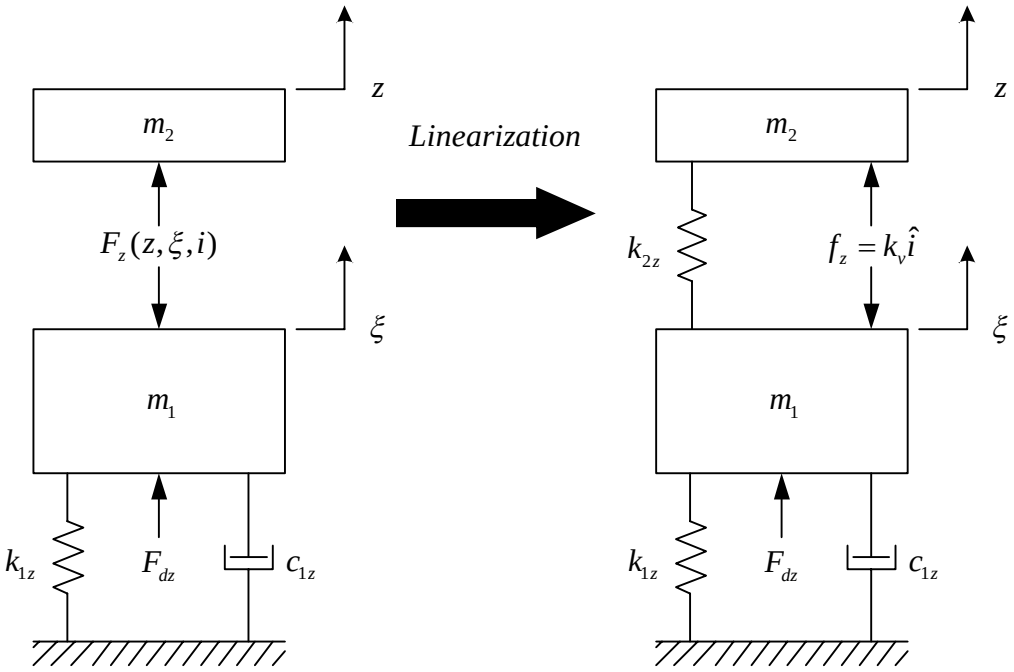


Fig. 4-5. (a) Nonlinear model of the maglev system. (b) Magnetic stiffness effect added in a linearized model.

and $i = i_0 + \tilde{i}$. Subscript 0 means values at an operation point. The variables with tilde are perturbation.

Using Taylor-series expansion, (4.3.1) becomes

$$m_2\left(\cancel{\ddot{z}_0} + \ddot{\tilde{z}}\right) = \cancel{F_z(z_0,\xi_0,i_0)} + \left.\frac{\partial F_z(z,\xi,i)}{\partial z}\right|_{z_0,\xi_0,i_0}\tilde{z} + \left.\frac{\partial F_z(z,\xi,i)}{\partial \xi}\right|_{z_0,\xi_0,i_0}\tilde{\xi} + \left.\frac{\partial F_z(z,\xi,i)}{\partial i}\right|_{z_0,\xi_0,i_0}\tilde{i} - \cancel{m_2 g} \tag{4.4.1}$$

The linearized EOM of the platen in the *z*-axis is

$$m_2\ddot{\tilde{z}} = \left(\left.\frac{\partial F_z}{\partial z}\right|_{z_0,\xi_0,i_0}\right)\tilde{z} + \left(\left.\frac{\partial F_z}{\partial \xi}\right|_{z_0,\xi_0,i_0}\right)\tilde{\xi} + \left(\left.\frac{\partial F_z}{\partial i}\right|_{z_0,\xi_0,i_0}\right)\tilde{i} \tag{4.4.2}$$

where $$\left.\frac{\partial F_z(z,\xi,i)}{\partial z}\right|_{z_0,\xi_0,i_0} = \left(2\alpha_2\left(z_0-\xi_0\right)+\alpha_1\right)i_0 \tag{4.4.3}$$

$$\left.\frac{\partial F_z(z,\xi,i)}{\partial \xi}\right|_{z_0,\xi_0,i_0} = -\left(2\alpha_2\left(z_0-\xi_0\right)+\alpha_1\right)i_0 \tag{4.4.4}$$

$$\left.\frac{\partial F_z(z,\xi,i)}{\partial i}\right|_{z_0,\xi_0,i_0} = \left(\alpha_2\left(z_0-\xi_0\right)^2+\alpha_1\left(z_0-\xi_0\right)+\alpha_0\right). \tag{4.4.5}$$

To determine the coefficients in (4.4.2), the value of $i_0$ should be found. At equilibrium point, the magnetic force should be balanced with the gravity in (4.4.6),

$$F_z(z_0,\xi_0,i_0) = \left(\alpha_2\left(z_0-\xi_0\right)^2+\alpha_1\left(z_0-\xi_0\right)+\alpha_0\right)i_0 = m_2 g. \tag{4.4.6}$$

Thus, the current at the operation point $\left(z_0-\xi_0\right)=250\ \mu\text{m}$ is

$$i_0 = \frac{m_2 g}{\left(\alpha_2\left(z_0-\xi_0\right)^2+\alpha_1\left(z_0-\xi_0\right)+\alpha_0\right)} = 0.3995\ \text{A}. \tag{4.4.7}$$

Finally, the linearized EOM of the platen is

$$m_2\ddot{\tilde{z}} = k_{2z}\left(\tilde{z}-\tilde{\xi}\right)+k_v\tilde{i} \tag{4.4.8}$$

where $k_{2z} = \left(2\alpha_2\left(z_0-\xi_0\right)+\alpha_1\right)\cdot i_0 = -3.38665\times10^2$ and

$k_v = \alpha_2\left(z_0-\xi_0\right)^2+\alpha_1\left(z_0-\xi_0\right)+\alpha_0 = 6.5563$.

Simlary, the linearized EOM of the optical table with vibration disturbance becomes

$$m_1\ddot{\tilde{\xi}}+c_{1z}\dot{\tilde{\xi}}+k_{1z}\tilde{\xi} = -k_{2z}\left(\tilde{z}-\tilde{\xi}\right)-k_v\tilde{i}+F_{dz}. \tag{4.4.9}$$

The platen and the optical table are coupled by the magnetic stiffness as shown in (4.4.8)–(4.4.9). Therfore, the vibration disturbance generated on the optical table affects the motion of the platen although there is no mechanical contact between the platen and the optical table.

## 4.5 Validation of the Linearized Model of the Maglev System in Vertical Motion

Model validation is a crucial step in any modeling procedure, since a model is useless if it has not been confirmed with experiments. The model of the maglev system with the optical table should be validated by experiments. Therefore, the comparisons between the experimental and simulation results with vibration disturbance are presented in Figs. 4-6–4-7 before applying the vibration control schemes. The experimental data were acquired with the 15.9 Hz vibration disturbance generated by the unbalanced motor. The simulation data was obtained by Simulink integrated with MATLAB®. The Simulink block diagram is presented in Appendix B.

While the position controller keeps the position at 250 μm in the *z*-axis, the motion of the platen with the vibration disturbance was measured and simulated. The same lead-lag position feedback controller designed by Verma [38] is applied to both experiment and simulation. The lead-lag compensator is

$$D_P(s) = 2.32003\times10^5 \frac{(s+57.47)(s+6.271)}{s(s+2103)}. \qquad (4.4.10)$$

The position response is very similar in both experimented and simulated plots in Fig. 4-6. The simulation shows the pure sinusoidal motion. But, there is a little difference in the experiment because of the unmodeled dynamics. The difference between the simulation and experiment is negligible level in this work.

Fig. 4-7 presents the velocity response. Since the reading from the capacitive analog position sensors contains high-frequency noise, the velocity was obtained by differentiating the position data, the high-frequency noise was amplified. To compare without the high-frequency noise, the filtered experimental and simulated results are shown in Fig. 4-8. This low-pass filter has the pass band edge at 100 Hz. The filter transfer function is

$$H(z) = \frac{0.0010592 + 0.0031775z^{-1} + 0.0031775z^{-2} + 0.038541z^{-3}}{z - 2.5919z^{-1} + 2.2715z^{-2} - 0.67117z^{-3}} \quad (4.4.11)$$

This pass band is only to show comparison the low-frequency motions between the simulations and the experiments. A real-time low-pass filter for velocity feedback control will be introduced in the next section. The velocity response is very similar in both filtered experimental and simulated plots in Fig. 4-8. There are still some higher-frequency components than 15.9 Hz vibration. The magnitude and behavior of the experiment data is very similar with the simulation. The difference between the simulation and experiment in velocity response is also neglectable level in this work. Therefore, the linearized model of the maglev stage with the optical table is validated to use in the controller design.

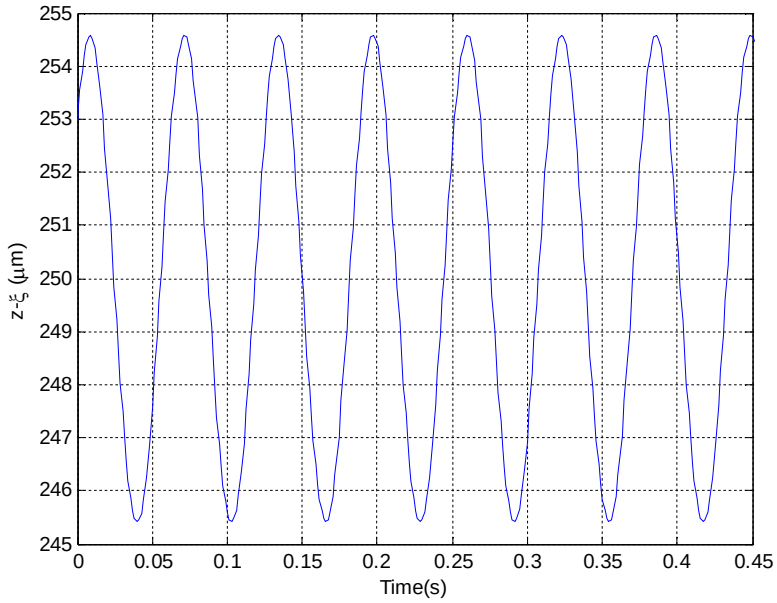


(a)

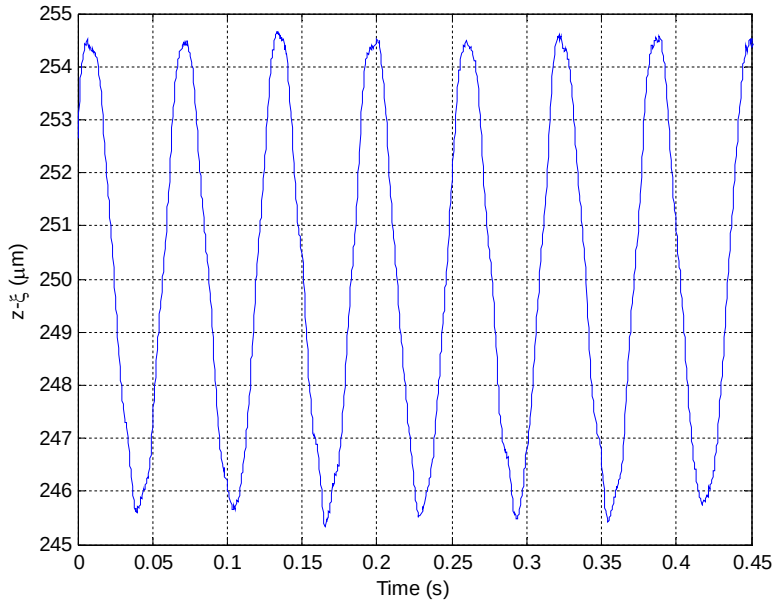


(b)

Fig. 4-6. Relative position response of the optical table and the platen with vibration disturbance. (a) and (b) are simulated and experimented positions.

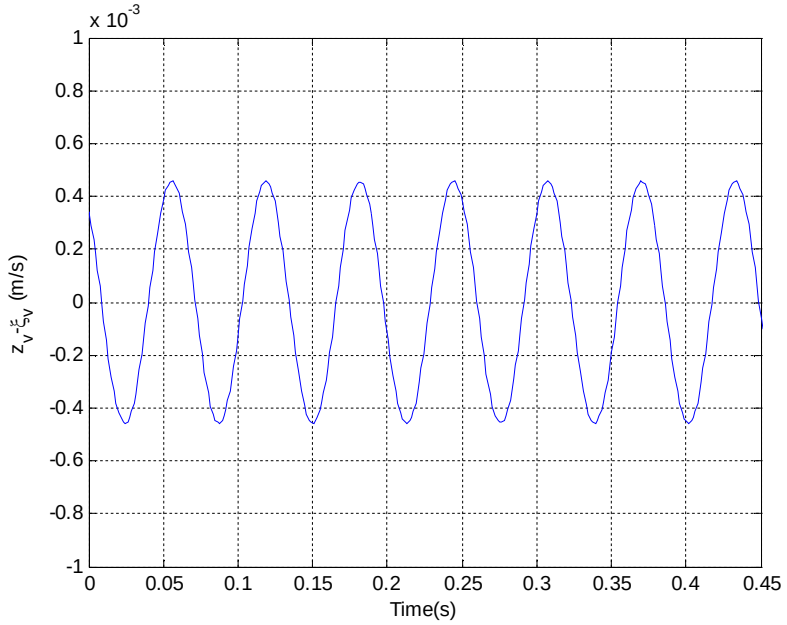


(a)

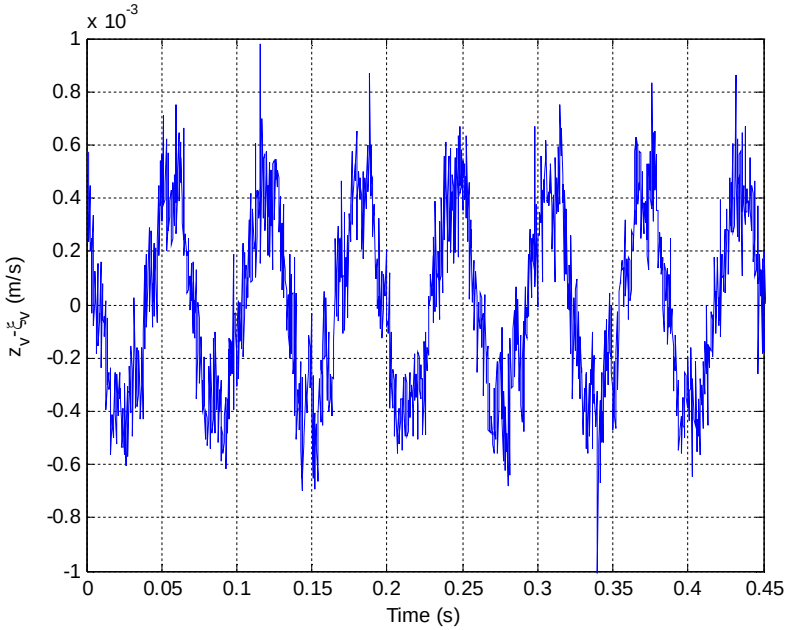


(b)

Fig. 4-7. Relative velocity between the optical table and the platen with vibration disturbance. (a) and (b) are simulated and experimented velocities.

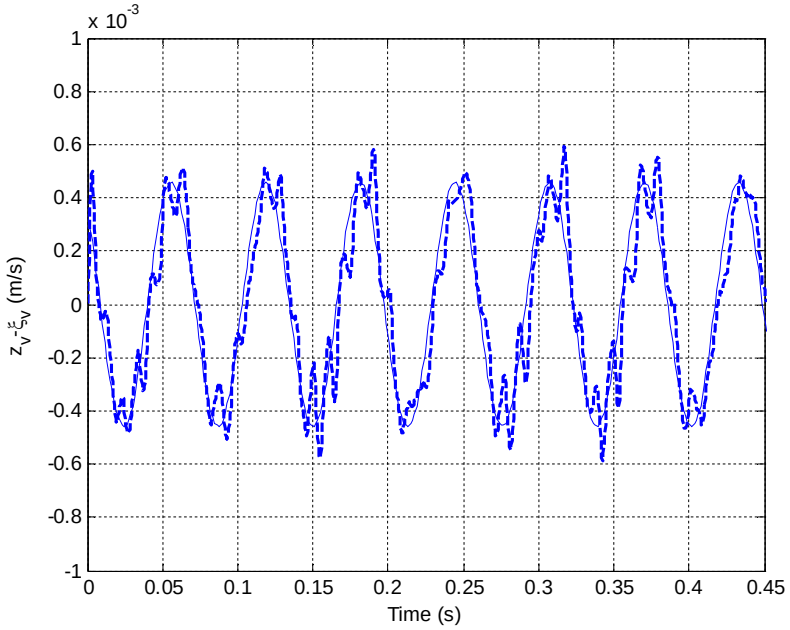


Fig. 4-8. Filtered relative velocity between the optical table and the platen with vibration disturbance. (a) solid line is the simulation, and (b) the dotted line is filtered data of the experiment.

## 4.6 Low-Pass Filter for Obtaining Velocity Data from Vertical Position Sensors

Because the high frequency noise amplified by the differentiation is not desired, a software low-pass filter is implemented to measure the vertical velocity. Chebyshev type I approximation is used to design the low-pass filer. The third-order low-pass filter with the pass band edge of 400 Hz and the ripple factor of 0.01 is designed in Fig 4-9 when the sampling rate is 5 kHz. If the pass band edge is too low, the phase lag is observed. If the pass band edge is too high, high-frequency noise is not filtered effectively. In the work, the pass band edge of 400 Hz is appropriate. The transfer function of the low-pass filter is

$$H(z) = \frac{0.038541 + 0.11562z^{-1} + 0.11562z^{-2} + 0.038541z^{-3}}{z - 1.38589z^{-1} + 0.90333z^{-2} - 0.20912z^{-3}}. \quad (4.4.12)$$

The magnitude output of the filter is unity up to 400 Hz and the phase lag is less than 69º.

To reject vibrations the filtered velocity signal should not be distorted by the filter up to 100 Hz. The phase lag of the filter at 100 Hz is 15.7º. This phase lag is sufficiently acceptable to use as a feedback control signal. The comparison between original and filtered velocity signals are shown in Fig. 4-10. The high-frequency noise is disappeared in filtered signal. The phase shift is observed in Fig. 4-10 (a) and (b), but it is ignorable. This filter makes less sensitive to high-frequency noise and is validated to use in the interesting frequencies of 10 to 100 Hz.

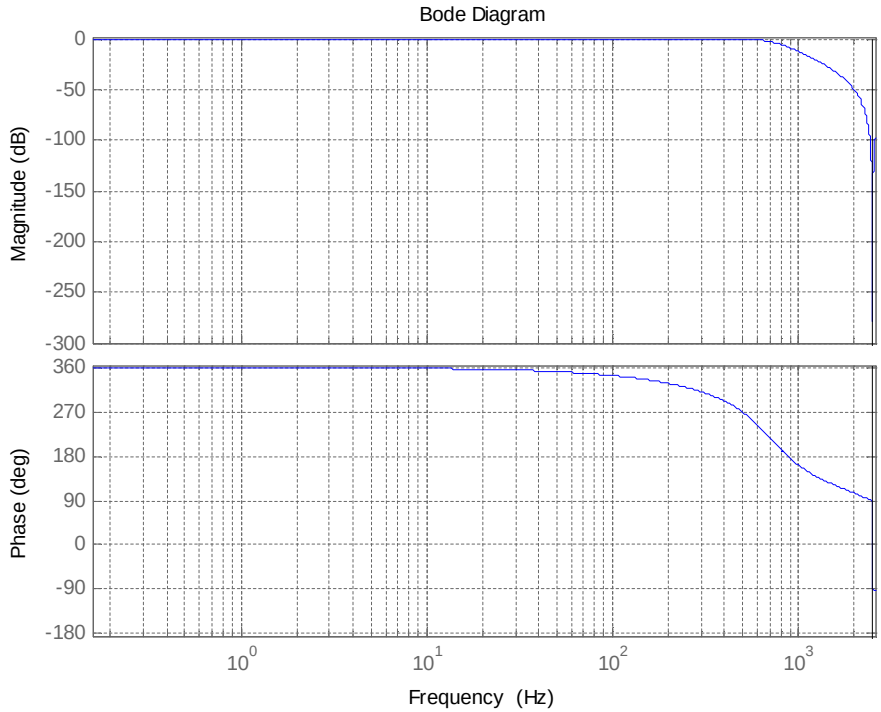


Fig. 4-9. A third-order Chebyshev Type I filter with the pass band edge of 400 Hz and the ripple factor of 0.01.

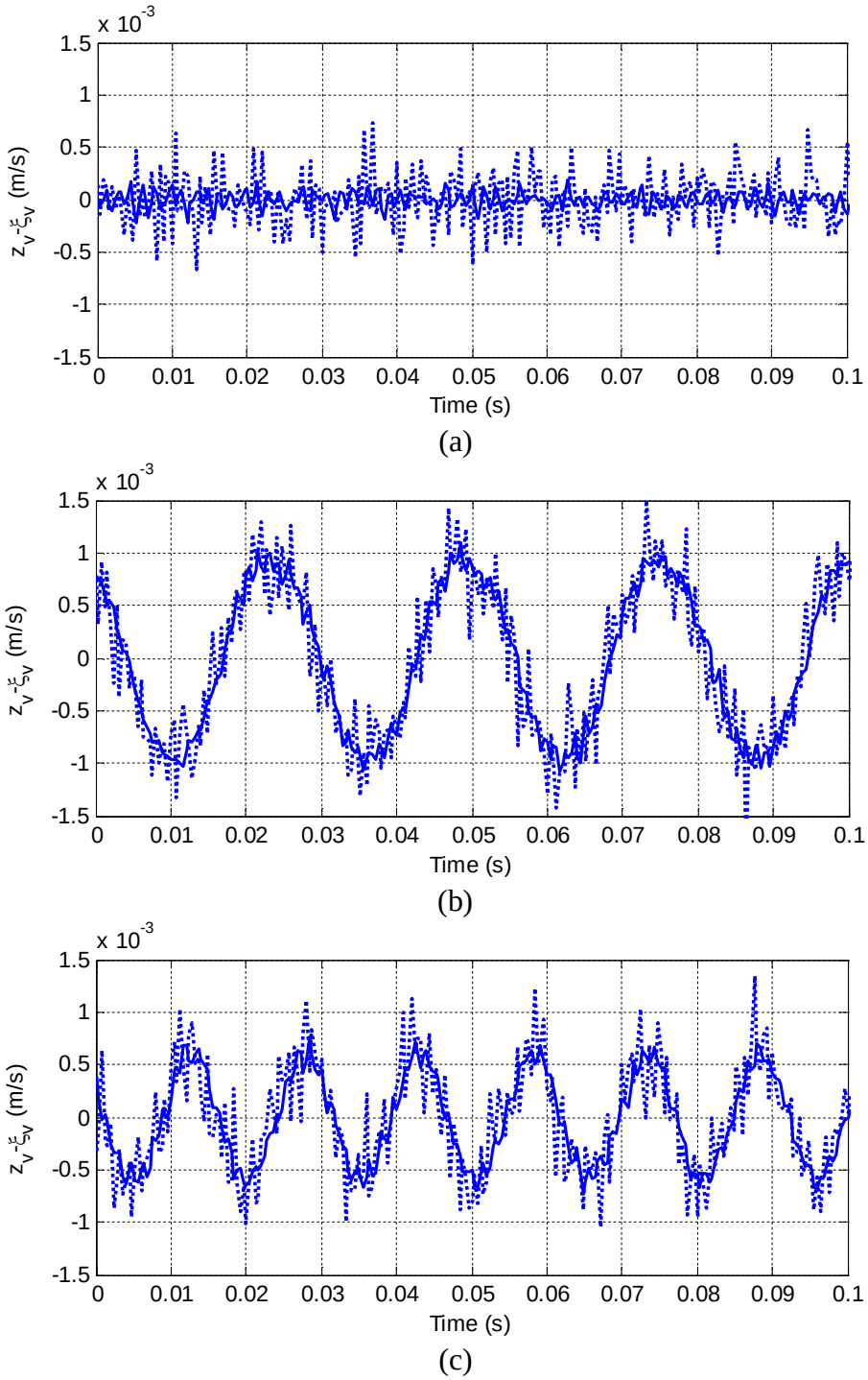


Fig. 4-10. Comparison between the original (dotted line) and the filtered (solid line) velocity signals when the vibration disturbance of (a) 0 Hz, (b) 38.8 Hz, and (c) 66.4 Hz are applied in the experiments.

# CHAPTER V

# VIBRATION CONTROL IN VERTICAL MOTION

## 5.1 Transfer Function of the Maglev System in Vertical Motion

To analyze the frequency response of the maglev system in the *z*-axis and to design the controllers, we take the Laplace transform of (4.4.8) with zero initial conditions.

$$L\left\{m_2\ddot{\tilde{z}}(t)\right\} = L\left\{k_{2z}\left(\tilde{z}(t)-\tilde{\xi}(t)\right)+k_v\tilde{i}(t)\right\} \tag{5.1.1}$$

$$\tilde{\Xi}(s) = \frac{-\left(m_2 s^2 - k_{2z}\right)}{k_{2z}}\tilde{Z}(s) + \frac{k_v}{k_{2z}}\tilde{I}(s) \tag{5.1.2}$$

From the Laplace transform of (4.4.9), we obtain

$$L\left\{m_1\ddot{\tilde{\xi}}(t)+c_{1z}\dot{\tilde{\xi}}(t)+k_{1z}\tilde{\xi}(t)\right\} = L\left\{-k_{2z}\left(\tilde{z}(t)-\tilde{\xi}(t)\right)-k_v\tilde{i}(t)+F_{dz}(t)\right\}. \tag{5.1.3}$$

$$\left(m_1 s^2 + c_{1z}s + \left(k_{1z}-k_{2z}\right)\right)\tilde{\Xi}(s) = -k_{2z}\tilde{Z}(s) - k_v\tilde{I}(s) + F_{dz}(s) \tag{5.1.4}$$

If (5.1.2) is substituted to (5.1.4), we obtain following transfer function (TF).

$$\tilde{Z}(s) = \frac{k_v\left(m_1 s^2 + c_{1z}s + k_{1z}\right)}{\lambda_z(s)}\tilde{I}(s) + \frac{-k_{2z}}{\lambda_z(s)}F_{dz}(s) \tag{5.1.5}$$

where

$$\lambda_z(s) = m_1 m_2 s^4 + c_{1z}m_2 s^3 + \left(\left(k_{1z}-k_{2z}\right)m_2 - k_{2z}m_1\right)s^2 - c_{1z}k_{2z}s - k_{1z}k_{2z}. \tag{5.1.6}$$

From (5.1.2), (5.1.5), and (5.1.6),

$$\tilde{\Xi}(s) = \frac{-k_v m_2 s^2}{\lambda_z(s)} \hat{I}(s) + \frac{m_2 s^2 - k_{2z}}{\lambda_z(s)} F_{dz}(s) \tag{5.1.7}$$

By combining (5.1.5) and (5.1.7), the system transfer functions in matrix form are

$$\begin{aligned} \begin{bmatrix} \tilde{Z}(s) \\ \tilde{\Xi}(s) \end{bmatrix} &= \frac{1}{\lambda_z(s)} \begin{bmatrix} k_v \left( m_1 s^2 + c_{1z} s + k_{1z} \right) & -k_{2z} \\ -k_v m_2 s^2 & m_2 s^2 - k_{2z} \end{bmatrix} \begin{bmatrix} \tilde{I}(s) \\ F_{dz}(s) \end{bmatrix} \\ &= \begin{bmatrix} G_{11}(s) & G_{12}(s) \\ G_{21}(s) & G_{22}(s) \end{bmatrix} \begin{bmatrix} \tilde{I}(s) \\ F_d(s) \end{bmatrix}. \end{aligned} \tag{5.1.8}$$

The equivalent block diagram of the transfer function is illustrated in Fig. 5-1.

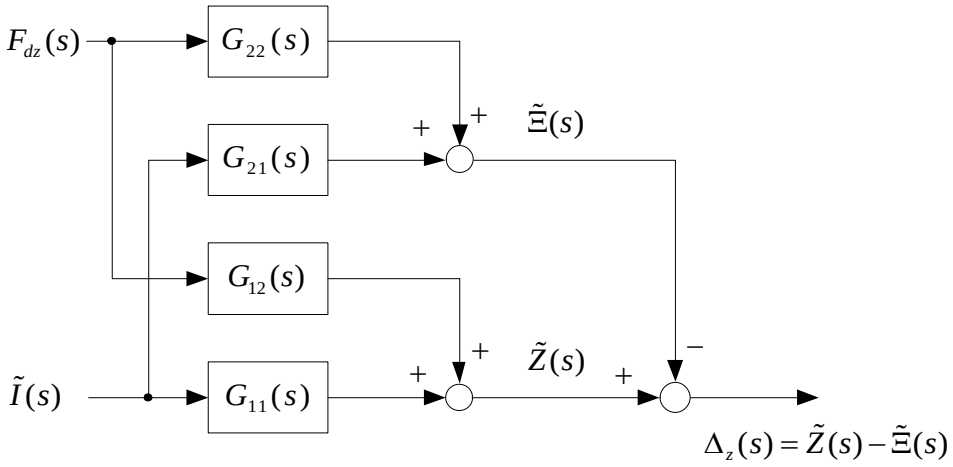


Fig. 5-1. Equivalent block diagram of the motion of maglev system in the *z*-axis.

From (5.1.5) and (5.1.7), the output $\Delta_z(s) = \tilde{Z}(s) - \tilde{\Xi}(s)$ is

$$\Delta_z(s) = \tilde{Z}(s) - \tilde{\Xi}(s) = (G_{11} - G_{21})\tilde{I}(s) + (G_{12} - G_{22})F_{dz}(s). \tag{5.1.9}$$

The block diagram from (5.1.9) with feedback control for positioning is presented in Fig.

5-2, where $G_P(s) = G_{11}(s) - G_{21}(s)$ and $G_d(s) = G_{12}(s) - G_{22}(s)$ are a plant transfer function and a disturbance transfer function.

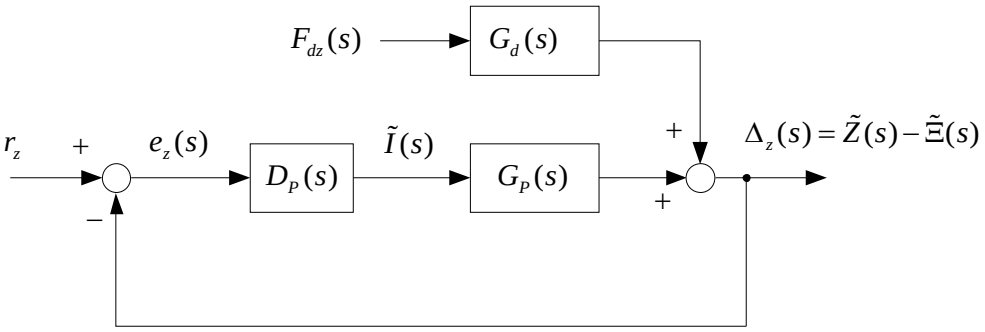


Fig. 5-2. Block diagram of a positioning feedback control of the maglev system.

The transfer function from the reference $r_z(s)$ and the vibration disturbance $F_{dz}(s)$ is

$$\Delta_z(s) = \frac{D_P(s)G_P(s)}{1 + D_P(s)G_P(s)} r_z(s) + \frac{G_d(s)}{1 + D_P(s)G_P(s)} F_{dz}(s) \qquad (5.1.10)$$

The loop transfer function of the maglev system becomes

$$\begin{aligned} D_P(s)G_P(s) &= a\frac{(s+z_1)(s+z_2)}{s(s+p_1)}\left(G_{11} - G_{21}\right) \\ &= \frac{\begin{aligned} &ak_v\left(m_1+m_2\right)s^4 + ak_v\left(c_{1z} + \left(m_1+m_2\right)\left(z_1+z_2\right)\right)s^3 \\ &+ak_v\left(k_{1z} + c_{1z}\left(z_1+z_2\right) + \left(m_1+m_2\right)z_1z_2\right)s^2 \\ &+ ak_v\left(k_{1z}\left(z_1+z_2\right) + c_{1z}z_1z_2\right)s + ak_vk_{1z}z_1z_2 \end{aligned}}{\begin{aligned} &m_1m_2s^6 + m_2\left(c_{1z} + m_1p_1\right)s^5 + \left(\left(k_{1z} - k_{2z}\right)m_2 - k_{2z}m_1 + c_{1z}m_2p_1\right)s^4 \\ &+\left(\left(k_{1z} - k_{2z}\right)m_2p_1 - k_{2z}\left(c_{1z} - m_1p_1\right)\right)s^3 \\ &-k_{2z}\left(k_{1z} + c_{1z}p_1\right)s^2 - k_{1z}k_{2z}p_1s \end{aligned}} \end{aligned}$$

(5.1.11)

$$D_P(s)G_P(s) = \frac{869457.0s^4 + 8.29471\times10^7 s^3 + 6.4158\times10^{10} s^2 + 3.9676\times10^{12} s + 2.23769\times10^{13}}{s^6 + 2134.68s^5 + 139347.0s^4 + 1.52981\times10^8 s^3 + 1.75117\times10^8 s^2 + 1.90583\times10^{11} s} \tag{5.1.12}$$

The position controller is a lead-lag compensator that was designed by Verma [38],

$$D_P(s) = a\frac{(s+z_1)(s+z_2)}{s(s+p_1)}. \tag{5.1.13}$$

The parameter values in vertical motion are summarized in Table 5-1.

Table 5-1. Parameter values in vertical motion

| Parameter | Value | Parameter | Value |
|---|---|---|---|
| $m_1$ | 436 kg | $a$ | $2.32003\times10^5$ |
| $m_2$ | 0.267 kg | $k_v$ | 6.5563 N/A |
| $z_1$ | 6.271 | $k_{1z}$ | $3.11548\times10^7$ N/m |
| $z_2$ | 57.47 | $k_{2z}$ | –338.665 N/m |
| $p_1$ | 2103 | $c_{1z}$ | $1.34917\times10^4$ N-s/m |

This lead-lag controller has phase margin of 70.1º at the crossover frequency of 65.7 Hz. The Bode plots of the loop transfer function and the closed-loop system for vertical motion with the position controller are shown in Figs. 5-3–5-4. This lead-lag compensator is well designed for positioning if there is no vibration disturbance. A 10-μm step response in vertical motion is shown in Fig. 5-5. The rise time for this step is 0.002 s, and it settles in 0.2667 s. However, this compensator was not designed for vibration disturbance rejection. Therefore, the influence of the vibration disturbance should be analyzed.

To analyze how the vibration is introduced in the position, the transfer function from the vibration disturbance $F_{dz}$ to the position $\Delta_z$ is presented as

$$\begin{aligned}\frac{\Delta_z(s)}{F_{dz}(s)} &= \frac{G_d(s)}{1+D_P(s)G_P(s)} \\ &= \frac{-\left(m_2 s^4 + m_2 p_1 s^3\right)}{\begin{aligned}&m_1 m_2 s^6 + m_2\left(c_{1z}+m_1 p_1\right)s^5 + \left(k_{1z}m_2 + \left(ak_v - k_{2z}\right)\left(m_1+m_2\right) + c_{1z}m_2 p_1\right)s^4 \\ &+\left(c_{1z}\left(ak_v-k_{2z}\right)+k_{1z}m_2 p_1 - k_{2z}p_1\left(m_1+m_2\right)+ak_v\left(m_1+m_2\right)\left(z_1+z_2\right)\right)s^3 \\ &+\left(\left(ak_v-k_{2z}\right)k_{1z} - c_{1z}k_{2z}p_1 + ac_{1z}k_v\left(z_1+z_2\right)+ak_v\left(m_1+m_2\right)z_1 z_2\right)s^2 \\ &+\left(\left(ak_v z_1 - k_{2z}p_1\right)k_{1z} + ak_v\left(k_{1z}+c_{1z}z_1\right)z_2\right)s + ak_v k_{1z} z_1 z_2\end{aligned}} \\ &= \frac{-\left(0.002294s^4 + 4.823s^3\right)}{s^6 + 2135s^5 + 1.009\times10^6 s^4 + 2.359\times10^8 s^3 + 6.433\times10^{10}s^2 + 4.158\times10^{12}s + 2.238\times10^{13}}\end{aligned}$$

(5.1.14)

where all parameter values in (5.1.13) is presented in Table 5-1. The frequency response of the transfer function, $\frac{\Delta_z(s)}{F_{dz}(s)}$, is shown in Fig. 5-6. The magnitude of the frequency response of the vibration in the range is required to be attenuate. The major sources of the vibration disturbance in the high-precision machine are fans and motors. The vibration caused by fans and motors is in the most interesting frequency range of 10 to 100 Hz.

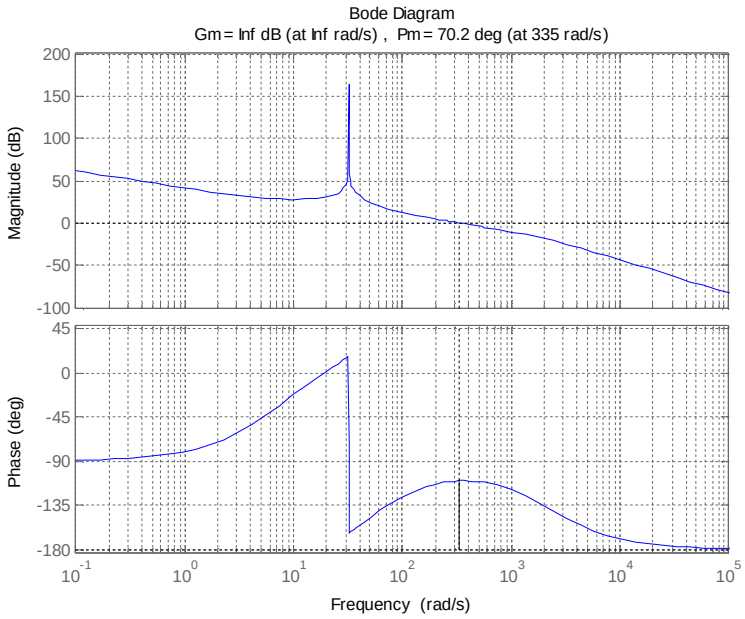


Fig. 5-3. Bode plot of the loop transfer function for vertical motion with the maglev system.

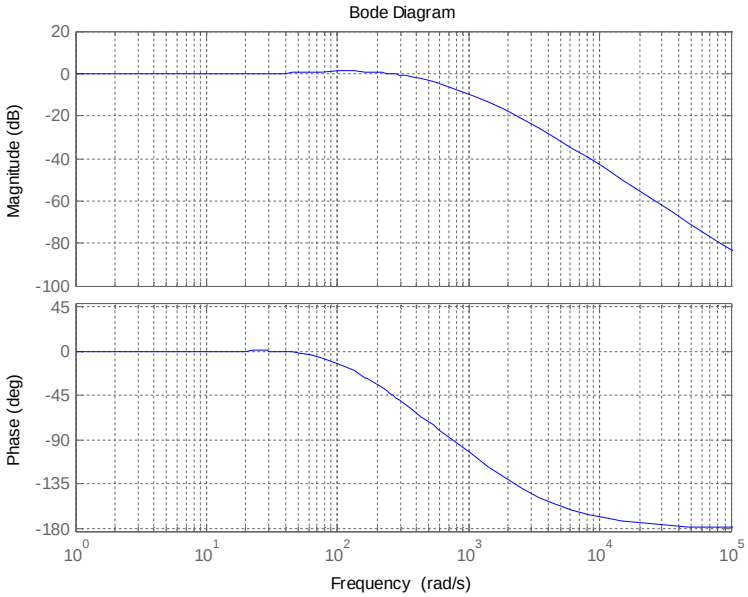


Fig. 5-4. Bode plot of the closed-loop system for vertical motion with the maglev system.

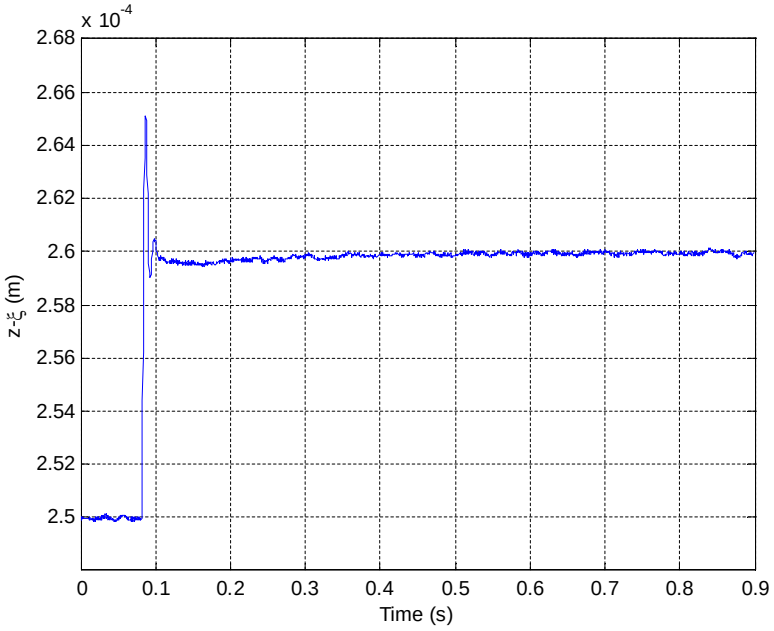


Fig. 5-5. 10-μm step response in vertical motion.

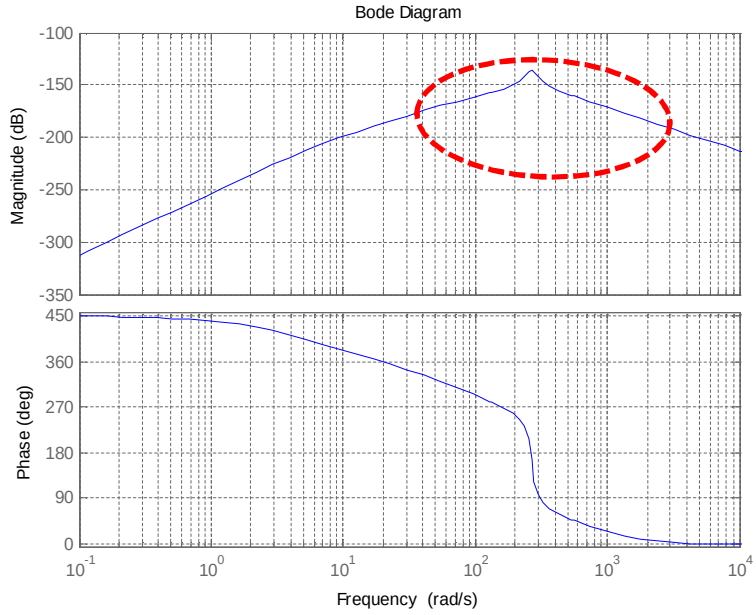


Fig. 5-6. Frequency response of the transfer function $\frac{\Delta_z(s)}{F_{dz}(s)}$. The dashed zone indicates the target frequency to be attenuated.

## 5.2 Design of a Dual-Loop Control System in the *z*-Axis Motion

### 5.2.1 Design of a Vibration Controller with Velocity Feedback in the *z*-Axis Motion

Since the key objective of this research is to reject or to reduce the effects of the vibration disturbance on the moving platen, a dual-loop control system is designed. A compensator in the inner-loop that attenuates the disturbance output $F_{dz}(s)$ is necessary.

Acceleration feedback and velocity feedback are well known as vibration control schemes [50-52]. These approaches are to increase the ability of the system in rejecting disturbances. An acceleration feedback increases the effective inertia of the system for disturbance rejection purposes. Acceleration feedback allows higher state feedback gains on the velocity and position loops to be employed without increasing the control loop bandwidths. This allows higher overall stiffness to be achieved. The effect is analogous to a mechanical inertia [52]. However, a reliable acceleration signal is necessary to apply an acceleration feedback. The acceleration signal can be obtained by twice differentiations from the position signal or accelerometer. Although a low-pass filter prevent the amplification of the noise, the signal distortion increases by twice filtering and differentiations. The accelerometer (PCB Piezotronics 356B18) has inherently a DC offset and drift when the signal conditioner's power is turned on. In this research, two accelerometers are required to measure the relative acceleration between the optical table and the platen. The DC offset and drift in acceleration signal make difficulty to apply

acceleration feedback in nanoscale or microscale applications. Therefore, the velocity feedback is appropriate in the research.

Now we compare two control schemes: a controller only with position feedback and a dual-loop control system with position plus velocity feedback. To analyze the ability of velocity feedback, an equivalent block diagram of control structure is shown in Fig. 5-7. A controller $D_P(s)$ acts as an outer-loop controller that controls the position of the platen. The lead-lag compensator suggested by Verma [38] is well designed as a position controller. Thus, a lead-lag compensator is used to the outer-loop controller $D_P(s)$. In addition, by comparing between vibration-reduction with and without the inner-loop controller, this compensator makes it easy to observe the effect of the inner-loop controller.

The other controller $D_V(s)$ acts as an inner-loop controller for velocity feedback. The inner-loop controller in Fig. 5-7 becomes a vibration controller. $D_V(s)$ could be a PID controller because a PID controller is one of the commonly used controllers in multi-loop control systems [53]:

$$D_V(s) = K_P + K_I \frac{1}{s} + K_D s = \frac{K_D s^2 + K_P s + K_I}{s}, \qquad (5.2.1)$$

The inner closed-loop transfer function is considered as a new modified plant transfer function in Fig. 5-7, and $G_{IN}(s)$ becomes

$$G_{IN}(s) = \frac{G_P(s)}{1 + sD_V(s)G_P(s)} \qquad (5.2.2)$$

From (5.1.8), (5.1.12), (5.2.1), and (5.2.2), the inner closed-loop TF is

$$G_{IN}(s)=\frac{kv\left(\left(m_1+m_2\right)s^2+c_{1z}s+k_{1z}\right)}{\left(m_1m_2+K_Dk_v\left(m_1+m_2\right)\right)s^4+\left(c_{1z}m_2+K_Dc_{1z}k_v+K_Pk_v\left(m_1+m_2\right)\right)s^3}$$
$$+\left(k_{1z}m_2+k_v\left(K_Pc_{1z}+K_Dk_{1z}\right)+\left(K_Ik_v-k_{2z}\right)\left(m_1+m_2\right)\right)s^2$$
$$+\left(\left(K_Ic_{1z}+K_Pk_{1z}\right)k_v-c_{1z}k_{2z}\right)s+\left(K_Ik_v-k_{2z}\right)k_{1z}$$

(5.2.3)

where all parameter values in (5.2.3) is presented in Table 5-1.

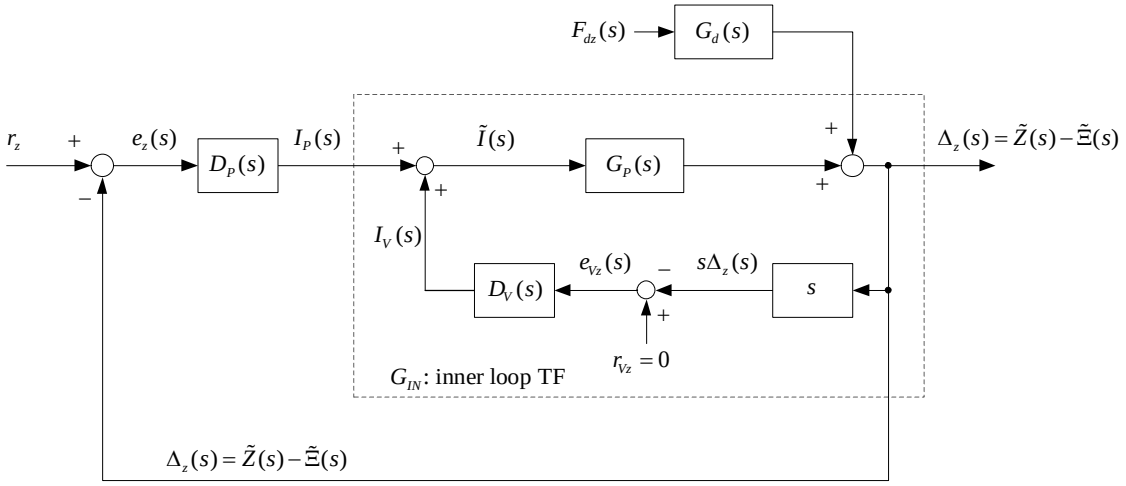


Fig. 5-7. Block diagram of the model of maglev system with positioning with a cascade velocity-regulation loop.

The inner closed-loop TF including a vibration controller should be stablized. Before we tune the control parameters, the stablizing region of the controller gains should be found.

$$0=d_4s^4+d_3s^3+d_2s^2+d_1s+d_0$$
$$=\left(m_1m_2+K_Dk_v\left(m_1+m_2\right)\right)s^4+\left(c_{1z}m_2+K_Dc_{1z}k_v+K_Pk_v\left(m_1+m_2\right)\right)s^3$$
$$+\left(k_{1z}m_2+k_v\left(K_Pc_{1z}+K_Dk_{1z}\right)+\left(K_Ik_v-k_{2z}\right)\left(m_1+m_2\right)\right)s^2$$
$$+\left(\left(K_Ic_{1z}+K_Pk_{1z}\right)k_v-c_{1z}k_{2z}\right)s+\left(K_Ik_v-k_{2z}\right)k_{1z}$$

(5.2.4)

where

$$d_4 = m_1 m_2 + K_D k_v \left( m_1 + m_2 \right) \tag{5.2.5}$$

$$d_3 = c_{1z} m_2 + K_D c_{1z} k_v + K_P k_v \left( m_1 + m_2 \right) \tag{5.2.6}$$

$$d_2 = k_{1z} m_2 + k_v \left( K_P c_{1z} + K_D k_{1z} \right) + \left( K_I k_v - k_{2z} \right) \left( m_1 + m_2 \right) \tag{5.2.7}$$

$$d_1 = \left( K_I c_{1z} + K_P k_{1z} \right) k_v - c_{1z} k_{2z} \tag{5.2.8}$$

$$d_0 = \left( K_I k_v - k_{2z} \right) k_{1z} \tag{5.2.9}$$

To determine its stability, the Routh-Hurwitz criterion is used.

| | | | |
|---|---|---|---|
| $s^4$ : | $d_4$ | $d_2$ | $d_0$ |
| $s^3$ : | $d_3$ | $d_1$ | 0 |
| $s^2$ : | $\frac{d_3 d_2 - d_4 d_1}{d_3} = A$ | $\frac{d_3 d_0 - d_4 \times 0}{d_3} = d_0$ | 0 |
| $s^1$ : | $\frac{A d_1 - d_3 d_0}{A} = B$ | 0 | 0 |
| $s^0$ : | $\frac{B d_0 - A \times 0}{B} = d_0$ | 0 | 0 |

From the stability analysis, as long as $K_P$, $K_D$, and $K_I$ have positive values, the inner-loop is stable because the other constants in (5.2.4) are all positive values. However, the outer closed-loop has different stabilizing region of the control gains.

The transfer function from the reference input to the position output is

$$\begin{aligned} \frac{\Delta_z(s)}{r_z(s)} &= \frac{D_P(s) G_{IN}(s)}{1 + D_P(s) G_{IN}(s)} \\ &= \frac{a_4 s^4 + a_3 s^3 + a_2 s^2 + a_1 s + a_0}{d_6 s^6 + d_5 s^5 + d_4 s^4 + d_3 s^3 + d_2 s^2 + d_1 s + d_0} \end{aligned} \tag{5.2.10}$$

where

$$a_4 = ak_v\left(m_1 + m_2\right) \tag{5.2.11}$$

$$a_3 = ak_v\left(c_{1z} + \left(m_1 + m_2\right)\left(z_1 + z_2\right)\right) \tag{5.2.12}$$

$$a_2 = ak_v\left(k_{1z} + c_{1z}\left(z_1 + z_2\right) + \left(m_1 + m_2\right)z_1z_2\right) \tag{5.2.13}$$

$$a_1 = ak_v\left(k_{1z}\left(z_1 + z_2\right) + c_{1z}z_1z_2\right) \tag{5.2.14}$$

$$a_0 = ak_vk_{1z}z_1z_2, \tag{5.2.15}$$

and

$$d_6 = k_v\left(m_1 + m_2\right)K_D + m_1m_2 \tag{5.2.16}$$

$$d_5 = k_v\left(m_1 + m_2\right)K_P + k_v\left(c_{1z} + p_1(m_1 + m_2)\right)K_D + c_{1z}m_2 + m_1m_2p_1 \tag{5.2.17}$$

$$\begin{aligned} d_4 = {} & k_v\left(c_{1z} + \left(m_1 + m_2\right)p_1\right)K_P + k_v\left(m_1 + m_2\right)K_I + k_v\left(k_{1z} + c_{1z}p_1\right)K_D \\ & + \left(ak_v - k_{2z}\right)\left(m_1 + m_2\right) + k_{1z}m_2 + c_{1z}m_2p_1 \end{aligned} \tag{5.2.18}$$

$$\begin{aligned} d_3 = {} & k_v\left(k_{1z} + c_{1z}p_1\right)K_P + k_v\left(c_{1z} + \left(m_1 + m_2\right)p_1\right)K_I + k_vk_{1z}p_1K_D \\ & + ak_v\left(c_{1z} + \left(m_1 + m_2\right)\left(z_1 + z_2\right)\right) + k_{1z}m_2p_1 - k_{2z}\left(c_{1z} + \left(m_1 + m_2\right)p_1\right) \end{aligned} \tag{5.2.19}$$

$$\begin{aligned} d_2 = {} & k_vk_{1z}p_1K_P + k_v\left(k_{1z} + c_{1z}p_1\right)K_I - \left(c_{1z}p_1 + k_{1z}\right)k_{2z} \\ & + ak_v\left(k_{1z} + c_{1z}\left(z_1 + z_2\right) + \left(m_1 + m_2\right)z_1z_2\right) \end{aligned} \tag{5.2.20}$$

$$d_1 = k_vk_{1z}p_1K_I + ak_v\left(k_{1z}(z_1 + z_2) + c_{1z}z_1z_2\right) - k_{1z}k_{2z}p_1 \tag{5.2.21}$$

$$d_0 = ak_vk_{1z}z_1z_2 \tag{5.2.22}$$

For stability analysis of the transfer function, let the denominator of $\dfrac{\Delta_z(s)}{r_z(s)}$ be $\delta(s)$,

$$\delta(s) = d_6s^6 + d_5s^5 + d_4s^4 + d_3s^3 + d_2s^2 + d_1s + d_0. \tag{5.2.23}$$

If all roots of $\delta(s)$ are in the left-half *s*-plane, the closed-loop transfer function $\frac{\Delta_z(s)}{r_z(s)}$ is stable. To determine its stability, the Routh-Hurwitz criterion is applied. The same lead-lag compensator $D_P(s)$ in (5.1.13) is used in (5.2.10).

| | | | | |
|---|---|---|---|---|
| $s^6$: | $d_6$ | $d_4$ | $d_2$ | $d_0$ |
| $s^5$: | $d_5$ | $d_3$ | $d_1$ | 0 |
| $s^4$: | $\frac{d_5 d_4 - d_6 d_3}{d_5} = A$ | $\frac{d_5 d_2 - d_6 d_1}{d_5} = B$ | $\frac{d_5 d_0 - d_6 \times 0}{d_5} = d_0$ | 0 |
| $s^3$: | $\frac{A d_3 - d_5 B}{A} = C$ | $\frac{A d_1 - d_5 d_0}{A} = D$ | 0 | 0 |
| $s^2$: | $\frac{CB - AD}{C} = E$ | $\frac{C d_0 - A \times 0}{C} = d_0$ | 0 | 0 |
| $s^1$: | $\frac{ED - C d_0}{E} = F$ | 0 | 0 | 0 |
| $s^0$: | $\frac{F d_0}{F} = d_0$ | 0 | 0 | 0 |

According to the Routh-Hurwitz criterion, all roots of the polynomial are in the left-half *s*-plane if all the elements in the first column of the Routh array are of the same sign. Since $k_v$ and $K_D$ are all positive from (5.2.16), $d_6$ is positive with the positive value of $K_D$. Therefore, $d_5$, $A$, $C$, $E$, $F$, and $d_6$ should be all positive for closed-loop stability.

Fig. 5-8 illustrates the stable region that is drawn by calculation iteration through $0 \le K_D \le 600$, $0 \le K_P \le 650$, and $0 \le K_I \le 100$. the As shown in Fig. 5-8, the stable region decreases with increasing $K_D$ and the derivative gain is not helpful to stabilize the system since the derivative control will reinforce the rapid change of the velocity. Thus, PI controller instead to the PID controller is appropriate as a velocity feedback controller. If the value of $K_D$ is zero, the system is stable if $K_P \ge 0$ and $K_I \ge 0$.

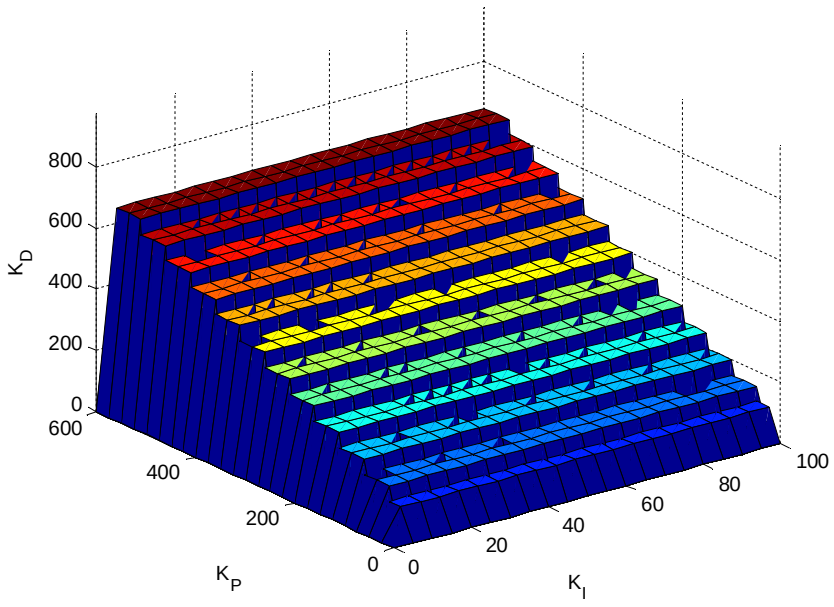


Fig. 5-8. The stabilizing region of $(K_P, K_I, K_D)$ values for a PID controller.

The inner-loop controller should attenuate the effect of vibration disturbance. To observe how the vibration disturbance influences the output, the transfer function $F_{dz}(s)$ from the disturbance to the output $\Delta_z(s)$ need to be analyzed. It is presented as

$$\frac{\Delta_z(s)}{F_{dz}(s)} = \frac{G_d(s)}{1+G_P(s)\left(D_p(s)+sD_v(s)\right)}$$

$$= \frac{-m_2\left(s^4+p_1s^3\right)}{\begin{array}{l} m_1m_2s^6+\left(c_{1z}m_2+K_Pk_v\left(m_1+m_2\right)+m_1m_2p_1\right)s^5 \\ +\left(\begin{array}{l} k_v\left(c_{1z}+\left(m_1+m_2\right)p_1\right)K_P+k_v\left(m_1+m_2\right)K_I \\ +\left(ak_v-k_{2z}\right)\left(m_1+m_2\right)+k_{1z}m_2+c_{1z}m_2p_1 \end{array}\right)s^4 \\ +\left(\begin{array}{l} k_v\left(k_{1z}+c_{1z}p_1\right)K_P+k_v\left(c_{1z}+\left(m_1+m_2\right)p_1\right)K_I \\ +ak_v\left(c_{1z}+\left(m_1+m_2\right)\left(z_1+z_2\right)\right)+k_{1z}m_2p_1-k_{2z}\left(c_{1z}+\left(m_1+m_2\right)p_1\right) \end{array}\right)s^3 \\ +\left(\begin{array}{l} k_vk_{1z}p_1K_P+k_v\left(k_{1z}+c_{1z}p_1\right)K_I-\left(c_{1z}p_1+k_{1z}\right)k_{2z} \\ +ak_v\left(k_{1z}+c_{1z}\left(z_1+z_2\right)+\left(m_1+m_2\right)z_1z_2\right) \end{array}\right)s^2 \\ +\left(k_v\left(K_Ik_{1z}p_1+ak_{1z}\left(z_1+z_2\right)+ac_{1z}z_1z_2\right)-k_{1z}k_{2z}p_1\right)s+ak_{1z}k_vz_1z_2 \end{array}}$$

$$= \frac{-m_2\left(s^4+p_1s^3\right)}{d_6s^6+d_5s^5+d_4s^4+d_3s^3+d_2s^2+d_1s+d_0}$$

(5.2.24)

where $d_6$, $d_5$, $d_4$, $d_3$, $d_2$, $d_1$, and $d_0$ are same as (5.2.16)–(5.2.22) if $K_D = 0$, and all parameter values in (5.2.24) is presented in Table 5-1.

If the $K_P$ = 100 and $K_I$ = 0 with the lead-lag compenstorin (5.1.15),

$$\frac{\Delta_z(s)}{F_{dz}(s)} = \frac{-\left(0.002294s^4+4.823s^3\right)}{s^6+2509s^5+1.809\times10^6s^4+2.876\times10^8s^3+1.206\times10^{11}s^2+4.158\times10^{12}s+2.238\times10^{13}}$$

(5.2.25)

The frequency response of the $\frac{\Delta_z(s)}{F_{dz}(s)}$ is shown in Fig. 5-9. The dashed line is without the velocity-regulation loop, and the solid line is with the velocity-regulation loop. The

magnitude of the transfer function $\frac{\Delta_z(s)}{F_{dz}(s)}$ with vibration contoller is reduced in the region from 20 rad/s to 2000 rad/s. It means that the velocity feedback control is effective to 3.18 Hz to 318 Hz of vibration disturbance.

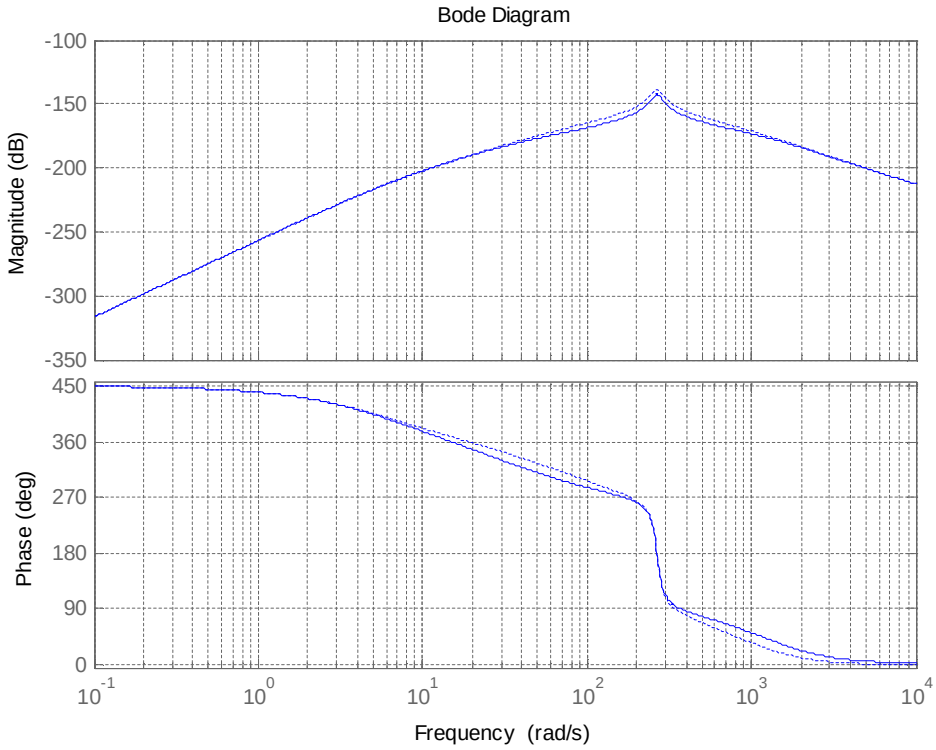


Fig. 5-9. Frequency responses of the transfer function $\frac{\Delta_z(s)}{F_{dz}(s)}$ from vibration disturbance to position in the *z*-axis. The solid line indicates the response with a PID vibration control ( $K_P = 100$, $K_I = 0$, $K_D = 0$ ), and the dotted line indicates that without the vibration control scheme.

Fig. 5-10 shows the zoomed frequency resposes from 10 Hz to 100 Hz of the transfer function $\frac{\Delta_z(s)}{F_{dz}(s)}$ in Fig. 5-9. The magnitude with vibration controller is reduced by about 2.58 dB to 4.27 dB between 10 Hz and 100 Hz as shown in Fig. 5-10. The reduction of 20 to 45 percent of the vibration disturbance was achived experimentally.

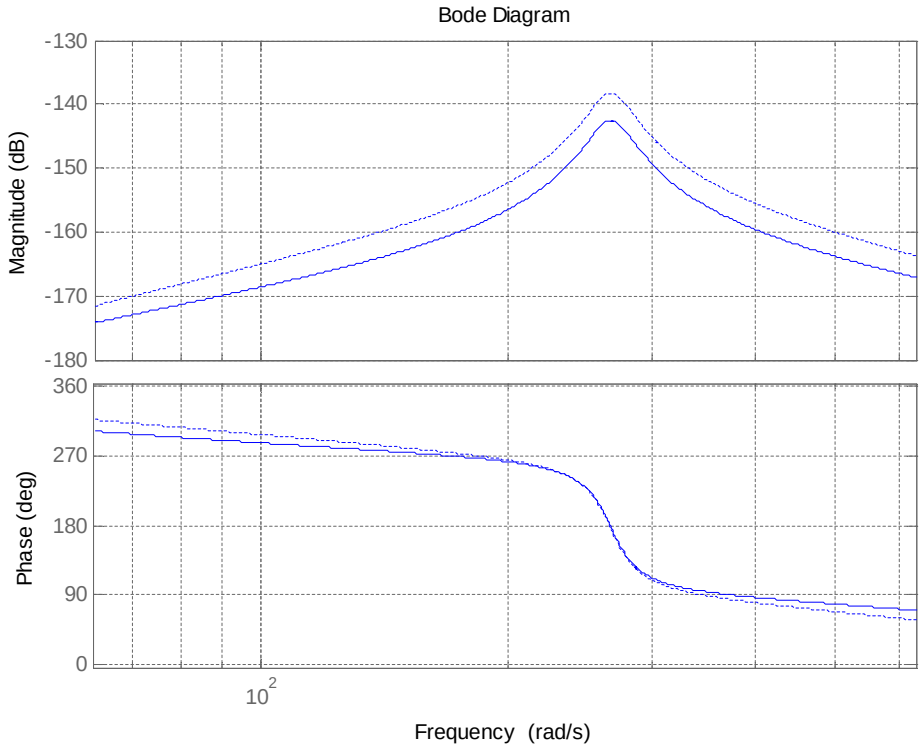


Fig. 5-10. Zoomed frequency responses of the transfer function $\frac{\Delta_z(s)}{F_{dz}(s)}$ from vibration disturbance to position in the *z*-axis from 10 Hz to 100 Hz. The solid line indicates the response with a PID vibration control ( $K_P = 100$, $K_I = 0$, $K_D = 0$ ), and the dotted line indicates that without the vibration control scheme.

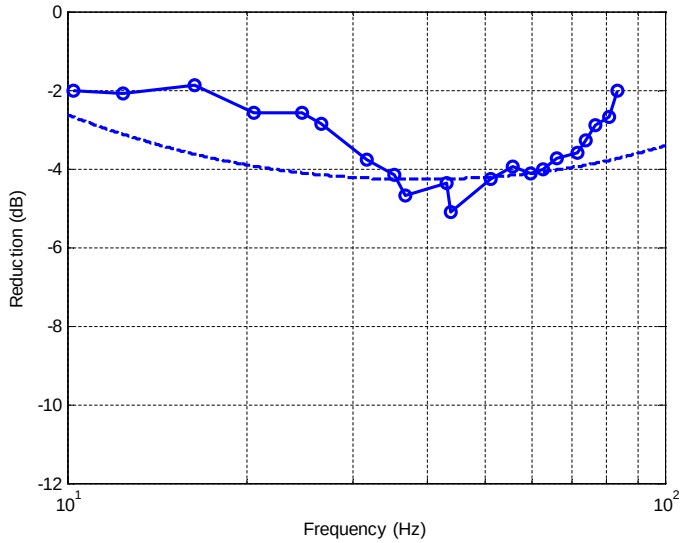


(a)

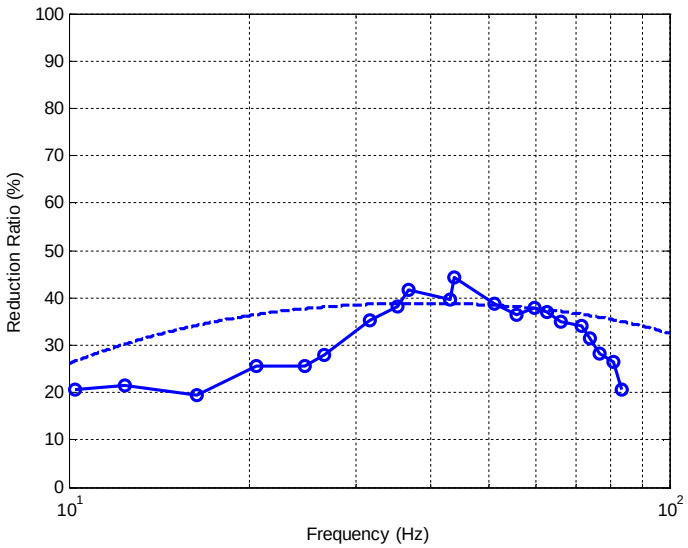


(b)

Fig. 5-11. (a) Magnitude reduction, and (b) reduction percentage of the magnitude of the transfer function $\frac{\Delta_z(s)}{F_{dz}(s)}$ from 10 Hz to 100 Hz with a PID vibration control ($K_P = 100$, $K_I = 0$, $K_D = 0$). The dashed line indicates the simulation and the circled line indicates the experiment.

The discrepancy between the simulation and experiment in Fig. 5-11 is caused by the unmodeled dynamics. Both the optical table and the platen have rolling and pitching motions about the *x*-axis and the *y*-axis. These rotaional vibrating motions are not considered in the dual-loop control system because the enhaced maglev stage model with the optical table in vertical motion is developed based on a single axis motion.

As the proportional gain $K_P$ of the inner-loop increases, the reduction ratio increases. Theoretically, the reduction ratio will increases by as much as increasing $K_P$. However, if $K_P$ is greater than 120, the crossover frequency of the loop TF is less than 10 Hz and unwanted oscillation increases in the step response in Figs. 5-12–5-13. Therefore, the proper value of $K_P$ is 100 for both the stability and the reduction performance.

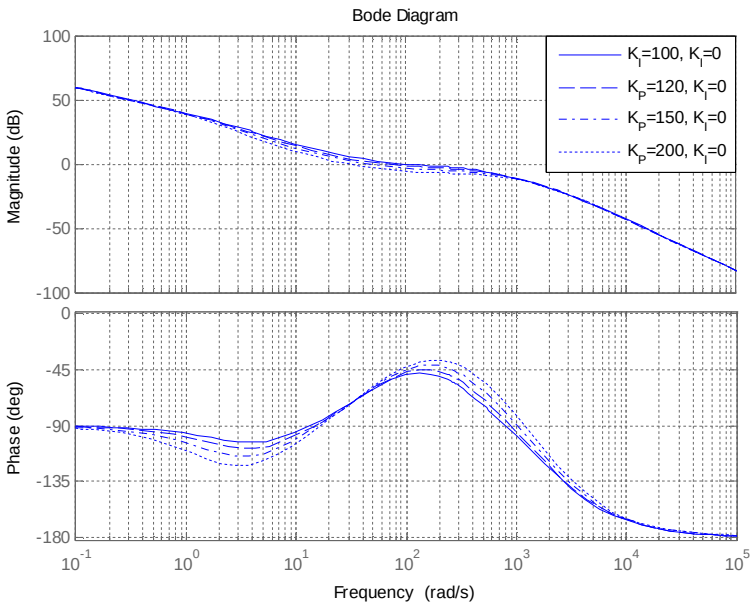


Fig. 5-12. Frequency responses of the open-loop transfer function $D_P(s)G_{IN}(s)$ with various $K_P$ values in vertical motion.

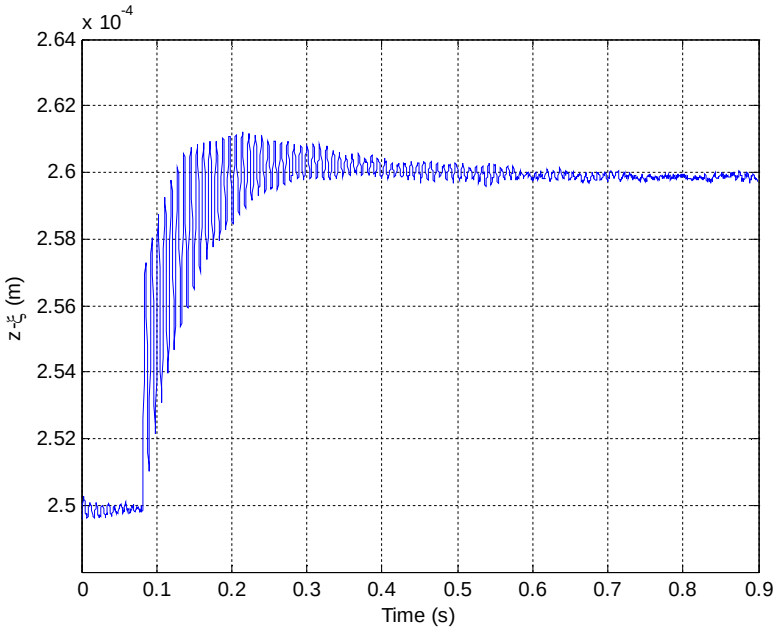


Fig. 5-13. Experimented step response of 10 μm with $K_P$ = 120 in vertical motion.

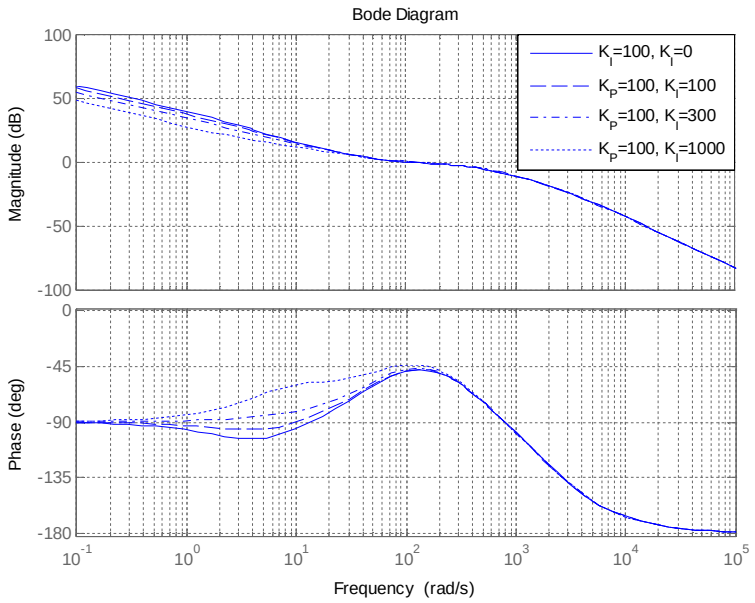


Fig. 5-14. Frequency responses of the open-loop transfer function $D_P(s)G_{IN}(s)$ with various $K_I$ values in vertical motion.

For the integral gain $K_I$, the magnitude and the phase change of the TF $\frac{\Delta_z(s)}{F_{dz}(s)}$ by increasing integral gain $K_I$ are ignorable unless $K_I$ is significantly increased. However, the magnitude slope of the open-loop TF at low frequency decreases by increasing $K_I$ in Fig 5-14. It means the rise time and the settling time increases. Hence, there is no advantage by the integral term that makes the system response slower. Therefore, the integral term is unnecessary. Finally, the velocity regulating compensator becomes a proportional controller that has the gain $K_P$ = 100.

### 5.2.2 Design of an Outer-Loop Controller in the *z*-Axis Motion

By adding the inner-loop controller to regulate the velocity, a new Bode plot of the loop transfer function is shown in Fig. 5-15. By comparing between Fig. 5-3 and Fig. 5-15, the loop transfer shape change is easily recognizable. The magnitude slope at low frequency is not changed, but the crossover frequency decreases to compare to the loop shape without the inner loop controller in Fig. 5-3. The comparison of step responses between two control systems is shown in Fig. 5-16. The crossover frequency is reduced from 335 rad/s to 210 rad/s. In addition, the rise time and the settling time decreases, and unwanted oscillation is observed in the real system in as shown Fig. 5-16. If the increased rise and settling times are not significantly important, the oscillation should be reduced by decreasing the value *a* of the lead-lag compensator designed in (5.1.13).

The value *a* of the lead-lag compensator is reduced as one-sixth of the original value, $a = 2.32003 \times 10^5$. The crossover frequency is decreased to 97.6 rad/s in Fig. 5-17.

The oscillation decreases enough not to affect overall performance in a step response in Fig. 5-18.

In the summary of the design of the dual-loop control system, the inner-loop compensator is

$$D_V(s) = K_P, \tag{5.2.26}$$

and the outer-loop compensator is

$$D_P(s) = a\frac{(s+z_1)(s+z_2)}{s(s+p_1)} \tag{5.2.27}$$

where, the values of $K_P$, $a$, $p_1$, $z_1$, and $z_2$ are 100, $3.8667\times10^4$, 2103, 57.47 and 6.271.

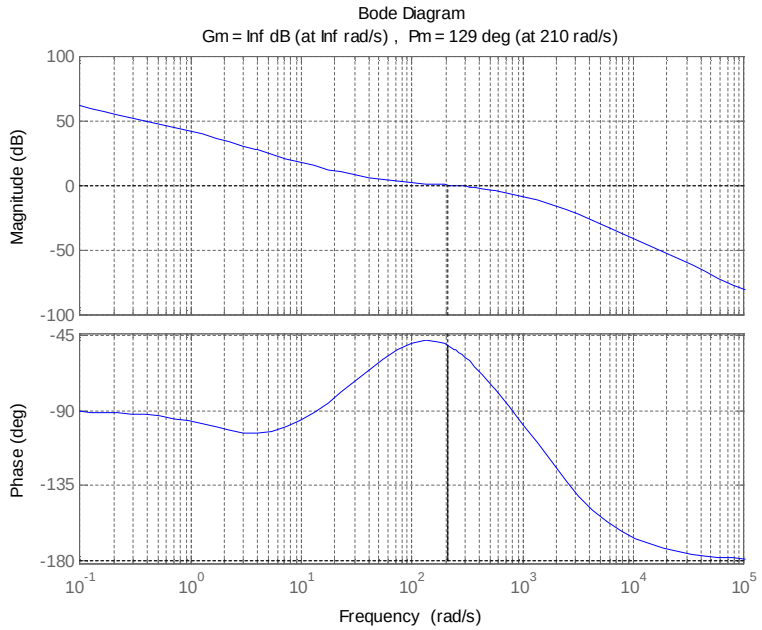


Fig. 5-15. Bode plot of the loop transfer function for the *z*-axis motion with vibration controller.

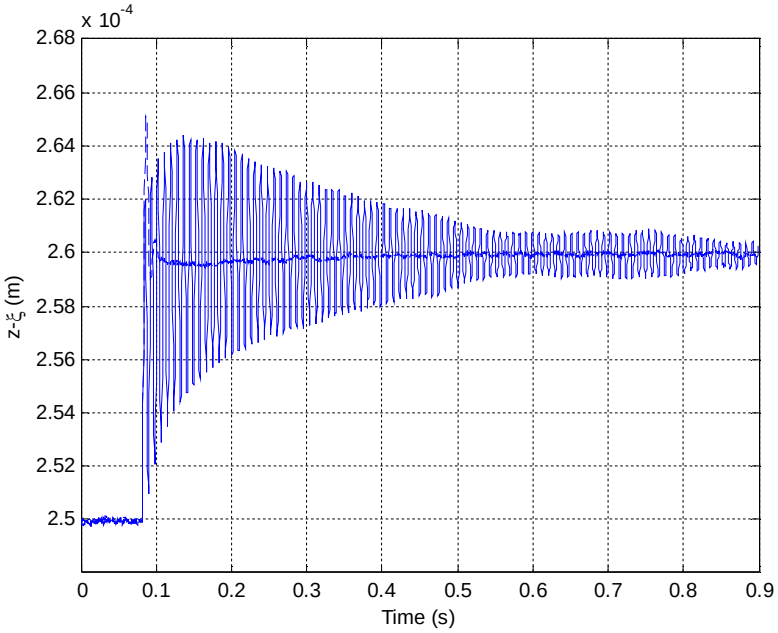


Fig. 5-16. Comparison of step responses (a) with the outer- and inner-loop compensators (highly-oscillating solid line) and (b) with only the outer-loop compensator (dashed line) in experiments.

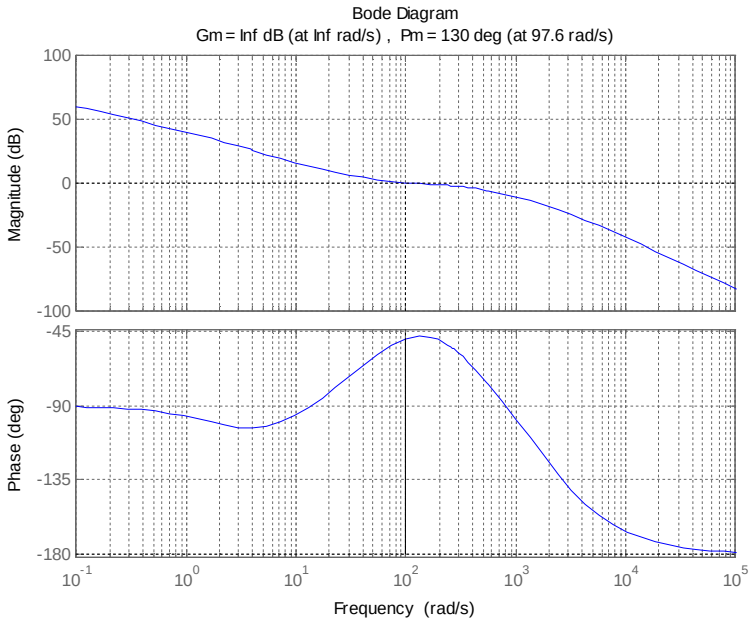


Fig. 5-17. Closed-loop Bode plot with one-sixth times decreased value *a* of the lead-lag compensator.

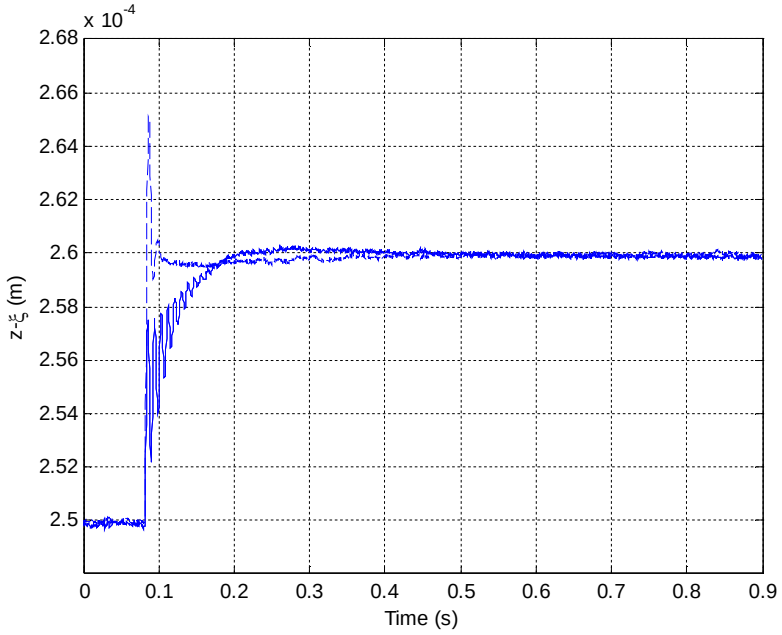


Fig. 5-18. Comparison of step responses (a) with the inner-loop controller and the outer lead-lag compensator with one-sixth times decreased value *a* (solid line) and (b) only with the modified outer lead-lag compensator (dashed line) in experiments.

## 5.3 Responses of Position with the Dual-Loop Controller in the *z*-Axis Motion

In the experiments, various frequencies of vibration disturbance are applied and used to obtain the vibration reduction ratio with a dual-loop controller in Fig. 5-11. The responses of position with the dual-loop controller in the *z*-axis are shown in Figs. 5-19–5-22 when vibration disturbances of about 10, 30, 50, 70, and 80 Hz are applied. Following five figures present the effectiveness of the dual-loop control system. The reduction ratio is at least about 20 percent and the maximun reduction ratio is 44 percent in the *z*-axis.

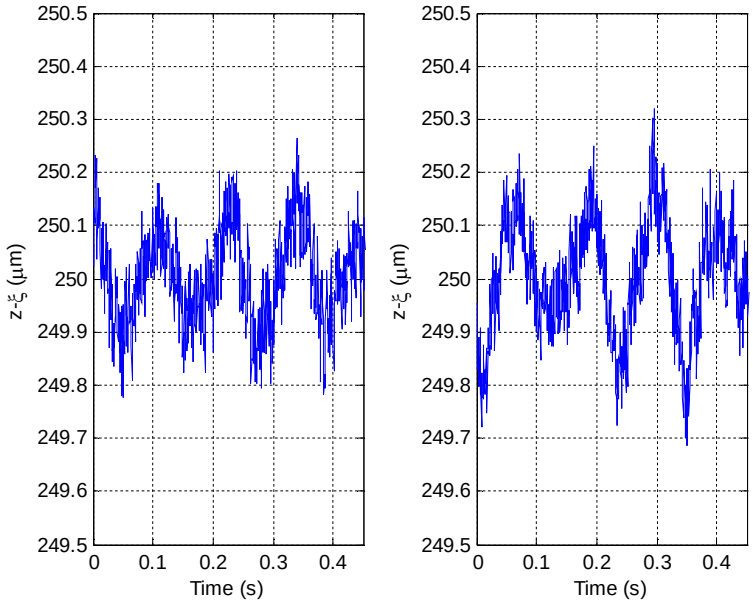


Fig. 5-19. Position regulation at 250 μm with (a) a dual-loop and (b) a lead-lag controllers when vibration disturbance of 10.24 Hz is applied.

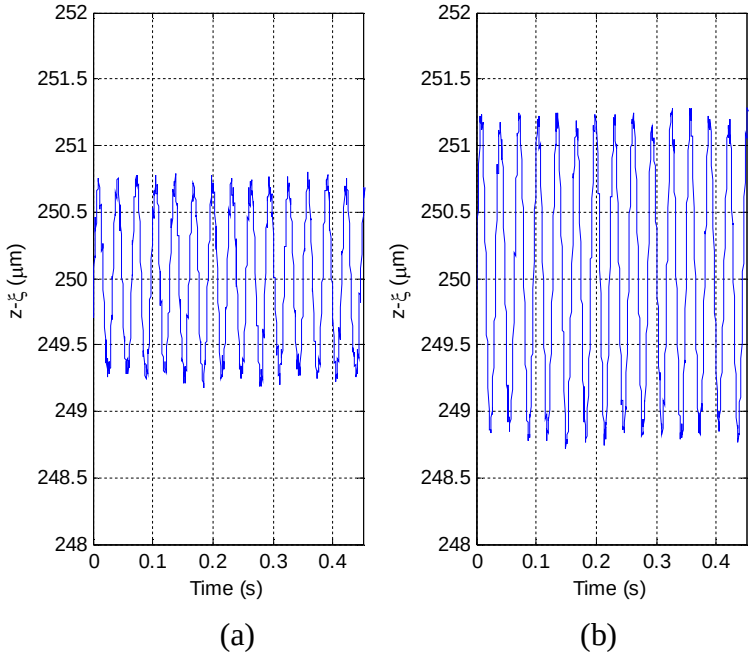


Fig. 5-20. Position regulation at 250 μm with (a) a dual-loop and (b) a lead-lag controllers when vibration disturbance of 31.64 Hz is applied.

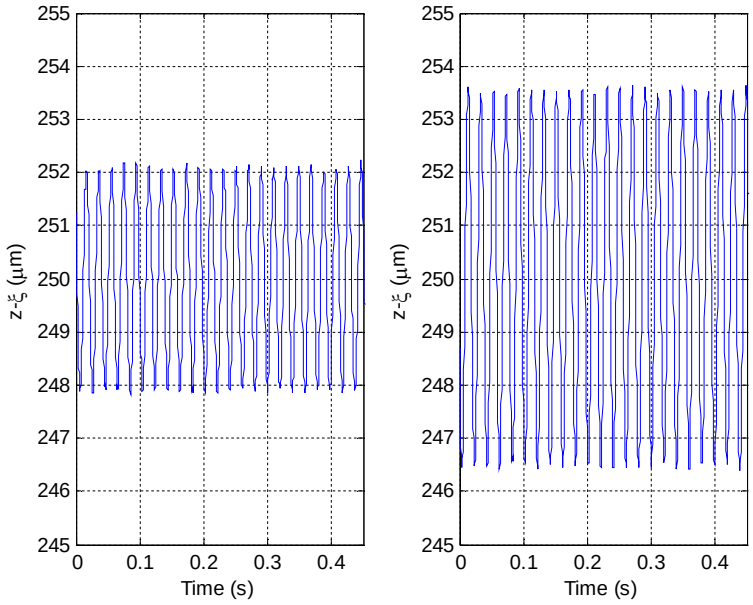


Fig. 5-21. Position regulation at 250 μm with (a) a dual-loop and (b) a lead-lag controllers when vibration disturbance of 51.02 Hz is applied.

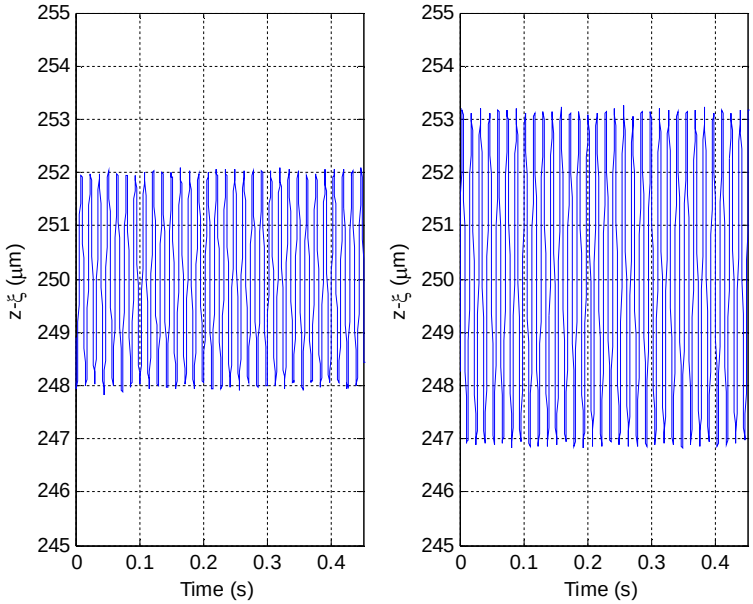


Fig. 5-22. Position regulation at 250 μm with (a) a dual-loop and (b) a lead-lag controllers when vibration disturbance of 71.43 Hz is applied.

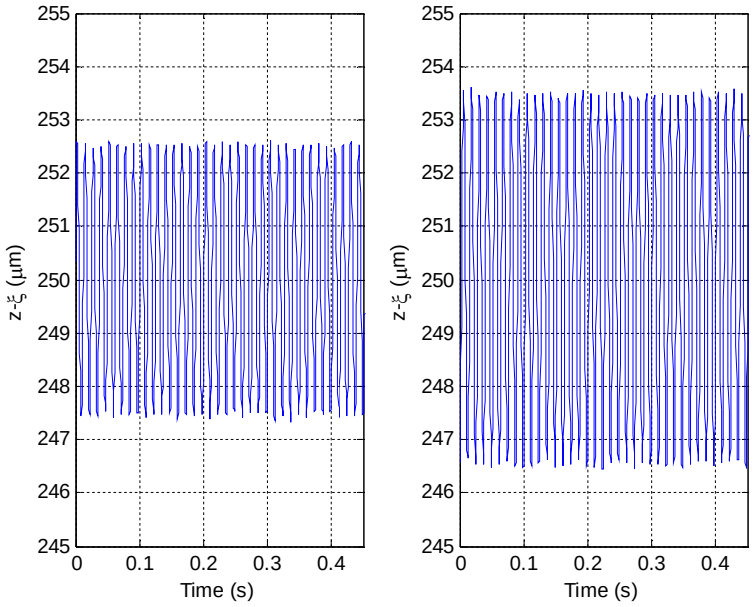


Fig. 5-23. Position regulation at 250 μm with (a) a dual-loop and (b) a lead-lag controllers when vibration disturbance of 80.65 Hz is applied.

# CHAPTER VI

# MODELING OF THE MAGLEV SYSTEM WITH THE OPTICAL TABLE IN HORIZONTAL MOTION

## 6.1 Equations of Motion of the Maglev System in Horizontal Axes

As shown in Fig. 6-1, we treat the maglev system as a two-mass system that includes two springs and two dampers. The vibration disturbance acts on the optical table and the magnetic force between the magnets of the moving platen and the coils is applied by controlling the current flow in the coil. Governing equations of motion of the maglev system in horizontal motion become

$$m_2\ddot{x} = F_x\left(x,\eta,i\right) \tag{6.1.1}$$

$$m_2\ddot{y} = F_y\left(y,\rho,i\right) \tag{6.1.2}$$

$$m_1\ddot{\eta} = -c_{1x}\dot{\eta} - k_{1x}\eta - F_x\left(x,\eta,i\right) + F_{dx} \tag{6.1.3}$$

$$m_1\ddot{\rho} = -c_{1y}\dot{\rho} - k_{1y}\rho - F_y\left(y,\rho,i\right) + F_{dy} \tag{6.1.4}$$

where magnetic forces are $F_x(x,\eta,i) = \left(\beta_2\left(x-\eta\right)^2 + \beta_1\left(x-\eta\right) + \beta_0\right)i$ in the *x*-axis and

$F_y(y,\rho,i) = \left(\beta_2\left(y-\rho\right)^2 + \beta_1\left(y-\rho\right) + \beta_0\right)i$ in the *y*-axis.

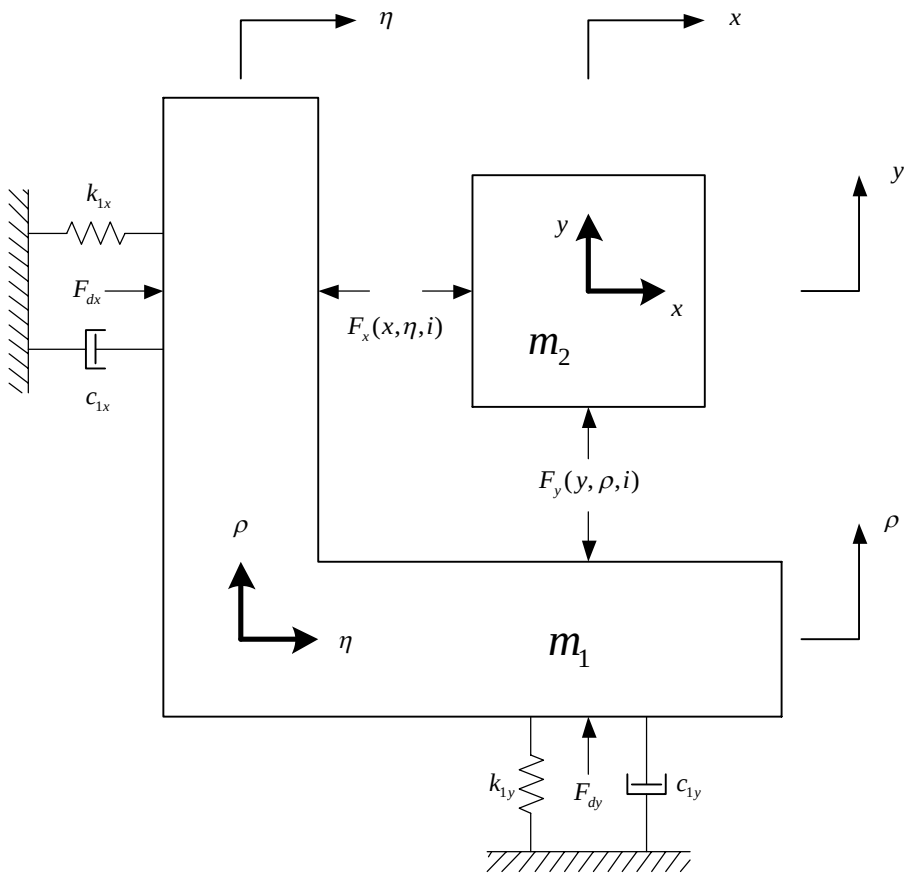


Fig. 6-1. Simplified model of the maglev system in horizontal motion.

The stiffness ($k_{1x}$, $k_{1y}$) and the damping coefficients ($c_{1x}$, $c_{1y}$) of the optical table in the *x*- and *y*-axes are determined by the same method introduced in Chapter IV. The impulse responses of the optical table in the *x*- and *y*-axis are shown in Figs. 6-2–6-3. From equations (4.1.1)–(4.1.2), the stiffness and the damping coefficient in the *x*-axis are calculated as $k_{1x} = 4.65305 \times 10^6$ N/m and $c_{1x} = 4.84471 \times 10^3$ N-s/m, and the stiffness and the damping coefficient in the *y*-axis are $k_{1y} = 1.89438 \times 10^6$ N/m and $c_{1y} = 7.7105613 \times 10^3$ N-s/m.

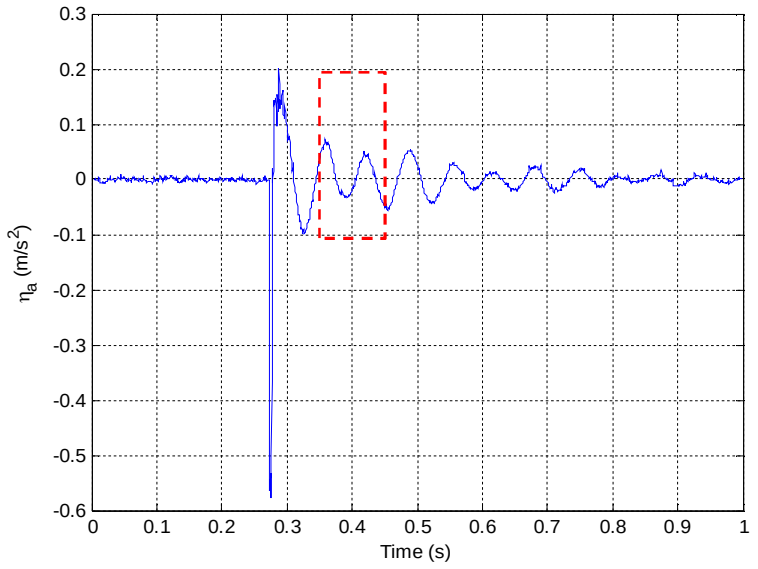


(a)

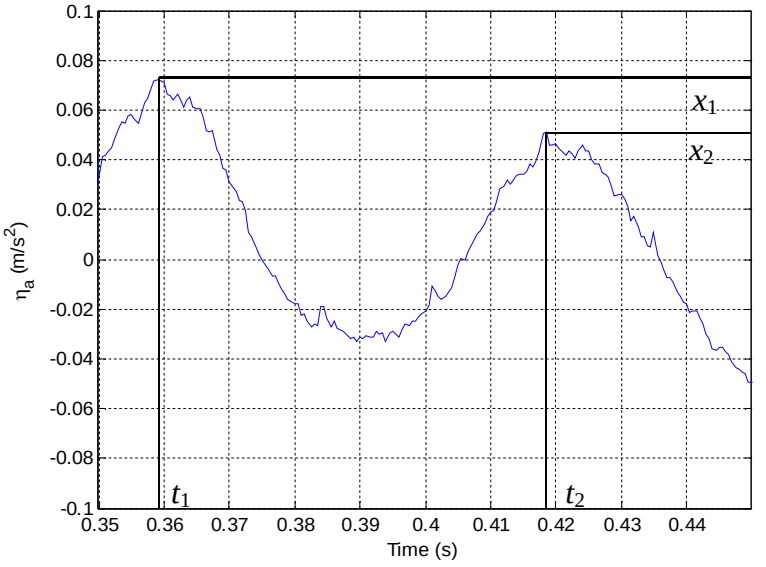


(b)

Fig. 6-2. Impulse response of the optical table in the *x*-axis: (a) original (b) zoomed in dashed zone.

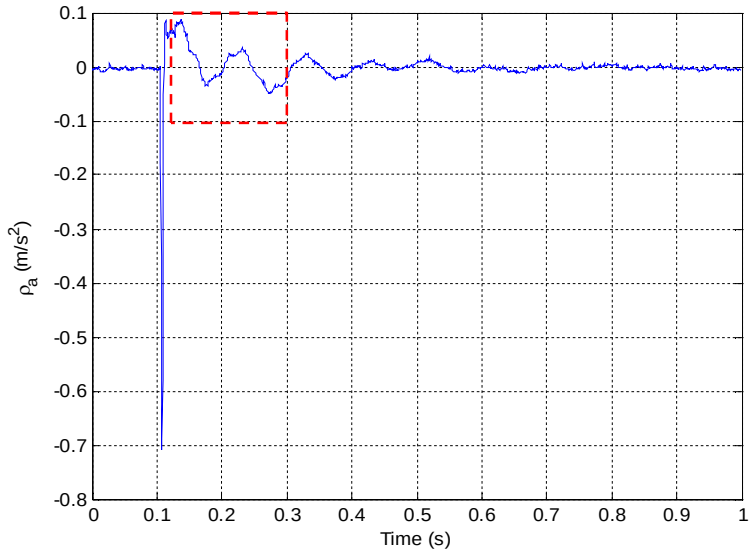


(a)

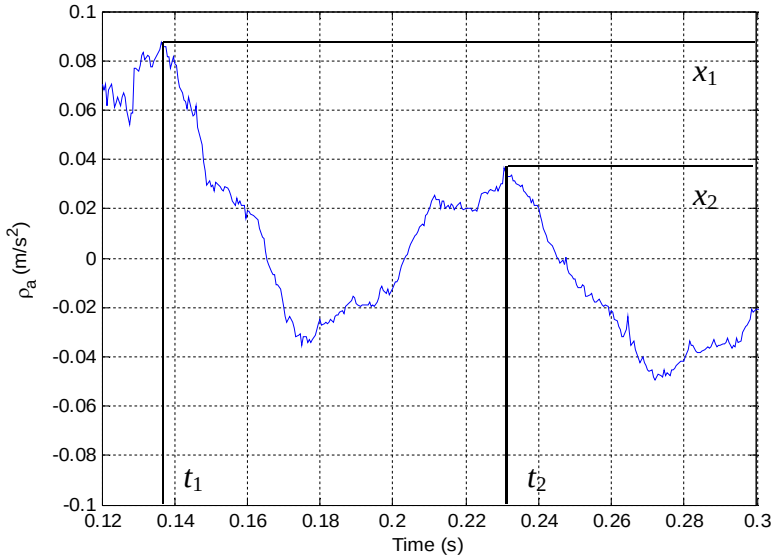


(b)

Fig. 6-3. Impulse response of the optical table in the *y*-axis: (a) original (b) zoomed in dashed zone.

## 6.2 Linearization of Nonlinear Equations of Motion and Magnetic Force in the *x*-Axis

As in vertical motion, the only nonlinear term in the EOMs is position dependences in the magnetic force in Fig. 6-4. To linearize the EOMs in the *x*-axis, let set the perturbation equations $x = x_0 + \tilde{x}, \eta = \eta_0 + \tilde{\eta}$, and $i = i_0 + \tilde{i}$. Constants $x_0, \eta_0,$ and $i_0$ means the values at an operation point. The variables with circumflexes are perturbation. Using Taylor series expansion, (6.1.1) becomes

$$m_2\left(\cancel{\ddot{x}_0} + \ddot{\tilde{x}}\right) = \cancel{F_x(x_0, \eta_0, i_0)} + \left.\frac{\partial F_x(x,\eta,i)}{\partial x}\right|_{x_0,\eta_0,i_0} \tilde{x} + \left.\frac{\partial F_x(x,\eta,i)}{\partial \eta}\right|_{x_0,\eta_0,i_0} \tilde{\eta} + \left.\frac{\partial F_x(x,\eta,i)}{\partial i}\right|_{x_0,\eta_0,i_0} \tilde{i} \tag{6.2.1}$$

The linearized EOM of the platen in the *x*-axis is

$$m_2\ddot{\tilde{x}} = \left(\left.\frac{\partial F_x}{\partial x}\right|_{x_0,\eta_0,i_0}\right)\tilde{x} + \left(\left.\frac{\partial F_x}{\partial \eta}\right|_{x_0,\eta_0,i_0}\right)\tilde{\eta} + \left(\left.\frac{\partial F_x}{\partial i}\right|_{x_0,\eta_0,i_0}\right)\tilde{i} \tag{6.2.2}$$

where

$$\left.\frac{\partial F_x(x,\eta,i)}{\partial x}\right|_{x_0,\eta_0,i_0} = \left(2\beta_2\left(x_0 - \eta_0\right) + \beta_1\right)i_0 \tag{6.2.3}$$

$$\left.\frac{\partial F_x(x,\eta,i)}{\partial \eta}\right|_{x_0,\eta_0,i_0} = -\left(2\beta_2\left(x_0 - \eta_0\right) + \beta_1\right)i_0 \tag{6.2.4}$$

$$\left.\frac{\partial F_x(x,\eta,i)}{\partial i}\right|_{x_0,\eta_0,i_0} = \left(\beta_2\left(x_0 - \eta_0\right)^2 + \beta_1\left(x_0 - \eta_0\right) + \beta_0\right). \tag{6.2.5}$$

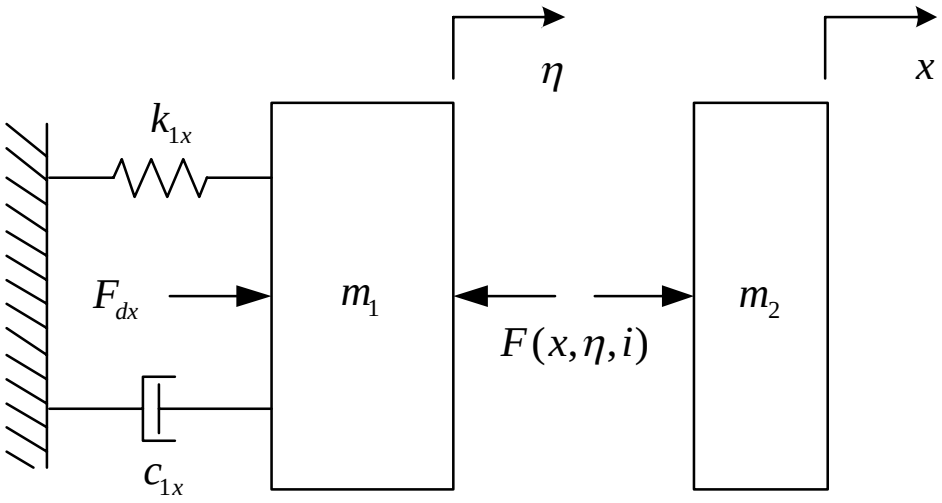


Fig. 6-4. Model of the maglev system in the *x*-axis.

To determine the coefficients in (6.2.2), the value of $i_0$ should be found. At the equilibrium point, the magnetic force is

$$F_{M_x}(x_0,\eta_{0,}i_0)=\left(\beta_2\left(x_0-\eta_0\right)^2+\beta_1\left(x_0-\eta_0\right)+\beta_0\right)i_0=0.$$

Thus, the current, $i_0$, at the operation point $\left(x_0-\eta_0\right)=0$ is

$$i_0=0 \tag{6.2.6}$$

where $\beta_2=1.3031\times10^4$, $\beta_1=-2.7161\times10^2$, and $\beta_0=2.2050$ [39].

Finally, the linearized equation of motion of the platen in the *x*-axis is

$$m_2\ddot{\tilde{x}}=k_{hx}\tilde{i} \tag{6.2.7}$$

where $k_{hx}=\beta_2\left(x_0-\eta_0\right)^2+\beta_1\left(x_0-\eta_0\right)+\beta_0$.

Similary, the linearized EOM of the optical table with vibration disturbance in

the *x*-axis becomes

$$m_1\ddot{\tilde{\eta}} + c_{1x}\dot{\tilde{\eta}} + k_{1x}\tilde{\eta} = -k_{hx}\tilde{i} + F_{dx}\,. \tag{6.2.8}$$

To verify the model of the maglev system with the magnetic stiffness in the *x*-axis, (6.2.7)–(6.2.8), the comparison between the experimental and simulation results with vibration disturbance is presented in Fig. 6-5 before applying the vibration control schemes.

The relative differences of the positions and velocities between the optical table and the platen are shown in Fig. 6-5 (a)–(d). The simulated position is very close to the experimented result. The magnitude of the relative velocity is little larger and noisy in the experimented data. The velocity data were acquired by the numerical differentiation from the position data in the laser-axis board. The high-frequency components of the position data are amplified by the differentiation. Except for the high-frequency components, the simulated velocity results are very similar to the experiments. Therefore, the linearized model of the platen with the optical table in the *x*-axis is well approximated.

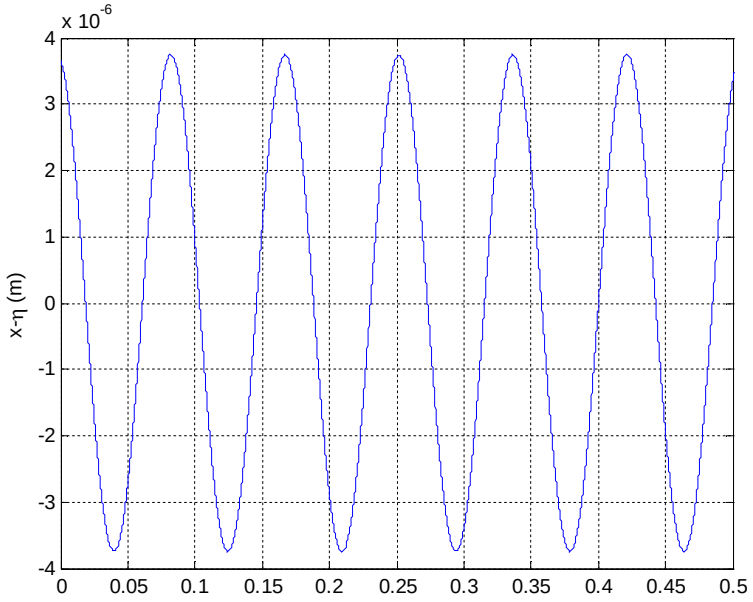


(a)

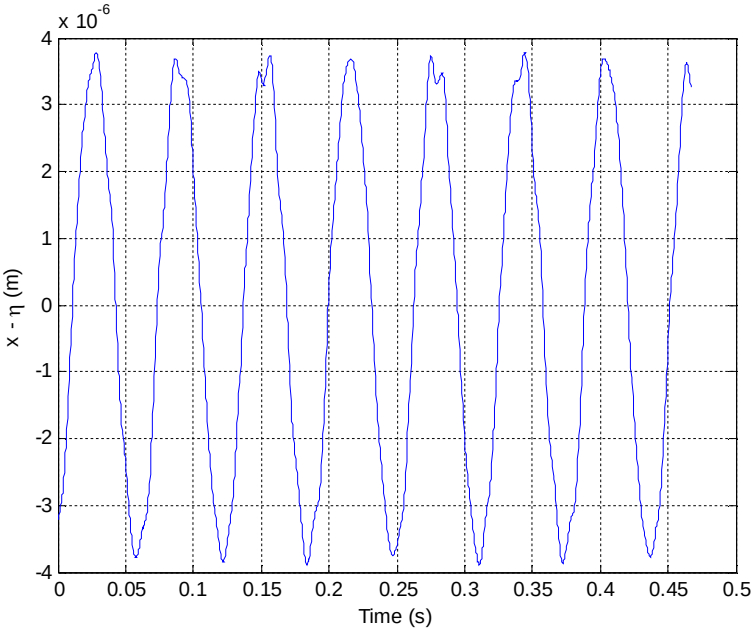


(b)

Fig. 6-5. The relative position and velocity between the optical table and the platen with vibration disturbance in the *x*-axis. (a) Simulated position, and (b) experimented position. (c) Simulated velocity, and (d) experimented velocity.

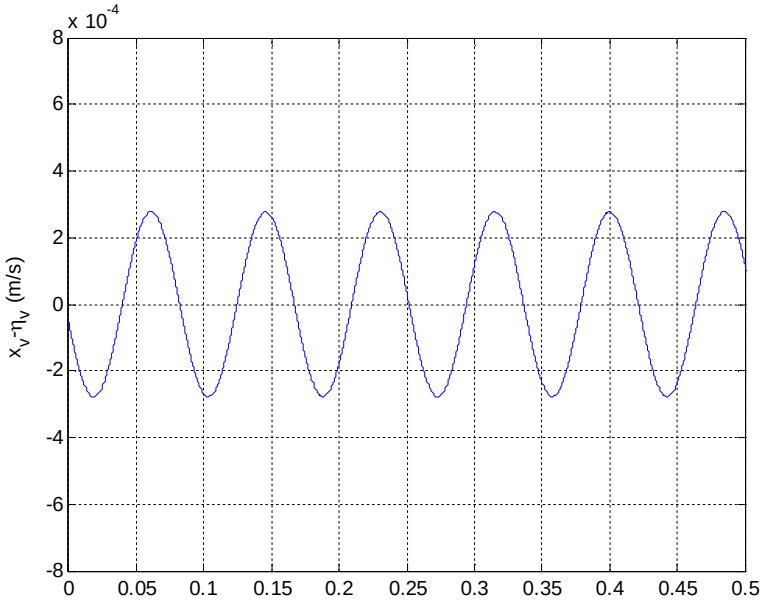


(c)

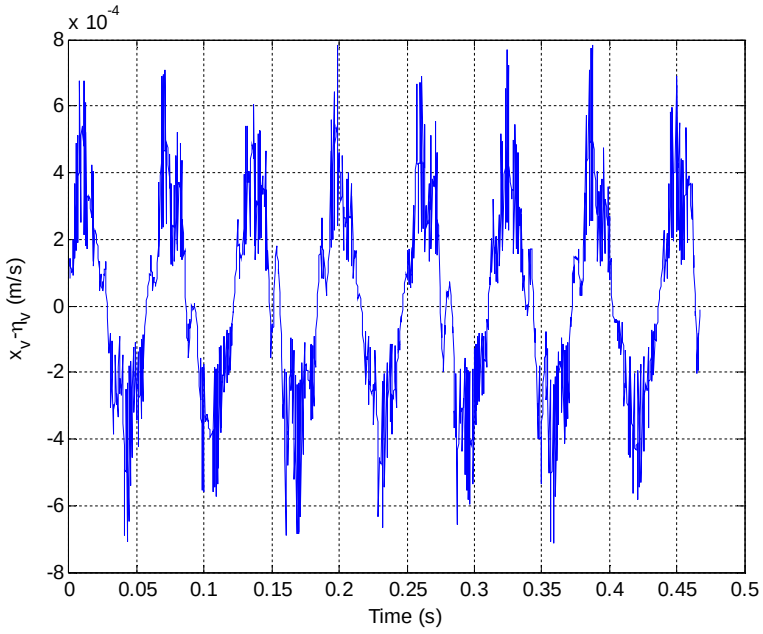


(d)

Fig. 6-5. Continued.

## 6.3 Linearization of Nonlinear Equations of Motion and Magnetic Force in the *y*-Axis

Linearization in the *y*-axis is almost the same in the *x*-axis except for *y* and $\rho$ replacing *x* and $\eta$. To linearize the EOMs in the *y*-axis, let set the perturbation equations $y = y_0 + \tilde{y}$ , $\rho = \rho_0 + \tilde{\rho}$ , and $i = i_0 + \tilde{i}$ in Fig. 6-6. Constants $y_0$ , $\rho_0$ , and $i_0$ mean the values at an operation point. The variables with circumflexes are perturbation. Using Taylor series expansion, (6.1.2) becomes

$$m_2\left(\cancel{\ddot{y}_0} + \ddot{\tilde{y}}\right) = \cancel{F_y(y_0, \rho_0, i_0)} + \left.\frac{\partial F_y(y,\rho,i)}{\partial y}\right|_{y_0,\rho_0,i_0} \tilde{y} + \left.\frac{\partial F_y(y,\rho,i)}{\partial \rho}\right|_{y_0,\rho_0,i_0} \tilde{\rho} + \left.\frac{\partial F_y(y,\rho,i)}{\partial i}\right|_{y_0,\rho_0,i_0} \tilde{i} \tag{6.3.1}$$

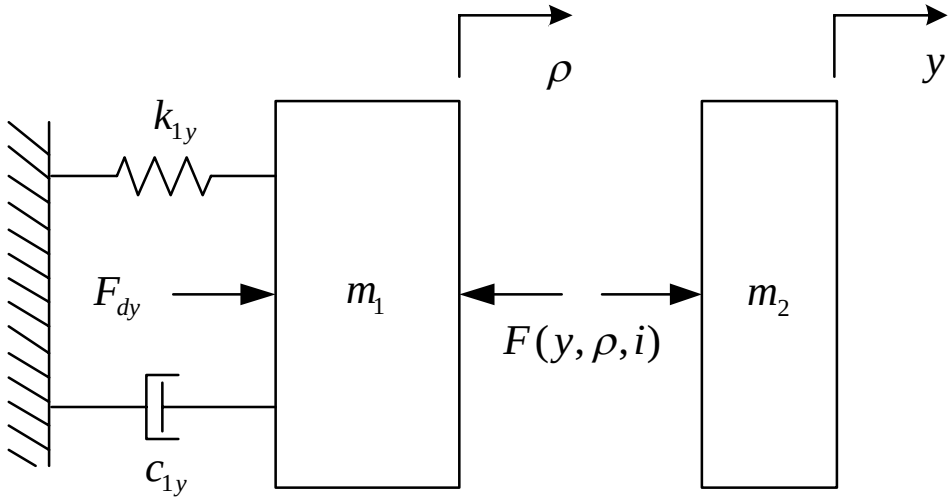


Fig. 6-6. Model of the maglev system in the *y*-axis.

The linearized EOM of the platen in the *y*-axis is

$$m_2\ddot{\tilde{y}} = \left( \left.\frac{\partial F_y}{\partial y}\right|_{y_0,\rho_0,i_0} \right)\tilde{y} + \left( \left.\frac{\partial F_y}{\partial \rho}\right|_{y_0,\rho_0,i_0} \right)\tilde{\rho} + \left( \left.\frac{\partial F_y}{\partial i}\right|_{y_0,\rho_0,i_0} \right)\tilde{i} \qquad (6.3.2)$$

where

$$\left.\frac{\partial F_y(y,\rho,i)}{\partial y}\right|_{y_0,\rho_0,i_0} = \left(2\beta_2\left(y_0-\rho_0\right)+\beta_1\right)i_0 \qquad (6.3.3)$$

$$\left.\frac{\partial F_y(y,\rho,i)}{\partial \rho}\right|_{y_0,\rho_0,i_0} = -\left(2\beta_2\left(y_0-\rho_0\right)+\beta_1\right)i_0 \qquad (6.3.4)$$

$$\left.\frac{\partial F_y(y,\rho,i)}{\partial i}\right|_{y_0,\rho_0,i_0} = \left(\beta_2\left(y_0-\rho_0\right)^2+\beta_1\left(y_0-\rho_0\right)+\beta_0\right). \qquad (6.3.5)$$

To determine the constant values of (6.3.2) – (6.3.5), the value of $i_0$ should be found. At the equilibrium point, the magnetic force is

$$F_y(y_0,\rho_0,i_0) = \left(\beta_2\left(y_0-\rho_0\right)^2+\beta_1\left(y_0-\rho_0\right)+\beta_0\right)i_0 = 0.$$

Thus, the current, $i_0$, at the operation point $\left(y_0-\rho_0\right)=0$ is

$$i_0 = 0 \qquad (6.3.6)$$

where $\beta_2 = 1.3031\times10^4$, $\beta_1 = -2.7161\times10^2$, and $\beta_0 = 2.2050$ [39].

Finally, the linearized equation of motion of the platen in the *y*-axis is

$$m_2\ddot{\tilde{y}} = k_{hy}\tilde{i} \qquad (6.3.7)$$

where $k_{hy} = \beta_2\left(y_0-\rho_0\right)^2+\beta_1\left(y_0-\rho_0\right)+\beta_0$.

Similary, the linearized EOM of the optical table with vibration disturbance in

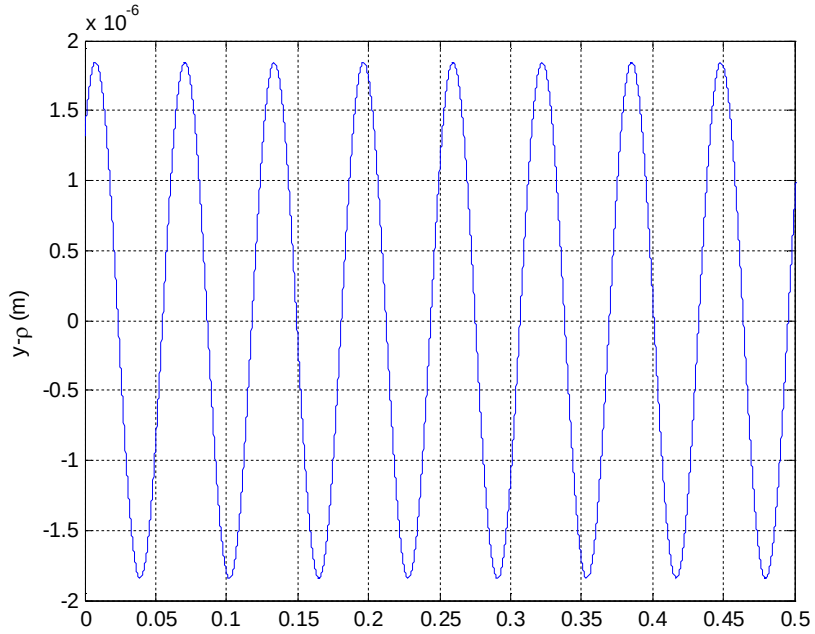


(a)

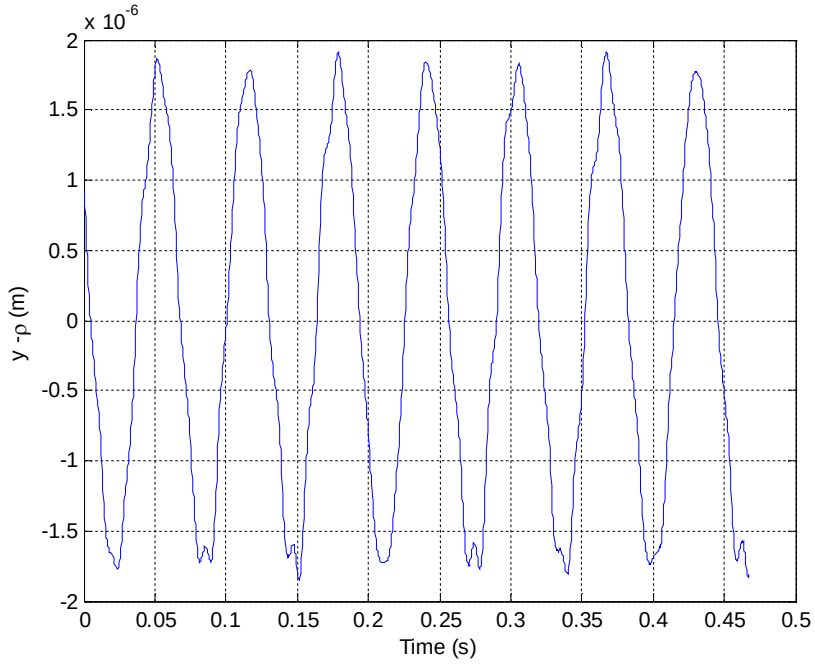


(b)

Fig. 6-7. The relative position and velocity between the optical table and the platen with vibration disturbance in *y*-axis. (a) Simulated position, and (b) experimented position. (c) Simulated velocity, and (d) experimented velocity.

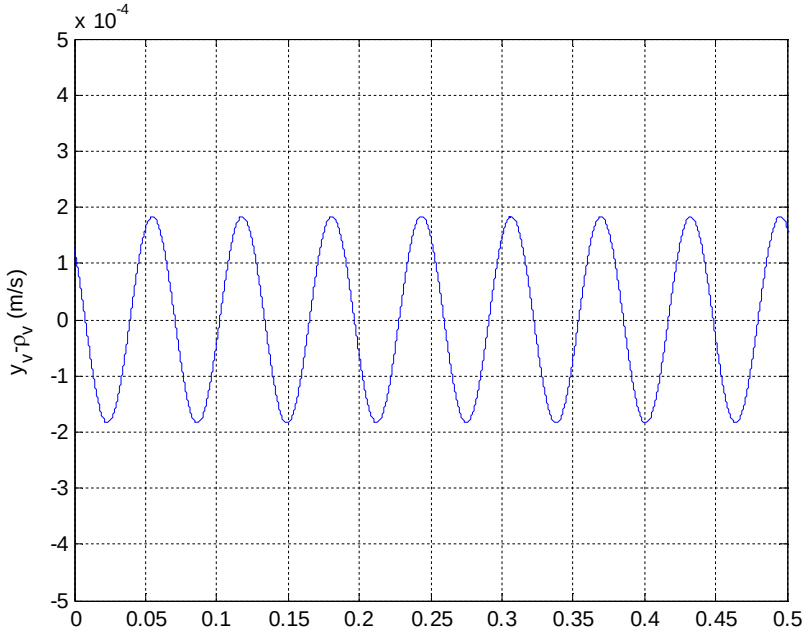


(c)

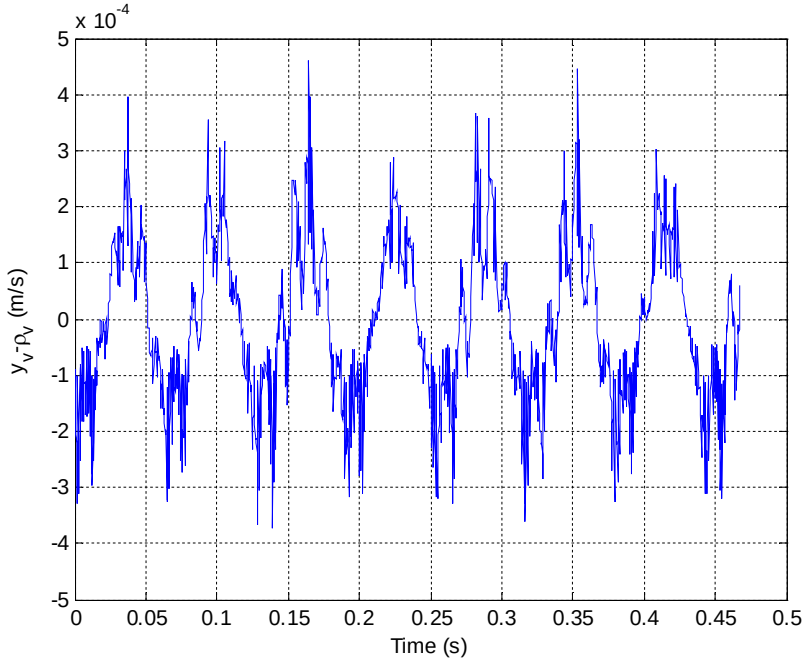


(d)

Fig. 6-7. Continued.

the *y*-axis becomes

$$m_1\ddot{\tilde{\rho}} + c_{1y}\dot{\tilde{\rho}} + k_{1y}\tilde{\rho} = -k_{hy}\tilde{i} + F_{dy}\,. \tag{6.3.8}$$

Likely in the *z*- and *x*-axes, the model of the maglev system with the magnetic stiffness in the *y*-axis, (6.3.7)–(6.3.8) are also verified. Fig. 6-7 shows the comparison between the experimental and simulation results with vibration disturbance.

The simulated position is very close to the experimented result. The magnitude of the relative velocity in the *y*-axis is little larger and noisy in the experimented data by the same reason mentioned in the *x*-axis model that high-frequency components of the position data is amplified by the differentiation. Except for the high-frequency components, the simulated velocity results are very similar to the experiments. Therefore, the linearized model of the platen with the optical table in the *y*-axis is validated.

# CHAPTER VII

# VIBRATION CONTROL IN HORIZONTAL MOTION

## 7.1 Transfer Function of the Maglev System in the *x*-Axis Motion

We take the Laplace transform of (6.2.7) with zero initial conditions.

$$L\left\{m_2\ddot{\tilde{x}}(t)\right\} = L\left\{k_{hx}\tilde{i}(t)\right\} \tag{7.1.1}$$

$$m_2 s^2 \tilde{X}(s) = k_{hx}\tilde{I}(s) \tag{7.1.2}$$

$$\tilde{X}(s) = \frac{k_{hx}}{m_2 s^2}\tilde{I}(s) \tag{7.1.3}$$

From the Laplace transform of (6.2.8), we obtain

$$L\left\{m_1\ddot{\tilde{\eta}}(t) + c_{1x}\dot{\tilde{\eta}}(t) + k_{1x}\tilde{\eta}(t)\right\} = L\left\{-k_{hx}\tilde{i}(t) + F_{dx}(t)\right\}. \tag{7.1.4}$$

$$\left(m_1 s^2 + c_{1x}s + k_{1x}\right)\tilde{H}(s) = -k_{hx}\tilde{I}(s) + F_{dx}(s) \tag{7.1.5}$$

$$\tilde{H}(s) = \frac{-k_{hx}}{\left(m_1 s^2 + c_{1x}s + k_{1x}\right)}\tilde{I}(s) + \frac{1}{\left(m_1 s^2 + c_{1x}s + k_{1x}\right)}F_{dx}(s) \tag{7.1.6}$$

By combining (7.1.3) and (7.1.6), the system transfer functions in matrix form in the *x*-axis is

$$\begin{bmatrix} \tilde{X}(s) \\ \tilde{H}(s) \end{bmatrix} = \begin{bmatrix} \dfrac{k_{hx}}{m_2 s^2} & 0 \\ \dfrac{-k_{hx}}{\left(m_1 s^2 + c_{1x} s + k_{1x}\right)} & \dfrac{1}{\left(m_1 s^2 + c_{1x} s + k_{1x}\right)} \end{bmatrix} \begin{bmatrix} \tilde{I}(s) \\ F_{dx}(s) \end{bmatrix} \tag{7.1.7}$$
$$= \begin{bmatrix} G_{11}(s) & G_{12}(s) \\ G_{21}(s) & G_{22}(s) \end{bmatrix} \begin{bmatrix} \tilde{I}(s) \\ F_{dx}(s) \end{bmatrix}.$$

The equivalent block diagram of the transfer function is illustrated in Fig. 7-1.

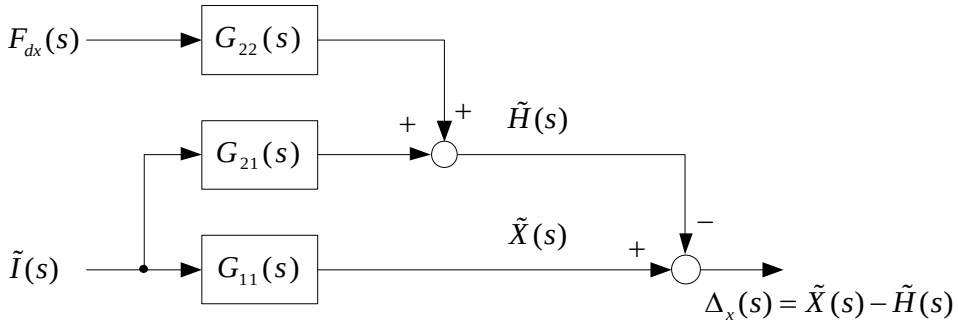


Fig. 7-1. Equivalent block diagram of the motion of maglev system in the *x*-axis.

From (7.1.11), the output $\Delta_x(s) = \tilde{X}(s) - \tilde{H}(s)$ is

$$\Delta_x(s) = \tilde{X}(s) - \tilde{H}(s) = (G_{11} - G_{21})\tilde{I}(s) - G_{22} F_{dx}(s). \tag{7.1.8}$$

The block diagram from (7.1.12) with feedback control for positioning is presented in Fig. 7-2, where $G_P(s) = G_{11}(s) - G_{21}(s)$ is a plant transfer function, and the vibration disturbance acts as an output disturbance.

The transfer function from the reference $r_x(s)$ and the vibration disturbance $F_{dx}(s)$ is

$$\Delta_x(s) = \frac{D_P(s)G_P(s)}{1 + D_P(s)G_P(s)} r_x(s) + \frac{-G_{22}(s)}{1 + D_P(s)G_P(s)} F_{dx}(s). \tag{7.1.9}$$

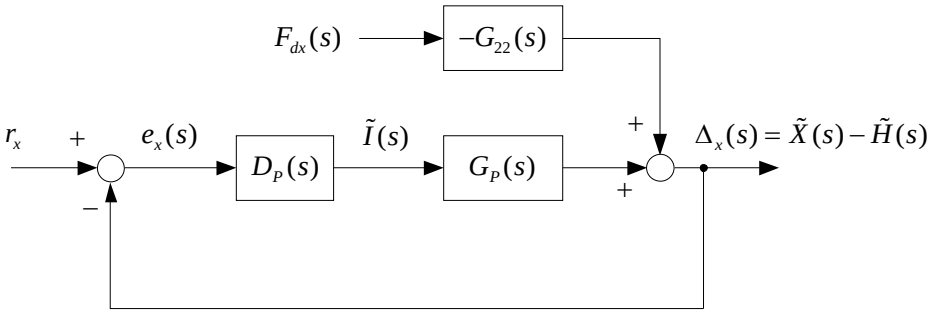


Fig. 7-2. Block diagram of a positioning feedback control of maglev system.

The loop transfer function of the maglev system becomes

$$D_P(s)G_P(s) = a\frac{(s+z_1)(s+z_2)}{s(s+p_1)}\left(G_{11}-G_{21}\right)$$

$$= \frac{\begin{array}{c} ak_{hx}\left(m_1+m_2\right)s^4 + ak_{hx}\left(c_{1x}+\left(m_1+m_2\right)z_1+\left(m_1+m_2\right)z_2\right)s^3 \\ +ak_{hx}\left(k_{1x}+\left(z_1+z_2\right)c_{1x}+\left(m_1+m_2\right)z_1z_2\right)s^2 \\ +ak_{hx}\left(k_{1x}\left(z_1+z_2\right)+c_1z_1z_2\right)s + ak_{1x}k_{hx}z_1z_2 \end{array}}{m_1m_2s^6 + m_2\left(c_{1x}+m_1p_1\right)s^5 + m_2\left(k_{1x}+c_{1x}p_1\right)s^4 + \left(k_{1x}m_2p_1\right)s^3} \quad (7.1.10)$$

$$= \frac{6.0923\times10^6 s^4 + 7.9484\times10^8 s^3 + 1.3276\times10^{10}s^2 + 4.3486\times10^{11}s + 4.1099\times10^{12}}{s^6 + 4016.9s^5 + 12399.0s^4 + 2.13\times10^6 s^3}$$

where all parameter values in (7.1.15) are presented in Table 7-1.

Table 7-1. Parameter values in horizontal motion

| Parameter | Value | Parameter | Value |
|---|---|---|---|
| $m_1$ | 436 kg | $k_h = k_{hx} = k_{hy}$ | 2.205 N/A |
| $m_2$ | 0.267 kg | $k_{1x}$ | $4.65305\times10^6$ N/m |
| $z_1$ | 10.91 | $k_{1y}$ | $1.89438\times10^6$ N/m |
| $z_2$ | 116.6 | $c_{1x}$ | $4.84471\times10^3$ N-s/m |
| $p_1$ | 4014 | $c_{1y}$ | $7.71056\times10^3$ N-s/m |
| $a$ | $7.3726\times10^5$ | | |

The position controller is a lead-lag compensator that was designed by Verma [38],

$$D_P(s) = a\frac{(s+z_1)(s+z_2)}{s(s+p_1)}. \tag{7.1.11}$$

The Bode plots of the loop transfer function and the closed-loop system are shown in Figs. 7-3–7-4. The controller was designed with phase margin of 69.7º at the 109.5 Hz. This lead-lag compensator's rise time and settling time are around 3 ms and 35 ms in a step response. The percentage overshoot is less than 35% with no steady-state error. However, in the nanotechnology, the influence by the vibration disturbance is not negligible.

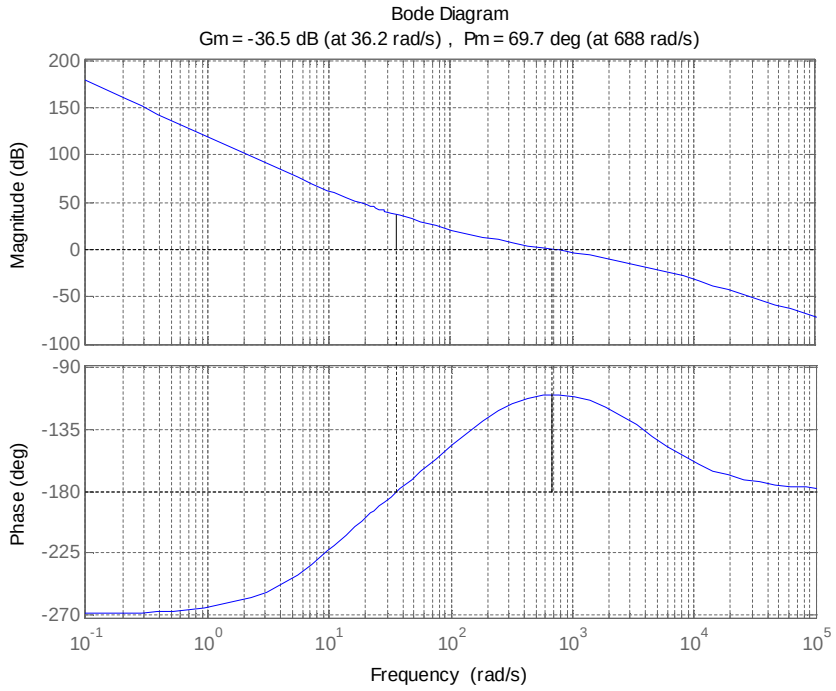


Fig. 7-3. Bode plot of the loop transfer function for the *x*-axis motion with maglev system.

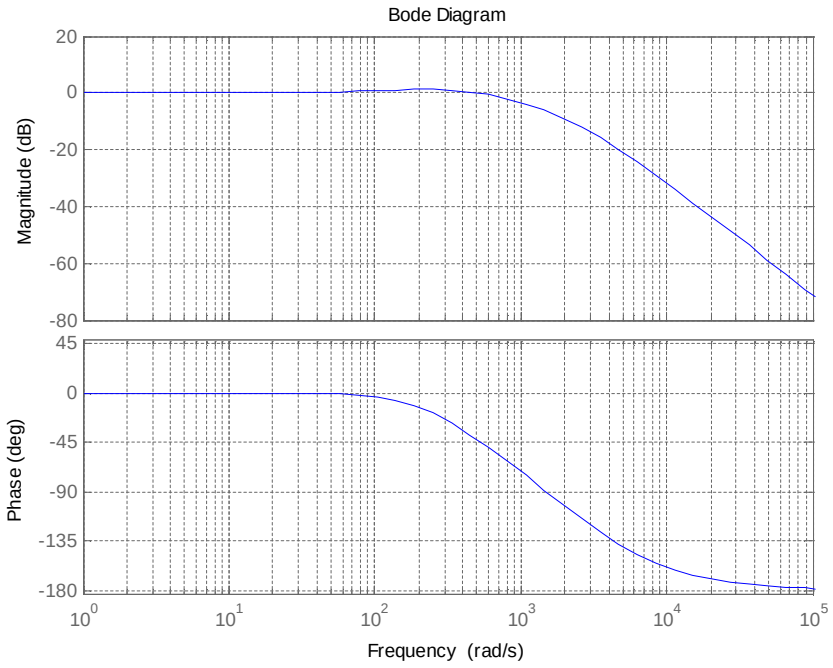


Fig. 7-4. Bode plot of the closed-loop system for the *x*-axis motion with maglev system.

To analyze how the vibration induce in the position, the transfer function from the vibration disturbance $F_{dx}$ to the position $\Delta_x$ is presented as

$$\begin{aligned}\frac{\Delta_x(s)}{F_{dx}(s)} &= \frac{m_2 s^4 + m_2 p_1 s^3}{m_1 m_2 s^6 + \left(c_{1x} m_2 + m_1 m_2 p_1\right) s^5 + \left(a k_h \left(m_1 + m_2\right) + m_2 \left(k_{1x} + c_{1x} p_1\right)\right) s^4} \\ &\quad + \left(a k_{hx} c_{1x} + k_{1x} m_2 p_1 + a k_{hx} \left(m_1 + m_2\right)\left(z_1 + z_2\right)\right) s^3 \\ &\quad + a k_{hx} \left(a k_{1x} + c_{1x} \left(z_1 + z_2\right) + \left(m_1 + m_2\right) z_1 z_2\right) s^2 \\ &\quad + a k_{hx} \left(k_{1x} \left(z_1 + z_2\right) + c_{1x} z_1 z_2\right) s + a k_{1x} k_{hx} z_1 z_2 \\ &\quad - \left(0.002294 s^4 + 9.206 s^3\right) \\ &= \frac{}{s^6 + 4017 s^5 + 6.105 \times 10^6 s^4 + 7.97 \times 10^8 s^3 + 1.328 \times 10^{10} s^2 + 4.349 \times 10^{11} s + 4.11 \times 10^{12}}\end{aligned}$$

(7.1.12)

where all parameter values in (7.1.17) are presented in Table 7-1.

The frequency response of the transfer function, $\frac{\Delta_x(s)}{F_{dx}(s)}$ is shown in Fig. 7-5. The magnitude of the frequency response of the vibration in the range is required to be attenuate. The vibration frequency caused by fans and motors is the most interesting frequency range of 10 to 100 Hz.

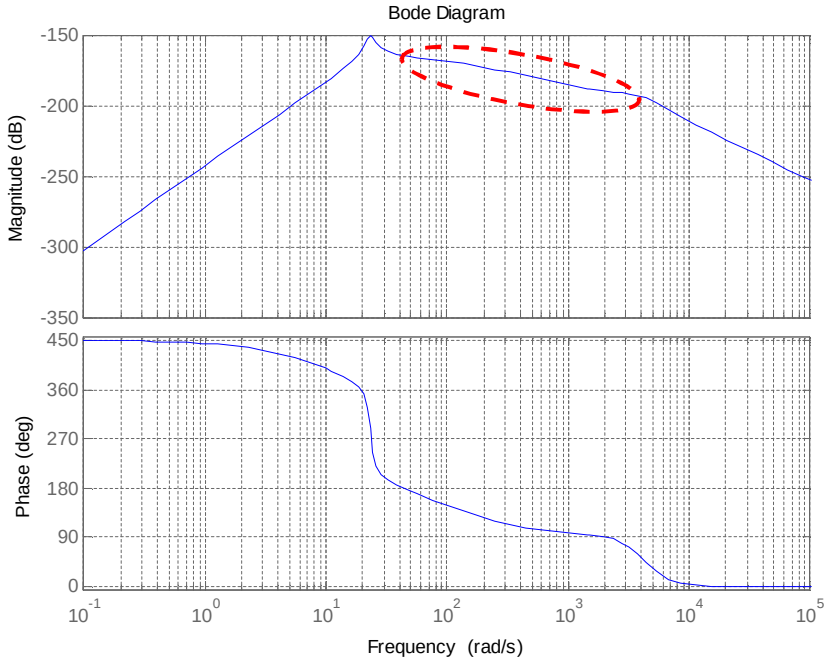


Fig. 7-5. Frequency response of the transfer function $\frac{\Delta_x(s)}{F_{dx}(s)}$. The dashed zone indicates the target frequency to be attenuated.

## 7.2 Design of a Dual-Loop Control System in the *x*-Axis Motion

### 7.2.1 Design of a Vibration Controller with Velocity Feedback in the *x*-Axis Motion

Since the key objective of this research is to reject or to reduce the effects of the vibration disturbance on the moving platen, a dual-loop control system with an additional cascade velocity-regulating loop for direct current control is designed in Fig. 7-6. An outer controller $D_P(s)$ acts as an outer-loop controller that controls the position of the platen. The other controller $D_V(s)$ acts as an inner-loop controller that controls more rapidly changing parameter, velocity. In addition, it requires a velocity measurement. The inner-loop controller becomes a vibration controller in Fig. 7-6.

The inner closed-loop transfer function is considered as a new modified plant transfer function in Fig. 7-6, and $G_{IN}$ becomes

$$G_{IN}(s) = \frac{G_P(s)}{1 + sD_V(s)G_P(s)}. \tag{7.2.1}$$

To design the inner loop controller, one of the commonly used controllers in classical control systems is applied. Let us the vibration controller be

$$D_V(s) = \frac{K_D s^2 + K_P s + K_I}{s}. \tag{7.2.2}$$

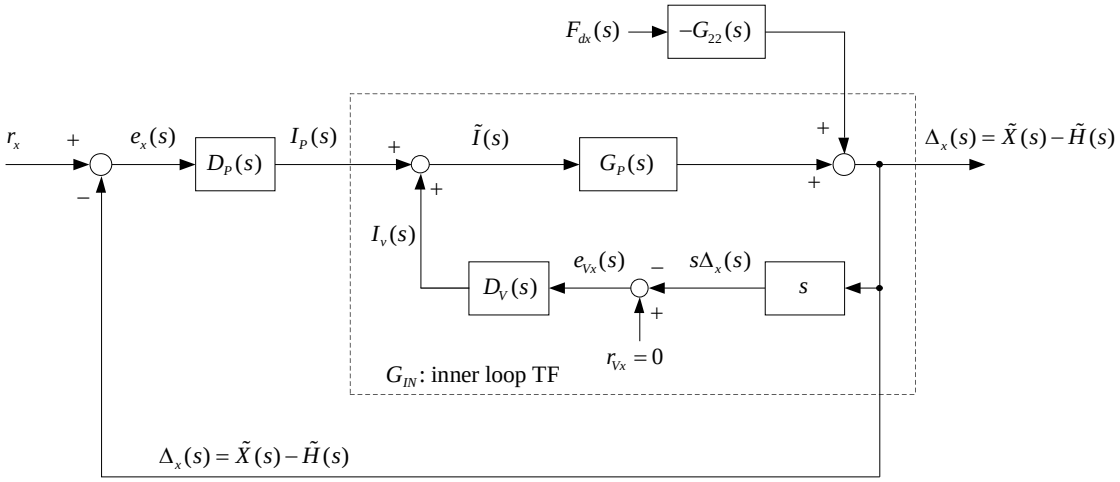


Fig. 7-6. Block diagram of the model of maglev system with positioning with a cascade velocity-regulation loop.

From (7.1.7), (7.2.1) and (7.2.2), the modified plant TF is

$$G_{IN}(s) = \frac{G_P(s)}{1 + sD_V(s)G_P(s)}$$

$$= \frac{k_{hx}(m_1 + m_2)s^2 + c_{1x}k_{hx}s + k_{1x}k_{hx}}{\left(m_1m_2 + K_Dk_{hx}\left(m_1 + m_2\right)\right)s^4 + \left(K_Dc_{1x}k_{hx} + c_{1x}m_2 + K_Pk_{hx}\left(m_1 + m_2\right)\right)s^3 + \left(k_{1x}m_2 + K_Dk_{1x}k_{hx} + K_Pc_{1x}k_{hx} + K_Ik_{hx}\left(m_1 + m_2\right)\right)s^2 + k_{hx}\left(K_Ic_{1x} + K_Pk_{1x}\right)s + K_Ik_{1x}k_{hx}} \quad (7.2.3)$$

where all parameter values in (7.2.3) are presented in Table 7-1. The modifited plant TF including a vibration controller should be stablized. The design parameters of the controller should be well tune. Before we determine the control parameters, the stablizing region of the controller gains need to be found.

The characteristic equation of the modified TF becomes

$$\begin{aligned} 0 &= d_4 s^4 + d_3 s^3 + d_2 s^2 + d_1 s + d_0 \\ &= \left(m_1 m_2 + K_D k_{hx}\left(m_1 + m_2\right)\right) s^4 + \left(K_D c_{1x} k_{hx} + c_{1x} m_2 + K_P k_{hx}\left(m_1 + m_2\right)\right) s^3 \\ &\quad + \left(k_{1x} m_2 + K_D k_{1x} k_{hx} + K_P c_{1x} k_{hx} + K_I k_{hx}\left(m_1 + m_2\right)\right) s^2 \\ &\quad + k_{hx}\left(K_I c_{1x} + K_P k_{1x}\right) s + K_I k_{1x} k_{hx} \end{aligned} \quad . \quad (7.2.4)$$

where,

$$d_4 = m_1 m_2 + K_D k_{hx}\left(m_1 + m_2\right) \quad (7.2.5)$$

$$d_3 = K_D c_{1x} k_{hx} + c_{1x} m_2 + K_P k_{hx}\left(m_1 + m_2\right) \quad (7.2.6)$$

$$d_2 = k_{1x} m_2 + K_D k_{1x} k_{hx} + K_P c_{1x} k_{hx} + K_I k_{hx}\left(m_1 + m_2\right) \quad (7.2.7)$$

$$d_1 = k_{hx}\left(K_I c_{1x} + K_P k_{1x}\right) \quad (7.2.8)$$

$$d_0 = K_I k_{1x} k_{hx} \quad (7.2.9)$$

For determining its stability, the Routh-Hurwitz criterion is used.

| | | | |
|---|---|---|---|
| $s^4$ : | $d_4$ | $d_2$ | $d_0$ |
| $s^3$ : | $d_3$ | $d_1$ | 0 |
| $s^2$ : | $\frac{d_3 d_2 - d_4 d_1}{d_3} = A$ | $\frac{d_3 d_0 - d_4 \times 0}{d_3} = d_0$ | 0 |
| $s^1$ : | $\frac{A d_1 - d_3 d_0}{A} = B$ | 0 | 0 |
| $s^0$ : | $\frac{B d_0 - A \times 0}{B} = d_0$ | 0 | 0 |

From the stability analysis, as long as $K_P$, $K_D$, and $K_I$ have positive values, the inner loop is stable because the other constants in (7.2.4) are all positive values. However, the entire

system combinded with inner and outer loops has different stabilizing region of the control gains.

The transfer function from the reference to postion output is

$$\begin{aligned}\frac{\Delta_x(s)}{r_x(s)} &= \frac{D_P(s)G_{IN}(s)}{1+D_P(s)G_{IN}(s)} \\ &= \frac{a_4 s^4 + a_3 s^3 + a_2 s^2 + a_1 s + a_0}{d_6 s^6 + d_5 s^5 + d_4 s^4 + d_3 s^3 + d_2 s^2 + d_1 s + d_0}\end{aligned} \tag{7.2.10}$$

where,

$$a_4 = ak_{hx}\left(m_1 + m_2\right) \tag{7.2.11}$$

$$a_3 = ak_{hx}\left(c_{1x} + \left(m_1 + m_2\right)\left(z_1 + z_2\right)\right) \tag{7.2.12}$$

$$a_2 = ak_{hx}\left(k_{1x} + c_{1x}\left(z_1 + z_2\right) + \left(m_1 + m_2\right)z_1 z_2\right) \tag{7.2.13}$$

$$a1 = ak_{hx}\left(k_{1x}\left(z_1 + z_2\right) + c_{1x}z_1 z_2\right) \tag{7.2.14}$$

$$a_0 = ak_{hx}k_{1x}z_1 z_2 \tag{7.2.15}$$

, and

$$d_6 = k_{hx}\left(m_1 + m_2\right)K_D + m_1 m_2 \tag{7.2.16}$$

$$d_5 = k_{hx}\left(m_1 + m_2\right)K_P + k_{hx}\left(c_{1x} + p_1(m_1 + m_2)\right)K_D + c_{1x}m_2 + m_1 m_2 p_1 \tag{7.2.17}$$

$$\begin{aligned}d_4 = {} & k_{hx}\left(c_{1x} + p_1(m_1 + m_2)\right)K_P + k_{hx}\left(m_1 + m_2\right)K_I \\ & + k_{hx}\left(k_{1x} + c_{1x}p_1\right)K_D + ak_{hx}\left(m_1 + m_2\right) + k_{1x}m_2 + c_{1x}m_2 p_1\end{aligned} \tag{7.2.18}$$

$$\begin{aligned}d_3 = {} & k_{hx}\left(k_{1x} + c_{1x}p_1\right)K_P + k_{hx}\left(c_{1x} + (m_1 + m_2)p_1\right)K_I + k_1 k_{hx}p_1 K_D \\ & + ak_{hx}\left(c_{1x} + m_1(z_1 + z_2) + m_2(z_1 + z_2)\right) + k_{1x}m_2 p_1\end{aligned} \tag{7.2.19}$$

$$\begin{aligned}d_2 = {} & k_{1x}k_{hx}p_1 K_P + k_{hx}\left(k_{1x} + c_{1x}p_1\right)K_I + ak_{hx}\left(k_{1x} + c_{1x}(z_1 + z_2)\right. \\ & \left. + z_1 z_2(m_1 + m_2)\right)\end{aligned} \tag{7.2.20}$$

$$d_1 = k_{1x}k_{hx}p_1K_I + ak_{hx}\left(k_{1x}(z_1+z_2)+c_{1x}z_1z_2\right) \tag{7.2.21}$$

$$d_0 = ak_{1x}k_{hx}z_1z_2 \tag{7.2.22}$$

where all parameter values in (7.2.11)–(7.2.22) are presented in Table 7-1.

For stability analysis of the transfer function, let the denominator of $\frac{\Delta_x(s)}{r_x(s)}$ be

$$\delta(s) = d_6s^6 + d_5s^5 + d_4s^4 + d_3s^3 + d_2s^2 + d_1s + d_0\,. \tag{7.2.23}$$

If all roots of $\delta(s)$ are in the left-half *s*-plane, the closed-loop transfer function $\frac{\Delta_x(s)}{r_x(s)}$ is stable. To determinr its stability, the Routh-Hurwitz criterion is applied. The same lead-lag compensator $D_P(s)$ in (7.1.15) is used to (7.2.10).

| | | | | |
|---|---|---|---|---|
| $s^6$: | $d_6$ | $d_4$ | $d_2$ | $d_0$ |
| $s^5$: | $d_5$ | $d_3$ | $d_1$ | 0 |
| $s^4$: | $\frac{d_5d_4 - d_6d_3}{d_5} = A$ | $\frac{d_5d_2 - d_6d_1}{d_5} = B$ | $\frac{d_5d_0 - d_6\times 0}{d_5} = d_0$ | 0 |
| $s^3$: | $\frac{Ad_3 - d_5B}{A} = C$ | $\frac{Ad_1 - d_5d_0}{A} = D$ | 0 | 0 |
| $s^2$: | $\frac{CB - AD}{C} = E$ | $\frac{Cd_0 - A\times 0}{C} = d_0$ | 0 | 0 |
| $s^1$: | $\frac{ED - Cd_0}{E} = F$ | 0 | 0 | 0 |
| $s^0$: | $\frac{Fd_0}{F} = d_0$ | 0 | 0 | 0 |

According to the Routh-Hurwitz criterion, all roots of the polynomial in the left-half *s*-plane if all the elements in the first column of the Routh array are of the same sign. Since $k_h$ and $K_D$ are all positive from (7.2.16), $d_6$ is positive with the positive value of $K_D$. Therefore, $d_5$, $A$, $C$, $E$, $F$, and $d_6$ should be all positive for closed-loop stability.

Fig. 7-7 illustrates the stable region that is drawn by calculation iteration through $0 \le K_D \le 100$, $0 \le K_P \le 1000$, and $0 \le K_I \le 100$. As shown in Fig. 7-7, the stable region decreases with increasing $K_D$ and the derivative gain is not helpful to stabilize the system since the derivative control will reinforce the rapid change of the velocity. Thus, PI controller instead to the PID controller is appropriate as a velocity feedback controller. If the value of $K_D$ is zero, the system is stable if $K_P \ge 0$ and $K_I \ge 0$.

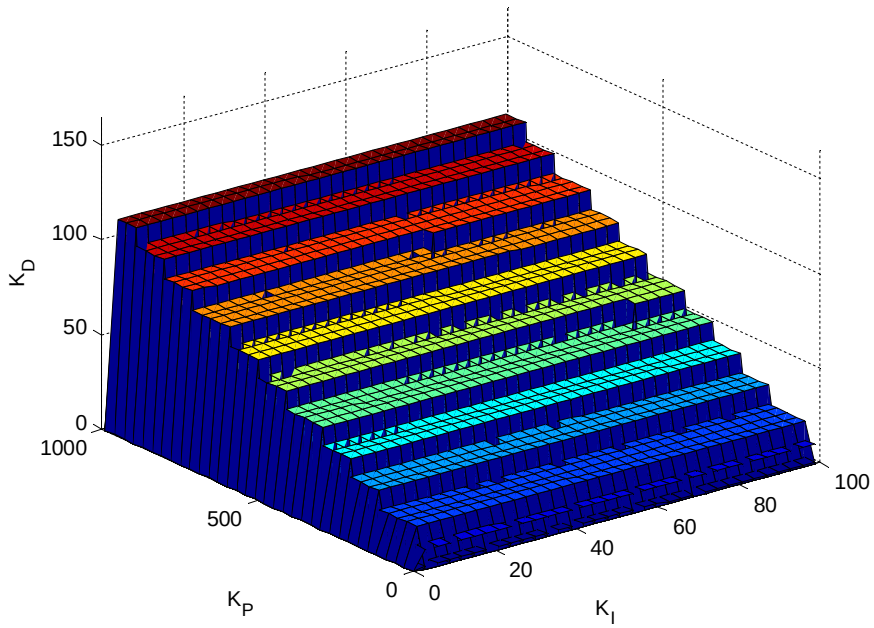


Fig. 7-7. The stabilizing region of $(K_P, K_I, K_D)$ values for a PID controller in the *x*-axis.

The inner-loop controller should attenuate the effect of vibration disturbance. To observe how the vibration disturbance influences the output, the transfer function $F_{dx}(s)$ from the disturbance to the output $\Delta_x(s)$ need to be analyzed. It is presented as

$$\frac{\Delta_x(s)}{F_{dx}(s)} = \frac{-G_{22}(s)}{1+G_P(s)\left(D_p(s)+sD_v(s)\right)}$$

$$= \frac{-m_2\left(s^4+p_1s^3\right)}{\begin{aligned} &m_1m_2s^6+\left(c_{1x}m_2+K_Pk_{hx}\left(m_1+m_2\right)+m_1m_2p_1\right)s^5 \\ &+\left(k_{1x}m_2+K_Pc_1k_{hx}+c_{1x}m_2p_1+k_{hx}\left(K_I+a+p_1K_P\right)\left(m_1+m_2\right)\right)s^4 \\ &+\left(\begin{aligned}&\left(K_I+a\right)c_{1x}k_{hx}+k_{1x}m_2p_1+K_Pk_{hx}\left(k_1+c_1p_1\right) \\ &+K_Ik_{hx}\left(m_1+m_2\right)p_1+ak_{hx}\left(m_1+m_2\right)\left(z_1+z_2\right)\end{aligned}\right)s^3 \\ &+k_{hx}\left(\left(K_I+a\right)k_{1x}+\left(K_Ic_{1x}+K_Pk_{1x}\right)p_1+ac_{1x}\left(z_1+z_2\right)+a\left(m_1+m_2\right)z_1z_2\right)s^2 \\ &+k_{hx}\left(K_Ik_{1x}p_1+ak_{1x}\left(z_1+z_2\right)+ac_{1x}z_1z_2\right)s+ak_{1x}k_{hx}z_1z_2\end{aligned}}$$

$$= \frac{-m_2\left(s^4+p_1s^3\right)}{d_6s^6+d_5s^5+d_4s^4+d_3s^3+d_2s^2+d_1s+d_0}$$

(7.2.24)

where, $d_6$, $d_5$, $d_4$, $d_3$, $d_2$, $d_1$, and $d_0$ are same as (7.2.16) – (7.2.22) if $K_D = 0$, and all parameter values in (7.2.24) are presented in Table 7-1.

If the $K_P$ = 300 and $K_I$ = 0 with the lead-lag compenstor in (7.1.15),

$$\frac{\Delta_x(s)}{F_{dx}(s)} = \frac{-\left(0.0022936s^4+9.2063s^3\right)}{s^6+5141.3s^5+7.292\times10^6s^4+3.77\times10^8s^3+8.415\times10^9s^2+1.972\times10^{11}s+1.864\times10^{12}}$$

(7.2.25)

The frequency response of the $\frac{\Delta_x(s)}{F_{dx}(s)}$ is shown in Fig. 7-8. The dashed line is without the velocity-regulation loop, and the solid line is with the velocity-regulation loop. The magnitude of the transfer function $\frac{\Delta_x(s)}{F_{dx}(s)}$ with vibration contoller is reduced in the region from 30 rad/s to 3000 rad/s. It means that the velocity feedback control is effective to 4.77 Hz to 477 Hz of vibration disturbance.

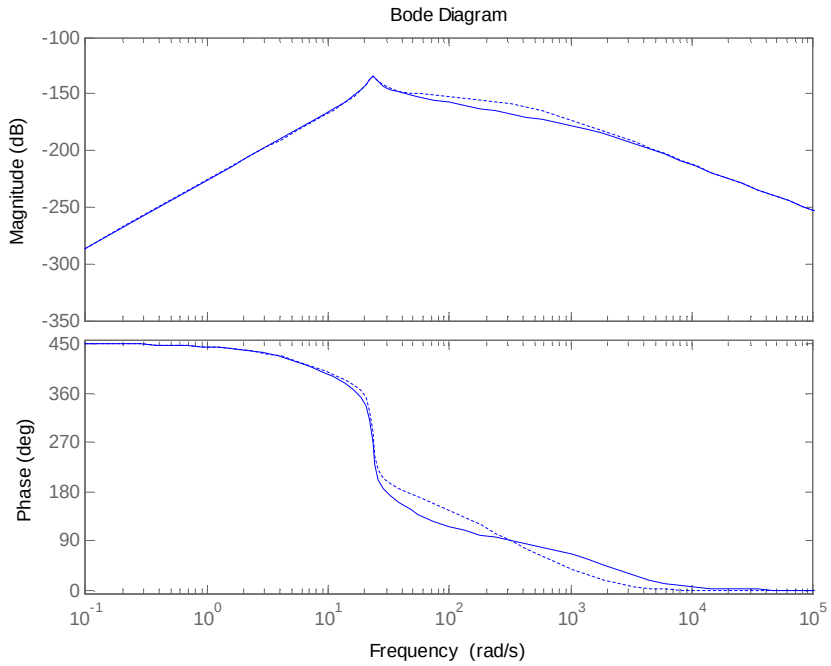


Fig. 7-8. Frequency responses of the transfer function from vibration disturbance to position in the *x*-axis. The solid line indicates the response with PI vibration control ($K_P = 300$, $K_I = 0$), and the dotted line indicates without the vibration control scheme.

Fig. 7-9 shows the zoomed frequency resposes from 10 Hz to 100 Hz of the the transfer function $\frac{\Delta_x(s)}{F_{dx}(s)}$ in Fig. 7-8. The magnitude with vibration controller is reduced about 3.3 dB to 8.7 dB between 10 Hz and 100 Hz in Fig. 7-10. The negative difference means the reduction of the influence by the vibration disturbance. The real differeces with the experiments and simulations in this frequency range is presented in Fig. 7-10. The parabolic trend of the reduction through the given frequency range in the experiment is very similar with the simulation.

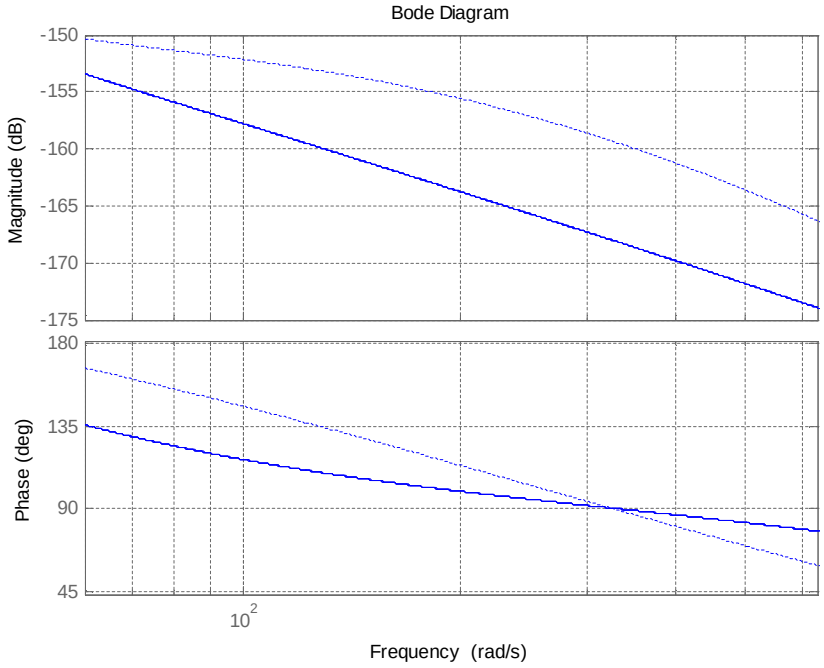


Fig. 7-9. Zoomed frequency responses of the transfer function from vibration disturbance to position in the *x*-axis from 10 Hz to 100 Hz. The solid line indicates the response with a proportional vibration control ($K_P = 300$, $K_I = 0$), and the dotted line indicates that without the vibration control scheme.

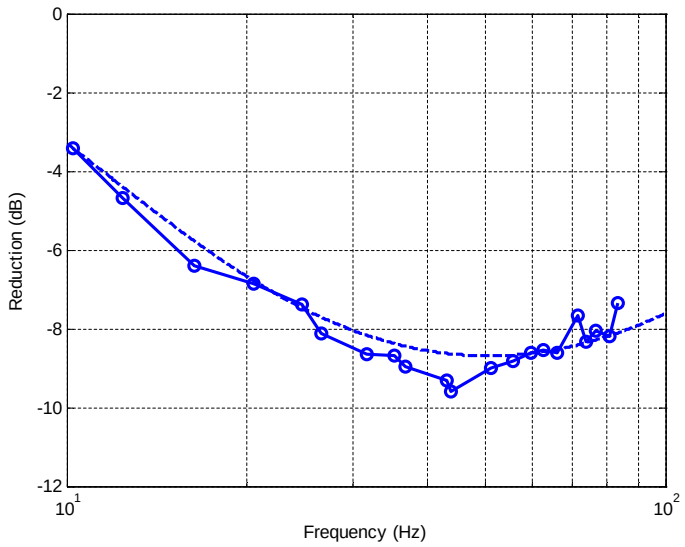


(a)

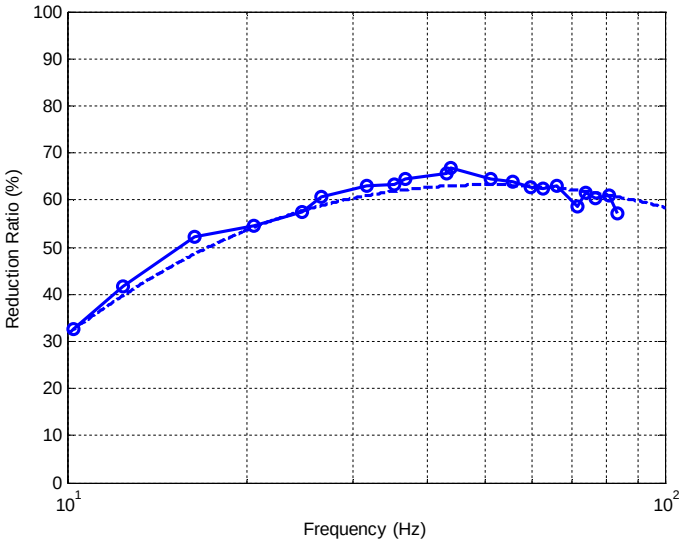


(b)

Fig. 7-10. (a) Magnitude reduction, and (b) reduction percentage of the magnitude in the frequency responses of the transfer function $\frac{\Delta_x(s)}{F_{dx}(s)}$ from 10 Hz to 100 Hz with a PID vibration control ($K_P = 300$, $K_I = 0$, $K_D = 0$). The dashed line indicates the response in the simulation and the circled line indicates the experiment.

The reduction ratio is various through the applied frequency range. As the proportional gain $K_P$ is increasing, the reduction ratio is also increasing. Theoretically, the reduction ratio will be increased by as much as increasing $K_P$. However, if $K_P$ is greater than 600, the system loses the stability in experiment. For both the stability and the reduction performance, the proper value of $K_P$ is 300.

For the integral gain $K_I$, the magnitude change by increasing integral gain $K_I$ is very small on the aspect of the TF $\frac{\Delta_x(s)}{F_{dx}(s)}$. Also, the phase shape does not change unless $K_I$ significantly increases. However, the magnitude slope of the open-loop TF at low frequency decreases by increasing $K_I$ in Fig 7-11. It means the rise time and the settling time increases. The $K_I$ in the inner-loop compensator does not affect in the steady-state error and the final value by the disturbance in the closed-loop system in Fig 7-12. The steady-state errors for a unit-step input in closed-loop (7.2.10) by the final value theorem is

$$e(\infty) = \lim_{t\to\infty} e(t) = \lim_{t\to\infty}\left(r(t) - y(t)\right) = 1 - \lim_{s\to 0} s \cdot \frac{\Delta_x(s)}{r_P(s)}\frac{1}{s} = 1 - \frac{a_0}{d_0} = 0 \qquad (7.2.26)$$

where $a_0 = d_0 = ak_{hx}k_{x1}z_1z_2$. For the disturbance TF $\frac{\Delta_x(s)}{F_{dx}(s)}$, the final value for a unit-step input is

$$\Delta_x(\infty) = \lim_{t\to\infty}\Delta_x(t) = \lim_{s\to 0} s\cdot\frac{\Delta_x(s)}{F_{dx}(s)}\left(\frac{1}{s}\right)$$
$$= \lim_{s\to 0}\frac{-m_2\left(s^4 + p_1 s^3\right)}{d_6 s^6 + d_5 s^5 + d_4 s^4 + d_3 s^3 + d_2 s^2 + d_1 s + d_0}. \qquad (7.2.27)$$
$$= \frac{0}{d_0} = 0$$

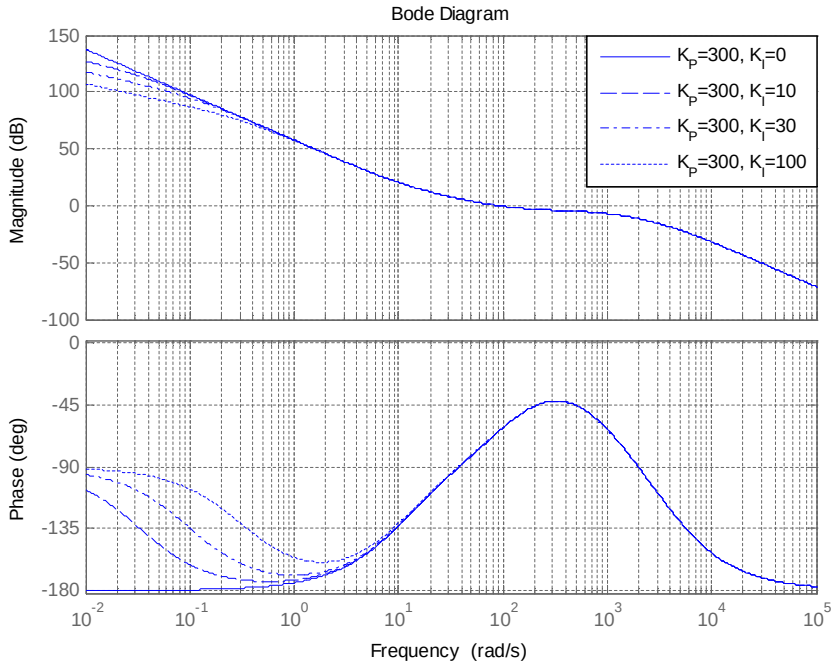


Fig. 7-11. Frequency responses of the open-loop transfer function $D_P(s)G_{IN}(s)$ with various $K_I$ values.

Hence, there is no advantage by the integral term that makes the system response slower. Therefore, the integral term is unnecessary. Finally, the velocity-regulating compensator becomes a proportional controller that has the gain $K_P$ = 300.

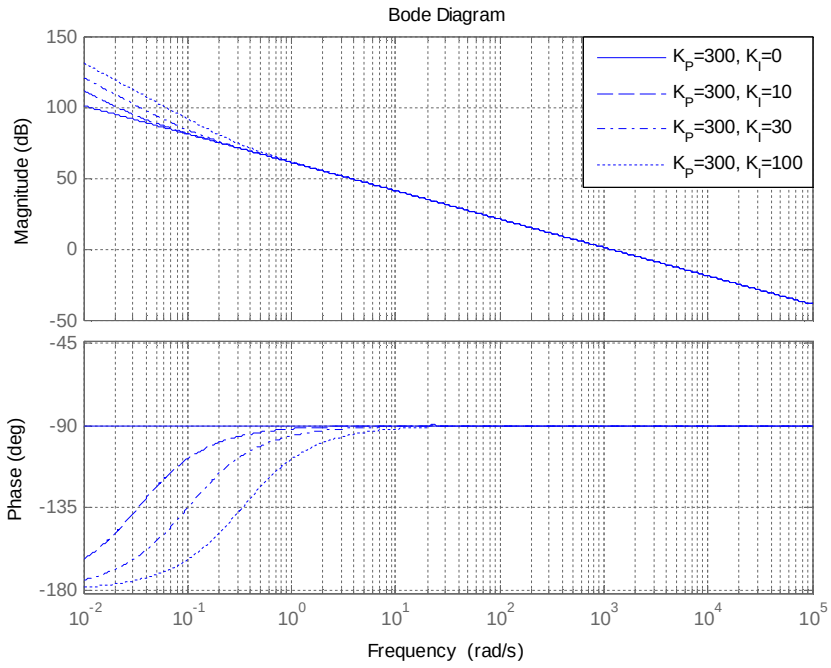


Fig. 7-12. Frequency responses of the inner-loop transfer function $sD_V(s)G_P(s)$ with various $K_I$ values.

### 7.2.2 Design of the Outer-Loop Controller in the *x*-Axis Motion

By adding the inner loop controller to regulate the velocity, the open-loop TF is changed in Fig. 7-13. The overall magnitude is shifted downward to compare to the loop shape without the inner-loop controller in Fig. 7-3. The roll-off of the magnitude is changed from –60 dB/decade to –40 dB/decade at lower frequency. The crossover frequency is reduced from 688 rad/s to 90.8 rad/s. Hence, the rise time and the settling time decreases. The comparison of step responses between two systems is shown in Fig. 7-14. The rise time and the settling time can decrease by increasing the gain in the outer lead-lag compensator. However, if the gain becomes too high, unwanted oscillation is

observed in the real system in Fig. 7-15. If the rise time and settling time are not significant, the lead-lag compensator designed in the previous work does not need to be modified.

In summary of the design of the dual-loop control system, the inner-loop compensator is

$$D_V(s) = K_P, \tag{7.2.28}$$

and the outer-loop compensator is

$$D_P(s) = a\frac{(s+p_1)(s+p_2)}{s(s+z_1)}. \tag{7.2.29}$$

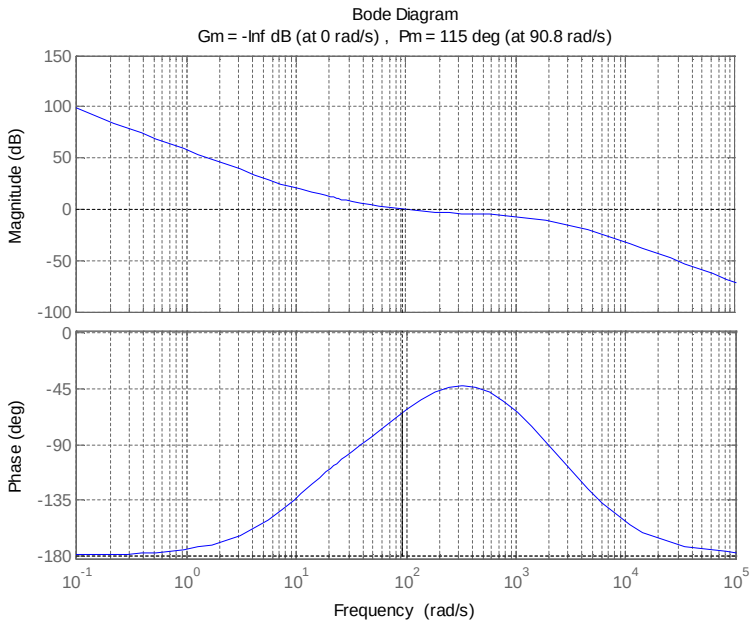


Fig. 7-13. Closed-loop Bode plot for the *x*-axis motion of maglev system with vibration controller.

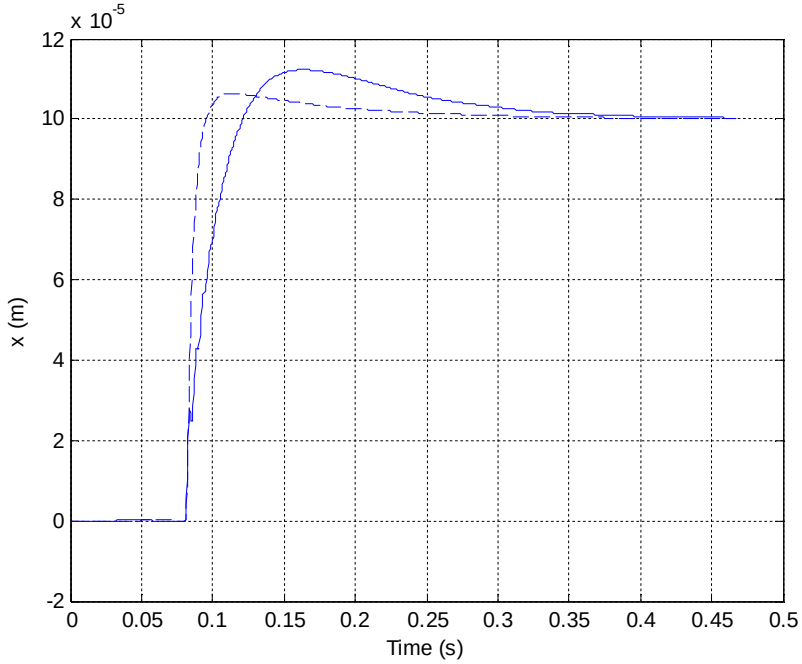


Fig. 7-14. Comparison of step responses (a) with a dual-loop compensator (solid line) and (b) with only an outer-loop compensator (dashed line) in experiments.

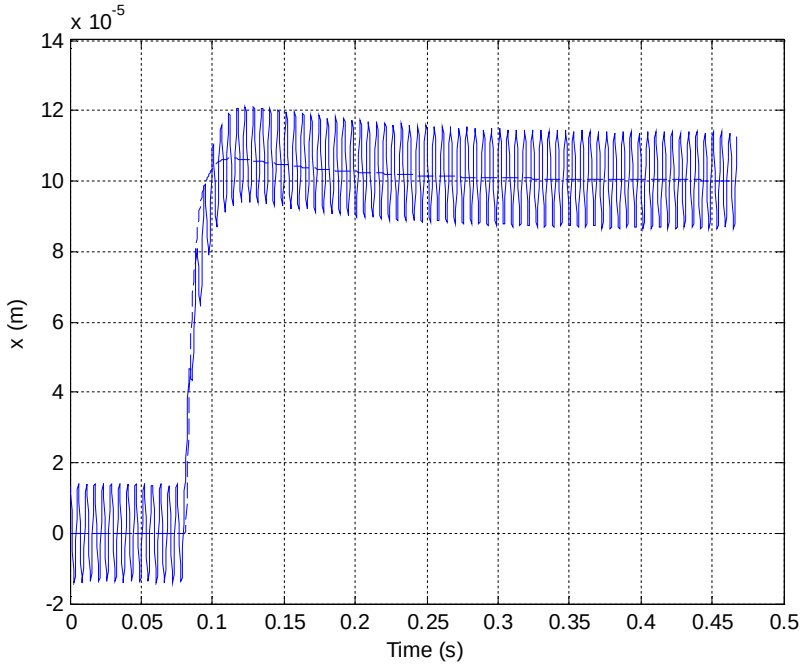


Fig. 7-15. Comparison of step responses (a) with the inner-loop controller and the outer lead-lag compensator with five times increased value *a* (solid line) and (b) only with the original modified outer lead-lag compensator (dashed line) in experiments.

## 7.3 Design of a Dual-Loop Control System in the *y*-Axis Motion

### 7.3.1 Design of a Vibration Controller with Velocity Feedback in *y*-Axis Motion

The dynamics of the maglev stage in the *y*-axis is identical to the motion in the *x*-axis except the values of the stiffness and the damping coefficient of the optical table. The same control system for vibration control is used in the *y*-axis motion. Hence, the stability analysis and design procedure of the controllers for the *y*-axis motion are skipped in this section. Some important transfer functions and figures are briefly presented in the following.

The transfer functions of the EOMs in the *y*-axis are presented in (7.3.1) and (7.3.2),

$$\tilde{Y}(s) = \frac{k_{hy}}{m_2 s^2}\tilde{I}(s) \tag{7.3.1}$$

$$\tilde{P}(s) = \frac{-k_{hy}}{\left(m_1 s^2 + c_{1y} s + k_{1y}\right)}\tilde{I}(s) + \frac{1}{\left(m_1 s^2 + c_{1y} s + k_{1y}\right)}F_{dy}(s). \tag{7.3.2}$$

By combining (7.3.1) and (7.3.2), the system transfer functions in matrix form in the *y*-axis is

$$\begin{bmatrix}\tilde{Y}(s)\\ \tilde{P}(s)\end{bmatrix} = \begin{bmatrix}\dfrac{k_{hy}}{m_2 s^2} & 0\\ \dfrac{-k_{hy}}{\left(m_1 s^2 + c_{1y} s + k_{1y}\right)} & \dfrac{1}{\left(m_1 s^2 + c_{1y} s + k_{1y}\right)}\end{bmatrix}\begin{bmatrix}\tilde{I}(s)\\ F_{dy}(s)\end{bmatrix} = \begin{bmatrix}G_{11}(s) & G_{12}(s)\\ G_{21}(s) & G_{22}(s)\end{bmatrix}\begin{bmatrix}\tilde{I}(s)\\ F_{dy}(s)\end{bmatrix}. \tag{7.3.3}$$

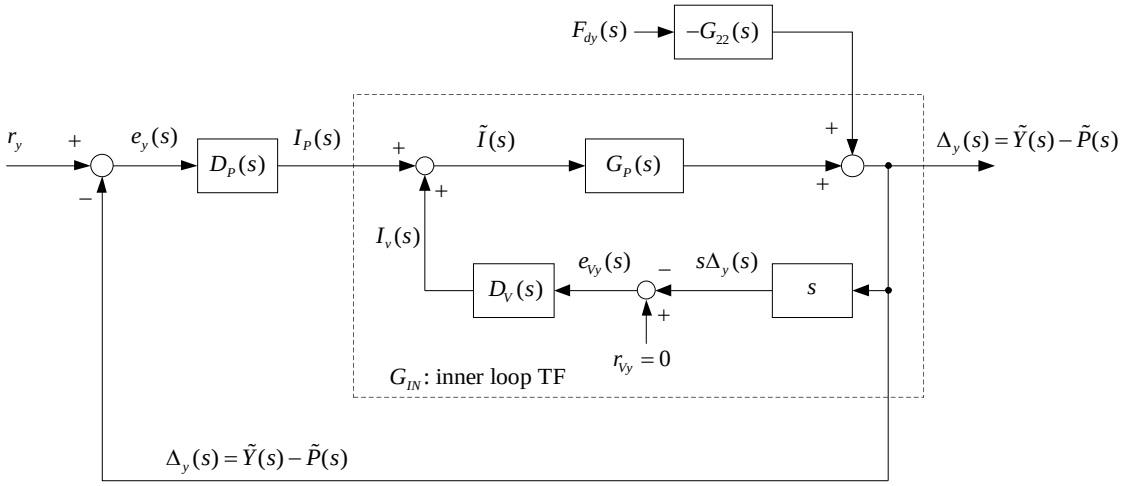


Fig. 7-16. Block diagram of the model of maglev system with positioning with a cascade velocity-regulation loop in the *y*-axis.

The inner closed-loop transfer function is considered as a new modified plant transfer function in Fig. 7-16, and $G_{IN}(s)$ becomes

$$G_{IN}(s) = \frac{G_P(s)}{1 + sD_V(s)G_P(s)}. \tag{7.3.4}$$

For the vibration controller, we discussed how to design the vibration controller as a proportional controller in the previous two sections. The same type of controller is used in the *y*-axis motion. It is presented as

$$D_V(s) = K_P. \tag{7.3.5}$$

The modified plant TF the in *y*-axis is

$$
\begin{aligned}
G_{IN}(s) &= \frac{G_P(s)}{1+sD_V(s)G_P(s)} \\
&= \frac{k_{hy}(m_1+m_2)s^2 + c_{1y}k_{hy}s + k_{1y}k_{hy}}{(m_1m_2)s^4 + \left(c_{1y}m_2 + K_Pk_{hy}(m_1+m_2)\right)s^3 + \left(k_{1y}m_2 + K_Pc_{1y}k_{hy} + \right)s^2 + k_{hy}K_Pk_{1y}s} \\
&= \frac{3.747s^2 + 14.78s + 1.439\times10^4}{s^4 + 1128s^3 + 8276s^2 + 4.317\times10^6 s}
\end{aligned}
\tag{7.3.6}
$$

where all parameter values in (7.3.6) are presented in Table 7-1 and $K_P = 300$.

The transfer function from the reference input to the postion output is

$$
\begin{aligned}
\frac{\Delta_y(s)}{r_y(s)} &= \frac{D_P(s)G_{IN}(s)}{1+D_P(s)G_{IN}(s)} \\
&= \frac{a_4s^4 + a_3s^3 + a_2s^2 + a_1s + a_0}{d_6s^6 + d_5s^5 + d_4s^4 + d_3s^3 + d_2s^2 + d_1s + d_0}
\end{aligned}
\tag{7.3.7}
$$

where

$$a_4 = ak_{hy}(m_1+m_2) \tag{7.3.8}$$

$$a_3 = ak_{hy}\left(c_{1y} + (m_1+m_2)(z_1+z_2)\right) \tag{7.3.9}$$

$$a_2 = ak_{hy}\left(k_{1y} + c_{1y}(z_1+z_2) + (m_1+m_2)z_1z_2\right) \tag{7.3.10}$$

$$a1 = ak_{hy}\left(k_{1y}(z_1+z_2) + c_{1y}z_1z_2\right) \tag{7.3.11}$$

$$a_0 = ak_{hy}k_{1y}z_1z_2 \tag{7.3.12}$$

and

$$d_6 = m_1m_2 \tag{7.3.13}$$

$$d_5 = k_{hy}(m_1+m_2)K_P + c_{1y}m_2 + m_1m_2p_1 \tag{7.3.14}$$

$$d_4 = k_{hy}\left(c_{1y} + p_1(m_1 + m_2)\right)K_P + ak_{hy}\left(m_1 + m_2\right) + k_{1y}m_2 + c_{1y}m_2 p_1 \quad (7.3.15)$$

$$d_3 = k_{hy}\left(k_{1y} + c_{1y}p_1\right)K_P + ak_{hy}\left(c_{1y} + m_1(z_1 + z_2) + m_2(z_1 + z_2)\right) + k_{1y}m_2 p_1 \quad (7.3.16)$$

$$d_2 = k_{1y}k_{hy}p_1K_P + ak_{hy}\left(k_{1y} + c_{1y}(z_1 + z_2) + z_1z_2(m_1 + m_2)\right) \quad (7.3.17)$$

$$d_1 = ak_{hy}\left(k_{1y}(z_1 + z_2) + c_{1y}z_1z_2\right) \quad (7.3.18)$$

$$d_0 = ak_{1y}k_{hy}z_1z_2 \quad (7.3.19)$$

where all parameter values in (7.3.8)–(7.3.19) are presented in Table 7-1.

To observe how the vibration disturbance influences the output in the *y*-axis, the transfer function $F_{dy}(s)$ from the disturbance to the output $\Delta_y(s)$ is presented as

$$\begin{aligned}
\frac{\Delta_y(s)}{F_{dy}(s)} &= \frac{-G_{22}(s)}{1 + G_P(s)\left(D_p(s) + sD_v(s)\right)} \\
&= \frac{-m_2\left(s^4 + p_1s^3\right)}{\begin{aligned}
&m_1m_2s^6 + \left(c_{1y}m_2 + K_Pk_{hy}\left(m_1 + m_2\right) + m_1m_2p_1\right)s^5 \\
&\quad + \left(k_{1y}m_2 + K_Pc_{1y}k_h + c_{1y}m_2p_1 + k_h\left(a + p_1K_P\right)\left(m_1 + m_2\right)\right)s^4 \\
&\quad + \left(ac_{1y}k_{hy} + k_{1y}m_2p_1 + K_Pk_{hy}\left(k_{1y} + c_{1y}p_1\right) + ak_{hy}\left(m_1 + m_2\right)\left(z_1 + z_2\right)\right)s^3 \\
&\quad + k_{hy}\left(ak_{1y} + K_Pk_{1y}p_1 + ac_{1y}\left(z_1 + z_2\right) + a\left(m_1 + m_2\right)z_1z_2\right)s^2 \\
&\quad + k_{hy}a\left(k_{1y}\left(z_1 + z_2\right) + c_{1y}z_1z_2\right)s + ak_{1y}k_{hy}z_1z_2
\end{aligned}} \\
&= \frac{-m_2\left(s^4 + p_1s^3\right)}{d_6s^6 + d_5s^5 + d_4s^4 + d_3s^3 + d_2s^2 + d_1s + d_0}
\end{aligned} \quad (7.3.20)$$

If $K_P$ = 300 and $K_I$ = 0 with the lead-lag compenstor in (7.1.15),

$$\frac{\Delta_y(s)}{F_{dy}(s)} = \frac{-\left(0.002294s^4 + 9.206s^3\right)}{s^6 + 5142s^5 + 7.302\times10^6 s^4 + 4.051\times10^8 s^3 + 3.659\times10^{10} s^2 + 1.545\times10^{12} s + 1.526\times10^{13}} \tag{7.3.21}$$

where all parameter values in (7.3.21) are presented in Table 7-1. To observe how to the vibration disturbance influence to the output, the frequency response of the $\frac{\Delta_y(s)}{F_{dy}(s)}$ is shown in Fig. 7-17. The dashed line is without the velocity-regulation loop and the solid line is with the velocity regulation loop. Fig.7-18 shows the zoomed frequency responses from 10 Hz to 100 Hz of the transfer function $\frac{\Delta_y(s)}{F_{dy}(s)}$ in Fig. 7-17. The magnitude response is shifted downward effectively from 10 Hz to 100 Hz like in the *x*-axis.

The magnitude difference by the vibration controller is presented in Fig. 7-19. The parabolic reduction ratio through the frequency in the experiment is a little better at lower frequency but is worse at higher frequency. Theoretically, EOMs in the *x*- and *y*-axes motions are identical except the stiffness and the damping coefficient of the optical table. In Fig. 7-19, experimental results in the *y*-axis are much different with the simulation unlike in the *x*-axis. The unmodeled dynamics in the *y*-axis makes this difference. The maglev stage is not located in the center on the top surface of the optical table. The unbalanced vibrating motor is also placed at a corner of the optical table. When the vibration generator is turned on, it shakes the optical table in not only the translational axis but the rotational axis. Although the vibrating motor generates in rolling, pitching, and yawing motions, the rotational motion of the optical table is not considered in the model of the maglev stage with the optical table.

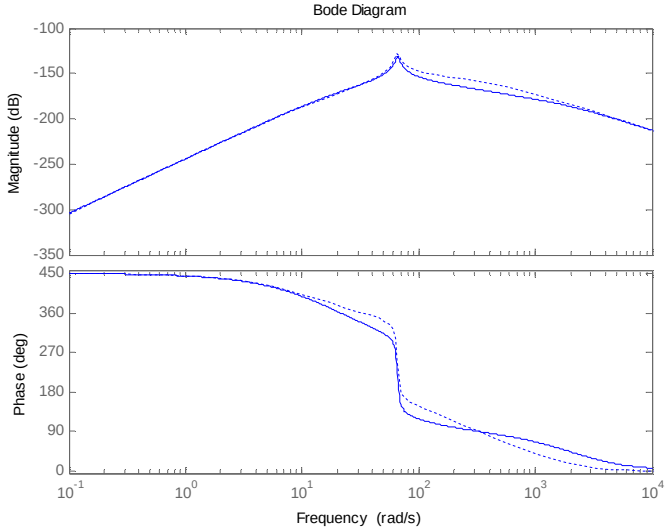


Fig. 7-17. Frequency responses of the transfer function from vibration disturbance to the position in the *y*-axis. The solid line indicates the response with a PID vibration control ($K_P = 300,\ K_I = 0,\ K_D = 0$), and the dotted line indicates that without the vibration control scheme.

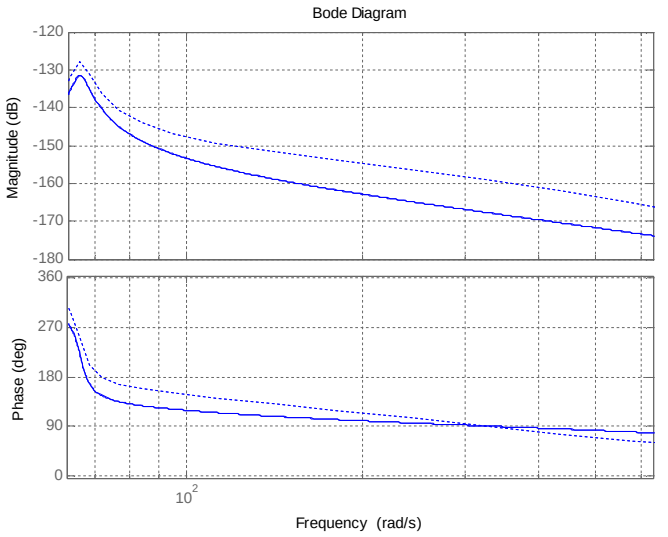


Fig. 7-18. Zoomed frequency responses of the transfer function from vibration disturbance to the position in the *y*-axis from 10 Hz to 100 Hz. The solid line indicates the response with a PID vibration control ($K_P = 300,\ K_I = 0,\ K_D = 0$), and the dotted line indicates that without the vibration control scheme.

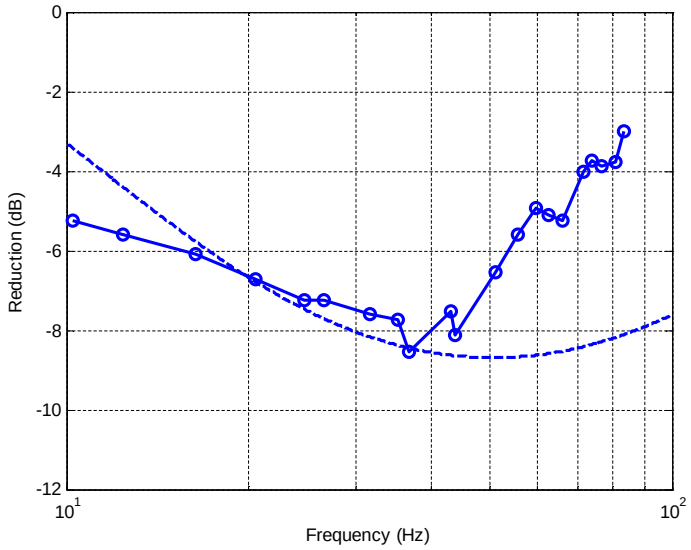


(a)

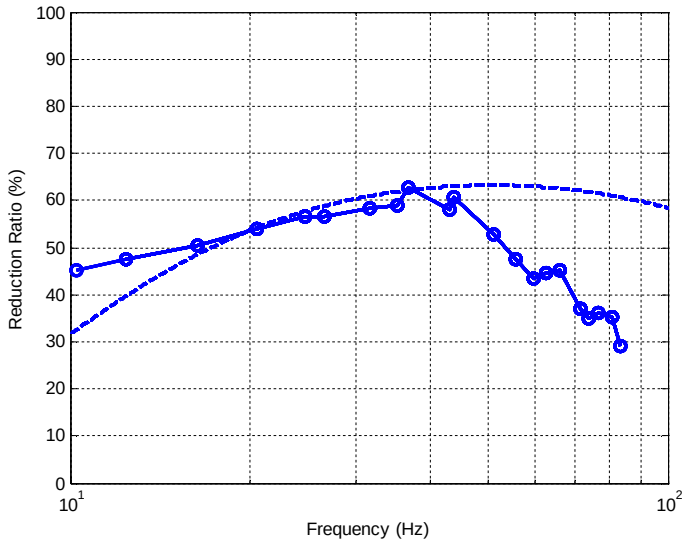


(b)

Fig. 7-19. (a) Magnitude reduction, and (b) reduction percentage of the magnitude in the frequency responses of the transfer function $\frac{\Delta_y(s)}{F_{dy}(s)}$ from 10 Hz to 100 Hz with a PID vibration control ($K_P = 300,\ K_I = 0,\ K_D = 0$). The dashed line indicates the response in the simulation and the circled line indicates the experiment.

For the disturbance reduction, as much as the proportional gain $K_P$ increases in the *y*-axis motion, the reduction ratio also increases. However, if $K_P$ is greater than 600, the system loses the stability in experiment. For both the stability and the reduction performance, the proper value of $K_P$ is 300.

### 7.3.2 Design of an Outer-Loop Controller in the *y*-Axis Motion

The open-loop TF with the velocity-regulating compensator in the *y*-axis is shown in Fig. 7-20. The roll-offs at low frequency, crossover frequency, and the loop shape in the *y*-axis motion is almost same as those in the *x*-axis motion. The crossover frequency is reduced from 688 rad/s to 90.8 rad/s by adding the inner loop compensator. It makes that the rise time and the settling time decrease. The comparison of the step responses between the two systems is shown in Fig. 7-21. Although the rise and the settling time can be reduced by increasing the value *a* of the lead-lag compensator in the outer-loop, if the *a* value is too high, it generates unwanted oscillation as shown in Fig. 7-22.

Therefore, if the increased the rise and settling times are insignificant, the lead-lag compensator does not need to be modified. If we summarize the design of the dual-loop control system, the inner-loop compensator and the outer-loop compensator are exactly the same as those presented in the *x*-axis motion (7.2.28) and (7.2.29).

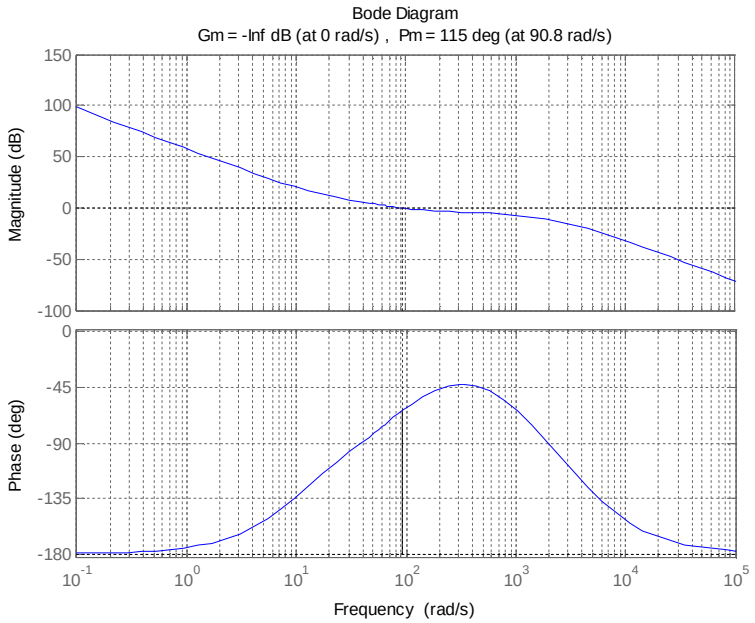


Fig. 7-20. Closed-loop Bode plot for the *y*-axis motion of maglev system with vibration controller.

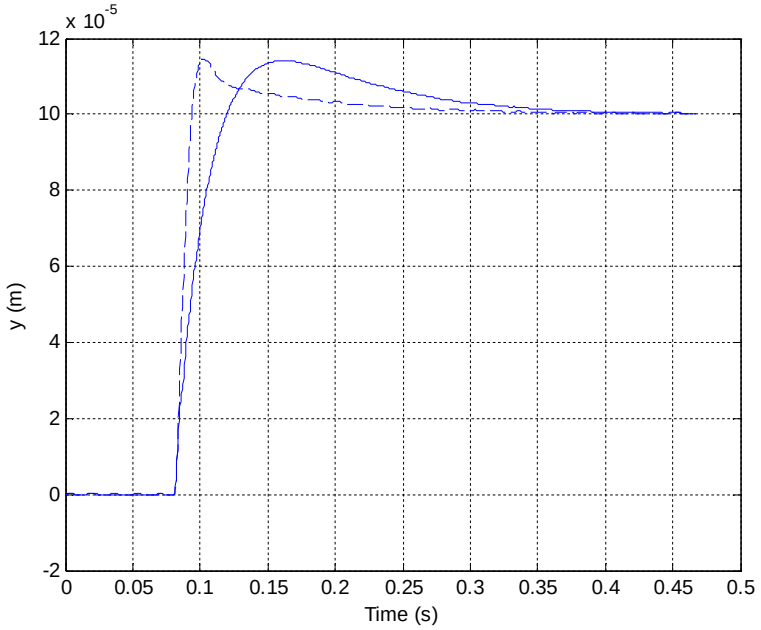


Fig. 7-21. Comparison of step responses (a) with outer- and inner-loop compensators (solid line) and (b) with only outer-loop compensator (dashed line) in experiments.

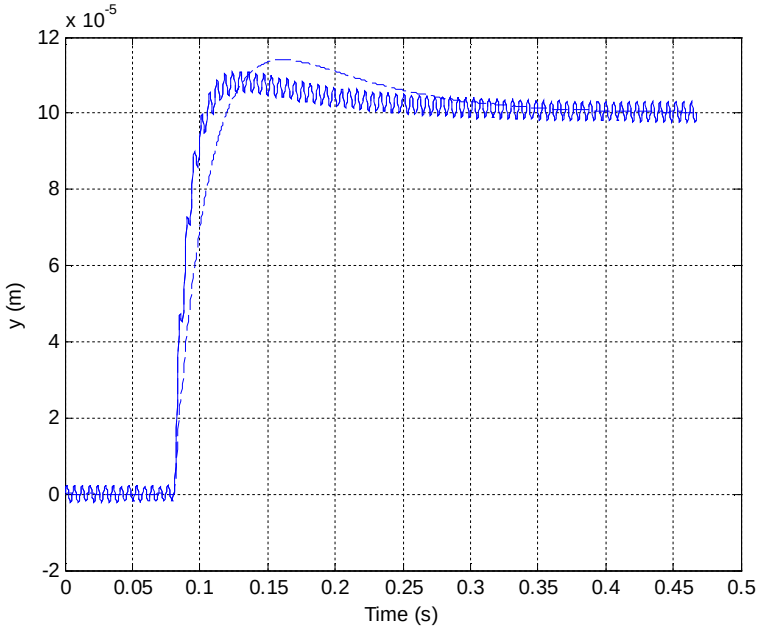


Fig. 7-22. Comparison of step responses (a) with the inner-loop controller and the outer lead-lag compensator with the five times higher *a* value (solid line) and (b) only with the not modified outer lead-lag compensator (dashed line) in experiments.

## 7.4 Vibration Reductions with the Dual-Loop Controller in the *x*- and *y*-Axes Motions

In the experiments, various frequencies are applied and used to obtain the vibration reduction ratio with a dual-loop controller in Figs. 7-10–7-19. The responses of position with the dual-loop controller in the *x*- and *y*-axes are shown in Fig. 7-23–7-28 when vibration disturbances of about 12, 30, 50, 70, and 80 Hz are applied. These five figures demonstrate the effectiveness of the dual-loop control system. The reduction ratio is at least about 30 percent in the *x*- and *y*-axes motions. The maximun reduction ratios are 66.8 and 62.6 percent in the *x*- and *y*-axes.

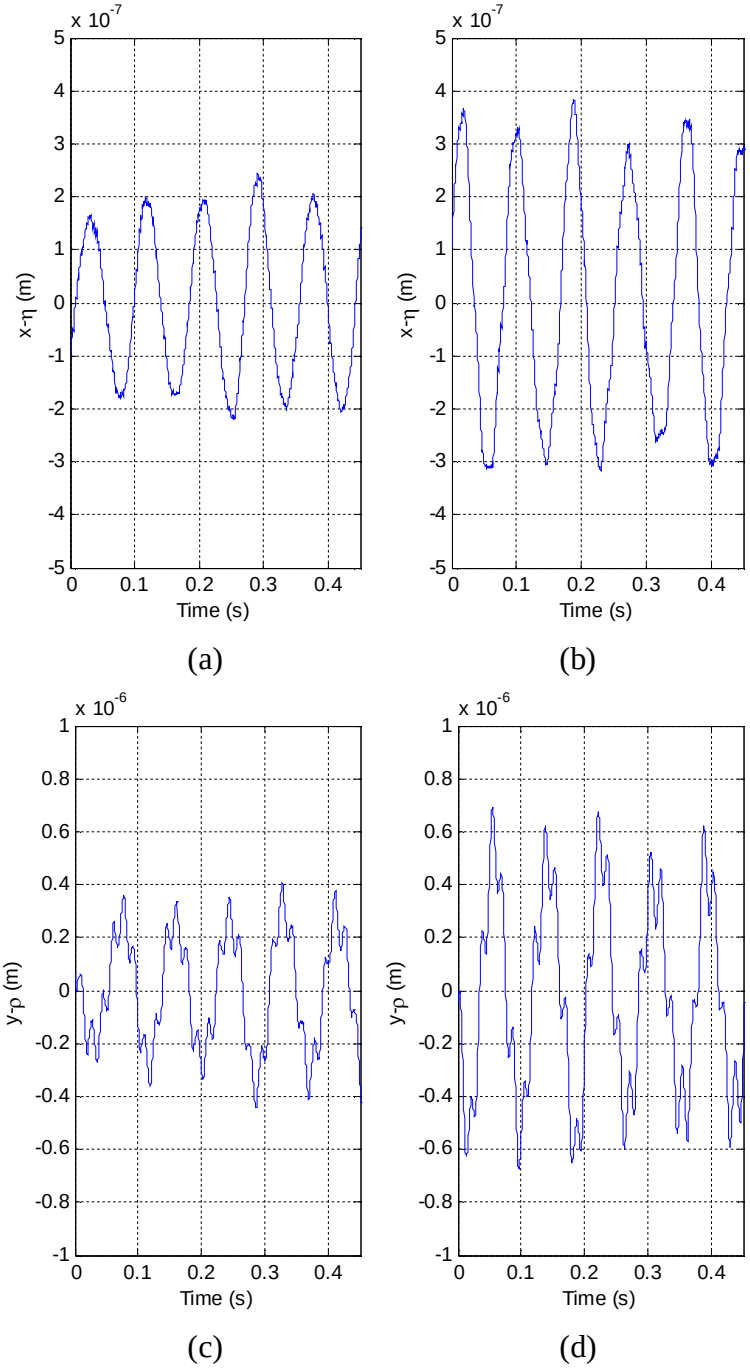


Fig. 7-23. Position regulation at the origin with (a) a dual-loop controller and (b) a lead-lag controller in the *x*-axis, and with (c) a dual-loop controller and (d) a lead-lag controller in the *y*-axis when vibration disturbance of 11.96 Hz is applied.

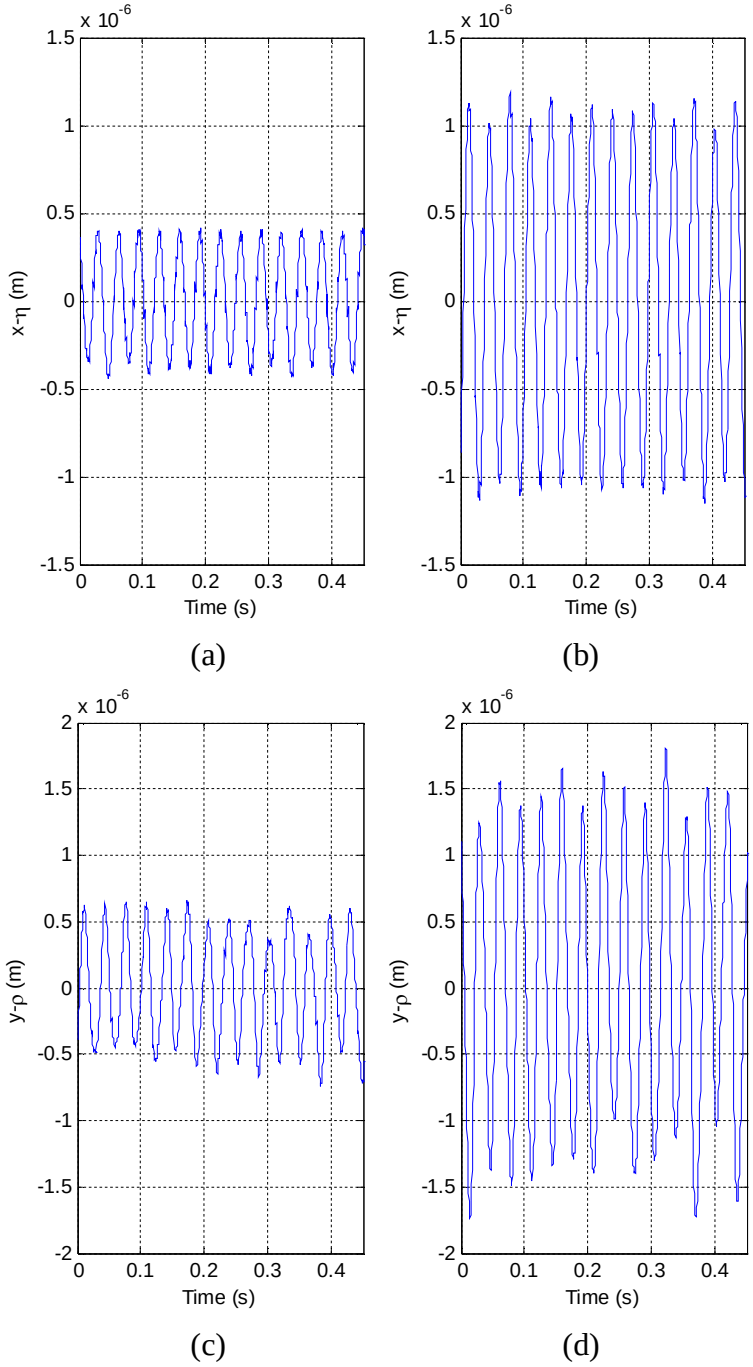


Fig. 7-24. Position regulation at the origin with (a) a dual-loop controller and (b) a lead-lag controller in the *x*-axis, and with (c) a dual-loop controller and (d) a lead-lag controller in the *y*-axis when vibration disturbance of 30.86 Hz is applied.

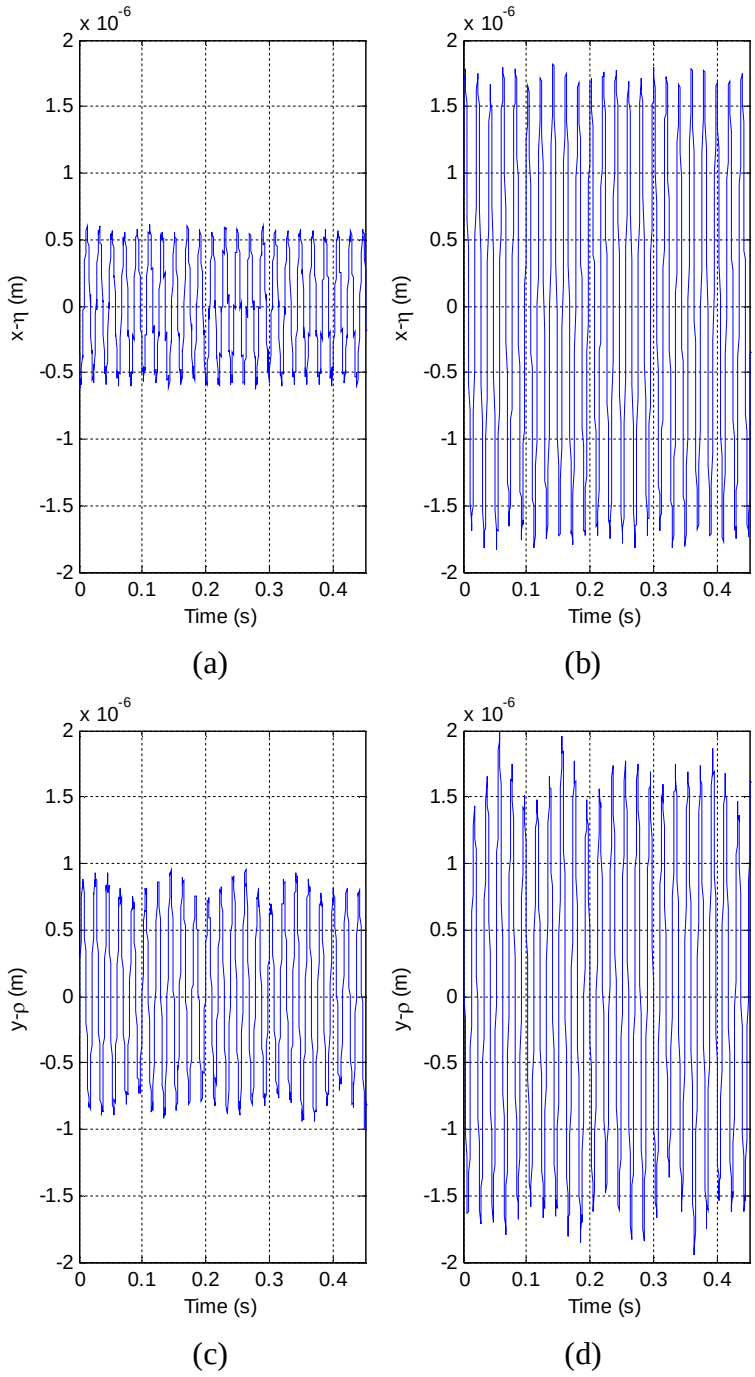


Fig. 7-25. Position regulation at the origin with (a) a dual-loop controller and (b) a lead-lag controller in the *x*-axis, and with (c) a dual-loop controller and (d) a lead-lag controller in the *y*-axis when vibration disturbance of 50 Hz is applied.

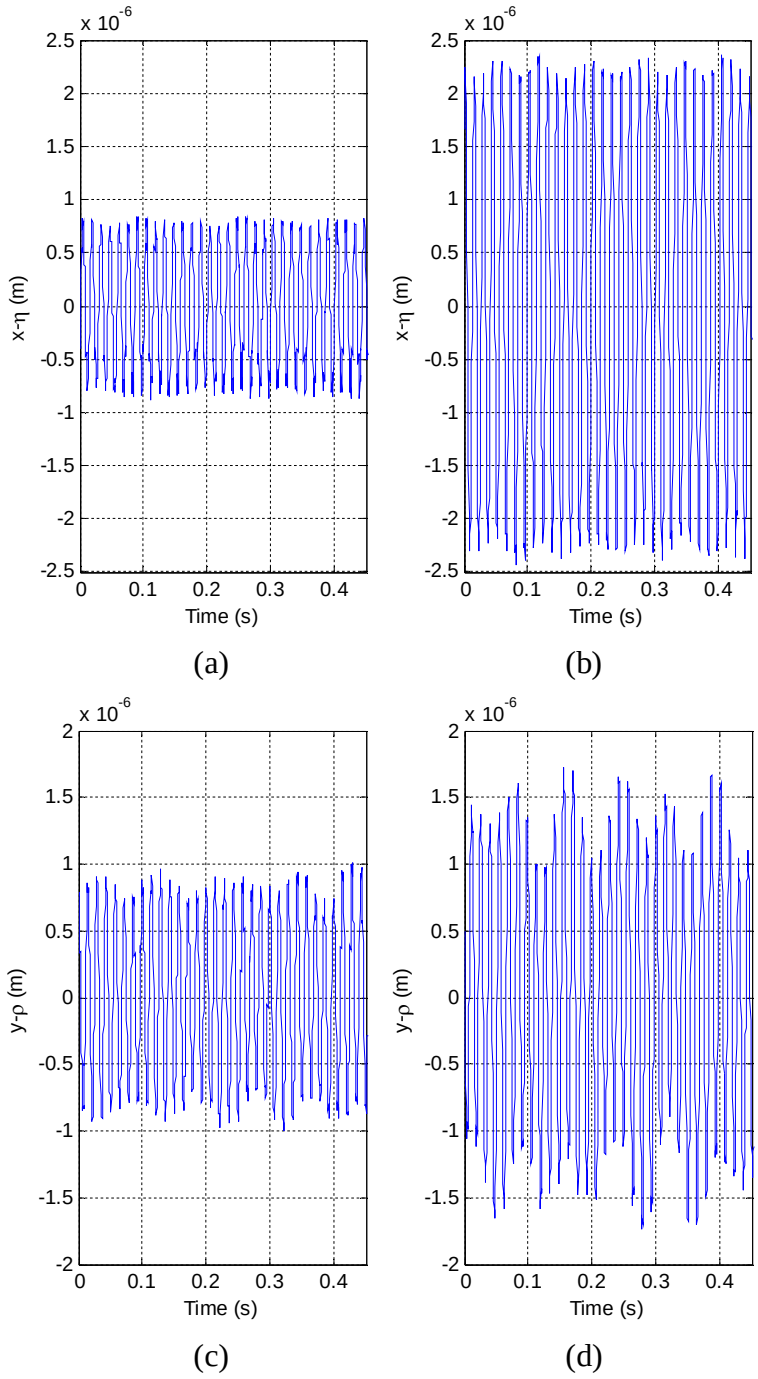


Fig. 7-26. Position regulation at the origin with (a) a dual-loop controller and (b) a lead-lag controller in the *x*-axis, and with (c) a dual-loop controller and (d) a lead-lag controller in the *y*-axis when vibration disturbance of 68 Hz is applied.

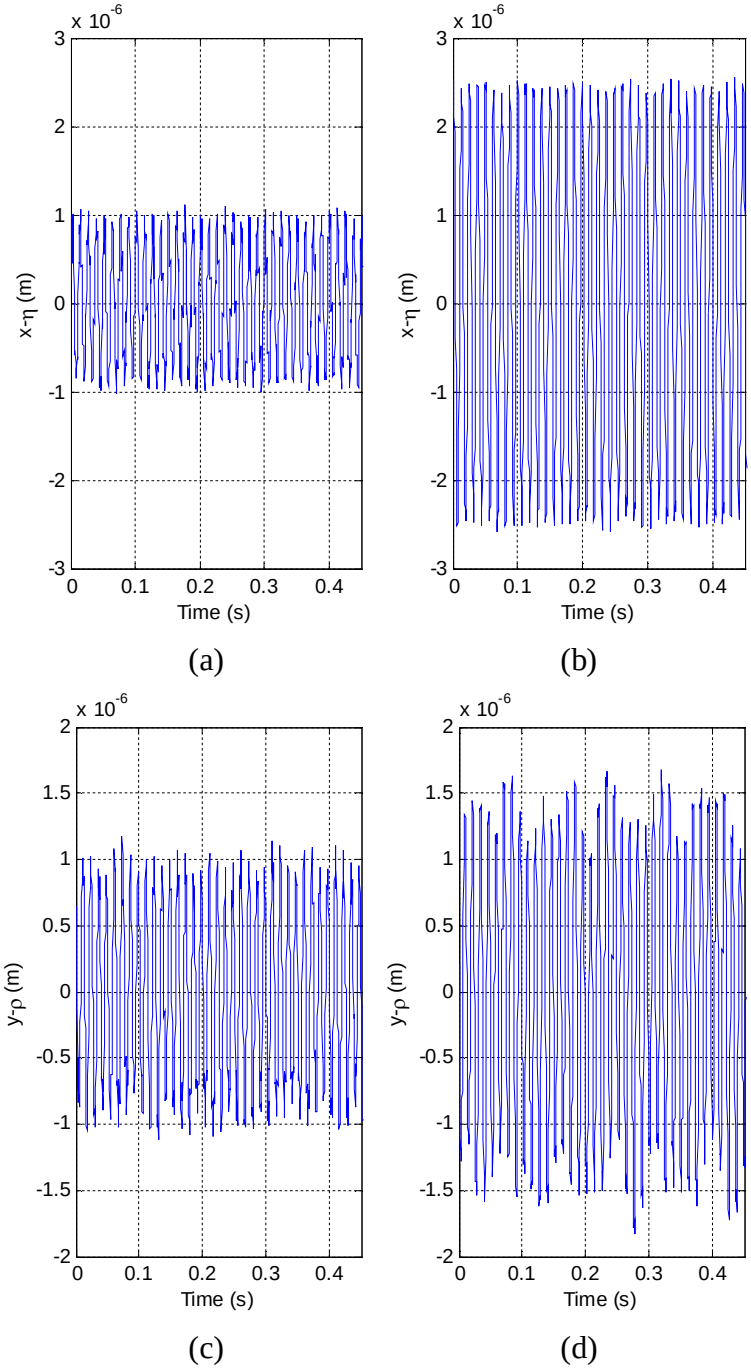


Fig. 7-27. Position regulation at the origin with (a) a dual-loop controller and (b) a lead-lag controller in the *x*-axis, and with (c) a dual-loop controller and (d) a lead-lag controller in the *y*-axis when vibration disturbance of 80.65 Hz is applied.

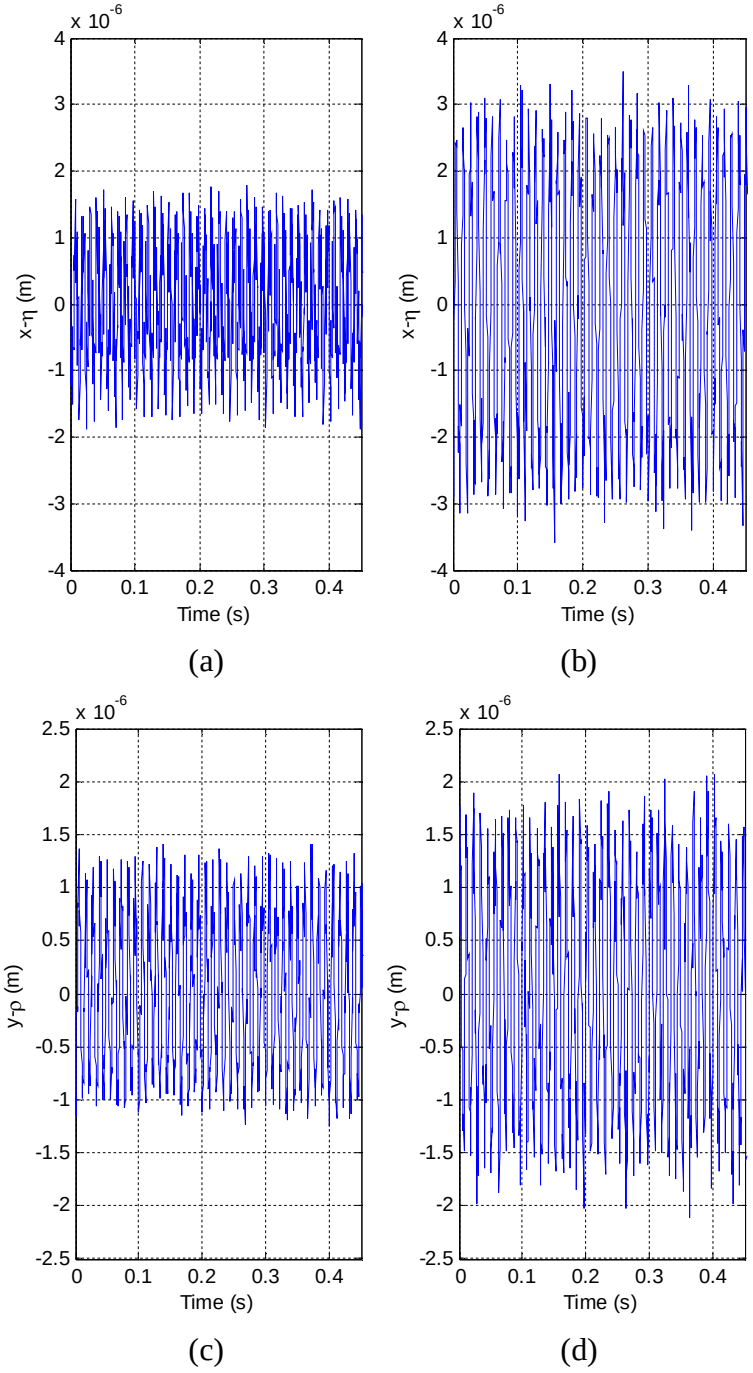


Fig. 7-28. Position regulation at the origin with (a) a dual-loop controller and (b) a lead-lag controller in the *x*-axis, and with (c) a dual-loop controller and (d) a lead-lag controller in the *y*-axis when vibration disturbance of 92.59 Hz is applied.

# CHAPTER VIII

# SIX-AXIS MOTION OF THE MAGLEV SYSTEM WITH VIBRATION CONTROL

## 8.1 Vibration Disturbances in Six-Axis Motions

The disturbance of the unbalanced vibrating motor acts not in a single axis independently but in all six axes. The motor shaft is aligned to the *y*-axis, and the unbalanced mass rotates about the *y*-axis. The vibrating motor is designed to generate vibrations in the *x*- and *z*-axes. However, the unbalanced mass is tilted and not perpendicular to the *y*-axis. Therefore, the unbalanced motor also generates vibrations in the *y*-axis. In addition, the vibrating motor is placed at a corner of the optical table. If the vibrating motor shakes the optical table at a corner, the optical table oscillates in not only translational but rotational motions. The disturbance forces $\left(F_{dx}, F_{dy}, F_{dz}\right)$ and torques $\left(\tau_{d\psi}, \tau_{d\theta}, \tau_{d\phi}\right)$ are generated by the vibrating motor as shown in Fig. 8-1. These disturbance torques generate rotational vibration disturbances on the optical table. In future work, additional modeling of the optical table with pneumatic isolators is required in rotational motion for the rotational vibration control. In addition, the rotational stiffness $\left(k_{1\psi}, k_{1\theta}, k_{1\phi}\right)$ and damping coefficients $\left(c_{1\psi}, c_{1\theta}, c_{1\phi}\right)$ should be determined.

However, the additional rotational modeling of the optical table is not considered and these rotational coefficients are not determined in this dissertation. Vibration controllers are designed for only translational vibrations in this work. Nevertheless, the vibration reduction effectiveness in six-axis motion with the translational vibration controllers is discussed in this chapter.

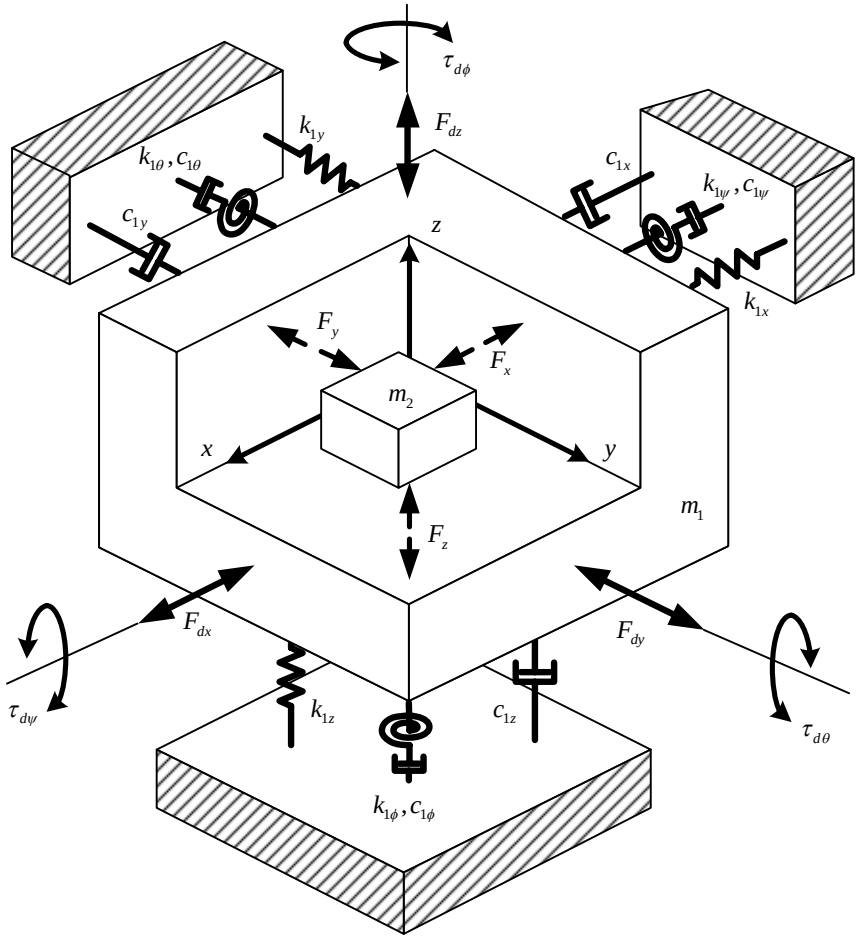


Fig. 8-1. The vibration disturbances generated by the disturbance forces and torques with the vibrating motor.

The angular position controllers for $\psi$-, $\theta$-, and $\phi$-axes regulate rotational angles. These controllers designed by Verma [38] are

$$D_{\psi}(s) = D_{\theta}(s) = 295.658\frac{(s+57.47)(s+6.271)}{s(s+2103)} \tag{8.1.1}$$

$$D_{\phi}(s) = 1804.1\frac{(s+116.6)(s+10.91)}{s(s+4014)}. \tag{8.1.2}$$

In addition, positioning and tracking performance with the vibration control is also evaluated with step responses.

## 8.2 Step-Response Analysis with Vibration Disturbances in Six-Axis Motions

Fig. 8-2 shows the differences of step responses between with vibration control and without vibration control in the *x*-, *y*-, and *z*-axes when the vibration disturbance of 21.19 Hz is applied. As explained in designing the vibration control systems in the previous chapters, the step responses with vibration control have longer rise and settling times, but the overshoot is less than that without vibration control. The vibration reduction ratios in the *x*-, *y*-, and *z*-axes are 55.2%, 58.7%, and 29.9% in Fig. 8-2. These ratios are very similar with the values in Figs. 7-11, 7-19, and 5-11.

The trajectories of the platen in the *x*-*y* plane show that the platen with the vibration control exhibits more accurate position regulation at the origin before departing to the other place in Fig. 8-3(a). During the travel from the origin to the other place with vibration control, some oscillations are observed but it does not leave the dotted area in Fig. 8-3. However, the trajectories of the platen without the vibration control are more

perturbed before leaving the origin and go cross the dotted zone during the travel in Fig. 8-3(b). Therefore, the performances in positioning and tracking with vibration control are better than that without vibration control except the rise and settling times.

The step inputs in the translational motion induce the rotational motion because of the coupling between axes. The angular responses are observed in Fig. 8-4. The magnitudes of the oscillations in angular positions with vibration control are tiny smaller those that without vibration control. The reduction ratios in rotational angles $(\psi, \theta, \phi)$ are 14.1%, 24.3%, and 9.4% in steady state, respectively. These reduction ratios are insignificant compared to translational motion. Nonetheless, the vibration controllers are effective in not only translational but rotational motions. However, the peak value with vibration control in the pitching motion $(\theta)$ is larger than that without vibration control. It is not a matter of the performance of the vibration control system but a matter of the time that a step input starts.

When the vibration disturbance of 45.45 Hz is applied, the differences of step responses between with vibration control and without vibration control in *x*-, *y*-, and *z*-axes are shown Fig. 8-5. As in Fig. 8-2, the step responses with vibration control have longer rise and settling times, but the overshoot is less than that without vibration control. The vibration reduction ratios in the *x*-, *y*-, and *z*-axes are 68.4%, 59.8%, and 47.1%, respectively. The vibration reduction schemes with vibration disturbance of 45.45 Hz work better than with vibration disturbance of 21.19 Hz because the reduction ratio is various through the frequency as shown in Figs. 5-11, 7-10, and 7-19.

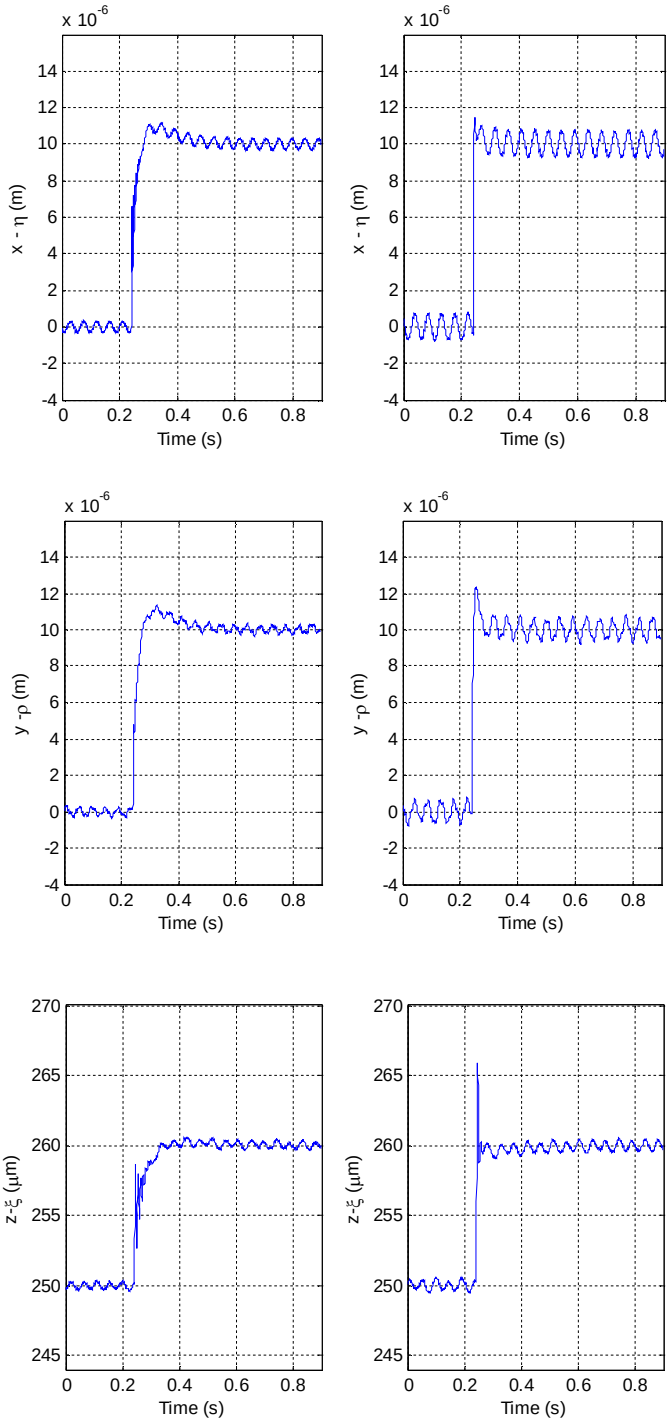


Fig. 8-2. The step responses of the maglev stage (a) with and (b) without vibration control in the *x*-, *y*- and *z*-axes when the vibration disturbance of 21.19 Hz is applied.

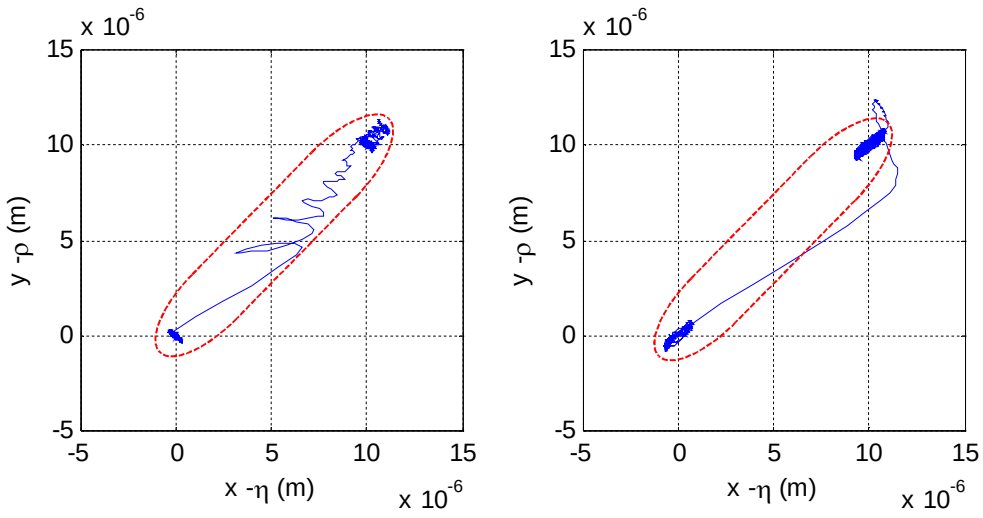


(a) (b)

Fig. 8-3. The trajectories of the platen (a) with and (b) without vibration control in the *x*-*y* plane when the vibration disturbance of 21.19 Hz is applied.

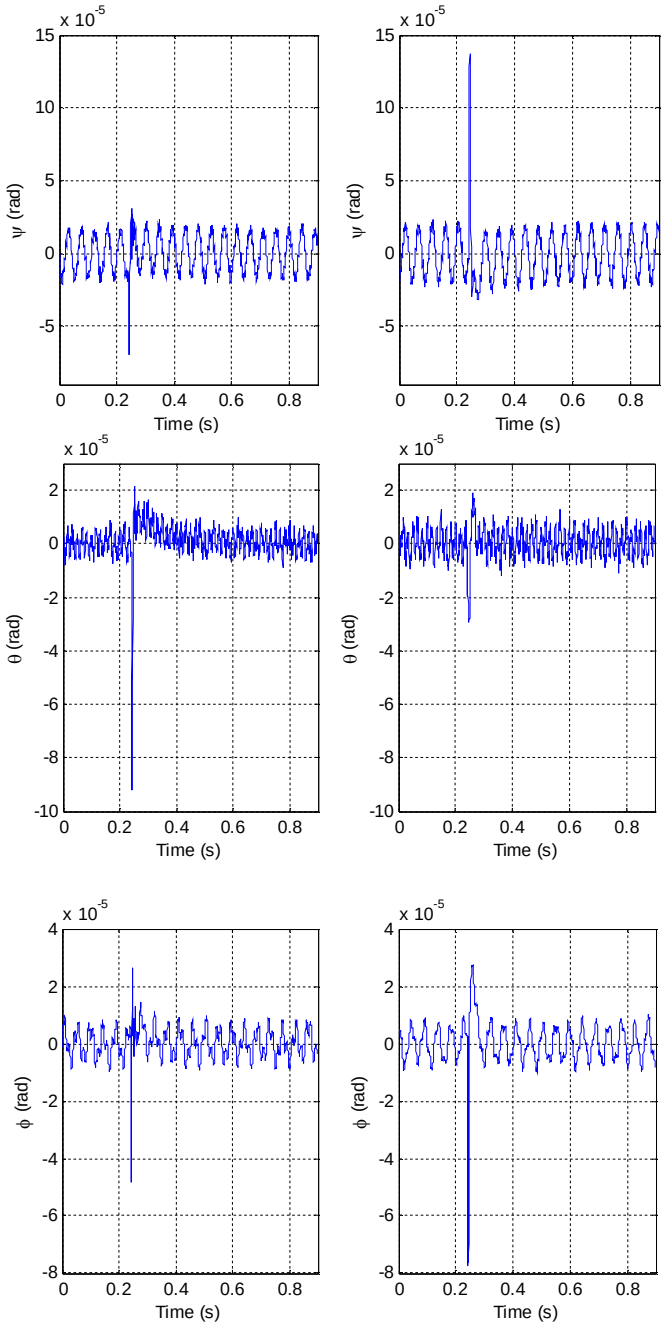


Fig. 8-4. The angular responses of the maglev stage (a) with and (b) without vibration control with step responses in the *x*-, *y*- and *z*-axes when the vibration disturbance of 21.19 Hz is applied.

The trajectories of the platen in the *x*-*y* plane shows that the platen with vibration control exhibits much more accurate position regulation at the origin before departing to the other position when larger vibration disturbance is applied in Fig. 8-6. During the travel from the origin to another location with vibration control, wandering motions are observed. The dotted area in Fig. 8-6 indicates the wandering range of the platen during the travel. The wandering range with vibration control is much smaller than that without vibration control. Hence, positioning and tracking accuracies with vibration control are better than those without vibration control except the rise and settling times.

Fig. 8-7 shows the angular responses that are induced by the step inputs in the translational motions. The magnitudes of the oscillations in angular positions with vibration control are smaller than without vibration control. The reduction ratios in rotational angles $(\psi, \theta, \phi)$ are 17.5%, 40.7%, and 3.7% in steady state, respectively. The reduction ratio in pitching angle $(\theta)$ increases significantly with vibration disturbance of 45.45 Hz but the reduction ratio in yawing $(\phi)$ motion decreases a lot. These rotational vibration reduction is caused by combining the translational vibration controllers and the angular position controllers. The coupling motions between axes are reduced the translational vibration controllers when the angular position controller regulate the angles. The vibration control schemes with vibration disturbance of 45.45 Hz are still effective in not only translational but rotational motions.

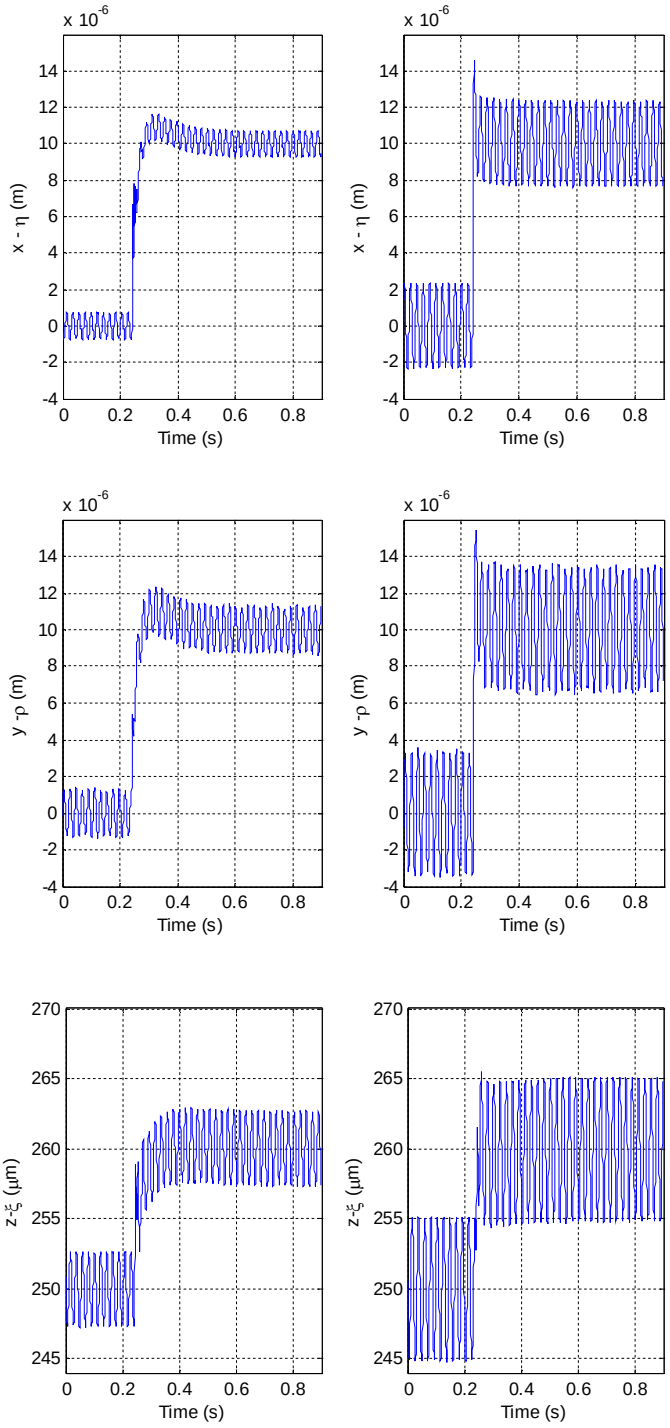


Fig. 8-5. The step responses of the maglev stage (a) with and (b) without vibration control in the *x*-, *y*- and *z*-axes when the vibration disturbance of 45.45 Hz is applied.

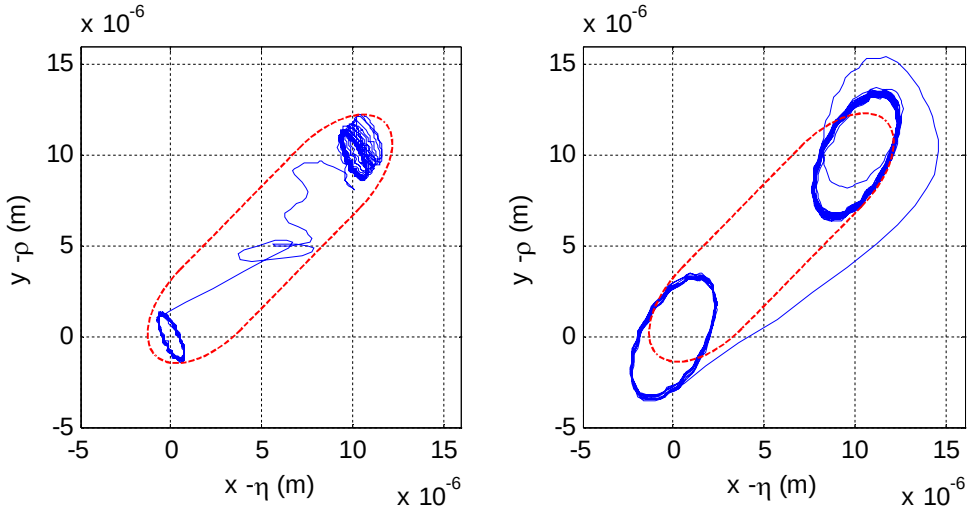


(a) (b)

Fig. 8-6. The trajectories of the platen (a) with and (b) without vibration control in the *x*-*y* plane when the vibration disturbance of 45.45 Hz is applied.

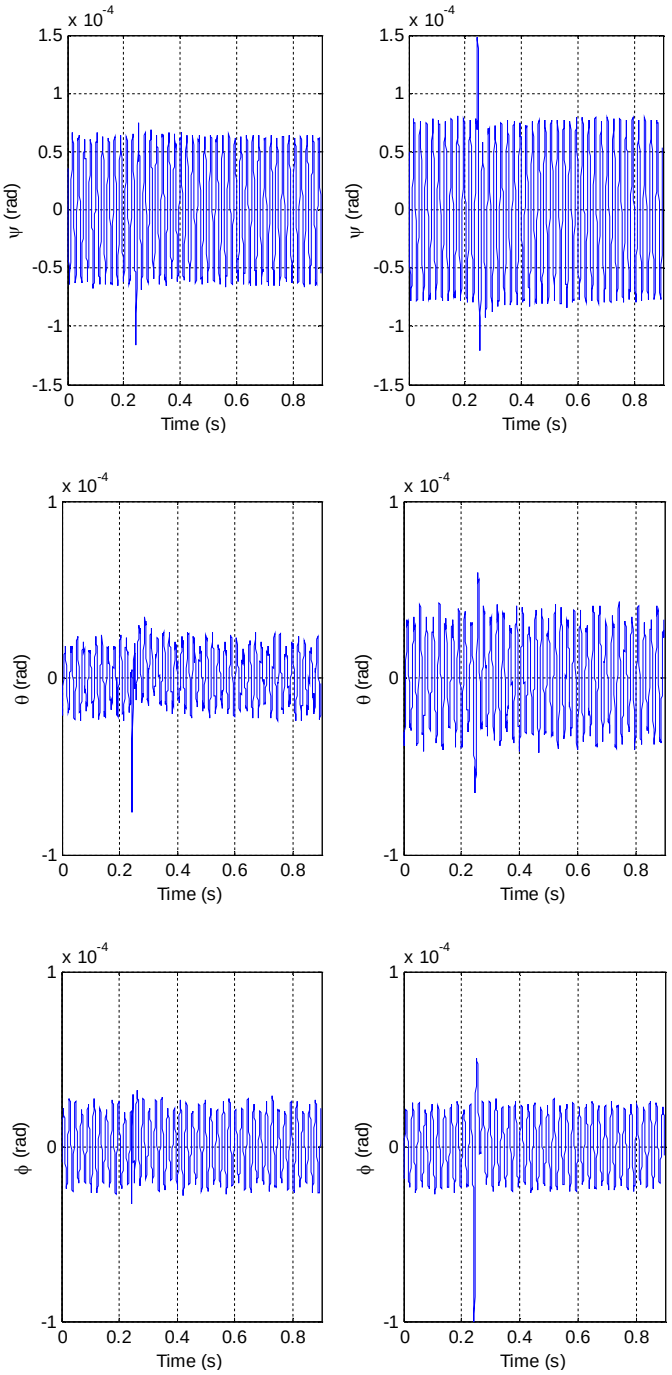


Fig. 8-7. The angular responses of the maglev stage (a) with and (b) without vibration control with step responses in the *x*-, *y*- and *z*-axes when the vibration disturbance of 45.45 Hz is applied.

# CHAPTER IX

# CONCLUSIONS AND SUGGESTIONS OF FUTURE WORK

## 9.1 Summary

The maglev positioning system is an excellent candidate for the precision positioning that has six DOFs, nanoscale resolution without any friction, hysteresis, creep and backlash. Because the maglev technology does not require any lubricants or generate wear particles, it is suitable for clean-room or vacuum environments. In addition, advanced instruments or high-precision machines used the nanotechnology are vibration-sensitive and must be operated in a stable environment. The vibration disturbances are major obstacles in nanotechnology. Therefore, vibration control systems are required.

By the present day, maglev systems have been developed for both servo applications to control movement and suspension purposes to reject vibration disturbances. This dissertation demonstrated that the maglev stage has capabilities to control movements and to reject vibration simultaneously.

The previously developed linearized model did not include the nonlinearity of the rotational motion and the differential kinematics. To design advanced control schemes, a more accurate model of the plant is required. Therefore, the full 6-DOF nonlinear

dynamic and differential kinematic equations were derived. These equations consider full rotational motion with kinematic equations and coupling among rotational motion.

To design robust control schemes in the MIMO system, the derived nonlinear EOMs and the magnetic forces are linearized and the state-space representation is introduced. An LQG/LTR controller is designed to reject vibration disturbance in a MIMO system.

Since the vibrations of the stationary coils on the optical table affect the magnetic force acting on the platen, adding the model of the optical table is required in the enhanced dynamic model. The optical table with pneumatic passive isolators is assumed as a mass-spring-damper system. The impulse response of the optical table was measured and the stiffness and the damping coefficient were determined. The enhanced model was validated by the comparing the simulation and experimental results.

To generate the vibration disturbance that has a specific frequency component, an unbalanced mass vibration generator was developed. By changing the eccentricity of the unbalanced mass and the input voltage in the motor, the vibration disturbance can be generated at a specific frequency.

The enhanced nonlinear EOMs and the magnetic forces were linearized. The magnetic stiffness term is added in the linearized model of vertical motion. For velocity feedback control, velocity in vertical motion is obtained by differentiating the noisy position signal from the capacitance probes. A software low-pass filter is designed to prevent amplification of the high frequency noise of a position signal by differentiation.

However, in lateral motion, the laser interferometry provides less noisy and high-resolution measurements of the position and velocity.

The dual-loop control system with velocity feedback makes it possible that the maglev system tracks positioning commands and rejects vibration disturbance simultaneously. The design procedures of the dual-loop control system are introduced in vertical and horizontal motions. The inner-loop compensator regulating the velocity is developed for vibration rejection, and the outer-loop compensator is designed for positioning of the platen.

The dynamic models of the maglev stage in the *x*- and *y*-axes are identical except for the stiffnesses and the damping coefficients. The same type of controller was applied in both the *x*- and *y*-axes motions.

The stability analysis to determine the control parameters was carried out. To analyze the effect of the vibration rejection of the inner-loop compensator, the frequency analysis of the transfer function between the vibration disturbance and position has shown the magnitude changes depend on the controller gains in specific frequency range.

The dual-loop controllers designed independently for the *x*-, *y*-, and *z*-axes were applied in the six-axis motion. The step responses in the *x*-, *y*-, and *z*-axes were shown to evaluate the performance of vibration reduction as well as positioning and tracking accuracy.

## 9.2 Conclusions

The full 6-DOF nonlinear dynamic and differential kinematic equations with the coupling among rotational motions were derived and linearized to design an LQG/LTR robust controller. The crossover frequency of the singular values of the open loop with the LQG/LTR was about 100 Hz. The controller attenuates a vibration disturbance of 15.5 Hz to 10% and 80% in the horizontal and vertical motions in simulation.

To model the maglev stage with the optical table including the pneumatic passive vibration isolators, the simulation results of the model were well matched with the experimental results. However, unmodeled motions were observed in experiments, but these were negligible in this work.

The dual-loop controllers with velocity feedback were verified in a vibration disturbance environment. The inner-loop controller initially suggested to be a PID controller was finalized as a proportional controller. In experiments, the inner-loop controllers with $K_P = 300$ and $K_P = 100$ in horizontal and vertical motions attenuated vibration disturbances by up to 65% and 45% in horizontal and vertical motions. However, the performance of the vibration controller varied through the frequency ranges.

In six-axis motion, the performance of vibration reduction of the dual-loop controllers applied in the translational motion was almost the same as that in the single axis motion. The vibration reduction in rotational motions was insignificant unlike that in translation motions. However, the vibration controllers were effective in not only

translation but rotational motions. The reduction ratios with vibration control when the vibration disturbance of 45.45 Hz was applied were 17.5%, 40.7%, and 3.7% in rolling, pitching, and yawing motions, respectively.

In step responses, the vibration control schemes reduced the wandering range in the travel from the origin to another location. Positioning and tracking accuracies with vibration controller were better than those without vibration controller.

In summary, these dual-loop control schemes with velocity feedback control improved the nanopositioning capability and vibration disturbance rejection in a maglev system.

## 9.3 Suggestions of Future Work

Although I tried to obtain the best possible performance in vibration rejections, there are certain issues that could not be addressed due to limitations in resources or time.

- At present, an LQG/LTR controller was not implemented and tested in the real system, yet. The estimated states are divergent because the Kalman-filter gain matrix is not appropriate in the real system. The noise covariance matrices should be chosen in proper way in the future.
- For rotational vibration control, if additional modeling of the optical table with pneumatic isolators in rotational motion was developed and the rotational stiffness and damping coefficients were determined, rotational dual-loop controllers could be designed to attenuate the rotational vibration disturbances.

The dual-loop controllers can be designed by the similar ways in translational motion.

- Acceleration feedback control has advantage to disturbance rejection if reliable acceleration signal could be obtain. Appropriate accelerometers with better resolution and measurement range provide the reliable acceleration signal. The acceleration signals from two accelerometers makes possible the maglev stage be applied to more various applications such as a microgravity vibration isolator in the space. The rotation and translation of platen can be controlled in not only the stationary frame but the body-fixed frame.

## REFERENCES

[1] G. Binnig, H. Rohrer, C. Gerber, and E. Weibel, "Tunneling through a controllable vacuum gap," *Applied Physics Letters*, vol. 40, no. 2, pp. 178–180, Jan. 1982.

[2] G. Binnig, C. F. Quate, and C. Gerber, "Atomic force microscope," *Physical Review Letters*, vol. 56, no. 9, pp. 930–933, Mar. 1986.

[3] Griffin Motion LLC, *XY Stage*, [Online]. Available: http://www.griffinmotion.com/product-selector.asp?series=CXY [Accessed: August 24, 2011].

[4] C. G. Masi, "Industrial machining embraces nanopositioning," *Control Engineering*, vol. 55, no. 11, pp. 38–40, Nov. 2008.

[5] Physik Instrumente L.P., *P-915K high-dynamics xy piezo scanner*, [Online]. Available: http://www.physikinstrumente.com/en/products/prspecs.php?sortnr=201680 [Accessed: August 24, 2011].

[6] W. Xu and T. King, "Flexure hinges for piezoactuator displacement amplifiers: flexibility, accuracy, and stress considerations," *Precision Engineering*, vol. 19, no. 1, pp. 4–10, Jul. 1996.

[7] H.-C. Yeh, W.-T. Ni, and S.-S. Pan, "Digital closed-loop nanopositioning using rectilinear flexure stage and laser interferometry," *Control Engineering Practice*, vol. 13, no. 5, pp. 559–566, May 2005.

[8] Physik Instrumente L.P., *P-734 XY Piezo Scanner*, [Online]. Available: http://www.physikinstrumente.com/en/products/prdetail.php?sortnr=201300 [Accessed: August 24, 2011].

[9] Physik Instrumente L.P., *Parallel and Serial Kinematics / Metrology*, [Online]. Available: http://www.physikinstrumente.com/en/products/prdetail.php?sortnr=400800.20 [Accessed: August 24, 2011].

[10] C. Moon, S. Lee, and J. K. Chung, "A new fast inchworm type actuator with the robust I/Q heterodyne interferometer feedback," *Mechatronics*, vol. 16, no. 2, pp. 105–110, Mar. 2006.

[11] Physik Instrumente L.P., "Hexapod & tripod precision parallel kinematic micropositioners," *PI Piezo / Micro- / Nanopositioning Catalog*, Karlsruhe, Germany: Physik Instrumente, 2008.

[12] Physik Instrumente L.P., *M-850 Hexapod 6-Axis Positioning System*, [Online]. Available: http://www.physikinstrumente.com/en/products/prdetail.php?sortnr=700800 [Accessed: August 24, 2011].

[13] S. Thiery, M. Kunze, A. Karimi, A. Curnier, and R. Longchamp, "Friction modeling of a high-precision positioning system," in *Proc. 24th Anuual American Control Conference*, Minneapolis, Minnesota, Jun. 2006, pp. 1863–1867.

[14] B. Armstrong-Helouvry, P. Dupont, and C. C. De Wit, “A survey of models, analysis tools and compensation methods for the control of machines with friction,” *Automatica*, vol. 30, no. 7, pp. 1083–1138, Jul. 1994.

[15] A. H. Slocum and D. B. Eisenhaure, “Design considerations for ultra-precision magnetic bearing supported slides,” in *Proc. NASA Magnetic Suspension Technology Conference*, Hampton, Virginia, Feb. 2–4 Feb. 1988, pp. 10–18.

[16] D. L. Trumper, “Magnetic suspension techniques for precision motion control,” Ph.D. Dissertation, Dept. of Electrical Engineering and Computer Science, Massachusetts Institute of Technology, Cambridge, MA, Sep. 1990.

[17] M. E. Williams, D. L. Trumper, and R. Hocken, “Magnetic bearing stage for photolithography,” *CIRP Annals - Manufacturing Technology*, vol. 42, no. 1, pp. 607–610, Jan. 1993.

[18] W.-J. Kim, “High-precision planar magnetic levitation,” Ph.D. Dissertation, Dept. of Electrical Engineering and Computer Science, Massachusetts Institute of Technology, Cambridge, MA, Nov. 1997.

[19] E. E. Ungar, J. A. Zapfe, and J. D. Kemp, “Predicting footfall-induced vibrations of floors,” *Sound and Vibration*, vol. 38, no. 11, pp. 16–22, Nov. 2004.

[20] C. L. Zhang, D. Q. Mei, and Z. C. Chen, “Active vibration isolation of a micro-manufacturing platform based on a neural network,” *Journal of Materials Processing Technology*, vol. 129, no. 1–3, pp. 634–639, Oct. 2002.

[21] E. E. Ungar and C. G. Gordon, “Vibration challenges in microelectronics manufacturing,” *Shock and Vibration Bulletin*, vol. 53, no. 1, pp. 51–58, May 1983.

[22] C. G. Gordon and E. E. Ungar, “Vibration criteria for microelectronics manufacturing equipment,” in *Proc. International Conference on Noise Control Engineering*, Edinburgh, UK, Jul. 1983, pp. 487–490.

[23] C. G. Gordon, “Generic vibration criteria for vibration-sensitive equipment,” in *Proc. Optomechanical Engineering and Vibration Control*, Denver, CO, 21 Jul. 1999, pp. 22–33.

[24] A. Soueid, H. Amick, and T. Zsirai, “Addressing the environmental challenges of the NIST advanced measurement laboratory,” in *Proc. SPIE Conference: Buildings for Nanoscale Research and Beyond*, San Diego, CA, Jul. 2005, pp. 169–181.

[25] E. I. Rivin, “Vibration isolation of precision equipment,” *Precision Engineering*, vol. 17, no. 1, pp. 41–56, Jan. 1995.

[26] H. Amick and A. Bayat, “Meeting the vibration challenges of next-generation photolithography tools,” in *Proc. ESTECH 2001, 47th Annual Technical Meeting, IEST*, Phoenix, Arizona, Apr. 2001, pp. 1–10.

[27] H. Amick, M. Gendreau, and C. G. Gordon, “Facility vibration issues for nanotechnology research,” in *Proc. Symposium on Nano Device Technology*, National Chiao-Tung University, Hsinchu, Taiwan, May 2002, pp. 1–4.

[28] A. M. Fraumeni, P. Heiland, and N. Judell, “Generic vibration criteria for nanotechnology experiments,” in *Proc. SPIE Conference: Buildings for Nanoscale Research and Beyond*, San Diego, CA, Jul. 2005, pp. 232–245.

[29] C. Erin, B. Wilson, and J. Zapfe, “An improved model of a pneumatic vibration isolator: theory and experiment,” *Journal of Sound and Vibration*, vol. 218, no. 1, pp. 81–101, Nov. 1998.

[30] Newport Corporation, *Optics Based Research—The Need for Vibration Isolated Rigid Support Structures*, [Online]. Available: http://www.newport.com/store/product.aspx?id=139774&lang=1033 [Accessed: August 24, 2011].

[31] G. Quaglia and M. Sorli, “Air suspension dimensionless analysis and design procedure,” *Vehicle System Dynamics: International Journal of Vehicle Mechanics and Mobility*, vol. 35, no. 6, pp. 443–475, Jun. 2001.

[32] P.-C. Chen and M.-C. Shih, “Modeling and robust active control of a pneumatic vibration isolator,” *Journal of Vibration and Control*, vol. 13, no. 11, pp. 1553–1571, Nov. 2007.

[33] K. Mizutani, Y. Fujita, and H. Ohmori, “Hybrid control system for microvibration isolation,” in *Proc. 4th International Workshop on Advanced Motion Control*, Mie University, Tsu-City, Japan, Mar. 1996, pp. 577–582.

[34] A. El-Sinawi and R. Kashani, “Active isolation using a Kalman estimator–based controller,” *Journal of Vibration and Control*, vol. 7, no. 8, pp. 1163–1173, Nov. 2001.

[35] J. Shaw, “Active vibration isolation by adaptive control,” in *Proc 1999 IEEE International Conference on Control Applications*, Hawaii, Aug. 1999, pp. 1509–1514.

[36] TMC Corperation, *TMC's Electro-Damp® II Active Pneumatic Vibration Damping System*, [Online]. Available: http://www.techmfg.com/products/advanced/electrodamp.htm [Accessed: August 24, 2011].

[37] K. Nagaya and M. Ishikawa, “A noncontact permanent magnet levitation table with electromagnetic control and its vibration isolation method using direct disturbance cancellation combining optimal regulators,” *IEEE Transactions on Magnetics*, vol. 31, no. 1, pp. 885–896, Jan. 1995.

[38] S. Verma, “Development of novel high-performance six-axis magnetically levitated instruments for nanoscale applications,” Ph.D. Dissertation, Dept. of Mechanical Engineering, Texas A&M University, College Station, TX, Aug. 2005.

[39] H. Shakir, “Control strategies and motion planning for nanopositioning applications with multi-axis magnetic-levitation instruments,” Ph.D. Dissertation, Department of Mechanical Engineering, Texas A&M University, College Station, TX, May 2007.

[40] M. Athans, “A tutorial on the LQG/LTR method,” in *Proc. 5$^{th}$ American Control Conference*, Seattle, WA, Jun. 1986, pp. 1289–1296.

[41] B. Kulcsar, "LQG/LTR controllers design for an aircraft model," *Periodica Polytechnica Ser. Transportation Engineering*, vol. 28, no. 1, pp. 131–142, Nov. 2000.

[42] J. Doyle and G. Stein, "Multivariable feedback design: concepts for a classical/modern synthesis," *IEEE Transactions on Automatic Control*, vol. 26, no. 1, pp. 4–16, Feb. 1981.

[43] G. Stein and M. Athans, "The LQG/LTR procedure for multivariable feedback control design," *IEEE Transactions on Automatic Control*, vol. 32, no. 2, pp. 105–114, Feb. 1987.

[44] W. H. Pfeil, M. Athans, and H. A. Spang, "Multi-variable control of the GE T700 engine using the LQG/LTR design methodology," in *Proc. 5th Annual American Control Conference*, Seattle, WA, 18-20 Jun. 1986, pp. 1297–1312.

[45] A. A. Rodriguez and M. Athans, "Multivariable control of a twin lift helicopter system using the LQG/LTR design methodology," in *Proc. 5th Annual American Control Conference*, Seattle, WA, 18-20 Jun. 1986, pp. 1325–1332.

[46] R. J. Martin, L. Valavani, and M. Athans, "Multivariable control of a submersible using the LQG/LTR design methodology," in *Proc. 5th Annual American Control Conference*, Seattle, WA, 18-20 Jun. 1986, pp. 1313–1324.

[47] J. L. Shearer, "Study of pneumatic processes in the continuous control of motion with compressed air–I & II," *Transactions of the ASME*, vol. 78, no. 3, pp. 233–249, Feb. 1956.

[48] C. M. Harris and C. E. Crede, *Shock and Vibration Handbook*, New York: McGraw-Hill, 1961.

[49] D. B. DeBra and J. Bryan, "Design of laminar flow restrictors for damping pneumatic vibration isolators," *CIRP Annals - Manufacturing Technology*, vol. 33, no. 1, pp. 351–356, Jan. 1984.

[50] I. Bar-Kana, R. Fischl, and P. Kalata, "Direct position plus velocity feedback control of large flexible space structures," *IEEE Transactions on Automatic Control*, vol. 36, no. 10, pp. 1186–1188, Oct. 1991.

[51] M. Balas, "Feedback control of flexible systems," *IEEE Transactions on Automatic Control*, vol. 23, no. 4, pp. 673–679, Aug. 1978.

[52] P. B. Schmidt and R. D. Lorenz, "Design principles and implementation of acceleration feedback to improve performance of DC drives," *IEEE Transactions on Industry Applications*, vol. 28, no. 3, pp. 594–599, May 1992.

[53] B. C. Kuo, *Automatic Control Systems*, 7th ed., pp. 337, New York: John Wiley & Sons, Inc., 1995.

# APPENDIX A

# MATLAB® CODES

## A.1 To Design an LQG/LTR Controller

```
m=0.267;
Ix=340.37e-6;
Iy=Ix;
Iz=653.61e-6;
g=9.81;
I1=Ix;I2=Iy;I3=Iz;
I=diag([I1,I2,I3]);

l1=0.050595;
l2=l1*0.5;
l3=l1*cos(30/180*pi);

a2=4.7418e4;
a1=-8.7132e2;
a0=6.7712;

b2=1.3031e4;
b1=-2.7161e2;
b0=2.2050;

c30=cos(pi*30/180);
s30=sin(pi*30/180);

% reference Input
z0=250e-6
y0=0;
x0=0;

kv=a2*z0^2+a1*z0+a0;
kh=b2*x0^2+b1*x0+b0;
kvh=[kv,kv,kv,kh,kh,kh];
```

```
Kvh=diag(kvh);

psi0=10e-6;
theta0=10e-6;
phi0=10e-6;

DCM0=[     1,-phi0,theta0;
       phi0,    1, -psi0;
    -theta0, psi0,     1]

B0=[1/I1, sin(psi0)*tan(theta0)/I2, cos(psi0)*tan(theta0)/I3;
      0,            cos(psi0)/I2,           -sin(psi0)/I3;
      0, sin(psi0)/cos(theta0)/I2, cos(psi0)/cos(theta0)/I3]

kv=a2*z0^2+a1*z0+z0;
kh=b2*x0^2+b1*x0+b0;

M=m*eye(3);
M_inv=inv(M);
I=[Ix 0 0;0 Iy 0;0 0 Iz];
I_inv=inv(I);

Tfm=[0,  0,  0,   0, c30, -c30;
   0,  0,  0,  -1, s30,  s30;
   1,  1,  1,   0,   0,    0;
   0, l3,-l3,   0,   0,    0;
 -l1, l2, l2,   0,   0,    0;
   0,  0,  0, -l1, -l1,  -l1]

Tfmi=Tfm
Tfmi=Tfm

T_f=Tfmi(1:3,:);
T_m=Tfmi(4:6,:);

B1=1/m*DCM0;
B2=B0;

%-------------------------------------------------------------
% States:
%  x, y, z, dz,dy,dz,   psi,        theta, phi, dpsi,dtheta, dphi
%-------------------------------------------------------------

A=[
```

```
   0, 0, 0, 1, 0, 0,      0,       0,       0, 0, 0, 0; % x
   0, 0, 0, 0, 1, 0,      0,       0,       0, 0, 0, 0; % y
   0, 0, 0, 0, 0, 1,      0,       0,       0, 0, 0, 0; % z
   0, 0, 0, 0, 0, 0,      0,       g,  g*psi0, 0, 0, 0; % dx
   0, 0, 0, 0, 0, 0,     -g,       0,g*theta0, 0, 0, 0; % dy
   0, 0, 0, 0, 0, 0,-g*psi0,-g*theta0,       0, 0, 0, 0; % dz
   0, 0, 0, 0, 0, 0,      0,       0,       0, 1, 0, 0; % psi
   0, 0, 0, 0, 0, 0,      0,       0,       0, 0, 1, 0; % theta
   0, 0, 0, 0, 0, 0,      0,       0,       0, 0, 0, 1; % phi
   0, 0, 0, 0, 0, 0,      0,       0,       0, 0, 0, 0; % dpsi
   0, 0, 0, 0, 0, 0,      0,       0,       0, 0, 0, 0; % dtheta
   0, 0, 0, 0, 0, 0,      0,       0,       0, 0, 0, 0];% dphi

B=[zeros(3,6);
   B1, zeros(3,3);
   zeros(3,6);
   zeros(3,3), B2];
C=eye(12);
D=zeros(12,6);

C=[eye(3), zeros(3,9);
    zeros(3,6),eye(3,3),zeros(3,3)]
D=zeros(6,6)

rank(ctrb(A,B))
rank(obsv(A,C))

qp=5e4*ones(1,3)
qv=1e-2*ones(1,3)
qt=1e3*ones(1,3)
qw=1e-1*ones(1,3)

qf=[qp qv qt qw]
Qf=diag(qf)


mu=1.5e3;

[Hft,Sf,ef]=lqr(A',C',Qf,eye(6)/mu)
H=Hft'
w=logspace(-2,4,1000)

figure(1)
sigma(A,H,C, zeros(6,6),w)
```

```
grid on
% hold on

rho=1e-11
Q=C'*C
R=eye(6)*rho

[G,S,e]=lqr(A,B,Q,R)

Gs=ss(A,B,C,zeros(size(C,1),size(B,2)))

Ks=ss((A-B*G-H*C),H,G,zeros(size(G,1),size(H,2)))

% GKs=series(Ks,Gs)
GKs=Gs*Ks
figure(2)
sigma(GKs,w)
grid on
```

## A.2 To Design a Low-Pass Filter

```
[zx,px,kx] = cheby1(3,0.01,400/2.5e3,'low');
[sos,g] = zp2sos(zx,px,kx);        % Convert to SOS form
Hd = dfilt.df2tsos(sos,g);         % Create a dfilt object

figure(1)
h = fvtool(Hd)                     % Plot magnitude response
set(h,'Analysis','freq')
[b,a]= cheby1(3,0.01,400/2.5e3,'low')

Ts=1/5e3;
H=tf(b,a,Ts)

w=logspace(2,4.210,1000);

figure(2)
g=bodeplot(H,w)
setoptions(g,'FreqUnits','Hz','PhaseVisible','on')
grid on
```

# APPENDIX B

## SIMULINK BLOCK DIAGRAMS

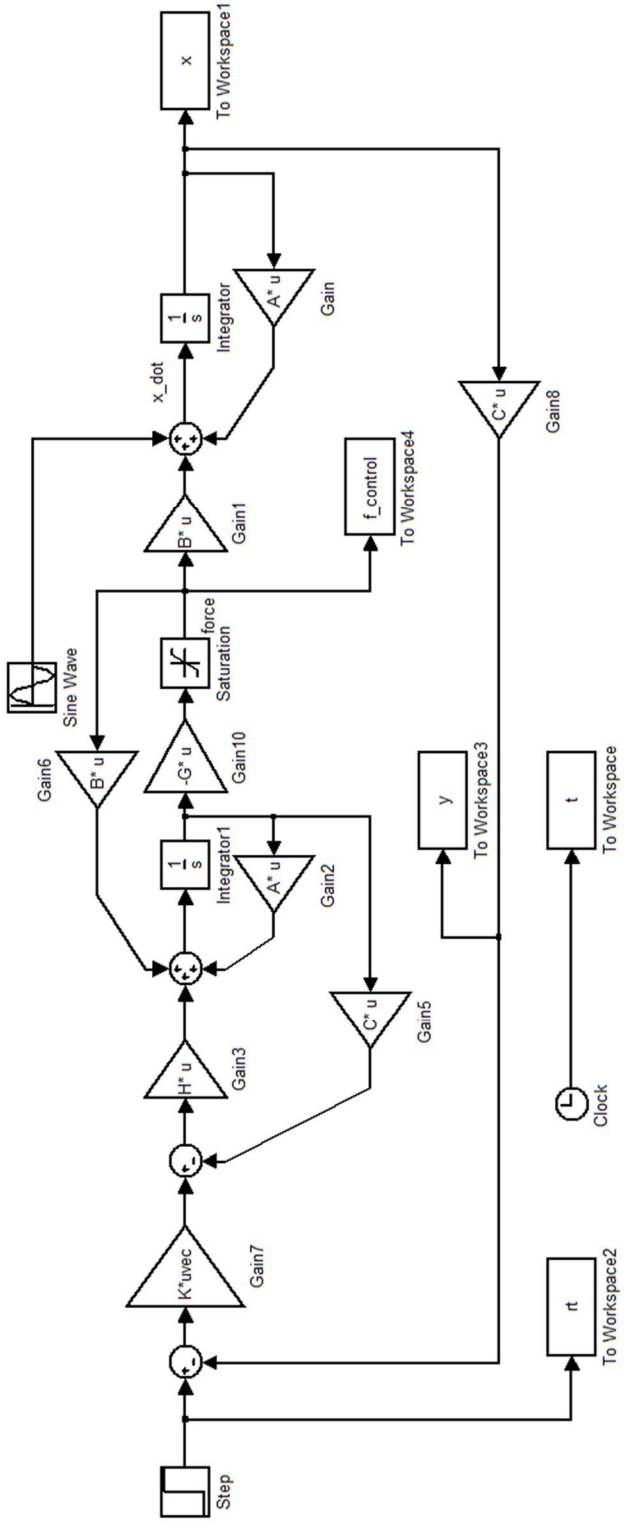


Fig. B-1. Simulink block diagram for LQG/LTR control

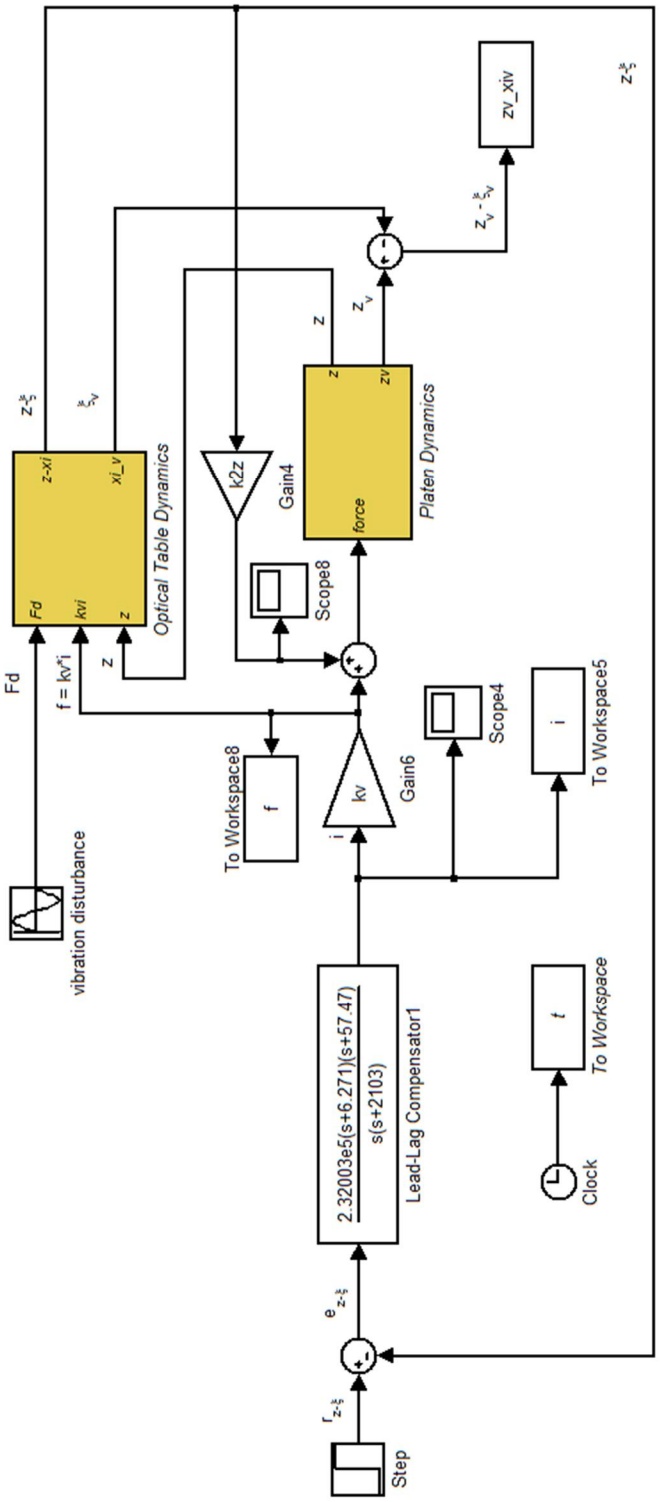


Fig. B-2. Simulink block diagram of the maglev stage model with the optical table in vertical motion

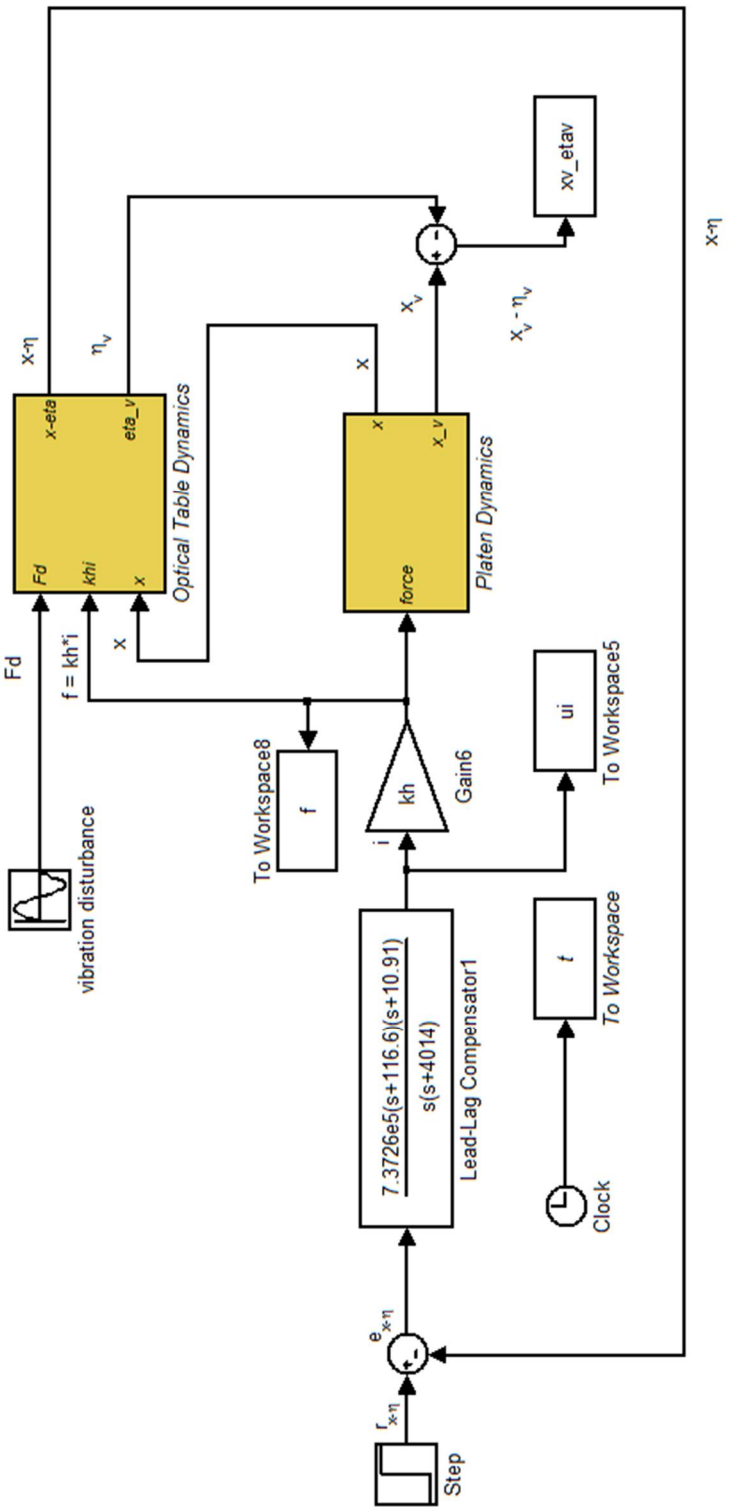


Fig. B-3. Simulink block diagram of the maglev stage model with the optical table in *x*-axis motion

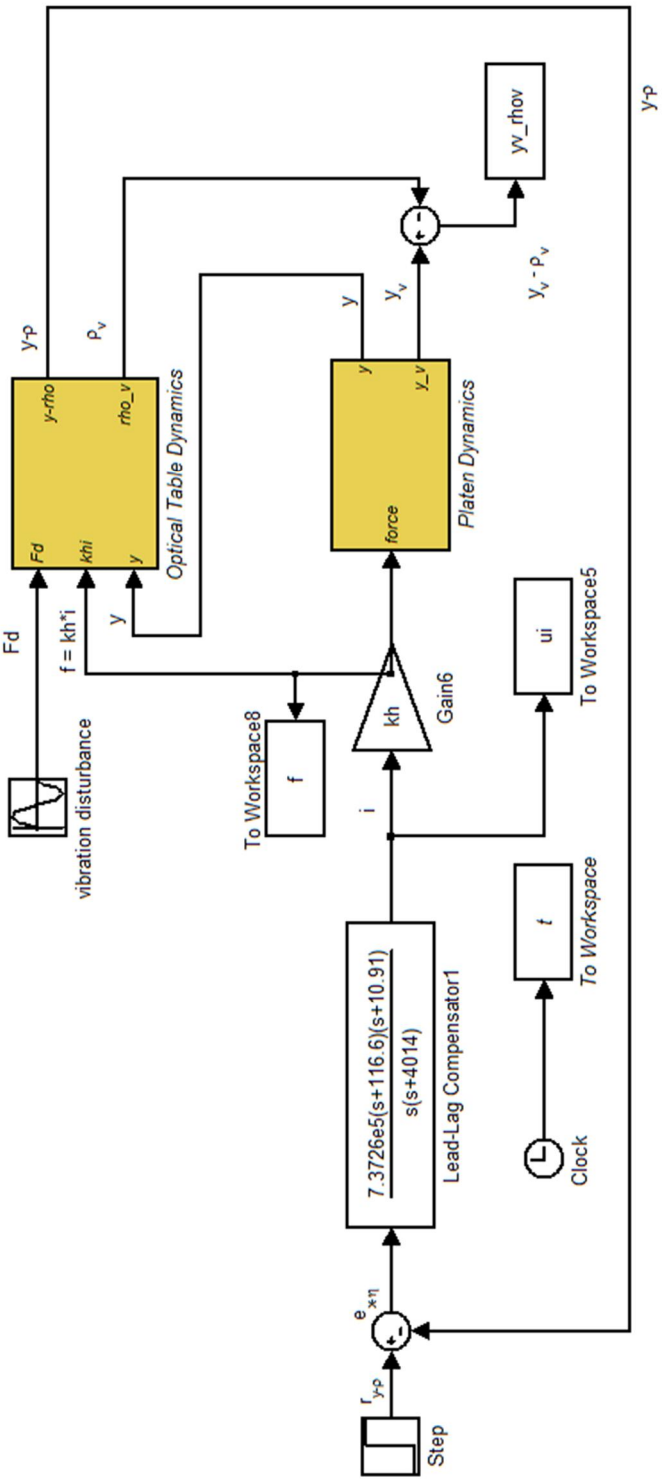


Fig. B-4. Simulink block diagram of the maglev stage model with the optical table in *y*-axis motion

# APPENDIX C

# C CODES

## C.1 For Model Validation in the *x*-, *y*-, and *z*-Axes

```
void c_int01()
{
                    unsigned long D1reading;
                    long ADreading, ADreading1, ADreading2, ADreadingA,
ADreadingB,ADreadingC,ADreadingD;
                    long vel_x_platen1,vel_x_platen2;
                    int i;
                    float z_mea,Kp,Ki,Kpz,Kiz;

/*----------------------------------*/
                    tr_low();

                    /**(unsigned int *)DA_FIFO_D1=(((unsigned int)((0.0)*6553.4))
<<16) & 0xffff0000 ;   /* timer test of interrupt */
                    *(unsigned long int *)0xb0300003=0x0041;
                    raw_x_pos  = (*(long int *)0xb0300048 << 16) & 0xffff0000;
                    raw_y1_pos = (*(long int *)0xb0310048 << 16) & 0xffff0000;
                    raw_y2_pos = (*(long int *)0xb0320048 << 16) & 0xffff0000;

                    raw_x_vel  = (*(long int *)0xb030004e << 16) & 0xffff0000;
   raw_y1_vel = (*(long int *)0xb031004e << 16) & 0xffff0000;
   raw_y2_vel = (*(long int *)0xb032004e << 16) & 0xffff0000;

                    tr_high();
                    raw_x_pos  |= ((*(long int *)0xb0300048 >> 16) & 0x0000ffff);
                    raw_y1_pos |= ((*(long int *)0xb0310048 >> 16) & 0x0000ffff);
                    raw_y2_pos |= ((*(long int *)0xb0320048 >> 16) & 0x0000ffff);

   raw_x_vel  |= ((*(long int *)0xb030004e >> 16) & 0x0000ffff);
   raw_y1_vel |= ((*(long int *)0xb031004e >> 16) & 0x0000ffff);
   raw_y2_vel |= ((*(long int *)0xb032004e >> 16) & 0x0000ffff);
```

```
                x_pos=raw_x_pos*6.1815119987e-10;       /* METERS-BIT approx
0.625 nm */
                y1_pos=raw_y1_pos*6.1815119987e-10;
                y2_pos=raw_y2_pos*6.1815119987e-10;

                x_vel = raw_x_vel * 3.77292037e-7;              /*
lamda/(F*2^22*100ns)= 3.77292037e-7, */

                y1_vel= raw_y1_vel* 3.77292037e-7;      /* where lamda is a laser
wavelength (632.991 nm) */
   y2_vel= raw_y2_vel* 3.77292037e-7;       /* F = 4 for plane mirror optics */



                /* ------------------------------*/

                tr_low();

/*-------------------------------------------------*/
                ADreading=*(unsigned long int *)AD_FIFO_A1;

                ADreading1 = ADreading & 0x0000ffff; /* Channel A1 */   /*
capacitance probe 1 */
                ADreading2 = ADreading & 0xffff0000;    /* Channel A2 */   /*
acceleration x in the platen */
                ADreading2 = (ADreading2 >> 16);

                if(ADreading1 & 0x8000) ADreading1 = ADreading1 | 0xffff0000;
   z_pos1=ADreading1*7.629627369e-9+250e-6;

/*-------------------------------------------------*/
                ADreading=*(unsigned long int *)AD_FIFO_B1;

                ADreading1 = ADreading & 0x0000ffff; /* Channel B1 */   /*
capacitance probe 2 */
                ADreading2 = ADreading & 0xffff0000;    /* Channel B2 */   /*
acceleration y in the platen */
                ADreading2 = (ADreading2 >> 16);

                if(ADreading1 & 0x8000) ADreading1 = ADreading1 | 0xffff0000;
   z_pos2=ADreading1*7.629627369e-9+250e-6;
```

```
/*-------------------------------------------------*/
                    ADreading=*(unsigned long int *)AD_FIFO_C1;

                    ADreading1 = ADreading & 0x0000ffff; /* Channel C1 */   /*
capacitance probe 3 */
                    ADreading2 = ADreading & 0xffff0000;    /* Channel C2 */   /*
acceleration z in the platen */
                    ADreading2 = (ADreading2 >> 16);

                    if(ADreading1 & 0x8000) ADreading1 = ADreading1 | 0xffff0000;
   z_pos3=ADreading1*7.629627369e-9+250e-6;

/*-------------------------------------------------*/
                    ADreading=*(unsigned long int *)AD_FIFO_D1;

                    ADreading1 = ADreading & 0x0000ffff; /* Channel D1 */   /*
acceleration x in the OPT table */
                    ADreading2 = ADreading & 0xffff0000;    /* Channel D2 */   /*
acceleration z in the OPT table */
                    ADreading2 = (ADreading2 >> 16);

                    /*****************************************/

                    /*NEW STAGE (begin)*/
                    /*L1 = y2_pos, L2 = y1_pos, L3 = x_pos*/

                    xr = -(      0*y2_pos + 0.5774*y1_pos - 0.5774*x_pos);
                    yr = -(-0.6667*y2_pos + 0.3333*y1_pos + 0.3333*x_pos);
                    hr =  ( 6.5928*y2_pos + 6.5928*y1_pos + 6.5928*x_pos);

                    zr =      0.333333*z_pos1 + 0.333333*z_pos2 + 0.333333*z_pos3;
                    sr = 1000*(               0*z_pos1 + 0.0400*z_pos2 - 0.0400*z_pos3);
                    tr = 1000*(-0.0462*z_pos1 + 0.0231*z_pos2 + 0.0231*z_pos3);

                    xr_dot = -(      0*y2_vel + 0.5774*y1_vel - 0.5774*x_vel);
                    yr_dot = -(-0.6667*y2_vel + 0.3333*y1_vel + 0.3333*x_vel);
                    hr_dot =  ( 6.5928*y2_vel + 6.5928*y1_vel + 6.5928*x_vel);



          /* 3rd order Cheby1 filter passband edge at 400Hz  */
         b1=  0.038540528;
         b2= 0.11562158;
         b3= 0.11562158;
```

```
b4= 0.038540528;

a2= -1.385891309;
a3=  0.903331647;
a4= -0.2091161133;


zr_filtered= b1*zr + b2*zr1 + b3*zr2 + b4*zr3 - a2*zr1_filtered - a3*zr2_filtered
             -a4*zr3_filtered;
zr_dot= (zr_filtered-zr1_filtered)/dt;

z_dot1= (z_pos1_old-z_pos1)/dt;
z_dot2= (z_pos2_old-z_pos2)/dt;
z_dot3= (z_pos3_old-z_pos3)/dt;

             /*NEW STAGE (end)*/


             /* controller */
             if (controller_flag == 1){

                 er0x=xc-xr;
                 er0y=yc-yr;
                 er0h=hc-hr;

                 er0z=zc-zr;
                 er0s=sc-sr;
                 er0t=tc-tr;

                 er0vx=0-xr_dot;
                 er0vy=0-yr_dot;


                 /*HORIZONTAL CONTROLLERS*/

             u0x = 1.42714428*u1x - 0.427144284*u2x + 532803.041*er0x + -
1052163.01*er1x + 519386.739*er2x;
                 u0y = 1.42714428*u1y - 0.427144284*u2y + 532803.041*er0y +
-1052163.01*er1y + 519386.739*er2y;
                 u0h = 1.44808411*u1h - 0.44808411*u2h +
(1769.3670617300*er0h + -3507.66909111000*er1h + 1738.3639498700*er2h);

    u0z = 1.65658873*u1z - 0.65658873*u2z + 232004.55154669*er0z + -
461593.23257734*er1z + 229591.41122804*er2z;
```

```
u0s = 1.65658873*u1s - 0.65658873*u2s +
0.5*(295.66660049*er0s + -588.25441560*er1s + 292.59129447*er2s);
u0t = 1.65658873*u1t - 0.65658873*u2t +
0.5*(295.66660049*er0t + -588.25441560*er1t + 292.59129447*er2t);


/*Force Transformation */
f1=u0z*0.3333 + u0s*0          - u0t*13.1765;
f2=u0z*0.3333 + u0s*11.4112 + u0t*6.5883;
f3=u0z*0.3333 - u0s*11.4112 + u0t*6.5883;

f4=              0*u0x - 0.6667*u0y - 6.5883*u0h;
f5= 0.5774*u0x + 0.3333*u0y - 6.5883*u0h;
f6=-0.5774*u0x + 0.3333*u0y - 6.5883*u0h;

/*6.3507 N/A is force constant (0.157463) */
/*5.4 N/A is force constant (0.18518) */
i1=0.18518*f1;
i2=0.18518*f2;
i3=0.18518*f3;


/* Considering the force to current conversion function of gap
between magnet and coil
     */
gap1 = 31e-4 - y2_pos;
gap2 = 31e-4 - y1_pos;
gap3 = 31e-4 - x_pos;

f2i1 = 1.41/(0.01469*gap1*gap1 - 0.3062*gap1 + 2.487);
f2i2 = 1.41/(0.01469*gap2*gap2 - 0.3062*gap2 + 2.487);
f2i3 = 1.41/(0.01469*gap3*gap3 - 0.3062*gap3 + 2.487);


i4 = -f2i3*f6;
i5 =  f2i1*f4;
i6 =  f2i2*f5;


/* Converion to DA voltage and limiting the maximum value
(i2v=2)  */
v1=i1*i2v;
if ((v1+vn1)>=2.5)  v1=2.4-vn1;
if ((v1+vn1)<=-2.5) v1=-2.4-vn1;
```

```
                    v2=i2*i2v;
                    if ((v2+vn2)>=2.5)  v2=2.4-vn2;
                    if ((v2+vn2)<=-2.5) v2=-2.4-vn2;
                    v3=i3*i2v;
                    if ((v3+vn3)>=2.5)  v3=2.4-vn3;
                    if ((v3+vn3)<=-2.5) v3=-2.4-vn3;

                    v4=i4*i2v;

                    if (v4>=4)  v4=4;
                    if (v4<=-4) v4=-4;
                    v5=i5*i2v;
                    if (v5>=4)  v5=4;
                    if (v5<=-4) v5=-4;
                    v6=i6*i2v;
                    if (v6>=4)  v6=4;
                    if (v6<=-4) v6=-4;

                }

                tr_low();

                if(flag_d2a==1)    {
                    *(unsigned int *)DA_FIFO_A1=(((unsigned
int)((v1+vn1)*6553.4)) <<16) & 0xffff0000 ;  /*6553.4=32767/5  */
                    *(unsigned int *)DA_FIFO_B1=(((unsigned
int)((v2+vn2)*6553.4)) <<16) & 0xffff0000;
                    *(unsigned int *)DA_FIFO_C1=(((unsigned
int)((v3+vn3)*6553.4)) <<16) & 0xffff0000;

                    *(unsigned int *)DA_FIFO_A2=(((unsigned
int)((prevA2+v5*hstart)*-6553.4)) <<16) & 0xffff0000;
                    *(unsigned int *)DA_FIFO_B2=(((unsigned
int)((prevB2+v6*hstart)*-6553.4)) <<16) & 0xffff0000;
                    *(unsigned int *)DA_FIFO_C2=(((unsigned
int)((prevC2+v4*hstart)*-6553.4*-1)) <<16) & 0xffff0000;
                }


                /* Set int_count for snap */
                if ((snap_begin==1) & (snap_enable==1))        {
                    int_count++;
                }
```

```
/*------------*/
/* For vibration control, u3z, er3z, ea3z, ea2z, ea1z, and ea0z were added */
/* For vibration control, u3z, er3z, ea3z, ea2z, ea1z, and ea0z were added */
                    u3z=u2z;
                    u2z=u1z;
                    u1z=u0z;

                    er3z=er2z;
                    er2z=er1z;
                    er1z=er0z;

                    u2s=u1s;
                    u1s=u0s;
                    er2s=er1s;
                    er1s=er0s;

                    u2t=u1t;
                    u1t=u0t;
                    er2t=er1t;
                    er1t=er0t;

                    u3x=u2x;
                    u2x=u1x;
                    u1x=u0x;

                    er3x=er2x;
                    er2x=er1x;
                    er1x=er0x;

                    u3y=u2y;
                    u2y=u1y;
                    u1y=u0y;

                    er3y=er2y;
                    er2y=er1y;
                    er1y=er0y;


                    u2h=u1h;
                    u1h=u0h;
                    er2h=er1h;
                    er1h=er0h;

                    display=1;
```

```
                MX_Int_Clr= 0x20000029;

                /**(unsigned int *)DA_FIFO_D1=(((unsigned int)((1.0)*6553.4))
<<16) & 0xffff0000 ;   /* timer test */
                *(unsigned int *)MX_Int_Clr=0x0;
}
```

## C.2 For Overall Vibration Control

```
void c_int01()
{
        unsigned long D1reading;
        long ADreading, ADreading1, ADreading2, ADreadingA,
DreadingB,ADreadingC,ADreadingD;
        long vel_x_platen1,vel_x_platen2;
        int i;
        float z_mea,Kp,Ki,Kpz,Kiz,abs_eraz;
        float dt,b1,b2,b3,b4,a2,a3,a4;   /* coefficients if Chebyshev Low pass filter
equation.*/

        dt=200e-6;  /* 200 ms = 1/5kHz : Time for one loop
        tr_low();

        *(unsigned long int *)0xb0300003=0x0041;
        raw_x_pos  = (*(long int *)0xb0300048 << 16) & 0xffff0000;
        raw_y1_pos = (*(long int *)0xb0310048 << 16) & 0xffff0000;
        raw_y2_pos = (*(long int *)0xb0320048 << 16) & 0xffff0000;

        raw_x_vel  = (*(long int *)0xb030004e << 16) & 0xffff0000;
        raw_y1_vel = (*(long int *)0xb031004e << 16) & 0xffff0000;
          raw_y2_vel = (*(long int *)0xb032004e << 16) & 0xffff0000;

        tr_high();
        raw_x_pos  |= ((*(long int *)0xb0300048 >> 16) & 0x0000ffff);
        raw_y1_pos |= ((*(long int *)0xb0310048 >> 16) & 0x0000ffff);
        raw_y2_pos |= ((*(long int *)0xb0320048 >> 16) & 0x0000ffff);

         raw_x_vel  |= ((*(long int *)0xb030004e >> 16) & 0x0000ffff);
         raw_y1_vel |= ((*(long int *)0xb031004e >> 16) & 0x0000ffff);
         raw_y2_vel |= ((*(long int *)0xb032004e >> 16) & 0x0000ffff);

        x_pos=raw_x_pos*6.1815119987e-10;       /* METERS-BIT approx 0.625 nm */
        y1_pos=raw_y1_pos*6.1815119987e-10;
```

```
y2_pos=raw_y2_pos*6.1815119987e-10;

x_vel = raw_x_vel * 3.77292037e-7;
                                /* lamda/(F*2^22*100ns)= 3.77292037e-7, */

y1_vel= raw_y1_vel* 3.77292037e-7;
                        /* where lamda is a laser wavelength (632.991 nm) */
y2_vel= raw_y2_vel* 3.77292037e-7;      /* F = 4 for plane mirror optics */


tr_low();

ADreading=*(unsigned long int *)AD_FIFO_A1;
ADreading1 = ADreading & 0x0000ffff;/* Channel A1  capacitance probe 1 */


if(ADreading1 & 0x8000) ADreading1 = ADreading1 | 0xffff0000;
z_pos1=ADreading1*7.629627369e-9+250e-6;

ADreading=*(unsigned long int *)AD_FIFO_B1;
ADreading1 = ADreading & 0x0000ffff; /* Channel B1 capacitance probe 2 */

if(ADreading1 & 0x8000) ADreading1 = ADreading1 | 0xffff0000;
 z_pos2=ADreading1*7.629627369e-9+250e-6;

ADreading=*(unsigned long int *)AD_FIFO_C1;
ADreading1 = ADreading & 0x0000ffff; /* Channel C1 capacitance probe 3 */

if(ADreading1 & 0x8000) ADreading1 = ADreading1 | 0xffff0000;
 z_pos3=ADreading1*7.629627369e-9+250e-6;


/*NEW STAGE (begin)*/
/*L1 = y2_pos, L2 = y1_pos, L3 = x_pos*/

xr = -(      0*y2_pos + 0.5774*y1_pos - 0.5774*x_pos);
yr = -(-0.6667*y2_pos + 0.3333*y1_pos + 0.3333*x_pos);
hr =  ( 6.5928*y2_pos + 6.5928*y1_pos + 6.5928*x_pos);

zr =      0.333333*z_pos1 + 0.333333*z_pos2 + 0.333333*z_pos3;
sr = 1000*(          0*z_pos1 + 0.0400*z_pos2 - 0.0400*z_pos3);
tr = 1000*(-0.0462*z_pos1 + 0.0231*z_pos2 + 0.0231*z_pos3);
xr_dot = -(      0*y2_vel + 0.5774*y1_vel - 0.5774*x_vel);
yr_dot = -(-0.6667*y2_vel + 0.3333*y1_vel + 0.3333*x_vel);
```

```
hr_dot =  ( 6.5928*y2_vel + 6.5928*y1_vel + 6.5928*x_vel);


sr_dot = 1000*(              0*z_pos1 + 0.0400*z_pos2 - 0.0400*z_pos3);
tr_dot = 1000*(-0.0462*z_pos1 + 0.0231*z_pos2 + 0.0231*z_pos3);


/* 3rd order Cheby1 filter passband edge at 400Hz  */
b1=  0.038540528;
b2= 0.11562158;
b3= 0.11562158;
b4= 0.038540528;

a2= -1.385891309;
a3=  0.903331647;
a4= -0.2091161133;


zr_filtered= b1*zr + b2*zr1 + b3*zr2 + b4*zr3 - a2*zr1_filtered - a3*zr2_filtered
             -a4*zr3_filtered;
zr_dot= (zr_filtered-zr1_filtered)/dt;

z_dot1= (z_pos1_old-z_pos1)/dt;
z_dot2= (z_pos2_old-z_pos2)/dt;
z_dot3= (z_pos3_old-z_pos3)/dt;


/*NEW STAGE (end)*/

/* controller */
if (controller_flag == 1){

er0x=xc-xr;
er0y=yc-yr;
er0h=hc-hr;

er0z=zc-zr;
er0s=sc-sr;
er0t=tc-tr;

er0vx=0-xr_dot;
er0vy=0-yr_dot;
er0vz=0-zr_dot;
```

```
/*HORIZONTAL CONTROLLERS*/

if (xc<=0){

u0x = 1.42714428*u1x - 0.427144284*u2x + 532803.041*er0x + -
1052163.01*er1x
        + 519386.739*er2x;
u0y = 1.42714428*u1y - 0.427144284*u2y + 532803.041*er0y + -
1052163.01*er1y
        + 519386.739*er2y;
 u0h = 1.44808411*u1h - 0.44808411*u2h + (1769.3670617300*er0h +
-3507.66909111000*er1h + 1738.3639498700*er2h);

u0z = 1.652482855*u1z - 0.652482855*u2z + 192913.035*er0z + -
383379.5985*er1z
+ 190469.3265*er2z;
u0s = 1.65658873*u1s - 0.65658873*u2s + 0.5*(295.66660049*er0s + -
588.25441560*er1s
+ 292.59129447*er2s);

u0t = 1.65658873*u1t - 0.65658873*u2t + 0.5*(295.66660049*er0t + -
588.25441560*er1t
+ 292.59129447*er2t);

}

else {

Kp=300;
Ki=0;

u0x = 1.42714428*u1x - 0.427144284*u2x + 532803.041*er0x + -
1052163.01*er1x
        + 519386.739*er2x;
u0x = u0x + (Kp+0.1e-3*Ki)*er0vx + (-1.42714428*Kp+Ki*0.572855716e-
4)*er1vx
         + (0.427144284*Kp + Ki*(-0.427144284e-4))*er2vx;

u0y = 1.42714428*u1y - 0.427144284*u2y + 532803.041*er0y + -
1052163.01*er1y
        + 519386.739*er2y;
u0y = u0y + (Kp+0.1e-3*Ki)*er0vy + (-1.42714428*Kp+Ki*0.572855716e-
4)*er1vy
        + (0.427144284*Kp + Ki*(-0.427144284e-4))*er2vy;
```

```
        u0h = 1.44808411*u1h - 0.44808411*u2h + (1769.3670617300*er0h +
                -3507.66909111*er1h + 1738.36394987*er2h);

        Kpz=100;
        Kiz=0;

        u0z = 1.652482855*u1z - 0.652482855*u2z + 0.6*(192913.035*er0z + -
383379.5985*er1z
                 + 190469.3265*er2z);
        u0z = u0z + (0.0001*Kiz + Kpz)*er0vz + (0.0000347517144*Kiz -
1.652482856*Kpz)*er1vz
                + (0.652482856*Kpz - 0.0000652482856*Kiz)*er2vz;

        u0s = 1.65658873*u1s - 0.65658873*u2s + 0.5*(295.66660049*er0s + -
588.25441560*er1s
                + 292.59129447*er2s);
        u0t = 1.65658873*u1t - 0.65658873*u2t + 0.5*(295.66660049*er0t + -
588.25441560*er1t
                + 292.59129447*er2t);
    }


/*Force Transformation */
        f1=u0z*0.3333 + u0s*0           - u0t*13.1765;
        f2=u0z*0.3333 + u0s*11.4112 + u0t*6.5883;
        f3=u0z*0.3333 - u0s*11.4112 + u0t*6.5883;

        f4=         0*u0x - 0.6667*u0y - 6.5883*u0h;
        f5= 0.5774*u0x + 0.3333*u0y - 6.5883*u0h;
        f6=-0.5774*u0x + 0.3333*u0y - 6.5883*u0h;

        /*6.3507 N/A is force constant (0.157463) */
        /*5.4 N/A is force constant (0.18518) */
        i1=0.18518*f1;
        i2=0.18518*f2;
        i3=0.18518*f3;

/* Considering the force to current conversion function of gap between magnet and coil
                        */
        gap1 = 31e-4 - y2_pos;
        gap2 = 31e-4 - y1_pos;
        gap3 = 31e-4 - x_pos;

        f2i1 = 1.41/(0.01469*gap1*gap1 - 0.3062*gap1 + 2.487);
```

```
        f2i2 = 1.41/(0.01469*gap2*gap2 - 0.3062*gap2 + 2.487);
        f2i3 = 1.41/(0.01469*gap3*gap3 - 0.3062*gap3 + 2.487);

        i4 = -f2i3*f6;
        i5 =  f2i1*f4;
        i6 =  f2i2*f5;
/* Converion to DA voltage and limiting the maximum value (i2v=2)  */
        v1=i1*i2v;
        if ((v1+vn1)>=2.5)  v1=2.4-vn1;
        if ((v1+vn1)<=-2.5) v1=-2.4-vn1;
        v2=i2*i2v;
        if ((v2+vn2)>=2.5)  v2=2.4-vn2;
        if ((v2+vn2)<=-2.5) v2=-2.4-vn2;
        v3=i3*i2v;
        if ((v3+vn3)>=2.5)  v3=2.4-vn3;
        if ((v3+vn3)<=-2.5) v3=-2.4-vn3;

        v4=i4*i2v;

        if (v4>=4)  v4=4;
        if (v4<=-4) v4=-4;
        v5=i5*i2v;
        if (v5>=4)  v5=4;
        if (v5<=-4) v5=-4;
        v6=i6*i2v;
        if (v6>=4)  v6=4;
        if (v6<=-4) v6=-4;

        }

        tr_low();

        if(flag_d2a==1)         {
                *(unsigned int *)DA_FIFO_A1=(((unsigned int)((v1+vn1)*6553.4))
<<16) & 0xffff0000 ;
                *(unsigned int *)DA_FIFO_B1=(((unsigned int)((v2+vn2)*6553.4))
<<16) & 0xffff0000;
                *(unsigned int *)DA_FIFO_C1=(((unsigned int)((v3+vn3)*6553.4))
<<16) & 0xffff0000;

                *(unsigned int *)DA_FIFO_A2=(((unsigned int)((prevA2+v5*hstart)*-
6553.4)) <<16) & 0xffff0000;
                *(unsigned int *)DA_FIFO_B2=(((unsigned int)((prevB2+v6*hstart)*-
6553.4)) <<16) & 0xffff0000;
```

```
                *(unsigned int *)DA_FIFO_C2=(((unsigned int)((prevC2+v4*hstart)*-
6553.4*-1)) <<16) & 0xffff0000;
        }

        /* Set int_count for snap */
        if ((snap_begin==1) & (snap_enable==1))    {
                int_count++;
        }

/* For vibration control, u3z, er3z, ea3z, ea2z, ea1z, and ea0z were added */
        u2s=u1s;
        u1s=u0s;
        er2s=er1s;
        er1s=er0s;
        u2t=u1t;
        u1t=u0t;

        er2t=er1t;
        er1t=er0t;7

        u3x=u2x;
        u2x=u1x;
        u1x=u0x;

        u3y=u2y;
        u2y=u1y;
        u1y=u0y;

        u3z=u2z;
        u2z=u1z;
        u1z=u0z;

        er3x=er2x;
        er2x=er1x;
        er1x=er0x;

        er3y=er2y;
        er2y=er1y;
        er1y=er0y;
        er3z=er2z;
        er2z=er1z;
        er1z=er0z;

        zr3=zr2;
```

```
        zr2=zr1;
        zr1=zr;

        zr3_filtered=zr2_filtered;
        zr2_filtered=zr1_filtered;
        zr1_filtered=zr_filtered;

        zr3_dot=zr2_dot;
        zr2_dot=zr1_dot;
        zr1_dot=zr_dot;

        z_pos1_old=z_pos1;
        z_pos2_old=z_pos2;
        z_pos3_old=z_pos3;

        er3vx=er2vx;
        er2vx=er1vx;
        er1vx=er0vx;

        er3vy=er2vy;
        er2vy=er1vy;
        er1vy=er0vy;

        er3vz=er2vz;
        er2vz=er1vz;
        er1vz=er0vz;

        er3az=er2az;
        er2az=er1az;
        er1az=er0az;

        u2h=u1h;
        u1h=u0h;
        er2h=er1h;
        er1h=er0h;

        display=1;
        MX_Int_Clr= 0x20000029;
        *(unsigned int *)MX_Int_Clr=0x0;
}
```

# VITA

## YOUNG HA KIM

### Education

**Texas A&M University**, College Station, December 2011,
Doctor of Philosophy in Mechanical Engineering
Dissertation advisor: Won-jong Kim

**Pennsylvania State University**, University Park, August 2001,
Master of Science in Aerospace Engineering
Thesis advisor: David B. Spencer

**Inha University**, Incheon, Republic of Korea, February 1999,
Bachelor of Engineering in Aerospace Engineering

### Publications

[1] Y. H. Kim and D. B. Spencer, "Optimal spacecraft rendezvous using genetic algorithms", *Journal of Spacecraft and Rockets*, vol. 39, no. 6, pp. 859–865, November 2002.

[2] D. B. Spencer and Y. H. Kim, "Optimal orbital rendezvous using genetic algorithms", AAS 01-477, in *Proceedings of AAS/AIAA Astrodynamics Specialists Conference*, Quebec City, Canada, July-August 2001.

### Permanent Address

Texas A&M University
Department of Mechanical Engineering
3123 TAMU
College Station TX 77843-3123
c/o Won-jong Kim

### Email Address:

kim.youngha@gmail.com